

PURDUE UNIVERSITY
GRADUATE SCHOOL
Thesis/Dissertation Acceptance

This is to certify that the thesis/dissertation prepared

By Zhuoxiong Sun

Entitled

Cyber-Physical Codesign of Wireless Structural Control System

For the degree of Doctor of Philosophy



Is approved by the final examining committee:

Shirley Dyke

Chair

Bin Yao

Ayhan Irfanoglu

Douglas Admas

To the best of my knowledge and as understood by the student in the Thesis/Dissertation Agreement, Publication Delay, and Certification Disclaimer (Graduate School Form 32), this thesis/dissertation adheres to the provisions of Purdue University's "Policy of Integrity in Research" and the use of copyright material.

Approved by Major Professor(s): Shirley Dyke

Approved by: Anil Bajaj

Head of the Departmental Graduate Program

10/13/2015

Date

CYBER-PHYSICAL CODESIGN OF WIRELESS STRUCTURAL CONTROL SYSTEM

A Dissertation

Submitted to the Faculty

of

Purdue University

by

Zhuoxiong Sun

In Partial Fulfillment of the

Requirements for the Degree

of

Doctor of Philosophy

December 2015

Purdue University

West Lafayette, Indiana

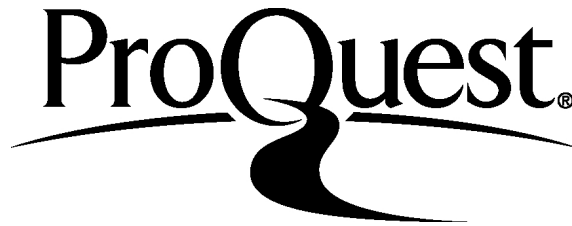
ProQuest Number: 10075595

All rights reserved

INFORMATION TO ALL USERS

The quality of this reproduction is dependent upon the quality of the copy submitted.

In the unlikely event that the author did not send a complete manuscript and there are missing pages, these will be noted. Also, if material had to be removed, a note will indicate the deletion.



ProQuest 10075595

Published by ProQuest LLC (2016). Copyright of the Dissertation is held by the Author.

All rights reserved.

This work is protected against unauthorized copying under Title 17, United States Code
Microform Edition © ProQuest LLC.

ProQuest LLC.
789 East Eisenhower Parkway
P.O. Box 1346
Ann Arbor, MI 48106 - 1346

To my wife Jia and my parents

ACKNOWLEDGEMENTS

I would like to express my deep gratitude to my advisor, Professor Shirley Dyke, for her guidance, encouragement and support during my PhD study. She has always been enthusiastic and dedicated to academic research and she has provided tremendous support to my work. She is an excellent mentor and friend. I am very lucky to be her student. I would also like to express my appreciation to the members of my committee, Professor Ayhan Irfanoglu, Professor Douglas Adams and Professor Bin Yao for their time and effort in reviewing this dissertation.

I would like to thank my collaborators Professor Chenyang Lu and Bo Li from Washington University in St. Louis. Our biweekly meeting has a lot of meaningful discussions on cyber-physical system. I would also like to thank Lauren Linderman and Kirill Mechitov from University of Illinois for sharing their knowledge on imote2 wireless sensor. I would like to thank Professor Bin Wu and Professor Hui Li for supporting the experimental study at Harbin Institute of Technology for one month.

I would like to thank my IISL lab members for their friendship. I have a lot of good memories with Gaby, Wei, Xiuyu, Nestor, Ali, Tony, Sriram, Fangshu, Cindy, Amin,

Chul Min, Christian, Francisco, Daniel, Alana, Chris, etc. I cannot imagine my PhD life without their company.

Finally, I would like to thank my parents and my wife Jia. Without their continuous encouragement, support and love, this work would not be possible.

The financial support for this research work is provided by National Science Foundation under Grant CNS-1035748.

TABLE OF CONTENTS

	Page
LIST OF TABLES	viii
LIST OF FIGURES	ix
ABSTRACT	xvii
CHAPTER 1.INTRODUCTION.....	1
1.1 Literature Review.....	5
1.1.1 Wireless Control Strategies	6
1.1.2 Wireless Control Algorithms	8
1.1.3 Wireless Sensor Network	15
1.1.4 Wireless Sensors for Civil Infrastructure	18
1.2 Overview of the Dissertation	26
CHAPTER 2.WIRELESS CYBER-PHYSICAL SIMULATOR (WCPS)	30
2.1 Introduction to WCPS.....	30
2.2 Case Study: Wireless Benchmark Building Control.....	34
2.2.1 Building Model	35
2.2.2 Building Network Model	36
2.2.3 Impact of Time Delay to the Control System	38
2.2.4 Codesign of Building Control System	45
2.2.4.1 Data Aggregation Strategy	45
2.2.4.2 Control Design	47
2.2.5 Wireless Building Control with Codesigned Control System	49
2.2.6 Additional Studies with Wireless Building Control	54
2.3 Case Study: Wireless Benchmark Bridge Control.....	58
2.3.1 Bridge Model	59
2.3.2 Bridge Network Model	60
2.3.3 Impact of Wireless Network to the Control System	61
2.3.4 Codesign of Bridge Control System	64
2.3.4.1 Data Transmission Strategy	64
2.3.4.2 Control Design	66
2.3.5 Wireless Bridge Control with Codesigned Control System	66
2.3.5.1 Evaluation Criteria	70

	Page
2.3.5.2 Evaluation Results	73
2.4 Summary	75
CHAPTER 3. ARDUINO BASED WIRELESS STRUCTURAL CONTROL PLATFORM DEVELOPMENT	76
3.1 Introduction to Arduino Board.....	76
3.2 Sensing Module Development.....	78
3.3 Communication Module Development.....	84
3.4 Actuation Module Tests	88
3.5 Summary	89
CHAPTER 4. WIRELESS CONTROL OF A 3-STORY SHEAR BUILDING.....	90
4.1 Numerical Simulation	90
4.1.1 Damper Model Identification	92
4.1.2 Control Design.....	98
4.1.3 Numerical Simulation	100
4.2 Experimental Study.....	113
4.2.1 System Identification	115
4.2.2 Control System Setup	122
4.2.3 Verification Tests.....	124
4.2.4 Experimental Results	129
4.3 Summary	146
CHAPTER 5. A CODESIGN APPROACH WITH PROPOSED SWITCHING ESTIMATOR	148
5.1 Proposed Estimator Switching Method	148
5.2 Numerical Study to Evaluate the Estimator Switching Method	153
5.3 Numerical Investigation of the Estimator Switching Method with Transmission Delay	165
5.4 Summary	175
CHAPTER 6. FAULT TOLERANCE IN WIRELESS CONTROL SYSTEM.....	176
6.1 Fault Tolerance Study with RTHS.....	176
6.1.1 RTHS Implementation.....	177
6.1.2 Structural Model	180
6.1.3 Wireless Sensor Network Model and Control Design.....	182
6.1.4 Actuator Tracking Control.....	183
6.1.5 Experimental Results of Fault Tolerance Study	185
6.1.6 Sensitivity of RTHS Tests	193
6.2 Evaluation of Estimator Switching Method with RTHS	195
6.3 Summary	201

	Page
CHAPTER 7. CONCLUSIONS AND FUTURE WORK.....	203
7.1 Summary of Conclusions	203
7.2 Future Work	207
LIST OF REFERENCES	210
APPENDICES	
APPENDIX A. WIRELESS NODE WIRING DIAGRAM	223
APPENDIX B. A/D CONVERTER BOARD DESIGN	235
APPENDIX C. CONTROLLER AND ESTIMATOR GAIN OF THE BRIDGE CASE STUDY	237
VITA	239

LIST OF TABLES

Table	Page
Table 1.1. Comparison of different wireless standards.....	16
Table 1.2. Representative wireless sensors.....	20
Table 2.1. Evaluation criteria.....	41
Table 2.2. Comparison of different strategies.....	46
Table 2.3. Evaluation results.....	54
Table 2.4. Evaluation results for 1 hop network.....	58
Table 2.5. Comparison of different strategies.....	65
Table 2.6. Evaluation results for wireless control.....	74
Table 2.7. Actuator requirements for wireless control.	74
Table 3.1. Wireless sensor platform comparison.....	78
Table 3.2. Measurement error.....	82
Table 3.3. Computational time.....	87
Table 4.1. Identified damper parameters.	97
Table 4.2. Comparison of natural frequencies.....	118
Table 4.3. Wireless control setup.....	123
Table 4.4. Experimental results I.....	139
Table 4.5. Experimental results II.....	146
Table 5.1. Switching cases.....	153
Table 5.2. Simulation results.	174
Table 6.1. RTHS implementation procedure.	179
Table 6.2. Tracking performance.....	185
Table 6.3. Data loss cases studied.....	185
Table 6.4. Control performance of different cases.	191
Table 6.5. Control performance of different cases with switching estimator.....	201

LIST OF FIGURES

Figure	Page
Figure 1.1. Wireless control strategies: (a) Centralized control, (b) Decentralized control, (c) Partially decentralized control, (d) Hierarchically decentralized control.....	7
Figure 1.2. The classical Smith predictor.	9
Figure 1.3. Network topologies.	17
Figure 1.4. Components of wireless nodes for structural control.	21
Figure 1.5. Wireless control system: (a) Developed control unit, (b) Control unit connected to wireless sensor.	22
Figure 1.6. MTS310CA sensor board.	23
Figure 1.7. Block diagram of the controller.....	23
Figure 1.8. (a) SHM-SAR board, (b) SHM-D2A board.	24
Figure 1.9. Martlet sensor board.	25
Figure 1.10. Arduino Due board.	26
Figure 2.1. Architecture of WCPS.....	34
Figure 2.2. Wireless benchmark building control.....	35
Figure 2.3. Bryan Hall used for collecting signal/noise traces deployment.	37
Figure 2.4. Wireless sensor deployment.	38
Figure 2.5. Noise traces of floor 1 to floor 4.	38
Figure 2.6. Peak interstory drift with different constant delay.	39
Figure 2.7. Peak acceleration with different constant delay.	40
Figure 2.8. Monte Carlo simulation results: (a) $J6$ with 8-step delay, (b) $J7$ with 8-step delay, (c) $J6$ with 9-step delay, (d) $J7$ sim with 9-step delay.	42
Figure 2.9. TDMA transmission of sensor data.	43
Figure 2.10. Received data at base station.	43
Figure 2.11. Received data at base station for proposed S1 strategy.....	44

Figure	Page
Figure 3.2. (a) Arduino based sensor board, (b) Developed ADC board.	80
Figure 3.3. SPI interface for communication with multiple devices.	80
Figure 3.4. ADC board test results: (a) ADC measurements at 0V, (b) PSD of the measurements in (a); (c) ADC measurements at 2V, (d) PSD of the measurements in (c).	82
Figure 3.5. Sensor tests: (a) Test setup, (b) Test results at 100Hz, (c) Zoomed view of (b), (d) Frequency domain comparison, (e) Test results at 200Hz, (f) Zoomed view of (e).	83
Figure 3.6. Transmission delay test.	85
Figure 3.7. Transmission test results for XBee S1 (a) Sensor 1, (b) Sensor 1 and 2; Transmission test results for XBee S2 (c) Sensor 1, (d) Sensor 1, 2 and 3. ...	86
Figure 3.8. Computational time.	88
Figure 3.9. Actuation module test: (a) DAC test, (b) Digital output test.	89
Figure 4.1. Three story shear building.	92
Figure 4.2. (a) Shear mode MR damper, (b) Bouc-Wen model.	93
Figure 4.3. Damper identification test setup.	95
Figure 4.4. Damper ID procedure.	95
Figure 4.5. Measured data vs filtered data (4Hz sine wave).	96
Figure 4.6. Filtered data vs identified model (3 Hz sine wave, 1.0V voltage).	96
Figure 4.7. Filtered data vs identified model (3 Hz sine wave, 1.5V voltage).	97
Figure 4.8. (a) Wireless case 1, (b) Wireless case 2, (c) Wireless case 3,	98
Figure 4.9. Simulink diagram for wireless control simulation.	101
Figure 4.10. Normalized acceleration vs normalized drift.	102
Figure 4.11. Normalized acceleration vs peak force.	103
Figure 4.12. RMS interstory drift response under BLWN excitation.	103
Figure 4.13. RMS acceleration response under BLWN excitation.	104
Figure 4.14. Power spectrum of 3 rd floor acceleration.	104
Figure 4.15. El Centro earthquake.	105
Figure 4.16. RMS interstory drift response under El Centro earthquake.	106
Figure 4.17. RMS acceleration response under El Centro earthquake.	106

Figure	Page
Figure 4.18. RMS acceleration response under E1: El Centro Earthquake, E2: Northridge Earthquake, E3: Kobe Earthquake, and E4: Hachinohe Earthquake.	107
Figure 4.19. RMS drift response under E1-E4 earthquakes.	107
Figure 4.20. RMS interstory drift response under El Centro earthquake.	110
Figure 4.21. RMS acceleration response under El Centro earthquake.	110
Figure 4.22. RMS interstory drift response under Northridge earthquake.	111
Figure 4.23. RMS acceleration response under Northridge earthquake.	111
Figure 4.24. RMS drift response under E1-E4 earthquakes.	112
Figure 4.25. RMS acceleration response under E1-E4 earthquakes.	112
Figure 4.26. Experimental structure on the shake table.	113
Figure 4.27. Ground input to shake table.	114
Figure 4.28. (a) dSPACE controller and I/O board, (b) Shore Western system.	114
Figure 4.29. BLWN ground input spectrum.	116
Figure 4.30. Transfer function from ground acceleration to 1 st floor acceleration.	117
Figure 4.31. Transfer function from ground acceleration to 2 nd floor acceleration.	117
Figure 4.32. Transfer function from ground acceleration to 3 rd floor acceleration.	118
Figure 4.33. Comparison of mode shapes.	119
Figure 4.34. Hammer test.	119
Figure 4.35. Hammer input power spectrum.	120
Figure 4.36. Transfer function from hammer force to 1 st floor acceleration.	120
Figure 4.37. Transfer function from hammer force to 2 nd floor acceleration.	121
Figure 4.38. Transfer function from hammer force to 3 rd floor acceleration.	121
Figure 4.39. Wireless control architecture.	123
Figure 4.40. (a) Wireless sensor on the 1st floor, (b) MR damper setup.	124
Figure 4.41. DAQ systems: (a) Vibpilot DAQ system, (b) Krypton system.	124
Figure 4.42. Force comparison.	126
Figure 4.43. Voltage comparison.	126
Figure 4.44. Acceleration comparison under BLWN excitation.	127
Figure 4.45. Acceleration comparison under El Centro excitation.	127

Figure	Page
Figure 4.46. Ground displacement with El Centro earthquake.....	128
Figure 4.47. Ground displacement with Kobe earthquake.	128
Figure 4.48. Wired control Simulink diagram for dSPACE.	129
Figure 4.49. Interstory drift responses under Chichi earthquake.....	131
Figure 4.50. Acceleration responses under Chichi earthquake.....	131
Figure 4.51. Force comparison.	132
Figure 4.52. Voltage comparison.....	132
Figure 4.53. Voltage comparison (zoomed view).....	133
Figure 4.54. Interstory drift responses under El Centro earthquake.	133
Figure 4.55. Acceleration responses under El Centro earthquake.	134
Figure 4.56. Interstory drift responses under Northridge earthquake.	134
Figure 4.57. Acceleration responses under Northridge earthquake.....	135
Figure 4.58. Interstory drift responses under Kobe earthquake.....	135
Figure 4.59. Acceleration responses under Kobe earthquake.....	136
Figure 4.60. Normalized RMS drift (J_3) under E1: El Centro Earthquake, E2: Chichi Earthquake, E3: Northridge Earthquake, and E4: Kobe Earthquake.	138
Figure 4.61. Normalized RMS acceleration (J_4) under E1-E4 earthquakes.....	139
Figure 4.62. Force comparison of wireless case 2.	141
Figure 4.63. Force comparison of wireless case 2 (Zoomed view).	142
Figure 4.64. Voltage comparison of wireless case 2.	142
Figure 4.65. Force comparison of wireless case 4.	143
Figure 4.66. Voltage comparison of wireless case 4.	143
Figure 4.67. Interstory drift responses under El Centro earthquake.	144
Figure 4.68. Acceleration responses under El Centro earthquake.	144
Figure 4.69. Normalized peak acceleration (J_2) under E1-E4 earthquakes.	145
Figure 4.70. Normalized RMS acceleration (J_4) under E1-E4 earthquakes.	145
Figure 5.1. Simulink model including switching estimator.....	156
Figure 5.2. Estimation of 3 rd story velocity with sensor failure.....	157
Figure 5.3. Zoomed view of figure 5.2.	157

Figure	Page
Figure 5.4. Estimation error with different probability of data loss.	158
Figure 5.5. Average estimation error with different probability of data loss.	158
Figure 5.6. Estimation error of original Kalman filter with different time step	159
Figure 5.7. Estimation error of switching estimator with different time step.....	159
Figure 5.8. Typical realization of wireless transmission with 20% of data loss.....	161
Figure 5.9. Estimation error of original Kalman filter with data loss in all sensors.	161
Figure 5.10. Estimation error of the switching estimator with data loss in all sensors. .	162
Figure 5.11. Estimation error of switching estimator with data loss in all sensors and 10% RMS measurement noises.....	162
Figure 5.12. Transfer function of the system (magnitude)	163
Figure 5.13. Transfer function of the system (phase)	163
Figure 5.14. Estimation error of switching estimator with data loss in all sensors and 2% modeling error.....	164
Figure 5.15. Estimation error of switching estimator with data loss in all sensors, 10% RMS measurement noises and 2% modeling error.	164
Figure 5.16. Estimation error of switching estimator with 20% data loss in all sensors and modeling error.	165
Figure 5.17. Simulink diagram for the 2 nd case study.....	167
Figure 5.18. Comparision of RMS drift response under BLWN excitation.	167
Figure 5.19. Comparision of RMS acceleration response under BLWN excitation.....	168
Figure 5.20. Comparision of 1 st story drift response under El Centro earthquake.	168
Figure 5.21. Comparision of 3 rd story acceleration response under El Centro earthquake.....	169
Figure 5.22. Comparision of RMS drift response under El Centro earthquake.....	169
Figure 5.23. Comparision of RMS acceleration response under El Centro earthquake.	170
Figure 5.24. Comparision of 1 st story drift response under Hachinohe earthquake.	170
Figure 5.25. Comparision of 3 rd story acceleration response under Hachinohe earthquake.....	171
Figure 5.26. Comparision of RMS drift response under Hachinohe earthquake.....	171
Figure 5.27. Comparision of RMS acceleration response under Hachinohe earthquake.....	172
Figure 5.28. Comparision of RMS drift response under Gebze earthquake.	172

Figure	Page
Figure 5.29. Comparison of RMS acceleration response under Gebze earthquake.	173
Figure 6.1. RTHS configuration for wireless control study.....	178
Figure 6.2. Schematic drawing of RTHS implementation.....	180
Figure 6.3. Three-story frame structure.	181
Figure 6.4. Comparison of experimental and identified transfer functions.	182
Figure 6.5. Experimental setup.	184
Figure 6.6. Comparison of desired displacement and measured displacement (BLWN) with RIAC controller.....	184
Figure 6.7. Comparison of desired displacement and measured displacement (Sine)....	184
Figure 6.8. Structural response under Mexico City earthquake.....	187
Figure 6.9. Structural response under Gebze earthquake.	187
Figure 6.10. Evaluation results for criterion J1.....	188
Figure 6.11. Evaluation results for criterion J2.....	188
Figure 6.12. Evaluation results for criterion J3.....	189
Figure 6.13. Evaluation results for criterion J4.....	189
Figure 6.14. Evaluation results for BLWN excitation.	190
Figure 6.15. Control system representation with 3 sensor measurements.	192
Figure 6.16. Evaluation results for BLWN excitation.	193
Figure 6.17. Boxplot of evaluation criterion (a) J1, (b) J2, (c) J3, and (d) J4 under El Centro earthquake.	194
Figure 6.18. Boxplot of criterion (a) J2 and (b) J4 under Mexico City earthquake.....	195
Figure 6.19. Boxplot of criterion (a) J2 and (b) J4 under Gebze earthquake.	195
Figure 6.20. Structural response under El Centro earthquake.	198
Figure 6.21. Structural response under Mexico City earthquake.....	198
Figure 6.22. Structural response under Gebze earthquake.	199
Figure 6.23. Evaluation results of J1 and J2.	199
Figure 6.24. Evaluation results of J3 and J4.	200

Appendix Figure	Page
Figure A.1. Wiring diagram of wireless node.....	223
Figure B.1. Electronic circuit of the ADC board.	235
Figure B.2. PCB layout design of the ADC board.....	236
Figure B.3. Fabricated ADC board.	236

ABSTRACT

Sun, Zhuoxiong. Ph.D., Purdue University, December 2015. Cyber-Physical Codesign of Wireless Structural Control System. Major Professor: Shirley Dyke, School of Mechanical Engineering.

Structural control systems play a critical role in protecting civil infrastructure from natural hazards such as earthquakes and extreme winds. Utilizing wireless sensors for sensing, communication and control, wireless structural control systems provide an attractive alternative for structural vibration mitigation. Although wireless control systems have advantages of flexible installation, rapid deployment and low maintenance cost, there are unique challenges associated with them, such as wireless network induced time delay and potential data loss. These challenges need to be considered jointly from both the network (cyber) and control (physical) perspectives. This research aims to develop a framework facilitating cyber-physical codesign of wireless control system. The challenges of wireless structural control are addressed through: (1) a numerical simulation tool to realistically model the complexities of wireless structural control systems, (2) a codesign approach for designing wireless control system, (3) a sensor platform to experimentally evaluate wireless control performance, (4) an estimation method to compensate for the data loss and sensor failure, and (5) a framework for fault tolerance study of wireless control system with real-time hybrid simulation. The results of this work not only provide codesign tools to evaluate and validate wireless control design,

but also the codesign strategies to implement on real-world structures for wireless structural control.

CHAPTER 1. INTRODUCTION

Civil infrastructure is vulnerable to natural hazards such as earthquakes and extreme weather conditions. Each year, structural damage and failure due to catastrophic natural hazards cause tremendous economic loss and loss of lives. During Wenchuan earthquake (magnitude 8.0) occurred in Sichuan China in 2008, about 70,000 people were killed, 370,000 were injured, 18,000 listed as missing and 4.8 million people were left homeless. The economic loss was over US \$130 billion. It took four years to rebuild the area ravaged by the earthquake (Sichuan earthquake, 2008). During the Chile earthquake (magnitude 8.8) in 2010, 525 people lost their lives, 25 people went missing and about 9% of the population in the affected regions lost their homes. The resulting financial losses to the economy of Chile have been estimated at US \$15-30 billion (Chile earthquake, 2010). In the Haiti earthquake (magnitude 7.0) in 2010, more than 200,000 people were killed and over 300,000 were injured. The damage due to this disaster reached an estimated total loss of US \$7.8 billion (Haiti earthquake, 2010). These tragedies highlight the importance of investigating and implementing innovative structural control strategies to protect civil structures from natural hazards.

Over the past few decades, serious research efforts have been undertaken to develop workable strategies for civil infrastructure, with particular emphasis on the alleviation of

seismic and wind response of buildings and bridges. One approach is to design structures with sufficient strength capacity and the ability to deform in a ductile manner (Anson, Ko, & Lam, 2002). Since the undesired disturbances are dynamic in nature and highly uncertain with respect to magnitude and arrival time, the uncertainties make the structural design challenging at times and costly (Hu, 2012). Another approach is to include structural control systems for structural vibration control. Structural control systems by increasing damping, altering mass, stiffness or providing active control force to the structures have shown great potential for mitigating structural vibrations (Housner, et al., 1997; Tanaka, et al., 2003; Spencer & Nagarajaiah, 2003; Saaed, et al., 2013).

There are four major categories of structural control systems (Symans & Constantinou, 1999) classified by the characteristics of the device employed: (1) passive control, (2) active control, (3) hybrid control, and (4) semi-active control. Passive control systems only act to dissipate energy from the structure and they do not require an external power supply. This character allows these systems to be bounded input bounded output (BIBO) stable. Examples of passive control systems include base isolation system (Wilde, et al., 2000), friction damper (Pall & Pall, 1996) and tuned mass damper (TMD) (Kwok & Samali, 1995). There are successful implementations of passive control systems in several real world buildings and bridges. The most famous one is the application of a TMD system in Taipei 101.

Passive control systems are simple and reliable. However, they are limited in that they cannot adapt to dynamic loadings with various magnitudes. Active control systems on the

contrary, can adapt to different loading conditions and apply appropriate control forces to the structure in real-time. In active control systems, sensors are installed in different locations of the structure to measure structural responses or excitation. Controller(s) utilize collected sensor measurements to generate control signals, and send the control commands to active control device for closed-loop feedback control. Active control systems include active bracing systems (Soong, et al., 1992), active mass drivers (AMD) (Spencer, et al., 1998) and active tendon systems (Bani-Hani & Ghaboussi, 1998). With the adaptability, active control systems can often provide superior response reductions to that of passive control systems. Also, because the control system is flexible, multiple control objectives can be achieved. However, there are also some limitations and drawbacks to active control systems including that they need external power to operate. Natural hazards can potentially disrupt the power source, and limit the effectiveness of the control system. Additionally, these system may become unstable due to improper control design, sensor failure or model uncertainty.

As an alternative, hybrid control systems are established utilizing both active and passive control systems. Because multiple control devices are adopted, hybrid control systems can alleviate some of the restrictions and limitations that exist when each system is acting alone. Thus, higher levels of performance may be achievable (Friedman, 2012). Additionally, the resulting hybrid control system can be more reliable than an active system, although it is often more complicated as well. Examples of hybrid control systems include hybrid mass damper (HMD) (Fisco & Adeli, 2011) and active base isolation (ABI) system (Chang, Wang, & Spencer, 2009). Hybrid mass dampers (HMD)

combine a passive control tuned-mass damper and an active control actuator, while ABI combines a passive base isolation system with hydraulic actuators.

The last category, semi-active control combines aspects of both passive and active control. On the one hand, semi-active control is dissipative in nature and inherently stable, similar to a passive control system. On the other hand, feedback measurements are used by a controller to produce an appropriate signal to the semi-active control device, so the semi-active control system is adaptable, like an active control system. Furthermore, only a small external power source is required for the operation of a semi-active control device. If a power outage happens, the semi-active control system will turn into a passive system. As with active control, the performance of semi-active control is reliant on the ability of control algorithms implemented in the system. Examples of semi-active devices include variable friction/stiffness dampers (Zhou & Peng, 2009), variable orifice dampers and controllable fluid dampers (Spencer, et al., 1997; Wang & Gordaninejad, 1999). These semi-active devices are implemented in the same manner as an active control device.

Traditional active, hybrid and semi-active structural control systems often employ cables for communication among sensors, controllers and actuators. In such systems, installation of wired sensors is usually quite time consuming and expensive. Additionally, it is inefficient to deploy such extensive cabling on large scale civil structures (Farrar, et al., 2006; Chintalapudi, et al., 2006; Loh, et al., 2007; Lynch, et al., 2008) such as bridges, buildings and dams. In recent years, wireless structural control has been given increased attention as an alternative to wired control systems. Reduced installation time and

maintenance cost coupled with low energy consumption (Nagayama & Spencer, 2007; Wang, et al., 2007b; Kim, et al., 2007; Casciati & Chen, 2013) makes wireless control very attractive compared to traditional wired control system.

Wireless control systems with wireless sensors, controller and actuation components fall into the category of cyber-physical systems. A cyber-physical system (CPS) is a system of collaborating computational elements controlling physical entities (Cyber-physical system, 2014). Although this concept does not define a type of new system, the recent development of CPS approach put special emphasis on the unification of the theories of control, networking, physics, and the interactions thereof in order to leverage enabling technological trends to solve grand challenges (Sztipanovits, et al., 2013; Ying, et al., 2013; Kane, 2014). The adoption of CPS codesign approach to wireless control systems in civil infrastructure enables us to consider the wireless sensor network (cyber) perspective and structural control (physical) perspective in a holistic manner to achieve better control performances than considering those two parts in an isolated way.

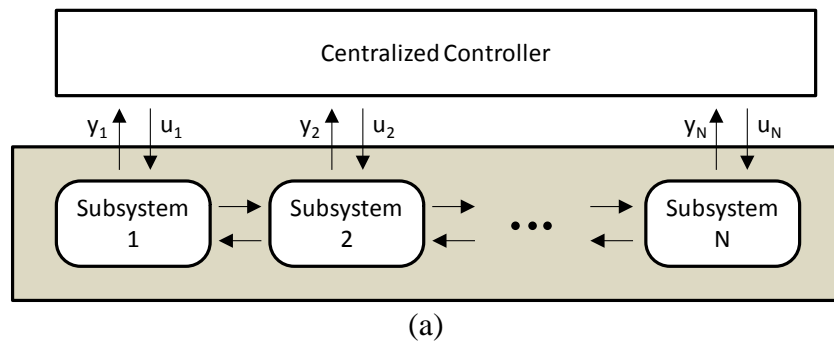
1.1 Literature Review

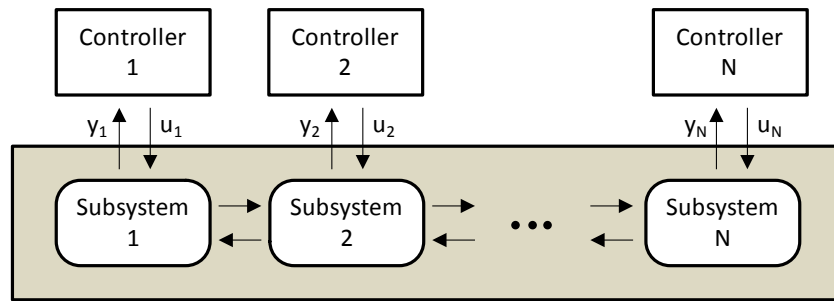
Wireless structural control systems utilize wireless sensors for sensing, communication, control and actuation. Each wireless sensor board has certain computational power which gives researchers the flexibility to explore different control strategies beyond that used with the wired control systems.

1.1.1 Wireless Control Strategies

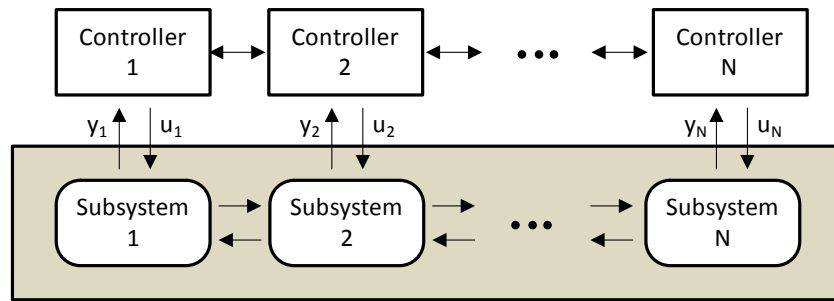
Researchers have developed multiple strategies for wireless structural control. Based on the centralization of control system, the wireless control system can be divided into four categories (Lynch & Law, 2002): (1) centralized control, (2) decentralized control, (3) partially decentralized control, and (4) hierarchically decentralized control. Centralized control is commonly used in a traditional wired control system as shown in Figure 1.1 (a). The sensor measurements from each subsystem is sent to a central control unit to make control decisions for the overall system, and control commands are sent back to each subsystem. However, this type of system is vulnerable to a single point of failure at the centralized controller. Also the wireless transmission delay will increase proportionally to the network size implementing this strategy. Decentralized control, on the contrary, has local controller for each subsystem (Figure 1.1 (b)). There is no data sharing among different subsystems. A decentralized control system is typically more reliable than centralized system and it minimizes wireless communication delay. However, the impact of local control effort on global responses is unknown. Partially decentralized system allows data sharing to some extent (i.e. with a neighboring subsystem) as shown in Figure 1.1 (c). It is a compromise between the centralized control and fully decentralized control.

The last type

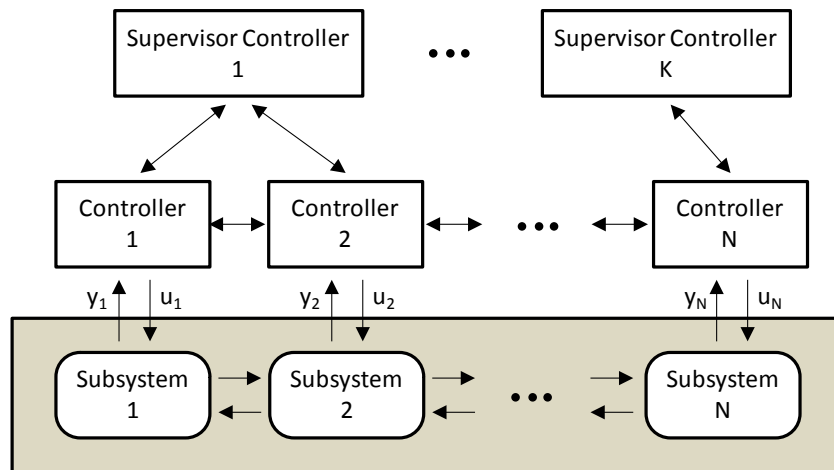




(b)



(c)



(d)

Figure 1.1. Wireless control strategies: (a) Centralized control, (b) Decentralized control, (c) Partially decentralized control, (d) Hierarchically decentralized control (Courtesy of Lynch & Law, 2002).

hierarchically decentralized control (Figure 1.1 (d)) has superior controllers to coordinate the behavior of local controllers to improve the global performances. Due to the complexity and economical considerations, the performances of hierarchically decentralized control has not been considered in the literature at this time.

1.1.2 Wireless Control Algorithms

In a wireless control system, the extensive cabling issue is minimized. However, there are inherent challenges associated with wireless system such as wireless transmission delay and data loss. One way to reduce those effects is to use decentralized or partial decentralized control strategies to reduce wireless communication. On the other hand, structural control algorithms which take these effects into account must also be considered.

Time delayed control systems are considered in different areas. For a linear time-invariant (LTI) system with long dead time (time delay), the Smith predictor (Smith, 1957) is a well-known control algorithm for process control as shown in Figure 1.2. It is a type of model-based predictive control for systems with deterministic time delay. The closed loop transfer function is given by

$$T(s) = \frac{Y(s)}{R(s)} = \frac{C(s)P(s)e^{-\tau s}}{1 + C(s)(P_m(s) + P(s)e^{-\tau s} - P_m(s)e^{-\tau_m s})} \quad (1.1)$$

where $C(s)$, $P_m(s)e^{-\tau_m s}$, $P(s)e^{-\tau s}$ are respectively, the controller, the dynamic model of the plant and the transfer function of the plant. If the model matches perfectly the plant dynamics, $P(s)e^{-\tau s} - P_m(s)e^{-\tau_m s} = 0$, the closed loop transfer function reduces to

$$T(s) = \frac{Y(s)}{R(s)} = \frac{C(s)P(s)e^{-\tau s}}{1+C(s)P_m(s)} \quad (1.2)$$

From Equation (1.2), the controller $C(s)$ which typically adopts PI or PID control algorithm can be determined using a model of the delay free part of the plant.

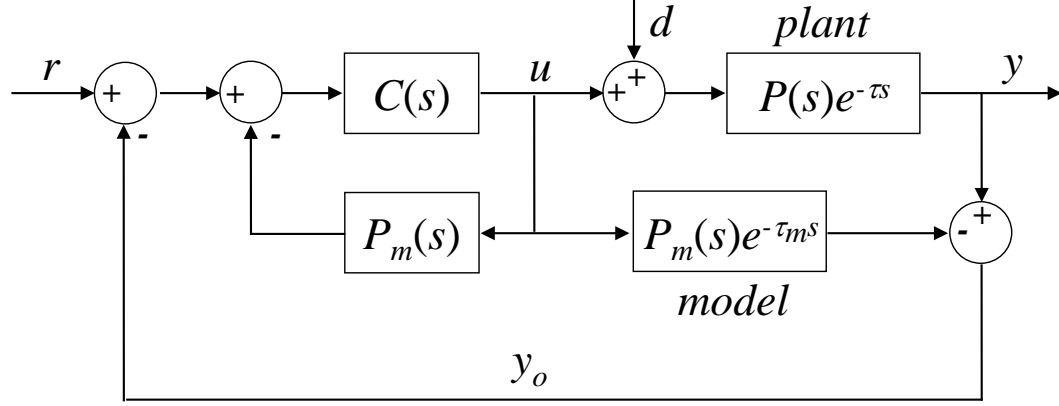


Figure 1.2. The classical Smith predictor.

There are also modified versions of the original Smith predictor. Bahill, (1983), for example, proposes a simple adaptive Smith predictor for systems with time varying model parameters. Sánchez-Peña, et al., (2009) extends the analysis of the Smith predictor to multiple-input, multiple-output (MIMO) systems with uncertain multiple delays. Dang, et al., (2012) combines the Smith predictor with neural network estimation scheme for compensating varying time delay in networked control system. Uma & Rao, (2014) develop an enhanced modified Smith predictor for second-order non-minimum phase unstable processes.

A second type of control algorithms adopts linear matrix inequality (LMI) and Lyapunov stability theory for evaluating the stability of systems with constant or time-variant delay.

Park, (1999) proposes a delay-dependent stability criterion for systems with uncertain time-invariant delays as in Equation (1.3). For uncertain time-invariant delay with an upper bound (i.e. $h \in [0, \bar{h}]$), the system is asymptotically stable, if a linear matrix inequality (LMI) equation is satisfied.

$$\dot{x}(t) = Ax(t) + Bx(t - h), \quad h \geq 0. \quad (1.3)$$

Gao, et al., (2008) proposes new LMI equations for a network-based control system. Network transmission delay, data package drop and measurement quantization are considered in the system. The problem of network-based H-infinity control is tackled in the study. Sun, et al., (2010) develops improved delay-range-dependent stability criteria for linear systems with time-varying delays. Utilizing the information on the lower bound of the delay, some new stability criteria are derived in terms of LMIs without introducing any free-weighting matrices. Li, et al., (2012) proposes a reliable fuzzy H-infinity controller for active suspension systems with actuator delay and fault. With this design, the resulting T-S fuzzy system is reliable, in the sense that it is asymptotically stable and has the prescribed H-infinity performance under given constraints. The existence condition of the reliable fuzzy H-infinity controller is obtained in terms of LMIs.

A third type of control algorithm for solving a time-delayed system utilizes the Lambert W function. A Lambert W function is any function $W(H)$ that satisfies Equation (1.4). Asl & Ulsoy, (2003) provides a new analytic approach to obtain the solution of delay differential equations (DDEs) based on Lambert functions. Stability criteria for the individual modes, free response, and forced response for delay equations in different

examples are studied. This approach is applied to obtain the stability regions for the individual modes of the linearized chatter problem. Sun, (2009) establishes an analytical approach for solving DDEs via the Lambert W function. Stability, controllability and observability of DDEs are analyzed with the Lambert W function. An eigenvalue assignment approach via the Lambert W function is applied to a robust controller design of perturbed DDEs and to systems with time-domain response specifications. Ivanovienė & Rimas, (2015) propose a complement for analysis of linear delay systems via the Lambert W function. The modified method expands the applicability of the base method to cases in which the coefficient matrices do not commute. The procedure of finding the auxiliary matrix Q_k is simpler.

$$W(H)e^{W(H)} = H \quad (1.4)$$

The algorithms mentioned above are appealing but implementation in wireless structural control systems still needs to be explored. The algorithm based on the Smith predictor does not guarantee stability, especially when the numerical model contains modeling errors in relation to the physical plant. Furthermore, the delay in the physical system must be known. LMI based control does guarantee stability. However, it does not ensure satisfactory control performance. In addition, for LMI based control algorithm, a feasible solution may not exist for a complex civil structural system with many degrees of freedom (DOFs). The Lambert W function based approach is powerful, yet it hinges on the determination of a matrix, Q_k which is solved numerically for each branch k . Conditions for the existence and uniqueness of Q_k are lacking. Compared to the above mentioned algorithms, the following control algorithms have been studied for wireless structural control.

An energy market-based control (EMBC) algorithm is proposed working with decentralized control approach (Lynch & Law, 2002, Lynch & Law, 2004). The derivation of EMBC is based upon a marketplace allocating the scarce commodity of control energy. In the marketplace, each floor of an idealized lumped mass structural model represents a single market buyer while sellers of control energy are represented by the batteries used to power semi-active variable dampers installed in the structure. The market demand and supply functions of the buyers and sellers are based on the dynamic energy of the structural system in addition to the wealth considerations of the buyers and sellers. The amount of control energy that is purchased by each system actuator is used to determine the applied control force. The control force is calculated by solving a static optimization problem at each point in time, since time is not explicit modelled in EMBC. The limitation of this method is that the stability of the system is not guaranteed.

A partially decentralized control strategy employing linear quadratic regulator (LQR) control algorithm working with state estimators proposed by Yook, et al. (2002) is numerically studied in Lynch & Tilbury, 2005. In the study, estimators are used at each wireless node to estimate the values of the outputs at the other nodes using available local measurements. The estimated states are then used to compute the control force at each node. When the difference between the estimated state and local measured state is larger than the predefined threshold, the actual measurement is broadcast to the rest of the system. All of the estimators are then updated to the current measurement. By using the estimated values instead of the true value at every node, a significant savings in the

bandwidth is achieved. The control strategy working with state estimator achieves good control performances in the simulation.

An optimal time-delayed control algorithm is experimentally studied using a 3-story half scale steel structure (Wang, et al., 2007a) installed with MR dampers. This control algorithm considers a system model with constant delay from the input.

$$x(k+1) = Ax(k) + Bu(k-l) \quad (1.5)$$

$$u(k-l) = Gx(k-l) \quad (1.6)$$

where $x(k)$ is the discrete-time system states at k^{th} time step, A , B are discrete-time state space matrices of appropriate dimension. $u(k-l)$ is the l step delayed control force. G is the optimal time-delay control gain. The cost function of the system is given by

$$J = \sum_{k=l}^{\infty} (x(k)^T Q x(k) + u(k-l)^T R u(k-l)) \quad (1.7)$$

where Q , R are the weighting matrices on the states and control force, respectively. The optimal time-delay control gain G can be obtained by solving three coupled nonlinear equations in the paper. The control performances of this algorithm working with centralized, partially decentralized, fully decentralized control strategies are compared. The fully decentralized control has the best reduction in peak floor accelerations and interstory drifts at most floors.

A decentralized H-infinity algorithm is studied in Wang, et al., (2007b). The transfer function of the closed loop system from disturbance $w(t)$ to output $z(t)$ is given by $H_{zw}(s)$. The objective of H-infinity control is to minimize the H-infinity norm of the transfer function with s on the imaginary axis

$$\|H_{zw}\|_\infty = \sup_w \bar{\sigma}[H_{zw}(jw)] = \sup_{w, \|w(t)\|_2 \neq 0} (\|z(t)\|_2 / \|w(t)\|_2) \quad (1.8)$$

where w represents the frequency, $\bar{\sigma}[\cdot]$ is the maximum singular value of the matrix and “sup” means the supremum value. A γ -suboptimal H-infinity controller ($\|H_{zw}\|_\infty < \gamma$) can be obtained if there exists a positive definite symmetric matrix satisfying a LMI in the paper. It is worth mentioning that the impact of time delay is not considered in the control design. Numerical simulations are performed on a 3-story and a 20-story structural model to illustrate the feasibility of control algorithm with different control strategies. It is illustrated that the decentralized control can achieve equivalent or even superior performance than the centralized counterpart since the centralized counterpart suffers from longer delay due to wireless communication.

A decentralized control algorithm is implemented in Linderman, (2014) on an actively controlled, single-story small-scale shear structure with one AMD installed. An input delay is added to the system by including a delay state in the discrete-time state-space representation

$$\begin{bmatrix} x[k+1] \\ u_d[k+1] \end{bmatrix} = \begin{bmatrix} A_d & B_d \\ 0 & 0 \end{bmatrix} \begin{bmatrix} x[k] \\ u_d[k] \end{bmatrix} + \begin{bmatrix} 0 \\ 1 \end{bmatrix} u[k] + \begin{bmatrix} E_d \\ 0 \end{bmatrix} w[k] \quad (1.9)$$

$$y[k] = \begin{bmatrix} 1 & 0 \end{bmatrix} \begin{bmatrix} x[k] \\ u_d[k] \end{bmatrix} \quad (1.10)$$

where u_d is the one step delayed input. Here A_d , B_d , E_d are the discrete-time system matrices. $y[k]$ is the measurement output at k^{th} time step. The single-story wireless controller achieves comparable performance to the wired system. After the single-story experiment, the control algorithm is applied to the four-story case with two AMDs located on the 2nd and 4th floor, respectively. Fully decentralized control and centralized

control experiments are conducted. The fully decentralized system operating at 725 Hz outperforms the centralized wireless control operating at 30 Hz. Despite the lack of complete sensor measurements, the fully decentralized system has the advantage of faster sampling rate and lack of data loss.

A time-delayed decentralized H2/LQG controller is proposed and studied on a benchmark cable-stayed bridge model in Fallah & Taghikhany, (2013). The wireless transmission time delay is modelled as one step delay in the discrete-time system measurement. The decentralized controller is calculated by solving three coupled nonlinear equations through a gradient-based method. Centralized control with/without wireless transmission delay and decentralized control with/without wireless transmission delay are simulated and compared with the original wired LQG control in the benchmark model. The time-delayed decentralized control can effectively mitigate the seismic responses of the cable-stayed bridge.

1.1.3 Wireless Sensor Network

There are multiple wireless protocols available for wireless data transmission. Among them, Zigbee, WiFi, and Bluetooth are commonly used. These three protocols are based on IEEE 802.15.4, IEEE 802.11 a/b/g/n and IEEE 802.15.1 standards, respectively. IEEE standards define the physical (PHY) and media access control (MAC) layers for wireless communication over a range of 10-100 meters. Users can develop upper layers based on the PHY and MAC Layers. A detailed comparison of these protocols is listed in Table 1.1 (Sidhu, et al., 2007; Lee, et al., 2007; Fornazier, et al., 2012). From the table, ZigBee and

WiFi are better choices than Bluetooth, in terms of transmission range. WiFi has the fastest transmission rate, while ZigBee consumes the minimum power. For battery operated wireless system (i.e. wireless structural health monitoring system) and wireless control system with small package size, Zigbee or basic IEEE 802.15.4 is a better choice.

Table 1.1. Comparison of different wireless standards.

Standard	ZigBee	WiFi	Bluetooth
IEEE spec.	802.15.4	802.11 a/b/g/n	802.15.1
Frequency Band	868/915 MHz; 2.4 GHz	2.4 GHz; 5GHz	2.4 GHz
Max Signal Rate	250 Kb/s	54 Mb/s	0.72 Mb/s
Bit Time (μs)	4	0.0185	1.39
Max Data Payload (bytes)	102	2312	339
Max Overhead (bytes)	31	58	158
Nominal TX/RX Power	(-25) - 0 dBm	15 - 20 dBm	0 -10 dBm
Nominal Range	100 m	100 m	10 m
Number of RF Channels	16	14	79
Channel Bandwidth	2 MHz	22 MHz	1 MHz
Network Topology	Ad-hoc, peer to peer, star, or mesh	Point to hub	Ad-hoc, very small networks
Power Consumption	Very Low	High	Medium
Applications	Remote Control; Battery-operated products	Internet browsing; file transfers	Wireless USB; headset

For the Zigbee protocol, several network topologies can be used. The common types are shown in Figure 1.3 (Faludi, 2010). In each network, there is one coordinator to form the network, hand out address and etc. A router is a full-featured wireless node which can join existing network, send information, receive information and route information. An

end device is a reduced-featured node which can join network, send and receive information but cannot route information. The simplest type of network topology is a single peer to peer network. One node is the coordinator, the other node can be either a router or an end device. The star type network is also fairly straightforward. Every message in the system must pass the coordinator. The mesh network employs the router node to route information from the end device to the coordinator. End devices can be attached to a router or to the coordinator. Multi-hop transmission can exist for this type network.

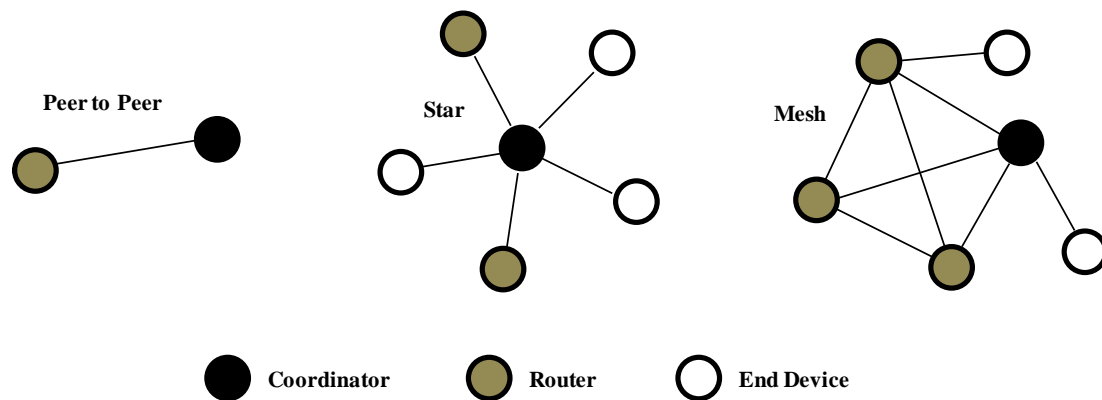


Figure 1.3. Network topologies.

When multiple devices communicate with the coordinator, a multiple access method must be available. The common types include the carrier sense multiple access with collision avoidance (CSMA/CA), time division multiple access (TDMA) and frequency division multiple access (FDMA). For CSMA/CA, carrier sense is performed prior to transmission. A node listens to the wireless channel to determine whether or not another node is transmitting. If the channel is clear, it will start transmitting, otherwise it will wait for a random backoff time before listening again. After the data is transmitted, an










acknowledgement (ACK) will be sent from the receiver to the sender. If the sender node does not receive the ACK, it will retransmit after a random backoff time. For TDMA, it allows multiple nodes to share the same frequency channel by synchronizing the nodes and assigning each node with a different time slot. This feature is beneficial for wireless control applications as the time delay is deterministic for each sensor. Several developed control systems are adopting TDMA (Lynch, et al., 2008; Swartz & Lynch, 2009; Linderman, 2014). For FDMA, each device is allocated with one or several frequency bands or frequency channels to avoid interfaces with other devices.

1.1.4 Wireless Sensors for Civil Infrastructure

Wireless sensors were first introduced to civil engineering for structural health monitoring (SHM) applications. A variety of wireless SHM systems are developed since 1998 for monitoring the behavior of structures under different conditions (i.e. healthy and damaged condition) (Straser & Kiremidjian, 1998; Kottapalli, et al., 2003; Sazonov, et al., 2004; Paek, et al., 2005; Kim, et al., 2007; Nagayama, Spencer, & Rice, 2009; Sim & Spencer, 2009; Rice & Spencer, 2009; Cho, et al., 2010; Jang, et al., 2010; Yi, et al., 2013; Kane, et al., 2014; Peckens, 2014; Hackmann, et al., 2014). In the literature, a large number of validation tests are performed on laboratory structures as well as upon bridges, buildings, aircraft, offshore oil platforms, naval ships, among many others. Several comprehensive literature reviews of wireless SHM systems are available (Sohn, et al., 2003; Lynch & Loh, 2006; Yick, et al., 2008). The representative wireless sensors developed by the research community and industry are listed in Table 1.2. Stanford WiMMS (Straser & Kiremidjian, 1998), Michigan Narada (Zimmerman, et al., 2008) and

Los Alamos National Lab (LANL) WiDAQ (Taylor, 2013) are academic wireless SHM platforms developed with commercial microprocessor, ADC chip, antenna, etc. These boards are verified through experimental tests and have been implemented on real world structures to study SHM algorithms. Commercial extensible wireless sensor boards include Meismic Micaz, TelosB and Imote2 (Memsic Inc., 2015). These boards are originally developed at the University of California-Berkeley and subsequently commercialized by Crossbow, Inc, which is later acquired by Memsic, Inc. These boards are popular since they use open source TinyOS software platform. Researchers can write and upload their own codes to the board. Also, they can develop sensor boards upon these platforms, i.e. SHM-A board on the Imote2 (Rice & Spencer, 2008). Wireless monitoring systems from Microstrain (Lord Microstrain Inc., 2015), BDI (Bridge Diagnostics Inc. 2015), National Instruments (National Instruments Inc. 2015) are commercial off-the-shelf sensor boards. These platforms are robust and easy to deploy. Each system contains ready-to-use power unit, transducer, signal conditioning circuit, antenna, wireless radio, computational core, etc. These systems can be directly deployed to structures for monitoring purpose, but they lack the flexibility to develop new features by end users.

Table 1.2. Representative wireless sensors
(Photos courtesy of Memsic Inc., Microstrain Inc., National Instrument Inc., Bridge Diagnostics Inc., Wang, et al., (2014)).

Academic wireless sensor prototypes			
Commercial extensible wireless sensors			
Commercial off-the- shelf wireless sensors			
	Microstrain WSDA	National Instrument	BDI STS-WiFi

Recently developed wireless SHM systems have improved sensing resolution, computational power, wireless transmission range, etc. compared to the early generations, taking advantage of the rapid development of wireless sensor hardware. With real-time sensing, onboard computation and wireless communication capabilities, wireless sensor platforms can be extended to structural control applications supplied with an actuation interface as shown in Figure 1.4.

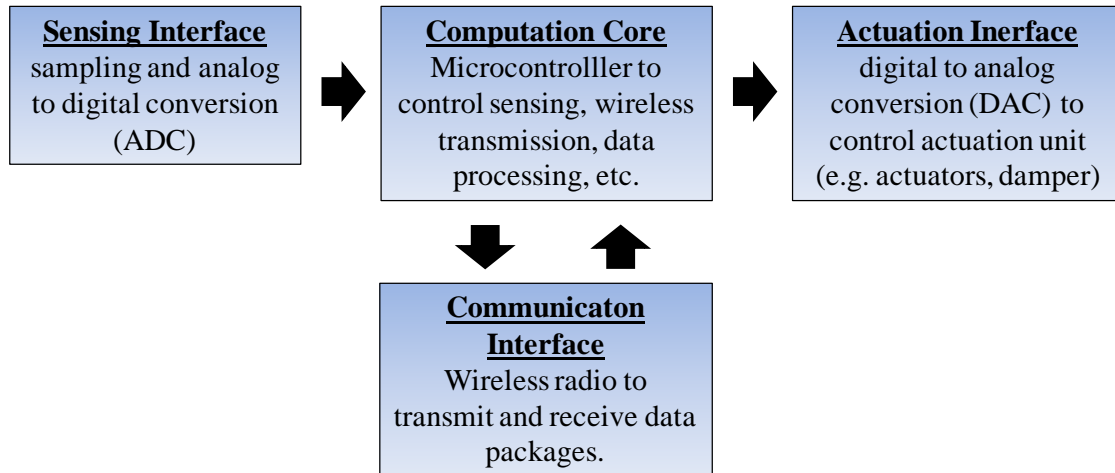


Figure 1.4. Components of wireless nodes for structural control.

In recent years, wireless structural control systems are given increased attention as a novel approach for structural vibration control. A number of wireless control systems are developed and experimentally implemented. Researchers from the University of Michigan have been pioneers in the study of wireless control systems for civil infrastructure (Seth, et al., 2005; Lynch & Tilbury, 2005). A prototype wireless control system (see Figure 1.5 (a)-(b)) embedded with decentralized control algorithm is first numerically evaluated using the 5-story Kajima-Shizuoka building and then experimentally implemented on a half-scale steel structure with MR dampers (Wang, et al., 2007a). The sensor board utilizes a 4-channel 16 bit Texas Instrument ADS8341 A/D converter. The digital sensor data is transferred to the computational core through a high-speed serial peripheral interface (SPI) port. The computational core consists of a low-power 8-bit Atmel ATmega128 microcontroller and an external 128kB static random access memory (SRAM) chip for data storage. For wireless communication, two types of wireless transceivers are explored: 900MHz MaxStream 9XCite and 2.4 GHz MaxStream

24XStream. The control signal generation module is the single-channel 16-bit D/A converter, the Analog Device AD5542. The AD5542 converts a 16-bit unsigned integer value from the ATmega128 to an analog voltage output ranging from -5 to 5V. The feasibility of this wireless structural control system is verified.

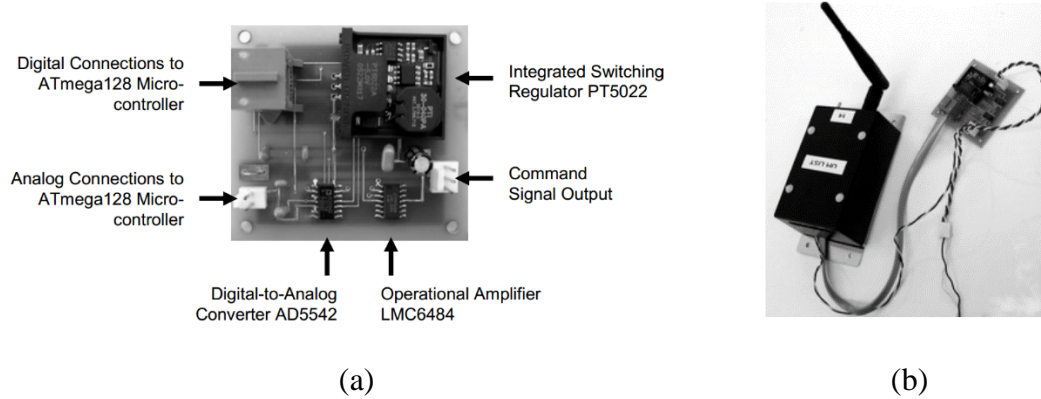


Figure 1.5. Wireless control system: (a) Developed control unit, (b) Control unit connected to wireless sensor.

Researchers from Washington University have developed a wireless control system, utilizing MICA2 wireless motes by Crossbow Technology, Inc. with MTS310CA sensor board (see Figure 1.6) (Liu, et al., 2007). MICA2 motes are programmed to acquire acceleration data in the range of -0.25 g to +0.25 g with 10 bit A/D converter. The system is implemented on a 3-story steel frame to control the structural vibration with MR damper. The data from MICA2 motes are wirelessly transmitted to a Notebook PC (base station). A primary H2/LQG controller is adopted to calculate the control force. A secondary bang-bang clipped optimal controller is used to determine the command voltage to the MR damper. The control signal is generated with dSpace real-time control system connected to the PC. The wireless control system has achieved reasonable performance in comparison with wired control system.

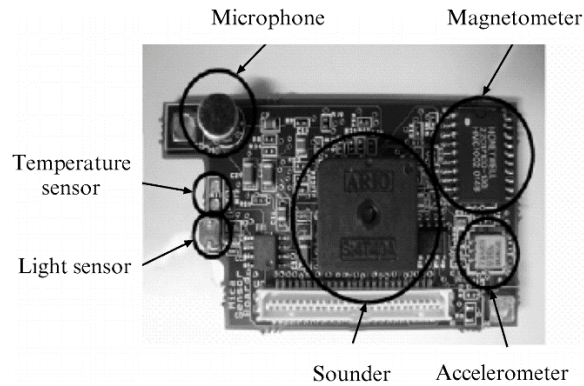


Figure 1.6. MTS310CA sensor board.

Researchers from the University of Catania, Italy, develop an AMD system for real-time wireless structural control (Casciati & Chen, 2012). The wireless sensor uses a CC1110 transceiver that includes an onboard microprocessor. The frequency division multiplexing (FDM) technique is adopted for wireless data transmission. Thus, data from different sensors can transmit simultaneously without conflicts. A digital PID controller has been implemented on the microcontroller to control the motion of the AMD. The block diagram for wireless control is shown in Figure 1.7.

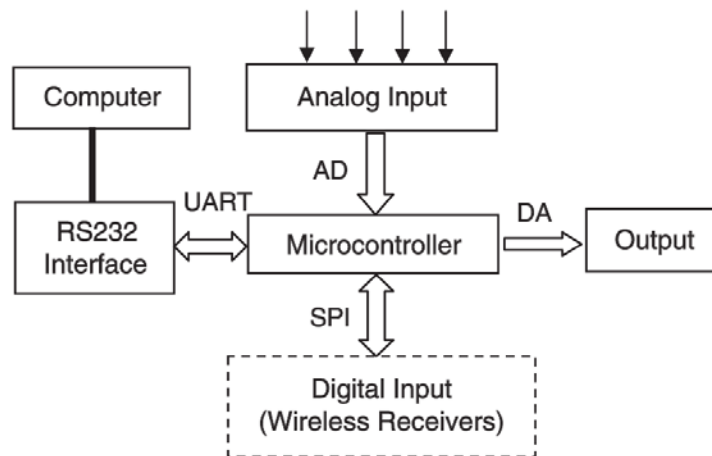


Figure 1.7. Block diagram of the controller.

Researchers from the University of Illinois develop a wireless control system based on imote2 platform (Linderman, Mechitov, & Spencer, 2013; Linderman, 2014). High speed 16-bit SAR type A/D conversion board (see Figure 1.8 (a)) is developed with the Analog Device AD 7682. The A/D conversion latency on the SHM-A board is reduced to 200 microseconds, which greatly reduced latency compared to Quickfilter QF4A512 ADC. The D/A board (see Figure 1.8 (b)) is built with the TI-AD8565. The four-channel DAC has 16-bit resolution and a short settling time of 10 microseconds. The analog output is in the range of 0 to 2.5V. The control system is implemented on a 4-story small-scale structure with two AMDs for centralized and decentralized active control.

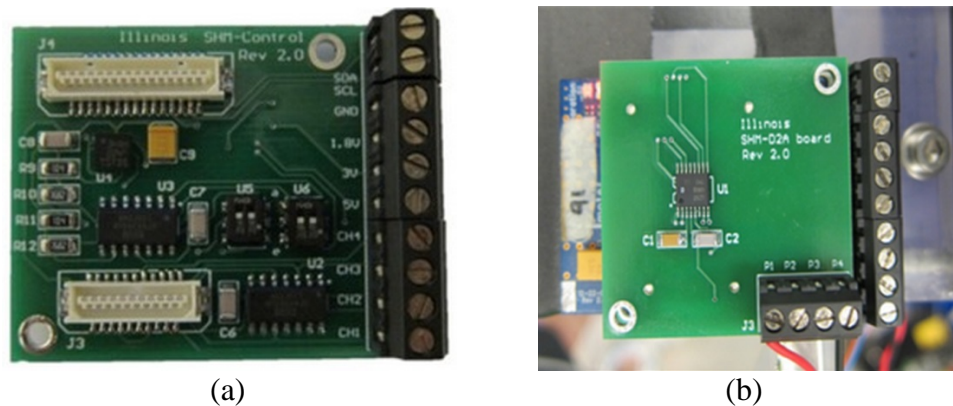


Figure 1.8. (a) SHM-SAR board, (b) SHM-D2A board.

Researchers from University of Michigan and Georgia Institute of Technology have also developed a dual-core wireless board named Martlet (see Figure 1.9) for structural health monitoring and control applications (Kane, et al., 2014). A Texas Instruments Piccolo microcontroller, running up to 90 MHz clock frequency, is adopted in Martlet to execute onboard computation and data acquisition. The dual-core board allows dedicating one core to sensing operations while the other core is reserved for embedded computation and

real-time control law execution. It also has 9-channel onboard 12-bit ADC. Validations tests have been successfully performed on a four-story shear structure.



Figure 1.9. Martlet sensor board.

The wireless control systems mentioned above make significant contributions to the development of wireless control systems for civil infrastructure. However, these sensor boards are only available within these research groups except for the MICA2 and imote2. MICA2 is outdated with very limited computational power. Imote2 boards were once widely adopted but are no longer available on the market. A state-of-the-art wireless control system which can be accessed and contributed by the research community is not available.

In this work, a wireless control system based on an open source Arduino platform (<http://arduino.cc/>) is developed for structural vibration control. Sensing module and communication module are developed upon the Arduino Due board (see Figure 1.10). This wireless control system is intended to be open source and shared with the wireless structural control research community.

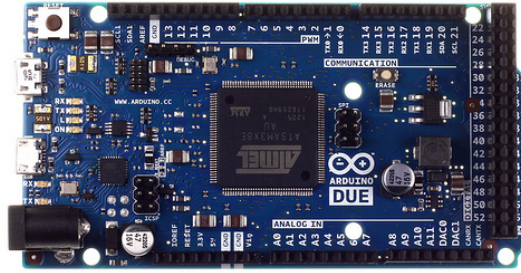


Figure 1.10. Arduino Due board.

The Arduino platform provides powerful, user-friendly hardware and software for any users to develop interactive projects. The Arduino family has a series of boards, ranging from 8-bit 16 MHz processor to 32-bit 1 GHz processor, from single core to dual core structure. A variety of projects such as robots, thermostats and motion detectors can be developed upon Arduino platform. The codes developed on old versions of Arduino boards can be transferred to later versions with little effort. Arduino platform has a broad user basis. As of 2013, over 700,000 official boards, not counting the unofficial derivatives and clone boards, are in the users' hands (Arduino, 2014).

1.2 Overview of the Dissertation

In this work, the objective is to develop a framework facilitating cyber-physical codesign of wireless control system. Chapter 2 first presents the developed wireless cyber-physical simulator (WCPS), an integrated environment that combines realistic simulations of civil infrastructure with that of wireless sensor networks. Second, two case studies are provided, each combining a structural model with wireless traces collected from real-world environments. The building case study combines a representative benchmark building model and wireless traces collected from a multi-story building on the

Washington University in St. Louis campus. The bridge study combines the structural model of the Cape Girardeau bridge over the Mississippi River and wireless traces collected from a similar bridge (the Jindo bridge) in South Korea. These case studies shed light on the challenges of wireless control system and the limitations of a traditional structural control approach under realistic wireless conditions. Finally, a cyber-physical codesign approach to wireless control system is illustrated which integrates a data aggregation strategy (for communication and control) and an optimal time delay controller that improves structural control performance.

Chapter 3 presents the wireless structural control system development based on Arduino Due. The developed system enables the experimental implementation and evaluation of cyber physical codesign. A low cost, low power tri-axial accelerometer board and a wireless transmission board are built on the Arduino platform. An 18 bit, high resolution ADC board is developed for taking voltage signals of ± 10 Volts amplitude onto the Arduino board. Structural control algorithms are embedded within the integrated wireless sensor board for feedback control. The developed wireless control system is validated through a series of experimental tests.

Chapter 4 discusses the numerical simulation and experimental study of wireless structural control of a 3-story shear building. In the numerical simulation, an identified MR damper is included. A wireless sensor network employing TDMA is simulated with time delay and data loss obtained from validation tests in Chapter 3. For the experimental study, system identification is performed first to identify the structural model for control

design. Then, wireless sensors are implemented on each floor of the structure. Shake table tests are conducted with historical earthquake records. The performance of various wireless control strategies (decentralized control, partially decentralized control, centralized control) are evaluated with the impact of modeling uncertainties, measurement noises as well as time delay and data loss induced by the wireless network.

Chapter 5 proposes a Kalman filter based estimator switching method (ESM) which reduces the estimation error due to data loss and sensor failure in the wireless control system. The method is computationally inexpensive for real-time implementation. Numerical study of the method is performed with the 3-story shear building in Chapter 4. The ESM method is proposed to work with OTD method as a codesign approach for wireless control. The robustness of the wireless control system with ESM is studied with modeling error and measurement noise.

Chapter 6 presents the fault tolerance study using real-time hybrid simulation (RTHS). The RTHS technique separates a full structure into physical (experimental) and numerical substructure. With RTHS, wireless control system can be studied without performing shake table tests while offering more realistic environment than numerical simulation of the entire system. In this study, a 3-story large-scale steel frame with wireless sensors and controller are included in the numerical substructure, and a semi-active control device (MR damper) with actuator is included in the experimental substructure. Fault tolerance is investigated considering sensor data loss and sensor failure cases in the codesigned

wireless control system. In addition, performance of the codesigned wireless control system with switching estimator is evaluated with the RTHS.

Chapter 7 summarizes the research work presented in this dissertation and discusses the future research directions for wireless structural control.

CHAPTER 2. WIRELESS CYBER-PHYSICAL SIMULATOR (WCPS)

In this chapter, the development of the WCPS for wireless structural control simulation is presented. The architecture of the WCPS is explained in detail. Two case studies are performed, each combining a structural model with wireless traces collected from real-world environments. These case studies shed light on the challenges of wireless control systems and the limitations of a traditional structural control approach under realistic wireless conditions. A cyber-physical codesign approach to wireless control system is illustrated which integrates data aggregation strategies (for communication and control) and an optimal time delay controller. Several evaluation criteria are adopted to evaluate control performance.

2.1 Introduction to WCPS

Although there are successful implementations of wireless control systems on small or large scale lab structures, a high-fidelity wireless structural control simulation platform which captures both the cyber (wireless sensor network) and physical (structural control) aspects is not available. In this work, a WCPS is developed to realistically simulate wireless structural control. The WCPS employs an integrated architecture that combines (1) Simulink for simulating the physical system (structural) dynamics, the controller and actuator(s) and (2) TOSSIM for simulating the wireless sensor network (Li, et al., 2013).

Simulink has been widely used by control and structural engineers to design and study structural control systems, while TOSSIM is specifically designed to simulate wireless sensor networks based on realistic wireless link models that have been validated in diverse real-world environments (Levis, et al., 2003; Lee, Cerpa, & Levis, 2007). By combining Simulink and TOSSIM, WCPS provides an integrated environment to realistically simulate wireless control systems. This integrated simulator is part of a collaboration work between IISL lab at Purdue University and Cyber-Physical Systems lab (CPSL) at Washington University in St. Louis.

Wireless control has been widely studied in many different areas (i.e. industry process automation (Akerberg, et al. 2011) and unmanned vehicle (Seiler, 2001)) and is a subset of networked control system (NCS) (Gupta & Chow, 2010). There are existing wireless network simulation tools like Truetime (Cervin, et al. 2003) and PiccSIM (Björkbom, 2010). Truetime, developed by researchers at the Lund University, Sweden, is a well-known Simulink based simulation tool for networked control systems. While Truetime supports wireless networks such as 802.11b WLAN and IEEE 802.15.4 Zigbee, its wireless models are relatively simple and only takes into account additive white Gaussian noise (AWGN) and thus coexistence with other co-located wireless systems cannot be easily evaluated (Ferrari, et al. 2013).

PiccSIM is a co-simulation platform for (wireless) networked control system using Matlab Simulink and ns-2. And ns-2 is a discrete event simulator with substantial support for simulation of TCP, routing, and multicast protocols over wired and

wireless networks (Issariyakul & Hossain, 2011). Despite its wide adoption as a network simulator, the wireless models in ns-2 are incapable of capturing the probabilistic and irregular packet receptions that are common in low-power wireless networks. In the WCPS, TOSSIM (Levis, et al. 2003; Levis, et al. 2005) is adopted as the wireless network simulator. Leveraging noise traces and statistical models, TOSSIM can capture complex temporal link dynamics that are crucial for realistic cyber-physical systems modeling. As the standard TinyOS wireless simulator, TOSSIM has been widely used for wireless sensor network research and has been validated in diverse real-world environments. Moreover, the trace-driven simulation approach of TOSSIM enables us to study the impacts of different wireless environments.

A wireless structural control system consists of a set of wireless sensors, controller(s) and actuator(s). In the development of the WCPS, centralized wireless structural control is adopted. Sensors form a wireless mesh network connected with a base station hosting the controller. A TDMA media access method is employed for data transmission. Since the controller is usually located adjacent to the actuators in the wireless control systems, wired connection between the controller and actuators are assumed and the transmission latency is negligible compared to that of the WSN.

The architecture of the WCPS is presented in Figure 2.1. The feedback control loop of a wireless control system is simulated as follows. Sensor data is generated from the structural model in Simulink. Data transmission through the wireless network is

accomplished by using a “python interface block” to call a python interface program. The interface program supplies the communication with TOSSIM. Following the routes and transmission schedule determined by the network manager module, TOSSIM simulates the end-to-end wireless communication of the sensor data packages from the sensors to the base station, and then return the packet delay and data loss information to the “python interface block” in Simulink through the python interface. Sensor data with delay and data loss information is provided to the “Data Block”, which send the delayed sensor data incorporating the data loss to the controller.

Users of the WCPS have the flexibility to change the earthquake excitation to the structure, the controller, number of sensor measurements and their locations, strength of measurement noise as input to Simulink model, and wireless signal/noise traces as input to TOSSIM. The network scheduler module in TOSSIM determines the transmission schedules. Network schedule is then deployed into the MAC layer of wireless nodes. The TDMA MAC layer in WCPS is developed based on the MAC layer architecture (MLA) library and further adapted for TOSSIM under TinyOS 2.1.1. Received signal strength indication (RSSI) and wireless noises traces are collected from real-world environments and provided to the wireless model (Lee, et al., 2007) used by TOSSIM for realistic wireless network simulations.

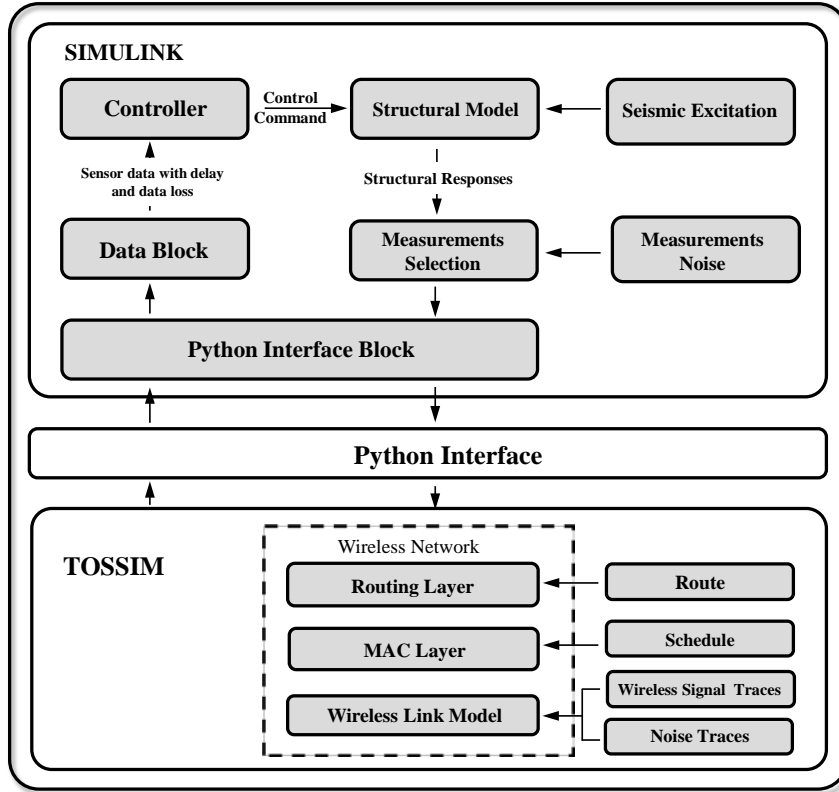


Figure 2.1. Architecture of WCPS.

2.2 Case Study: Wireless Benchmark Building Control

This section presents the first case study considering wireless benchmark building control. This case study integrates a representative benchmark AMD building model developed by Spencer, et al., (1998) and a simulated wireless network developed with TOSSIM. The setup of the wireless building control model is shown in Figure 2.2. Sensor measurements obtained from the structural model are fed through the simulated wireless network. Thus, delayed measurements that incorporate realistic data loss are used for closed-loop feedback control. The computed control command from the controller block is applied to the AMD to control the structural vibrations due to the earthquake disturbance.

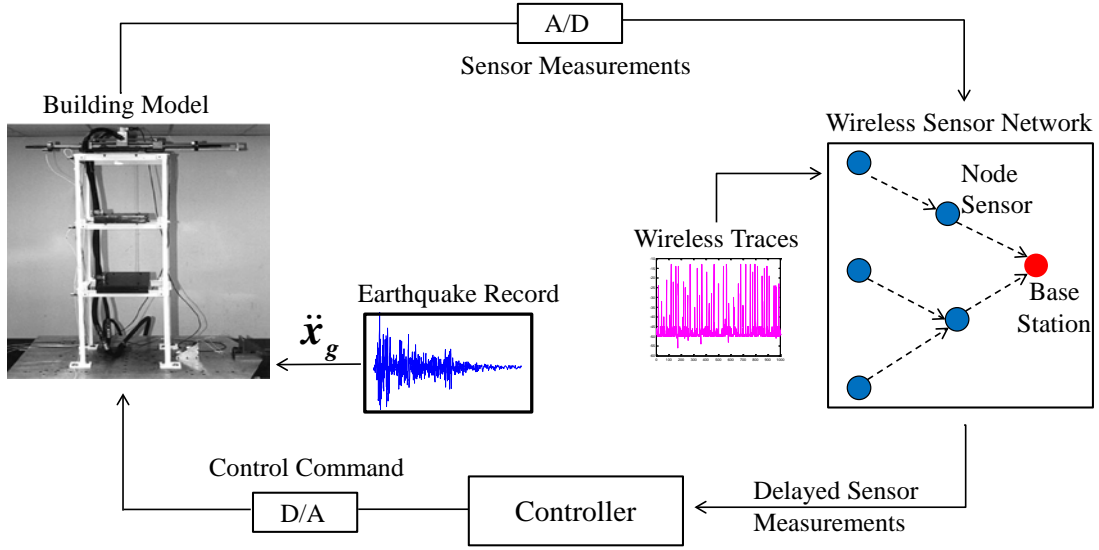


Figure 2.2. Wireless benchmark building control.

2.2.1 Building Model

The benchmark AMD structure is a scaled model of a three-story building equipped with an AMD. The structure represents a prototype building with scaling parameters defined in the original benchmark AMD model: force = 1:60, mass = 1:206, time = 1:5, displacement = 4:29 and acceleration = 7:2. The first three modes of the structure are at 5.81 Hz, 17.68 Hz and 28.53 Hz, with associated damping ratios 0.33%, 0.23% and 0.30%. The AMD consists of a single hydraulic actuator with steel masses attached to the ends of the piston rod. The moving mass of the AMD is 1.7% of the total mass of the structure. The structural dynamics, actuator dynamics along with control structure interaction (CSI) are included in the experimentally identified evaluation model of the structural system. The evaluation model provided with this benchmark problem statement has good representation of the structure up to 100 Hz (Spencer, et al., 1998). Four absolute acceleration measurements $[\ddot{x}_{a1}, \ddot{x}_{a2}, \ddot{x}_{a3}, \ddot{x}_{am}]$ from the 1st floor, 2nd floor, 3rd floor of the 3-story structure and the AMD may be

selected in any combination for feedback in the controller. The original building benchmark model that considered this structure has been investigated by numerous researchers around the world (e.g. Ahlawat & Ramaswamy, 2001; Battaini, et al. 1998; Yuen & Beck, 2003) to compare and contrast wired control system performance.

2.2.2 Building Network Model

To realistically simulate the wireless network, experimentally collected noise traces and RSSI traces are utilized as inputs to TOSSIM, which predicts the transmission success or failure based on a probabilistic signal to noise ratio model (Lee, et al., 2007). The traces are collected using Telosb devices (Polastre, et al., 2005) each equipped with a TI CC2420 radio (compatible with the IEEE 802.15.4 standard) deployed in a five-story building at Washington University in St. Louis as shown in Figure 2.3. The building is a typical 1970's reinforced concrete construction with 3m floor height. A Telosb device is placed 10cm above the floor slab on each floor between the 2nd floor and the 5th floor as shown in Figure 2.4. A single base station is placed on the 5th floor because the control device (AMD) is located on the top of the original benchmark AMD structure. The physical setup of the AMD anticipates the base station to be located on the top floor collocated with the control device. The recorded noise traces from node 1 to node 4 are shown in Figure 2.5. The network employs a TDMA protocol that divides time into time slots synchronized among all sensors and each time slot can accommodate the transmission of a data package. WSN standards based on IEEE 802.15.4 radios commonly employ 10msec time slot

(Gutierrez, et al., 2011). Each slot can accommodate the transmission of a data package and the local processing time. As the building model used for this benchmark is a scaled model and both time and length are scaled in the simulation using standard similitude laws, the 10msec time slot is scaled to 2msec to incorporate the 1:5 time scale into the same system simulation.

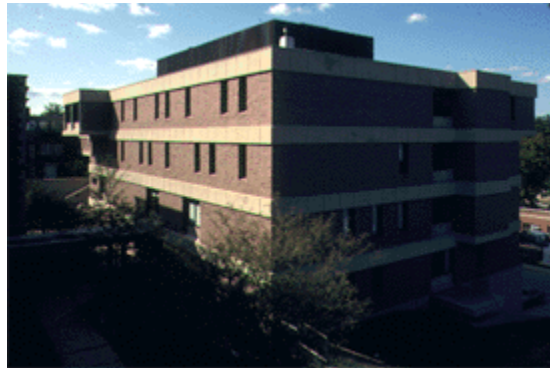


Figure 2.3. Bryan Hall used for collecting signal/noise traces deployment.

The sensor on the second floor is two hops from the base station located on the top floor, whereas the others are within one hop from the base station. Here, hop count is the number of wireless links on the route from source to destination. A sensor is one hop away from the base station if it can communicate directly with the base station. Our current implementation adopts a single frequency channel TDMA network. A TDMA network is desirable for control systems because network delays are deterministic under a TDMA network.

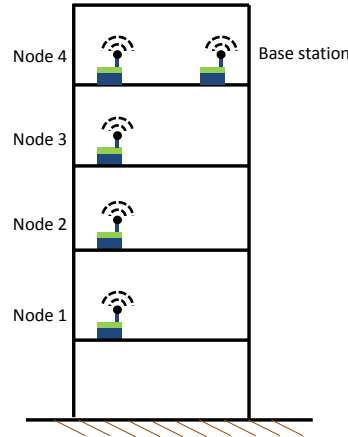


Figure 2.4. Wireless sensor deployment.

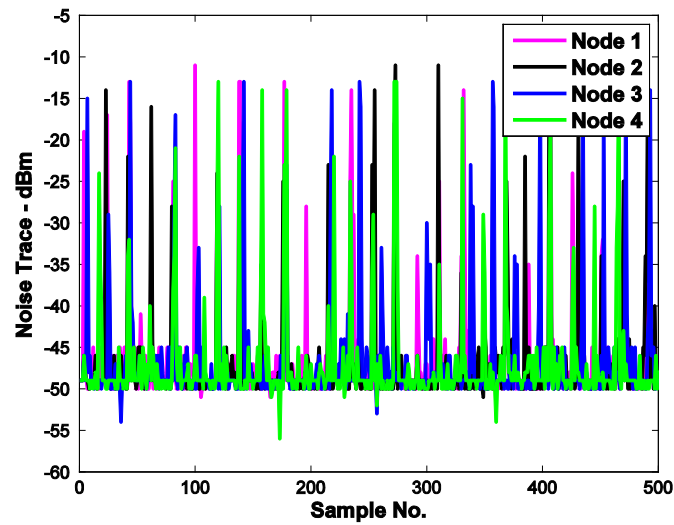


Figure 2.5. Noise traces of floor 1 to floor 4.

2.2.3 Impact of Time Delay to the Control System

The original benchmark model adopts a H2/LQG optimal control algorithm to control the structural vibration. The impact of time delay to the original control system is first analyzed. Constant delay is added to all 4 sensor channels to examine the control performance. The delay is increased from 2 time steps (one time step is 1msec in the model) up to 11 time steps. The A/D and D/A converters of the digital controller have

12-bit resolution and a span of $\pm 3V$. The measurements contain a root mean square (RMS) noise of 0.01 Volts which is 0.3% of the full span of the A/D converters. The earthquake excitation is simulated with the Kanai-Tajimi spectrum as shown in Equation (2.1), which is commonly used for simulating earthquake (Spencer, et al., 1998).

$$S_{\ddot{x}_g \ddot{x}_g}(w) = \frac{S_0(4\zeta_g^2 w_g^2 w^2 + w_g^4)}{(w^2 - w_g^2)^2 + 4\zeta_g^2 w_g^2 w^2} \quad (2.1)$$

$$S_0 = \frac{0.03\zeta_g}{\pi w_g(4\zeta_g^2 + 1)} g^2 \cdot sec \quad (2.2)$$

where ω_g and ζ_g are parameters need to be determined. Here we choose $\omega_g = 37.3$ rad/sec, $\zeta_g = 0.3$. With this excitation, the peak interstory drifts and peak accelerations are obtained as shown in Figure 2.6 Figure 2.7. Based on the simulation results, the control performance gets worse than the uncontrolled case after 8-step constant delay, especially for the peak acceleration. In order to achieve a more indepth understanding, Monte Carlo simulations are performed with simulated earthquake following Kanai-Tajimi spectrum. One thousand simulations are performed.

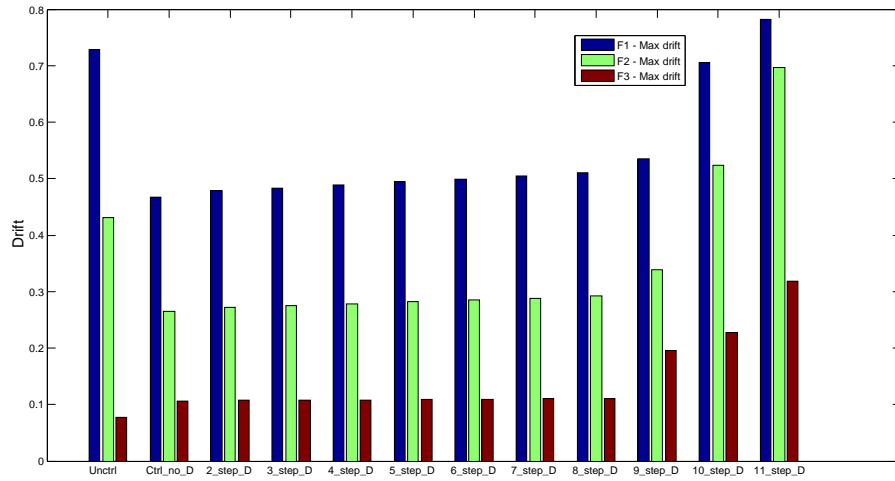


Figure 2.6. Peak interstory drift with different constant delay.

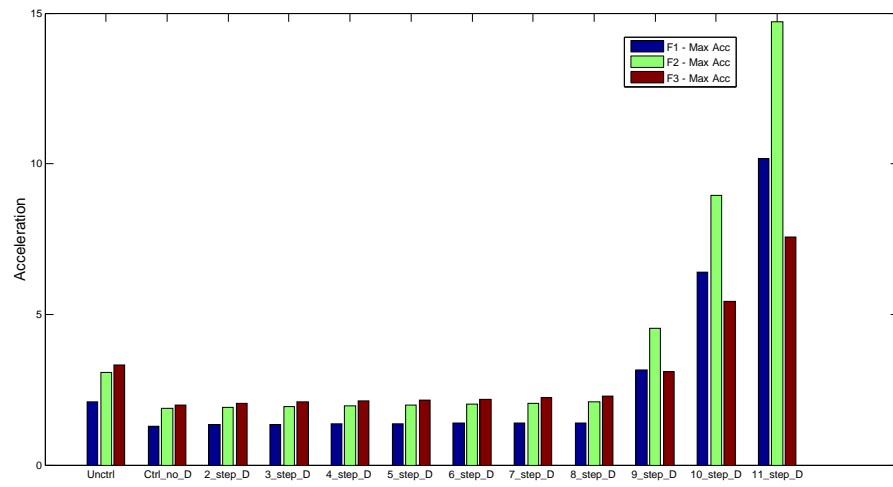


Figure 2.7. Peak acceleration with different constant delay.

To evaluate the control performance, seven evaluation criteria are adopted as presented in Table 2.1. These criteria have been normalized with respect to uncontrolled structural responses.

Table 2.1. Evaluation criteria.

Evaluation Criteria	Equation	Description
J_1	$J_1 = \max \left\{ \frac{\sigma_{d_1}}{\sigma_{x_{3o}}}, \frac{\sigma_{d_2}}{\sigma_{x_{3o}}}, \frac{\sigma_{d_3}}{\sigma_{x_{3o}}} \right\}$	Normalized Maximum RMS interstory drift
J_2	$J_2 = \max \left\{ \frac{\sigma_{\ddot{x}_{a1}}}{\sigma_{\ddot{x}_{a3o}}}, \frac{\sigma_{\ddot{x}_{a2}}}{\sigma_{\ddot{x}_{a3o}}}, \frac{\sigma_{\ddot{x}_{a3}}}{\sigma_{\ddot{x}_{a3o}}} \right\}$	Normalized Maximum RMS absolute acceleration
J_3	$J_3 = \max \left\{ \frac{\sigma_{x_m}}{\sigma_{x_{3o}}} \right\}$	Normalized RMS actuator displacement
J_4	$J_4 = \max \left\{ \frac{\sigma_{\dot{x}_m}}{\sigma_{\dot{x}_{3o}}} \right\}$	Normalized RMS actuator velocity
J_5	$J_5 = \max \left\{ \frac{\sigma_{\ddot{x}_{am}}}{\sigma_{\ddot{x}_{a3o}}} \right\}$	Normalized RMS actuator acceleration
J_6	$J_6 = \max \left\{ \max_t \left\{ \frac{ d_1(t) }{d_{1o}}, \frac{ d_2(t) }{d_{1o}}, \frac{ d_3(t) }{d_{1o}} \right\} \right\}$	Normalized Maximum peak interstory drift
J_7	$J_7 = \max \left\{ \max_t \left\{ \frac{ \ddot{x}_1(t) }{\ddot{x}_{3o}}, \frac{ \ddot{x}_2(t) }{\ddot{x}_{3o}}, \frac{ \ddot{x}_3(t) }{\ddot{x}_{3o}} \right\} \right\}$	Normalized Maximum peak acceleration

where σ_{d_i} is the RMS interstory drift of the i^{th} floor, $\sigma_{x_{3o}}$ is the RMS displacement of the 3^{rd} floor of the uncontrolled building relative to the ground, $\sigma_{\ddot{x}_{ai}}$ is the RMS absolute acceleration of the i^{th} floor, $\sigma_{\ddot{x}_{a3o}}$ is the RMS absolute acceleration of the 3^{rd} floor of the uncontrolled building, σ_{x_m} is the RMS displacement of the actuator piston relative to the 3^{rd} floor, $\sigma_{\dot{x}_m}$ is the RMS velocity of the actuator piston relative to the 3^{rd} floor, and $\sigma_{\ddot{x}_{am}}$ is the RMS absolute acceleration of the actuator piston, $d_i(t)$ is the interstory drift of the i^{th} floor, $d_{1o}(t)$ is the peak interstory drift of the 1^{st} floor of the uncontrolled building, and $\ddot{x}_{ai}(t)$ is the absolute acceleration of the i^{th} floor.

The evaluation results for $J6$ and $J7$ criteria (the sensitive criteria) with 8-step and 9-step constant delay are shown in Figure 2.8 (a)-(d). The red line in these plots is the threshold for each evaluation criterion. From the results, it is clear that in most cases, $J6$ criterion is satisfied with 8-step or 9-step delay; however, considering the $J7$ criterion, it is clear that the control performance is not acceptable with a 9-step delay (Sun, et al., 2012).

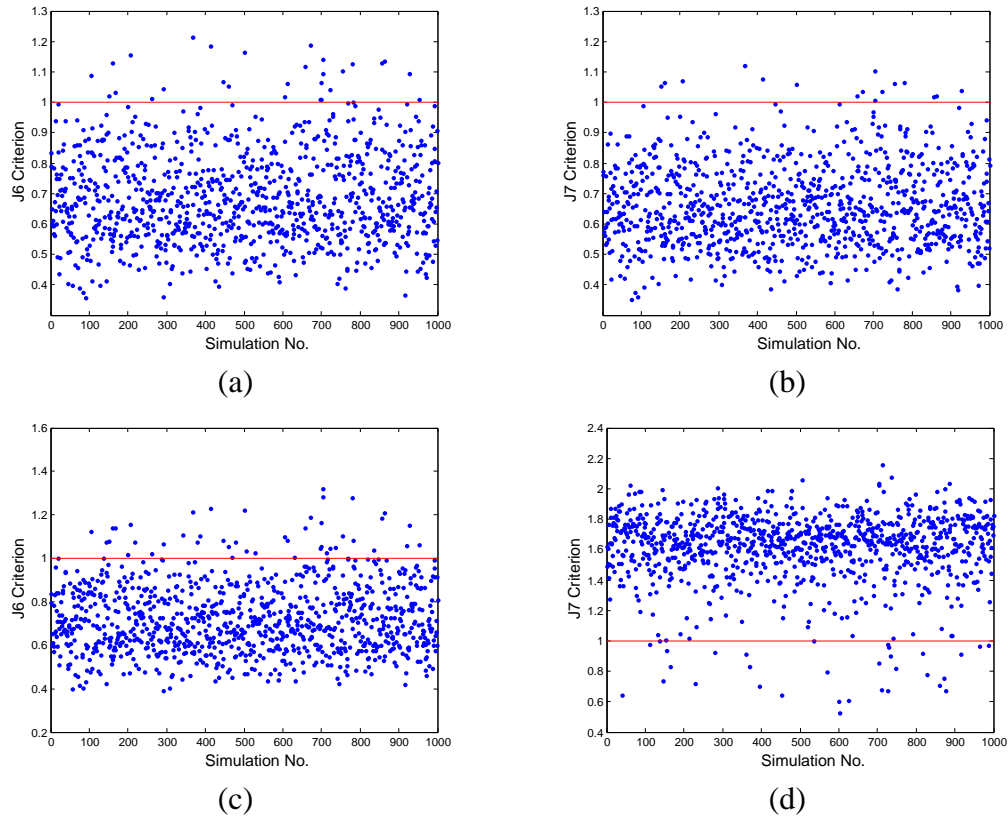


Figure 2.8. Monte Carlo simulation results: (a) $J6$ with 8-step delay, (b) $J7$ with 8-step delay, (c) $J6$ with 9-step delay, (d) $J7$ sim with 9-step delay.

After the analysis with constant delay, the impact of transmission delay due to TDMA network is studied. For the current network with four wireless nodes, the 1^{st} sensor uses two hops to the base station, while the other sensors use one hop. A single hop takes one TDMA time slot which is 2msec, and the sampling interval is 1msec in the

model. Note that independence of sampling and transmission is assumed. The TDMA transmission is shown in Figure 2.9. The red dots are the data transmitted with wireless network. Transmitting all four sensors' data in a round takes 10 sampling steps. The data received at base station is shown in Figure 2.10. $s_{j,i}$ is the received data from sensor j , sampled at i^{th} time step. From the figure, it is clear to see the impact of TDMA network to data transmission. For the original H2/LQG controller, the control calculation is performed until all data is received, thus the control interval is 10 msec. The structural responses are provided in Figure 2.13. The measured acceleration is saturated as shown in Figure 2.14. The system is unstable with this slow control rate and time delay.

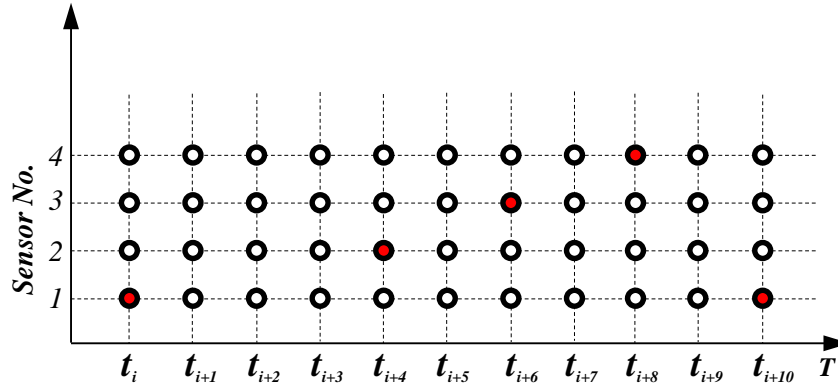


Figure 2.9. TDMA transmission of sensor data.

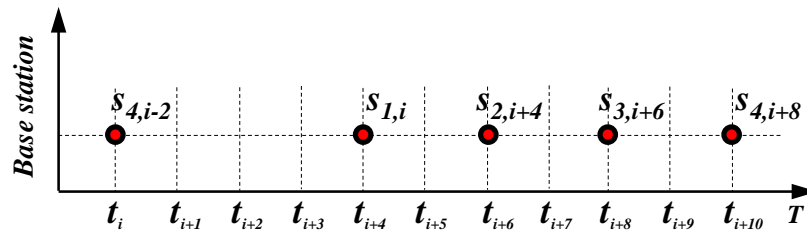


Figure 2.10. Received data at base station.

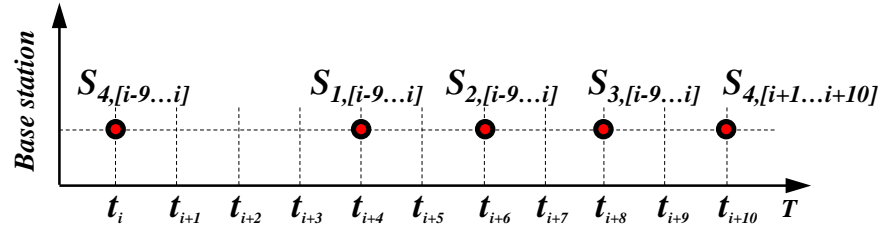


Figure 2.11. Received data at base station for proposed S1 strategy.

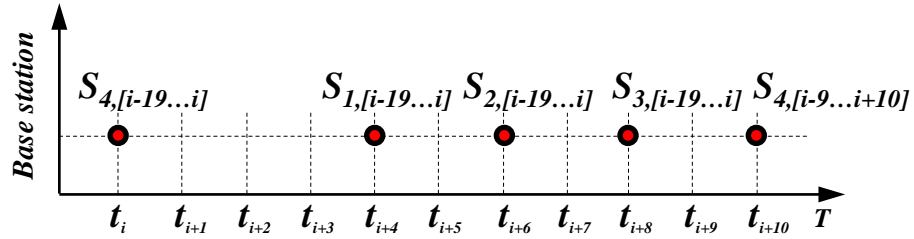


Figure 2.12. Received data at base station for proposed S2 strategy.

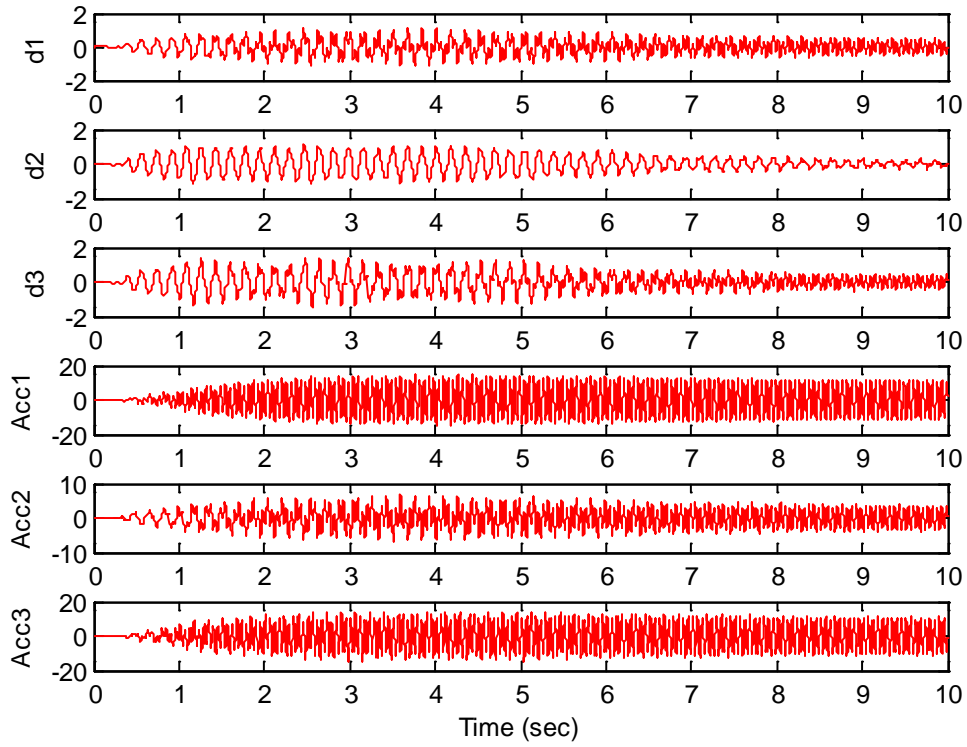


Figure 2.13. Responses of the structure.

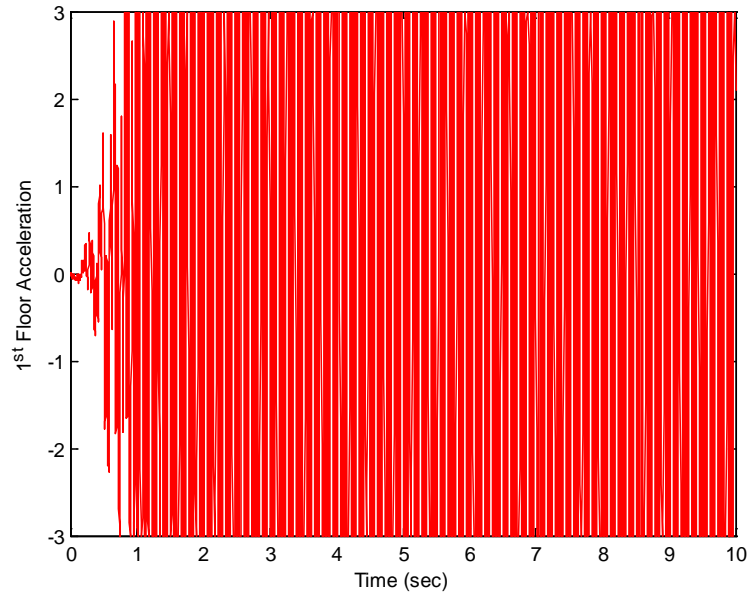


Figure 2.14. Measured acceleration of 1st floor.

2.2.4 Codesign of Building Control System

From the previous section, it has been illustrated that with the TDMA network, a direct wireless implementation of the control system provided in the original benchmark model will not result in a stable implementation. To effectively control the structural vibration, a codesign approach is developed and demonstrated for this building control system, which considers both the cyber and physical aspects.

2.2.4.1 Data Aggregation Strategy

The TDMA network degrades the control performance since the transmission rate is much slower than the sampling rate as shown in Figure 2.9. If more data is transmitted and utilized, better control performance will result. With this in mind, a data aggregation strategy (S1) is proposed. Here the strategy aggregates a set of 10 samples into a package, i.e. TDMA network transmission as follows, $t_i \rightarrow s[1, i-9 \dots i]$

(which means sensor 1 at time step i transmits data from step $i-9$ to step i), $t_{i+4} \rightarrow S_{[2, i-9 \dots i]}$, $t_{i+6} \rightarrow S_{[3, i-9 \dots i]}$, $t_{i+8} \rightarrow S_{[4, i-9 \dots i]}$. The data received at the base station is shown in Figure 2.11. The control calculation at t_{i+10} uses delayed measurements at t_{i-9} . In this way, the TDMA network induced delay is transformed to a constant 20 sample step delay for each measurement. With this approach, control algorithms for systems with a deterministic delay can be applied. When data loss occurs, the most recent data from previous steps are adopted for state estimation and control force calculation. Another strategy (S2) with data aggregation of 20 samples in a package is also proposed. In this case, TDMA network transmission as follows, $t_i \rightarrow S_{[1, i-19 \dots i]}$, $t_{i+4} \rightarrow S_{[2, i-19 \dots i]}$, $t_{i+6} \rightarrow S_{[3, i-19 \dots i]}$, $t_{i+8} \rightarrow S_{[4, i-19 \dots i]}$; $t_{i+10} \rightarrow S_{[1, i-9 \dots i+10]}$, $t_{i+14} \rightarrow S_{[2, i-9 \dots i+10]}$, $t_{i+16} \rightarrow S_{[3, i-9 \dots i+10]}$, $t_{i+18} \rightarrow S_{[4, i-9 \dots i+10]}$. The data received at the base station is shown in Figure 2.12. The control calculation at t_{i+10} uses delayed measurements at t_{i-19} . Then, the TDMA network induced delay is transformed into a constant 30 sample step delay for all measurements. In this implementation, adjacent packages from each sensor have 10 overlapping samples. Data loss is reduced in the 2nd strategy with the tradeoff of longer delay (Sun, et al. 2013). The comparison of proposed strategies with the original TDMA transmission without data aggregation (T1) is provided in Table 2.2.

Table 2.2. Comparison of different strategies.

Strategy	Data aggregation	Sample delay*	Control interval	Data loss reduction
T1	No	10msec	10msec	No
S1	Yes	20msec	1msec	No
S2	Yes	30msec	1msec	Yes

Sample delay*: largest delay of all four nodes.

2.2.4.2 Control Design

An optimal time delay (OTD) controller proposed by Chung, et al., (1995) is adopted which considers a linear time-invariant system with a constant delay from the control input. The discrete system model can be represented as

$$z[k + 1] = A_d z[k] + B_d u[k - l] + E_d w[k] \quad (2.3)$$

$$y[k] = C_d z[k] + D_d u[k - l] + F_d w[k] \quad (2.4)$$

where $z[k] \in R^{n \times 1}$ is the discrete-time system states at k^{th} step, $u[k - l] \in R^{m \times 1}$ is the $k-l$ step delayed control force, $w[k] \in R^{p \times 1}$ is the external earthquake loading, $y[k] \in R^{q \times 1}$ is the measured outputs at k^{th} step. $A_d, B_d, C_d, D_d, E_d, F_d$ are discretized state space matrices with proper dimensions. $w[k]$ is the disturbance which is not included in the control design. Therefore, Equation (2.3) becomes

$$z[k + 1] = A_d z[k] + B_d u[k - l] \quad (2.5)$$

$$u[k - l] = G z[k - l] \quad (2.6)$$

$$J = \sum_{k=l}^{\infty} (z^T[k] Q z[k] + u^T[k - l] R u[k - l]) \quad (2.7)$$

where G is the optimal control gain, Q is the weighting matrix for the states, R is the weighting matrix for the input control force. The states $z[k-l]$ is estimated from measurements $y[k-l]$ with Kalman filter. The cost function to be minimized is shown in Equation (2.7).

The system equation can be rewritten in augmented form as

$$\bar{z}[k + 1] = \bar{A} \bar{z}[k] + \bar{B} \bar{u}[k] \quad (2.8)$$

$$\bar{A} = \begin{bmatrix} A_d & 0 & \cdots & 0 & 0 \\ I & 0 & \cdots & 0 & 0 \\ 0 & I & \cdots & 0 & 0 \\ \vdots & \vdots & \vdots & \ddots & \vdots \\ 0 & 0 & \cdots & I & 0 \end{bmatrix}, \quad \bar{B} = \begin{bmatrix} B_d \\ 0 \\ \vdots \\ 0 \\ 0 \end{bmatrix}, \quad \bar{Q} = \begin{bmatrix} Q & 0 & \cdots & 0 & 0 \\ 0 & 0 & \cdots & 0 & 0 \\ 0 & 0 & \cdots & 0 & 0 \\ \vdots & \vdots & \vdots & \ddots & \vdots \\ 0 & 0 & \cdots & 0 & 0 \end{bmatrix}$$

where $\bar{z}[k] = [z[k] \ z[k-1] \ \cdots \ z[k-l+1] \ z[k-l]]^T$ is the augmented state vector, $\bar{A} \in R^{n(l+1) \times n(l+1)}$, $\bar{B} \in R^{n(l+1) \times m}$, $\bar{Q} \in R^{n(l+1) \times n(l+1)}$ are augmented A , B , Q matrices.

$$\bar{u}[k] = u[k-l] \quad (2.9)$$

where $\bar{u}[k]$ is the augmented control input.

$$\bar{u}[k] = G\bar{y}[k] = G\bar{D}\bar{z}[k] = Gz[k-l] \quad (2.10)$$

$$\bar{D} = [0 \ 0 \ \cdots \ 0 \ I]$$

Based on the above equations, a cost function in the form of Equation (2.11) can be obtained (Chung, et al., 1995)

$$J = \sum_{k=l}^{\infty} \bar{z}_l^T [(\bar{A} + \bar{B}G\bar{D})^{k-l}]^T (\bar{Q} + \bar{D}G^T R G \bar{D}) (\bar{A} + \bar{B}G\bar{D})^{k-l} \bar{z}_l = \bar{z}_l^T \Lambda \bar{z}_l \quad (2.11)$$

$$\bar{J}_a = tr(\Lambda \bar{Z}_l) + tr\{L[(\bar{A} + \bar{B}G\bar{D})^T \Lambda (\bar{A} + \bar{B}G\bar{D}) - \Lambda + (\bar{Q} + \bar{D}G^T R G \bar{D})]\} \quad (2.12)$$

where \bar{J}_a is the augmented cost function, $\bar{Z}_l = E(\bar{z}_l^T \Lambda \bar{z}_l)$ is the 2^{nd} moment of initial disturbance. As a result, the following coupled equations are solved simultaneously to obtain an optimal control gain G , Lagrangian matrix L , and a constant matrix Λ .

$$(\bar{A} + \bar{B}G\bar{D})^T \Lambda (\bar{A} + \bar{B}G\bar{D}) - \Lambda + (\bar{Q} + \bar{D}^T G^T R G \bar{D}) = 0 \quad (2.13)$$

$$\frac{\partial \bar{J}_a}{\partial \Lambda} = (\bar{A} + \bar{B}G\bar{D})L[(\bar{A} + \bar{B}G\bar{D})]^T - L + \bar{Z}_l = 0 \quad (2.14)$$

$$\frac{\partial \bar{J}_a}{\partial G} = \bar{B}^T \Lambda [(\bar{A} + \bar{B}G\bar{D})]L\bar{D}^T + R G \bar{D} L \bar{D}^T = 0 \quad (2.15)$$

The three Equations (2.13-2.15) are solved iteratively until the error is acceptable (Wang, et al., 2007a). And $\bar{Z}_l = I$ when solving Equations (2.13-2.15). The control gain G is pre-calculated based on the state space matrices and the known constant delay. With weighting matrices chosen as $Q = C_d^T C_d$, $R = D_d^T D_d$, the obtained control gain G is $[-29.84 \ -34.27 \ 31.45 \ 30.18 \ -12.78 \ 29.81 \ -0.16 \ 4.79 \ -0.21 \ -2.44]$ for the

system with 20 step delay, and the gain G is [13.46 -37.90 -34.10 20.25 -18.62 22.26 0.02 -0.10 0.01 -1.08] for the system with 30 step delay.

2.2.5 Wireless Building Control with Codesigned Control System

The codesigned control system is implemented in the case study as shown in Figure 2.15. The data aggregation strategies are adopted in the “*data block*”. The controller working with S1 strategy is denoted as OTD, while the controller working with S2 is denote as OTD-S2. The TDMA wireless network with 10000 package transmissions is simulated in TOSSIM with the experimentally collected RSSI and noise traces. The data loss ratio of S1 and S2 strategies are shown in Figure 2.16 (a)-(b). Clearly, the sensor on the 1^{st} floor is more likely to have data loss due to multi-hop transmission. For the single hop sensors on the 2^{nd} to 4^{th} floor, closer distance to base station introduces less data loss. Compared to S1, the S2 strategy has effectively reduced the data loss ratio.

The integrated simulation is compared with simulation in Matlab using the delay and data loss traces pre-generated in TOSSIM to verify the integrated model. The structural responses for both cases under scaled El Centro earthquake are shown in Figure 2.17-2.18. The responses exactly match each other. This verifies the integrated model.

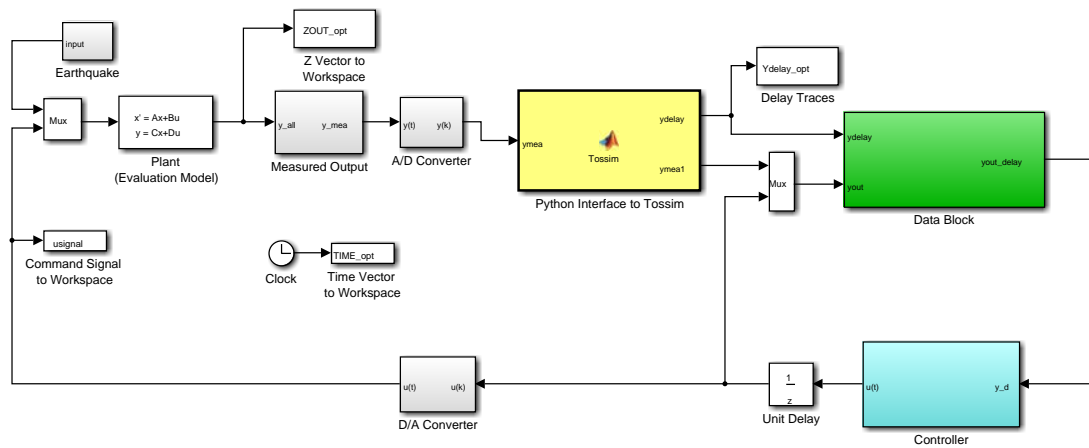


Figure 2.15. Simulink diagram for the case study.

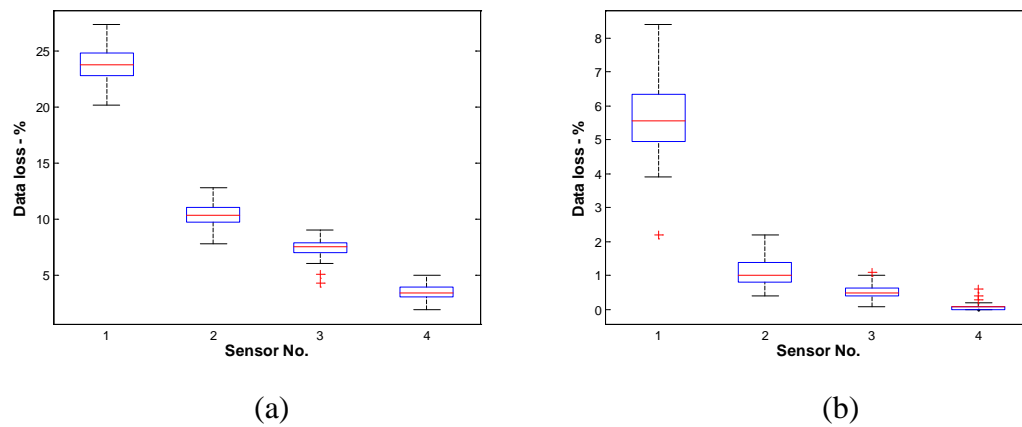


Figure 2.16. Data loss of (a) TDMA network, and (b) TDMA network with S2.

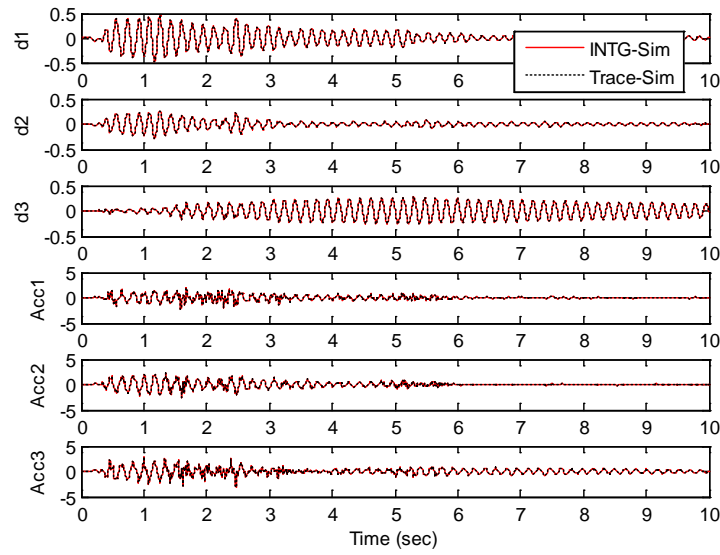


Figure 2.17. Comparison of integrated simulation and trace simulation.

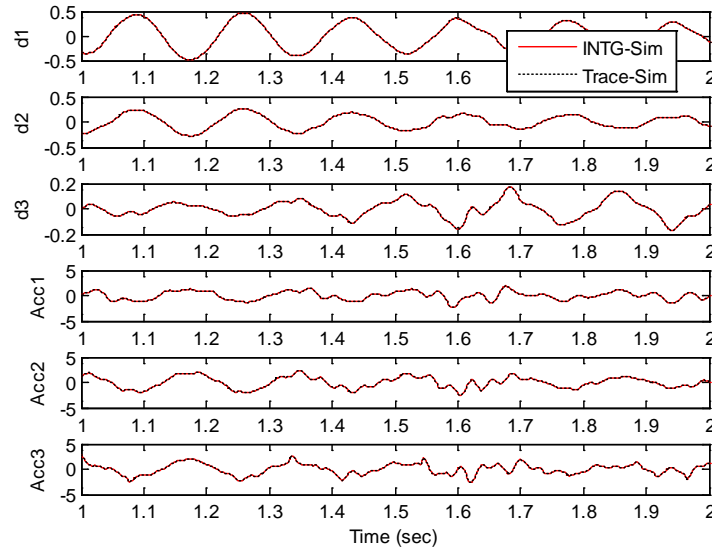


Figure 2.18. Zoomed view of Figure 2.17.

After verification of integrated model, numerical simulation is performed with scaled El Centro earthquake, scaled Hachinohe earthquake, scaled Kobe earthquake and scaled Gebze earthquake records. A time scale of 1:5 and a magnitude (acceleration) scale of 1:3.5 are used for these earthquakes and for the simulated earthquake with

Kanai-Tajimi spectrum. The simulation results for one realization under different earthquakes are illustrated in Figure 2.19. The results for ideal OTD and OTD-S2 implementation without data loss have also been provided for comparison. The OTD and OTD-S2 controllers have reduced the interstory drifts and accelerations of the structure effectively. Note that as data loss is reduced in the OTD-S2 design, the interstory drifts and accelerations are closer to the ideal implementation without data loss. Since the simulation results will vary due to the wireless network, one hundred realizations has been simulated for each case. Evaluation criteria are used to evaluate the control performance. The average evaluation results are provided in Figure 2.20 for El Centro earthquake. The complete list of evaluation results for all five seismic inputs are listed in Table 2.3. From the evaluation results, the OTD controller outperforms the OTD-S2 controller in most cases. Even though OTD-S2 strategy reduces the data loss due to wireless network, the longer delay compared to OTD degrades the control performance in this sample design. It has been noted some criteria (i.e. J_3) are exceeded (red numbers) in one or two earthquakes in the table, but are within the acceptable range in all the other earthquakes. The results are taken as acceptable with an exceedance of less than 10% in these cases.

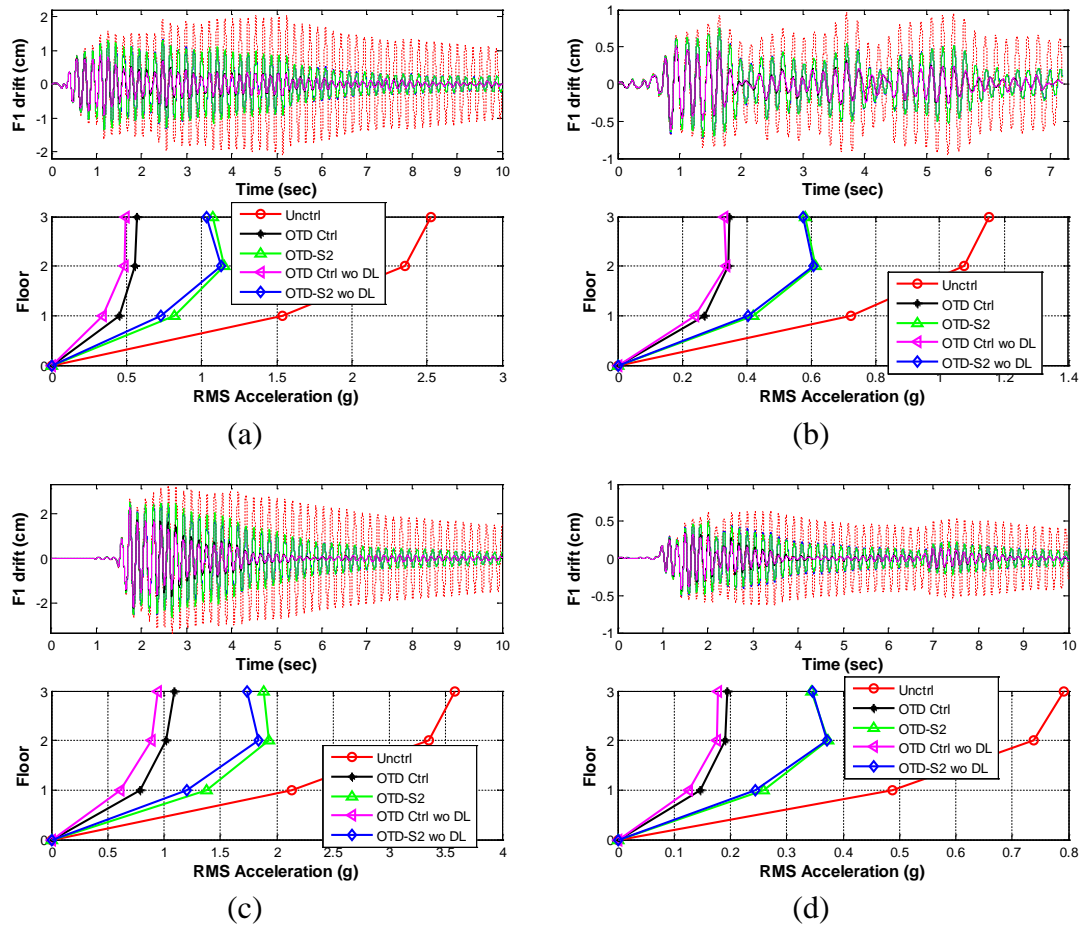


Figure 2.19. Simulation results under (a) El Centro earthquake, (b) Hachinohe earthquake, (c) Kobe earthquake, (d) Gebze earthquake (Sun, et al., 2015).

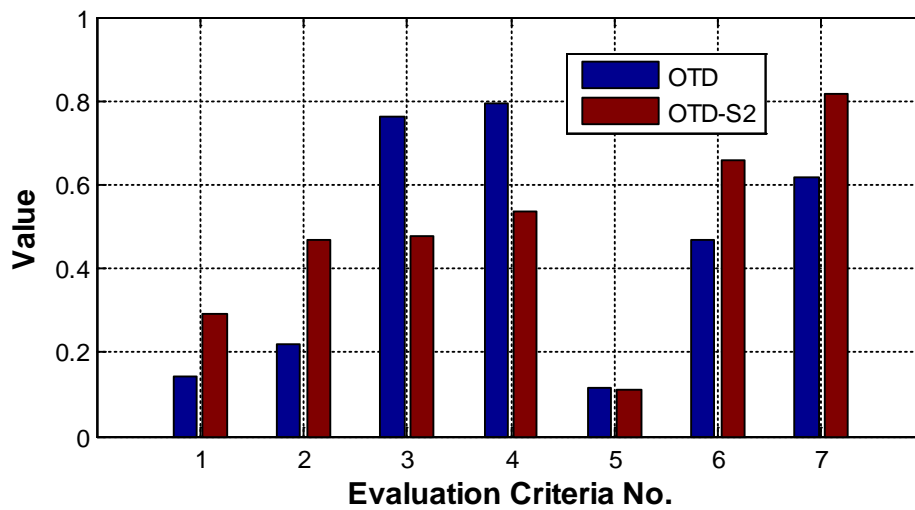


Figure 2.20. Evaluation results for El Centro earthquake.

Table 2.3. Evaluation results.

		<i>J1(%)</i>	<i>J2(%)</i>	<i>J3(%)</i>	<i>J4(%)</i>	<i>J5(%)</i>	<i>J6(%)</i>	<i>J7(%)</i>
EI Centro	<i>OTD</i>	14.4	22.4	76.4	79.9	11.6	47.2	66.3
	<i>OTD wo DL*</i>	14.6	19.6	77.3	77.2	8.3	44.9	40.1
	<i>OTD-S2</i>	28.8	46.1	47.7	52.6	10.3	65.6	78.0
	<i>OTD-S2 wo DL</i>	28.6	44.9	47.6	48.1	6.6	64.4	65.6
Hachinohe	<i>OTD</i>	19.6	32.0	108.0	110.0	16.4	63.9	78.7
	<i>OTD wo DL</i>	19.0	29.3	110.0	106.0	11.4	63.4	61.9
	<i>OTD-S2</i>	33.7	54.1	55.3	61.1	12.4	78.4	80.5
	<i>OTD-S2 wo DL</i>	33.5	52.8	55.2	55.4	8.0	78.1	68.9
Kobe	<i>OTD</i>	18.7	31.7	84.7	89.7	13.8	68.9	92.3
	<i>OTD wo DL</i>	16.7	26.3	85.7	85.8	9.2	67.2	69.4
	<i>OTD-S2</i>	32.9	54.6	47.2	55.2	13.5	79.0	107.0
	<i>OTD-S2 wo DL</i>	31.8	51.3	47.1	49.5	9.5	75.0	91.7
Gebze	<i>OTD</i>	15.9	25.9	86.1	89.8	13.7	68.4	82.1
	<i>OTD wo DL</i>	14.9	22.4	87.0	86.2	9.5	66.5	58.3
	<i>OTD-S2</i>	30.1	48.1	49.8	54.9	10.8	80.3	82.6
	<i>OTD-S2 wo DL</i>	30.0	47.0	49.6	50.1	7.1	79.2	70.7
Kanai-Tajimi	<i>OTD</i>	21.7	34.9	103.0	107.0	16.4	43.0	63.2
	<i>OTD wo DL</i>	20.5	30.1	103.0	99.7	9.9	39.2	35.9
	<i>OTD-S2</i>	34.3	54.0	49.9	55.7	11.8	63.0	73.3
	<i>OTD-S2 wo DL</i>	33.9	52.4	48.9	49.0	7.1	62.3	58.6

(* wo DL means without data loss)

2.2.6 Additional Studies with Wireless Building Control

To illustrate the capabilities of the wireless building control model, several additional tests are included. The first one is to reduce the received signal strength indicator (RSSI) using the text input file. The RSSI of all sensors are uniformly reduced 1dB to 5 dB in each case. As the RSSI decreases, the data loss ratio will generally increase

for all sensors as shown in Figure 2.21. The sensor 1 which uses 2-hop transmission is most sensitive to decreased RSSI. With 5dBm reduction of RSSI, sensor 1 behaves almost like a sensor failure. The averaged evaluation results with OTD controller are shown in Figure 2.22(a)-(b). Based on the results, the performance gets degraded with decreased RSSI which is as expected.

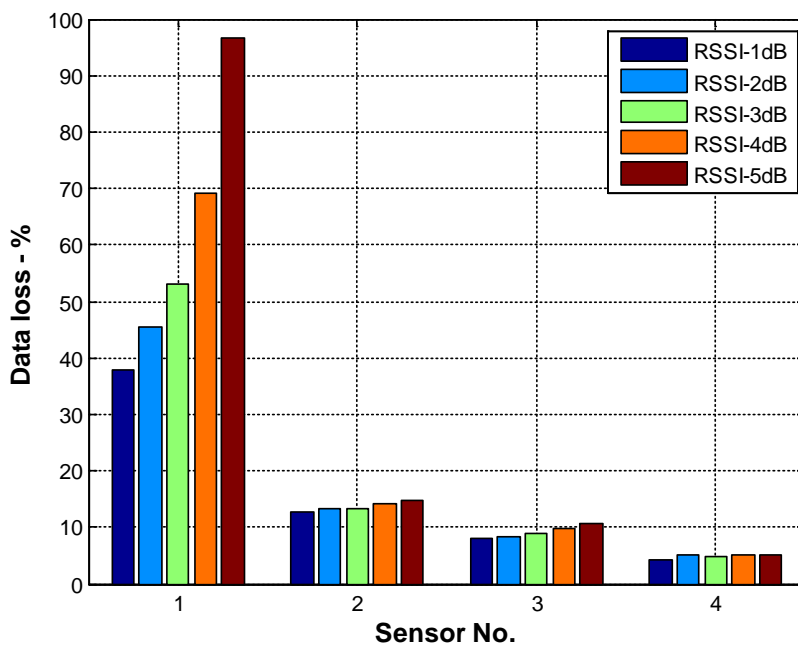


Figure 2.21. Mean value of data loss at different sensors with TDMA network.

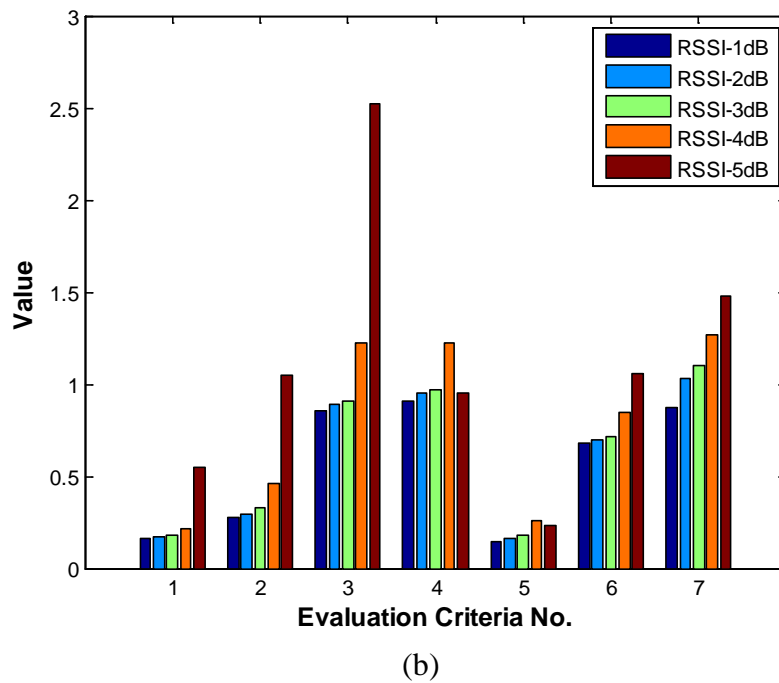
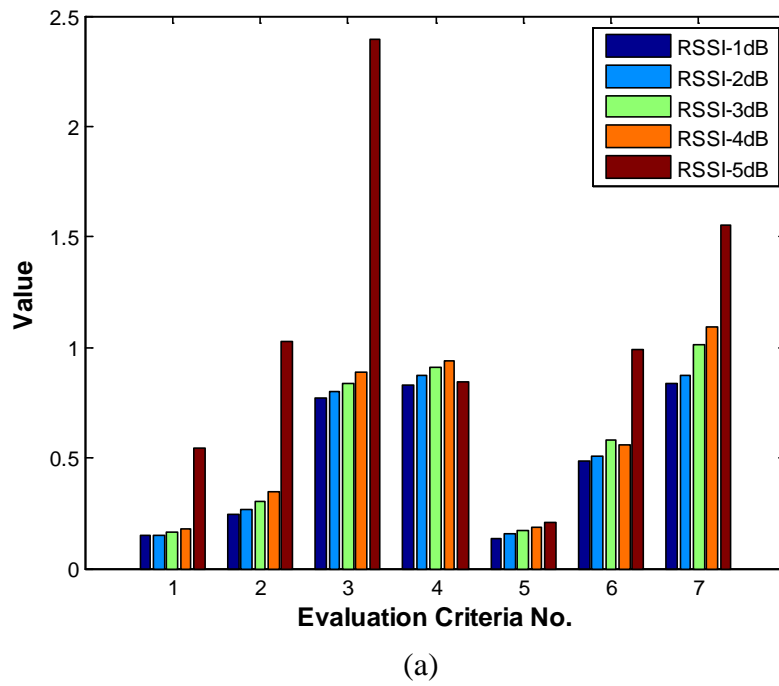


Figure 2.22. Performance of control system under: (a) El Centro earthquake, (b) Gebze earthquake.

Another test to understand the codesign is conducted by changing the 2-hop transmission from sensor 1 to single hop transmission. This represents the case in which sensor 1 has an enhanced antenna to amplify signal strength such that the signal is able to transmit to the base station with one hop. In this case, there are four sensors in the TDMA network using single hop transmission. The time delay due to network is changed accordingly. The control gain must be recalculated for this case adopting the same control algorithm and data utilization strategy as before. The data loss for this network is shown in Figure 2.23. With enhanced antenna, sensor 1 has similar data loss ratio as sensor 2. The evaluation results for 1 hop network are shown in Table 2.4.

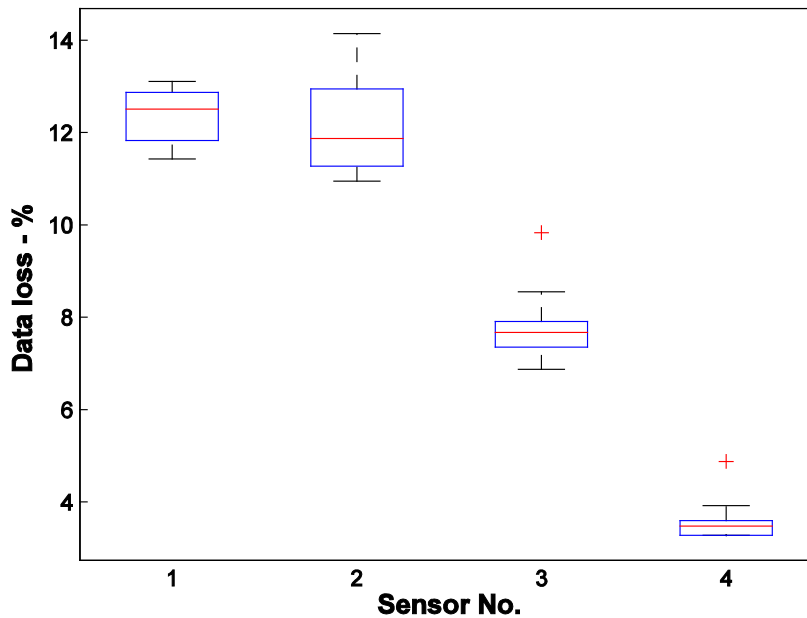


Figure 2.23. Data loss of TDMA network.

Table 2.4. Evaluation results for 1 hop network.

		<i>J1(%)</i>	<i>J2(%)</i>	<i>J3(%)</i>	<i>J4(%)</i>	<i>J5(%)</i>	<i>J6(%)</i>	<i>J7(%)</i>
EI Centro	<i>OTD</i>	15.2	24.3	73.3	74.7	9.6	50.3	54.0
	<i>OTD wo DL*</i>	14.7	22.9	74.8	74.8	8.1	49.4	45.3
	<i>OTD-S2</i>	25.6	39.4	51.7	52.4	6.3	63.1	63.5
	<i>OTD-S2 wo DL</i>	25.6	38.9	50.0	50.6	5.3	62.7	69.4
Hachinohe	<i>OTD</i>	20.7	32.5	97.9	97.6	12.9	65.1	74.7
	<i>OTD wo DL</i>	20.0	31.4	100.0	97.3	10.6	65.1	63.0
	<i>OTD-S2</i>	30.6	47.7	60.5	60.6	7.8	75.2	68.4
	<i>OTD-S2 wo DL</i>	30.4	46.9	58.6	58.6	6.5	74.9	67.4
Kobe	<i>OTD</i>	16.9	27.0	81.1	82.0	11	69.6	74.7
	<i>OTD wo DL</i>	19.2	31.2	79.2	79.6	9.1	69.2	69.4
	<i>OTD-S2</i>	27.1	41.8	53.9	54.5	6.8	77.3	74.7
	<i>OTD-S2 wo DL</i>	30.0	46.0	50.2	51.0	6.0	74.7	89.2
Gebze	<i>OTD</i>	20.0	33.3	77.7	79.7	10.7	70.4	72.5
	<i>OTD wo DL</i>	16.5	25.6	82.5	82.0	9.0	69.3	59.6
	<i>OTD-S2</i>	29.5	45.8	51.7	52.5	6.9	75.0	80.5
	<i>OTD-S2 wo DL</i>	27.0	41.1	52.4	52.8	5.7	77.4	69.4
Kanai-Tajimi	<i>OTD</i>	22.8	34.4	90.6	89.8	10.9	44.0	46.7
	<i>OTD wo DL</i>	22.2	32.7	91.5	89.0	8.8	41.9	37.9
	<i>OTD-S2</i>	32.3	49.3	53.3	53.5	6.8	58.7	57.1
	<i>OTD-S2 wo DL</i>	32.7	49.7	53.1	53.0	5.8	60.8	57.1

(* wo DL means without data loss)

2.3 Case Study: Wireless Benchmark Bridge Control

A second wireless control case study is performed by integrating a benchmark bridge model developed by Dyke, et al., (2003) and TOSSIM with experimentally collected traces from a real bridge by the researchers from smart structures technology laboratory at University of Illinois (<http://sstl.cee.illinois.edu/>).

The bridge case study simulates wireless control of the Cape Girardeau Bridge in Missouri, USA. The cable-stayed bridge is spanning the Mississippi River near Cape Girardeau, Missouri, designed by the HNTB Corporation. Since no wireless sensors have been deployed on this particular bridge, wireless traces are adopted from a wireless sensor network deployed on the cable-stayed Jindo bridge (Jang, et al., 2010) in South Korea, which has similar dimensions (e.g., tower height and span range) as the Cape Girardeau bridge. The wireless sensor on the Jindo deployment is then mapped onto the Cape Girardeau bridge simulation. This approach takes advantage of the flexibility of WCPS to combine structural models and wireless traces from different (but similar) structures for integrated wireless control system simulations.

2.3.1 Bridge Model

The finite element model (FEM) of the Cape Girardeau bridge has a total of 579 nodes, 420 rigid links, 162 beam elements, 134 nodal masses, and 128 cable elements. The main span of the bridge is 350.6 m in length, the side spans are 142.7 m. The first ten natural frequencies of this model are 0.162, 0.267, 0.372, 0.454, 0.501, 0.565, 0.619, 0.649, 0.696, and 0.709 Hz. A one-dimensional ground acceleration is applied in the longitudinal direction which is typically considered to be the most destructive direction in cable-stayed bridges. Five acceleration and four displacement measurements are used for control purposes. Four of the accelerometers are located on top of the tower legs, and one is located on the deck at mid span. Two displacement sensors are between the deck and pier 2; the other two displacement sensors are located between the deck and pier 3. Due to the symmetry of the bridge

along the longitudinal direction, these 9 sensors can be reduced to 5 sensors including 3 accelerometers (node 240, 353 and 34) and 2 displacement sensors (node 151 and 185) as shown in Figure 2.24. In the bridge WSN, these 5 sensors are used for centralized wireless control.

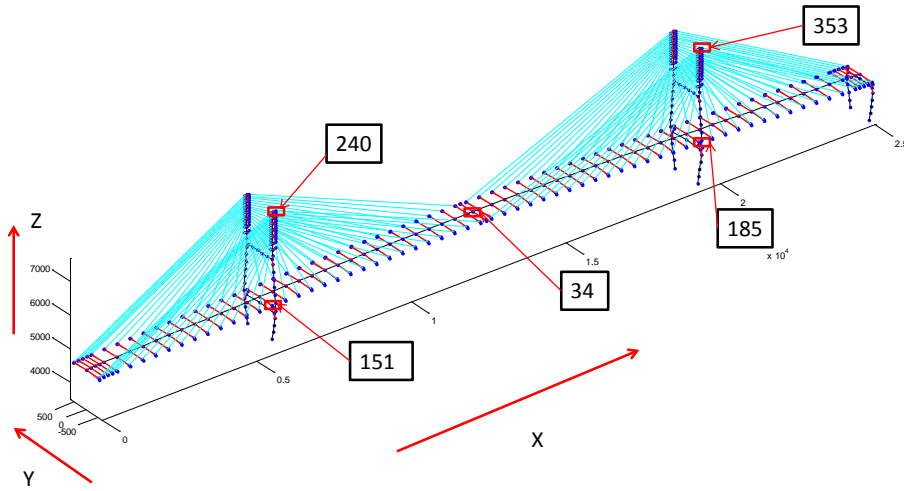


Figure 2.24. Feedback measurements in the benchmark bridge control model.

2.3.2 Bridge Network Model

The wireless traces collected on the Jindo bridge deployment are used to simulate the wireless transmission for Cape Girardeau bridge. The Jindo bridge is a three-span steel-box girder cable-stayed bridge composed of a 344 m of main span and 70 m of side spans. The WSN deployment utilizes the MEMSIC Imote2 platform and a total of 113 Imote2 sensor nodes are deployed with 659 distinct sensor channels as presented in Figure 2.25. Each wireless node includes the Imote2 board, the ISM400 sensor board, and a rechargeable battery supplied by a solar panel (Jang, et al., 2010). Combined with the Illinois SHM Services Toolsuite (SHM Toolsuite, 2015), these

powerful nodes allow for synchronized data collection, onboard processing and multi-hop transmission.

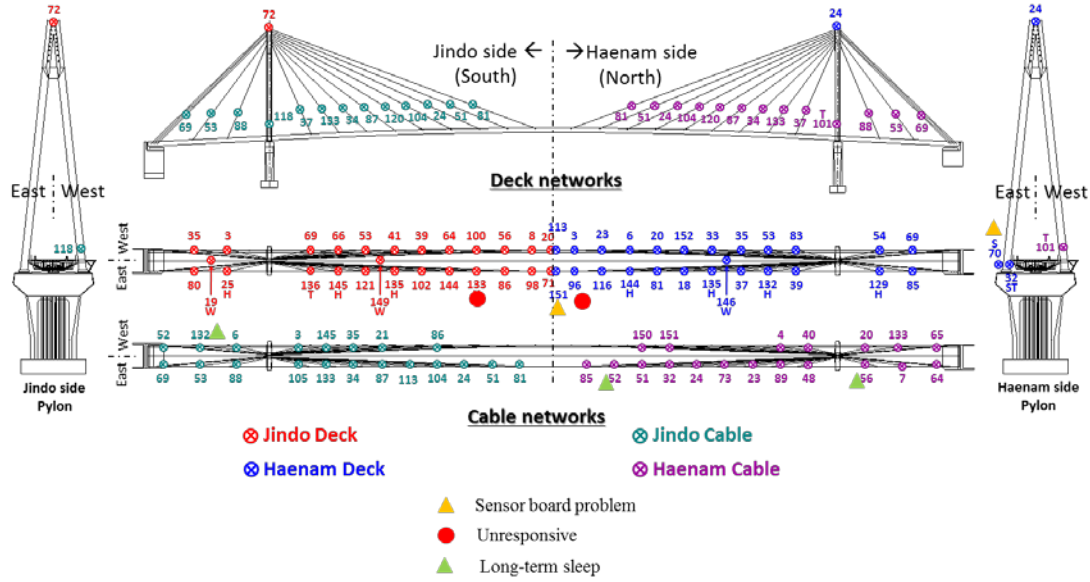


Figure 2.25. Wireless sensor deployment of Jindo bridge (Courtesy of Mechitov).

Sensor nodes 72, 136, 71, 39 and 24 selected from the Jindo bridge are roughly corresponding to the location of sensor nodes 240, 151, 34, 185 and 353 on the Cape Girardeau bridge. To test the accuracy of the TOSSIM simulation, the packet reception ratio (PRR) simulated from TOSSIM is compared with that from the field tests on the Jindo bridge for all 467 wireless links. Of all the wireless links, over 85% of them have the same PRR, indicating that TOSSIM can deliver high fidelity link simulations based on real-world traces (Li, et al., 2012).

2.3.3 Impact of Wireless Network to the Control System

Similar to the wireless building control case study, the impact of wireless network to the original control system is studied. The benchmark bridge control system also

adopts a H2/LQG controller. A total of 24 hydraulic actuators are employed in simulation to provide the control force. These actuators are located between the deck and abutment as well as the deck and the towers and control forces are applied in the longitudinal direction. The control devices act as ideal force actuators, and actuator dynamics and control-structure interaction is neglected in the benchmark model.

In the bridge network, five wireless sensor nodes are selected for feedback. The TDMA time slot is 10 msec while the sampling time step is 20 msec. Similar to the building model, independence of sampling and transmission is assumed. The TDMA transmission of sensor data is shown in Figure 2.26. Transmission of five sensors' data requires 3 sampling steps totaling 60 msec. The data received at the base station is presented in Figure 2.27. The control time step is 60 msec in this case. The structural control system with a TDMA network is simulated under El Centro earthquake. The dynamics of the long span bridge system are relatively slow with the 1st mode at 0.162 Hz. Control of such a bridge system is possible with a much slower rate compared to the building model. However, due to the delay in the wireless network, the control system is still unstable with the direct application of a wired controller, as shown in Figure 2.28. A codesign approach is needed here to design a stable control system which can mitigate structural vibration under seismic excitations.

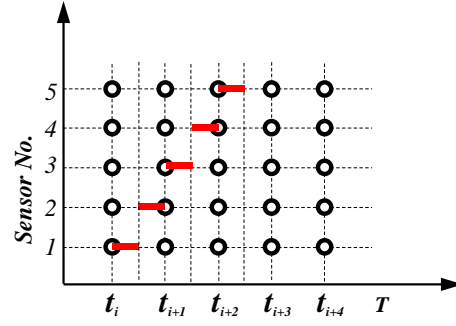


Figure 2.26. TDMA transmission of sensor data.

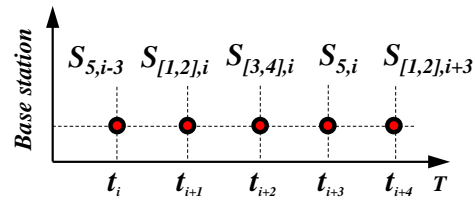


Figure 2.27. Received data at base station.

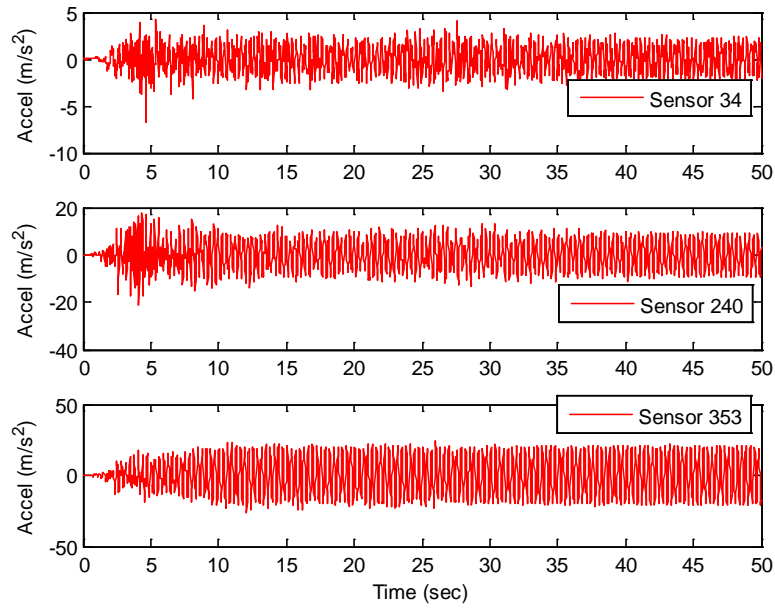


Figure 2.28. Structural responses under El Centro earthquake.

2.3.4 Codesign of Bridge Control System

For the wireless bridge control case study, the codesign approach is discussed in this section.

2.3.4.1 Data Transmission Strategy

For the bridge wireless sensor network, a multi-channel TDMA is adopted. The transmission process is shown in Figure 2.29. In multi-channel TDMA, different pairs of sensor nodes can transmit data at the same time slot using different frequency channels without interfering with each other (i.e. node 72 to node 136 and node 39 to base station). In this way, the TDMA transmission efficiency is improved. This multi-channel TDMA is simulated in TOSSIM with experimentally collected traces from the Jindo bridge. The data loss of 1000 transmissions are given in Figure 2.30. The data loss rate is less than 1% for all channels due to the clean wireless environment, the line-of-sight sensor placement and strong wireless antennas in the Jindo deployment, resulting in large signal to noise ratio between the RSSI and noise traces.

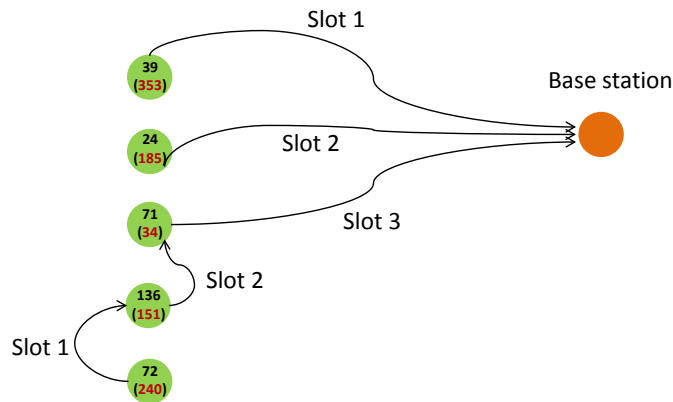


Figure 2.29. Multi-channel TDMA transmission.

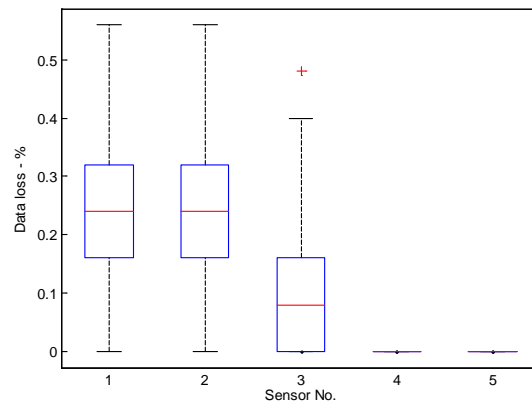


Figure 2.30. Data loss of TDMA network.

Data aggregation strategy (S1) is used to aggregate every 2 samples into a package, i.e. TDMA network transmission as follows, $t_{i,1}\{s_{5, [i-1, i]} \rightarrow \text{base station}\}$ (which means sensor 5 at TDMA slot 1 between t_i and t_{i+1} , transmits data samples from step $i-1$ to step i to base station), $t_{i,1}\{s_{1, [i-1, i]} \rightarrow s_2\}$, $t_{i,2}\{s_{4, [i-1, i]} \rightarrow \text{base station}\}$, $t_{i,2}\{s_{2, [i-1, i]} \rightarrow s_3\}$, $t_{i+1,1}\{s_{3, [i-1, i]} \rightarrow \text{base station}\}$. Control calculation at t_{i+2} uses delayed measurements at t_{i-1} . In this way, the TDMA network induced delay is transformed to a constant 3 sample step delay for each measurement. Control algorithms suitable for systems with constant delay can be applied. Since the data loss rate is very low in the bridge network, a data aggregation strategy to reduce data loss (similar to S2 for wireless building control) is not necessary. The data aggregation strategy (S1) is compared with the original TDMA transmission (T1), as presented in Table 2.5

Table 2.5. Comparison of different strategies.

Strategy	Data aggregation	Sample delay*	Control interval	Data loss reduction
T1	No	60msec	60msec	No
S1	Yes	60msec	20msec	No

Sample delay*: largest delay of all five nodes.

2.3.4.2 Control Design

The OTD control algorithm introduced in the building control case study is applied to the wireless bridge control as well. The constant delay is three time steps. Weighting matrices are chosen as $Q = [I]$ and $R = 0.001*[I]$ (where I is identity matrices of the appropriate dimension). Solving the three coupled nonlinear Equations (2.13-2.15), the optimal control gain G is obtained (listed in the Appendix C).

A Kalman filter is used to estimate the delayed states of the system. The Kalman filter gain L is obtained with Matlab function *lqew* with weighting matrices $S_w = 25*[I]$ and $S_v = [I]$. The obtained L matrix is listed in the Appendix C.

2.3.5 Wireless Bridge Control with Codesigned Control System

The control performance of the codesigned control system is studied in this section. The Simulink diagram for the bridge case study is provided in Figure 2.31. The multi-channel TDMA network is simulated in TOSSIM. The delay due to the data aggregation strategy is implemented in the “delay block”. Three historical earthquakes are used for simulation: i) El Centro. The North-South component recorded at the Imperial Valley Irrigation District substation in El Centro, California, during the Imperial Valley, California earthquake of May, 18, 1940; ii) Mexico City. Recorded at the Galeta de Campos station with site Geology of Meta-Andesite Breccia in September 19, 1985; iii) Gebze, Turkey. The North-South component of the Kocaeli earthquake recorded at the Gebze on Aug. 17, 1999. The responses of wireless control under these earthquakes are shown in Figure 2.32-2.37. Note that the

codesigned wireless control system is able to achieve a significant reduction in the base shear force and moment at the pier as compared to the uncontrolled system. The cable tensions of 128 cables are within the acceptable range specified in the control constraints in the benchmark problem definition.

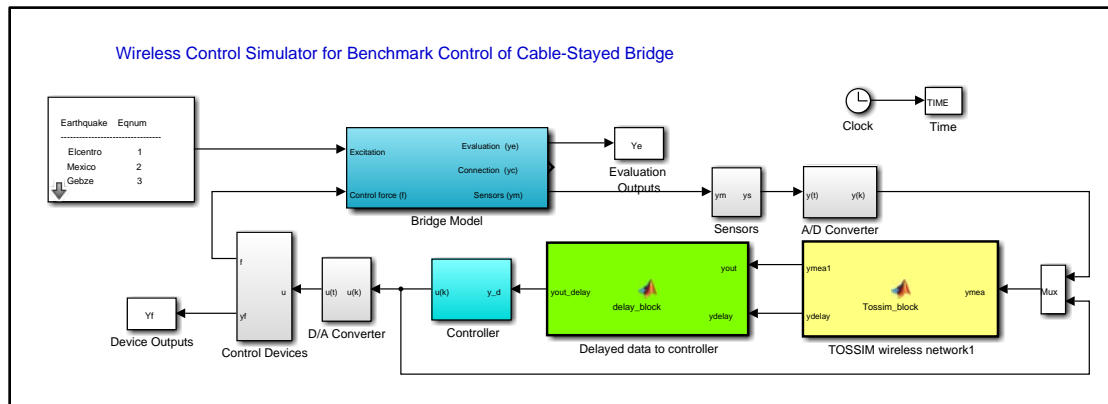


Figure 2.31. Simulink diagram for the bridge case study.

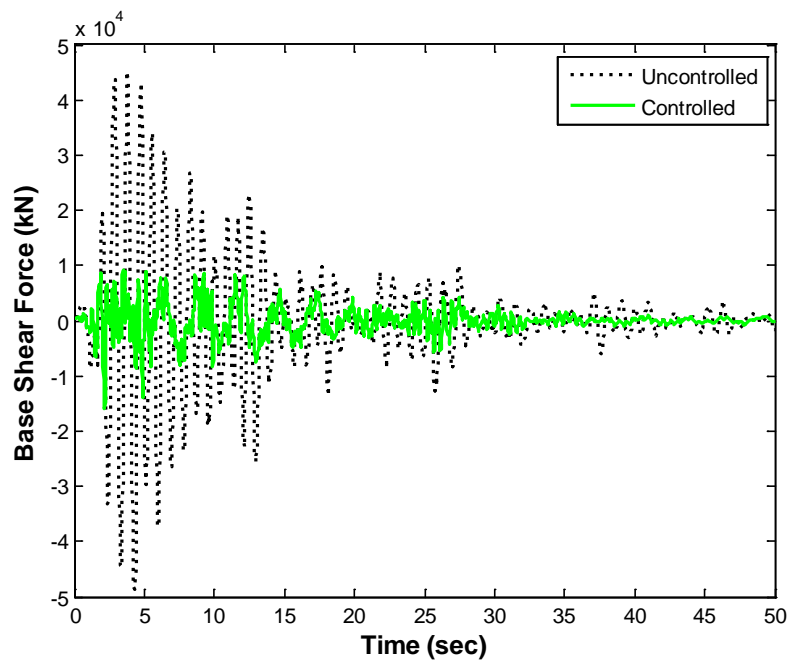


Figure 2.32. Base shear under El Centro earthquake.

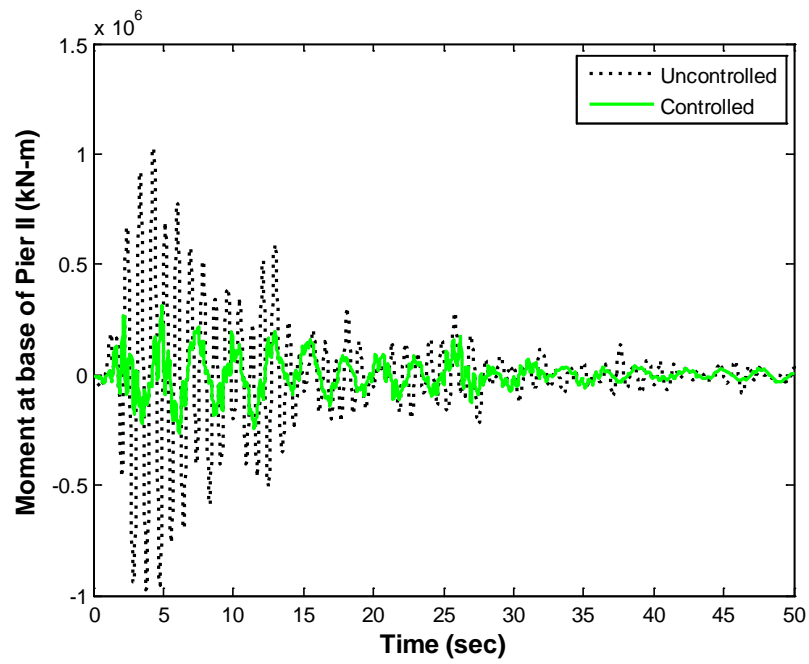


Figure 2.33. Moment at base under El Centro earthquake.

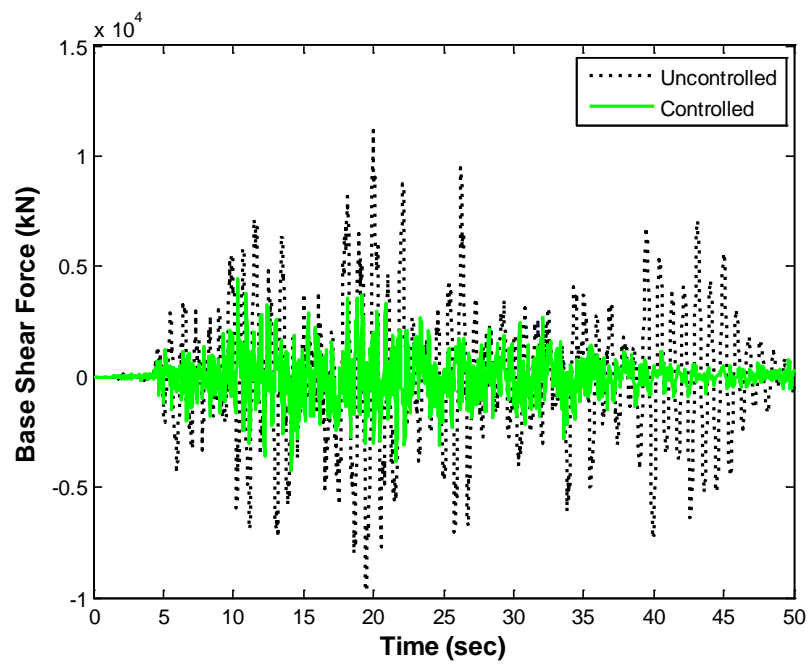


Figure 2.34. Base shear under Mexico earthquake.

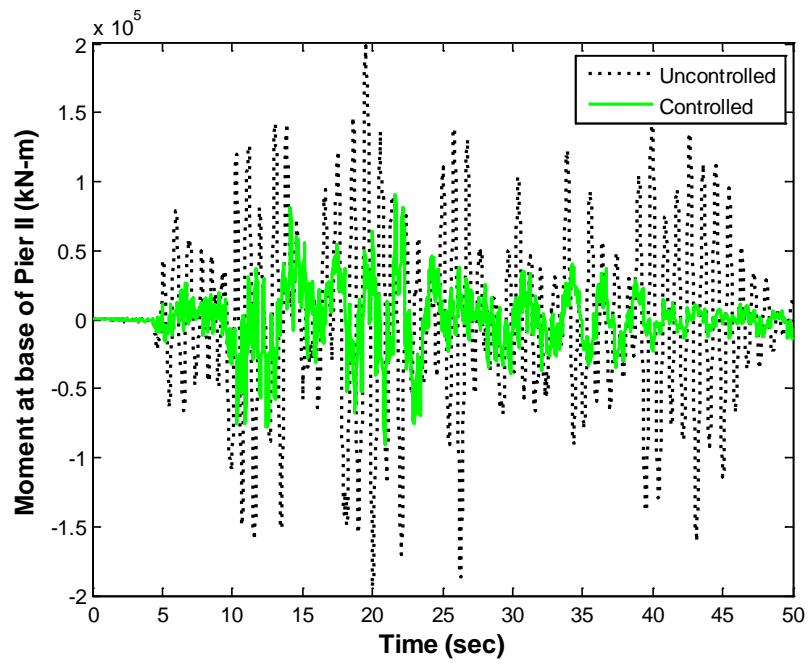


Figure 2.35. Moment at base under Mexico earthquake.

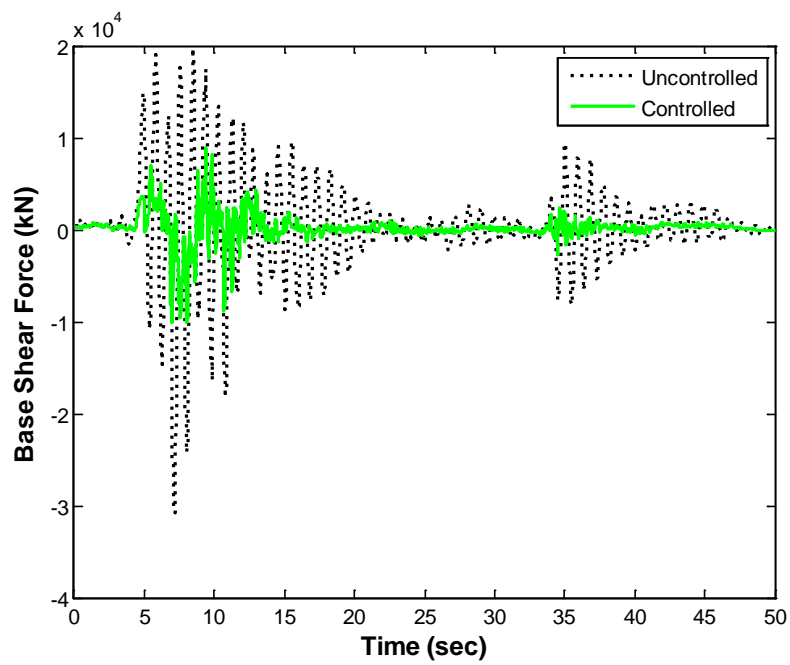


Figure 2.36. Base shear under Gebze earthquake.

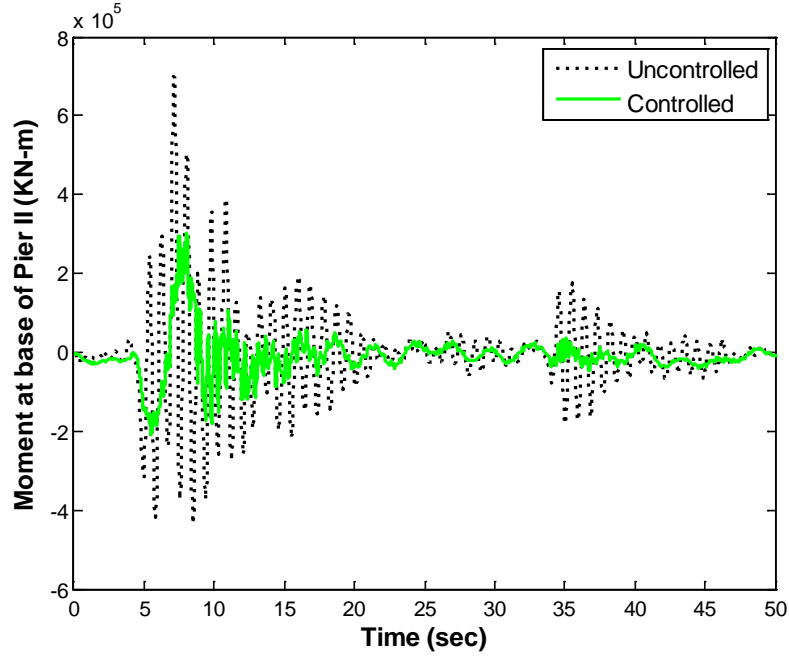


Figure 2.37. Moment at base under Gebze earthquake.

2.3.5.1 Evaluation Criteria

Twelve evaluation criteria are selected from the original benchmark model to evaluate the structural control performance. These criteria are introduced as follows

$$J_1 = \frac{\max_{i,t} |F_{bi}(t)|}{F_{0b}^{max}} \quad (2.16)$$

$$J_2 = \frac{\max_{i,t} |F_{di}(t)|}{F_{0d}^{max}} \quad (2.17)$$

where $F_{bi}(t)$ is the base shear at the i^{th} tower, F_{0b}^{max} is the maximum uncontrolled base shear (of the values at the two towers), $F_{di}(t)$ is the shear at the deck level in the i^{th} tower, F_{0d}^{max} is the maximum uncontrolled shear at the deck level, and $|\cdot|$ indicates absolute value. These two criteria evaluate the shear force at key locations in the towers.

$$J_3 = \frac{\max_{i,t} |M_{bi}(t)|}{M_{0b}^{max}} \quad (2.18)$$

$$J_4 = \frac{\max_{i,t} |M_{di}(t)|}{M_{0d}^{max}} \quad (2.19)$$

where $M_{bi}(t)$ is the moment at the base of the i^{th} tower, M_{0b}^{max} is the maximum uncontrolled moment at the base of the two towers, $M_{di}(t)$ is the moment at the deck level in the i^{th} tower, and M_{0d}^{max} is the maximum uncontrolled moment at the deck level in the two towers. These two criteria evaluate the moments in the towers at the same key locations.

The fifth criterion is a measure of the deviation of the tension in the stay cables from the nominal pretension, given by

$$J_5 = \max_{i,t} \left| \frac{T_{ai}(t) - T_{0i}}{T_{0i}} \right| \quad (2.20)$$

where T_{0i} is the nominal pretension in the i^{th} cable and $T_{ai}(t)$ is the actual tension in the cable as a function of time. This criterion is selected to reduce the likelihood of failure or unseating of the cables.

The sixth criterion is a measure measures of the normed values of the base shear

$$J_6 = \frac{\max_i \|F_{bi}(t)\|}{\|F_{0b}(t)\|} \quad (2.21)$$

where $\|F_{0b}(t)\|$ is the maximum of the normed value of the uncontrolled base shear of the two towers.

The seventh criterion measures the normed values of the overturning moment

$$J_7 = \frac{\max_i \|M_{bi}(t)\|}{\|M_{0b}(t)\|} \quad (2.22)$$

where $\|M_{ob}(t)\|$ is the maximum of the normed value of the uncontrolled base shear of the two towers.

The eighth evaluation criterion is a measure of the normed value of the deviation of the tension in the stay cables from the nominal pretension, given by

$$J_8 = \max_{i,t} \frac{\|T_{ai}(t) - T_{0i}\|}{T_{0i}} \quad (2.23)$$

The ninth evaluation criterion is a measure of the maximum force generated by the control device(s), given by

$$J_9 = \max_{i,t} \left(\frac{f_i(t)}{W} \right) \quad (2.24)$$

where $f_i(t)$ is the force generated by the i^{th} control device over the time history of each earthquake, and W is the seismic weight of bridge.

The tenth criterion is based on the maximum stroke of the control device(s). This performance measure is given as

$$J_{10} = \max_{i,t} \left(\frac{|y_i^d(t)|}{x_0^{\max}} \right) \quad (2.25)$$

The eleventh evaluation criterion measures the maximum instantaneous power required to control the bridge, and is given by

$$J_{11} = \frac{\max_t [\sum_i P_i(t)]}{\dot{x}_0^{\max W}} \quad (2.26)$$

where $P_i(t)$ is a measure of the instantaneous power required by the i^{th} control device, and \dot{x}_0^{\max} is the peak uncontrolled velocity at the top of the towers relative to the ground.

The twelfth criterion is a measure of the total power required to control the bridge, given by

$$J_{12} = \frac{\sum_i \left(\int_0^{t_f} P_i(t) dt \right)}{x_0^{max_W}} \quad (2.27)$$

where x_0^{max} is the peak uncontrolled displacement at the top of the tower relative to the ground.

2.3.5.2 Evaluation Results

One hundred simulations are carried out under each of the three historic earthquakes. The evaluation results for codesigned wireless control system are shown in Table 2.6. The data loss ratio of the network is too low to observe its impact in the results. The wireless control performance is identical to the ideal data loss free case. Some of the evaluation results are greater than 1 (i.e. J_2 and J_4). This outcome is also observed in the original wired control case and is regarded as acceptable for these criteria. The force requirement as well as the displacement and velocity requirements are shown in Table 2.7. These numbers are feasible in a control device of this size. Note that the maximum force under all three earthquakes are the same. This result is due to the maximum force saturation for the control input at 1000 kN. The time history of control force under El Centro earthquake is provided in Figure 2.38 to illustrate the saturation at some points in time.

Table 2.6. Evaluation results for wireless control.

	<i>El Centro</i>	<i>Mexico</i>	<i>Gebze</i>	<i>Max</i>
J_1	0.437	0.433	0.427	0.437
J_2	1.16	1.07	1.30	1.30
J_3	0.350	0.486	0.458	0.486
J_4	0.761	0.572	1.18	1.18
J_5	0.221	0.055	0.147	0.221
J_6	0.504	0.712	0.617	0.712
J_7	0.625	0.688	0.880	0.880
J_8	0.066	0.012	0.023	0.066
J_9	2.0e-3	2.0e-3	2.0e-3	2.0e-3
J_{10}	1.05	1.12	2.03	2.03
J_{11}	6.2e-3	5.9e-3	7.2e-3	7.2e-3
J_{12}	9.8e-4	7.9e-4	6.8e-4	9.8e-4

Table 2.7. Actuator requirements for wireless control.

	<i>El Centro</i>	<i>Mexico</i>	<i>Gebze</i>	<i>Max</i>
<i>Force (kN)</i>	1000	1000	1000	1000
<i>Stroke (m)</i>	0.156	0.054	0.266	0.266
<i>Vel (m/s)</i>	0.791	0.362	0.576	0.791

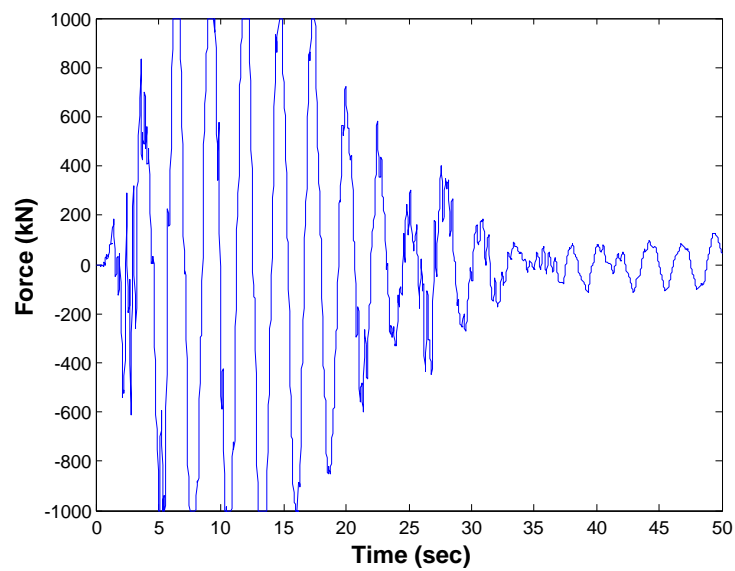


Figure 2.38. Actuator force under El Centro earthquake.

2.4 Summary

In this Chapter, the WCPS is developed to realistically capture and simulate both the cyber (wireless network) and physical (structural) aspects of the wireless control system. The WCSP integrates Matlab (Simulink) and TOSSIM for realistic wireless control simulation. Two case studies are examined, each combining a structural model with wireless traces collected from real-world environments. The building case study combines a representative benchmark building model and wireless traces collected from a multi-story building on the Washington University in St. Louis campus. The bridge study combines the structural model of the Cape Girardeau bridge over the Mississippi River and wireless traces collected from a similar bridge (the Jindo bridge) in South Korea. These case studies shed light on the challenges of wireless control system and the limitations of a traditional structural control approach under realistic wireless conditions. Finally, a cyber-physical codesign approach to wireless control system is illustrated which integrates data aggregation strategies (for communication and control) and an optimal time delay controller that improves structural control performance. The cyber-physical codesigned wireless control system not only represents a promising step toward smart civil infrastructure, but also provides insights and tools that can be generalized to other cyber-physical systems employing wireless control.

CHAPTER 3. ARDUINO BASED WIRELESS STRUCTURAL CONTROL PLATFORM DEVELOPMENT

In the previous chapter, the WCPS is developed as the numerical simulator to realistically simulate wireless control system and to investigate codesign approaches with two case studies. In this chapter, a state-of-the-art wireless structural control platform is developed to enable experimental studies of codesigned wireless control systems. As introduced in Figure 1.4 in chapter 1, a functional wireless sensing and control node must have the sensing module, wireless transmission module and actuation module. In this chapter, those modules are developed based on the open source Arduino platform.

3.1 Introduction to Arduino Board

The wireless control system is developed based on Arduino Due platform (Arduino Due, 2012), which is the first Arduino board based on the 32 bit microcontroller. It has 54 digital I/O pins, 12 analog inputs, 4 UARTs, 2 DAC, a SPI header, a JTAG header, an 84 MHz clock and etc., as shown in Figure 1.10. The numerous I/O options makes it flexible for different applications. An integrated development environment (IDE) is available from the Arduino website for writing, debugging code and uploading to the board (see Figure 3.1). The Arduino programming language is based on C/C++. It links against AVR Libc, a high quality C library for use with GCC on ATMEL AVR microcontrollers (AVR Libc, 2012).

The Arduino environment runs on Windows, Mac OS X, and Linux operating systems. Both the hardware and software of the board are open source.

The Arduino Due platform is compared with other state-of-the-art wireless sensor platforms in Table 2.1 (Imote2 Datasheet, TelosB Datasheet, Swartz & Lynch, 2009). Comparing these platforms, Arduino Due and imote2 both use a 32 bit processor, which allows operation on 4 bytes data in a single CPU clock. Imote2 has the fastest processor speed and RAM among all these platforms. However, Memsic Inc. stopped producing imote2 boards around 2012. In terms of programming, coding with NesC language on the Tinyos system of imote2 and TelosB is not as intuitive as coding with C/C++ on Arduino. The Arduino board has a large community of users (more than 700,000 users by 2013) providing a valuable resource for discussion of hardware and software related issues.

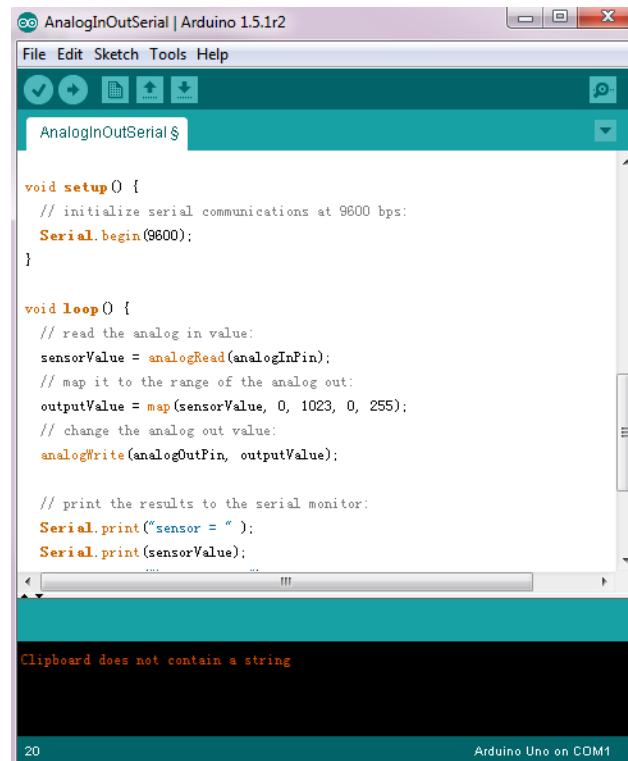


Figure 3.1. Integrated development environment of Arduino.

Table 3.1. Wireless sensor platform comparison.

	TelosB (2004)	Narada (2005)	iMote 2 (2007)	Arduino Due (2013)
Processor	TI MSP 430	Atmel ATMega 128	PXA271 XScale	AT91SAM3X8E
Processor Speed	8 MHz	8 MHz	13 - 416 MHz	84 MHz
Bus Size	16 bit	8 bit	32 bit	32 bit
Flash Memory	48 KB	128 KB	32 MB	512 KB
RAM	10KB SRAM	4 KB SRAM	256 KB SRAM+ 32 MB SDRAM	96KB SRAM
ADC Channels	8	4	-	12
DAC Channels	2	2	-	2
ADC/DAC Resolution	12 bit	16/12 bit	-	12 bit
Digital I/O Channels	-	-	-	54
Radio	Chipcon CC2420	Chipcon CC2420	Chipcon CC2420	-
Transmission Range	Indoor: 30 m; Outdoor: 50 m	Indoor: 100 m; Outdoor: 300 m	Indoor: 30 m; Outdoor: 50 m	-
Programming Language	NesC	C	NesC	C/C++
Dimension (cm x cm x cm)	6.5, 3.1, 0.6	6, 6, 2	4.8, 3.6, 0.9	10.4, 5.3, 1.5
Other Feature			Open source software	Open source software & hardware

3.2 Sensing Module Development

A tri-axial accelerometer ADXL 345 from Analog Device is selected as the sensing component as shown in Figure 3.2 (a). The ADXL 345 uses a MEMS accelerometer and has a maximum measurement range of ± 16 g in all three directions with 13 bit resolution. The sampling rate is user selectable from 6.25 Hz to 3200 Hz. The accelerometer has low power consumption, requiring about 40 μ A in measurement mode and 0.1 μ A in standby

mode (25 °C, 2.5V) (ADXL 345 Datasheet). Data transmission from the ADXL 345 to the Arduino Due uses the serial peripheral interface (SPI).

To obtain force measurements from force transducer, an analog to digital conversion (ADC) board is developed for BNC input within ± 10 Volts amplitude as shown in Figure 3.2 (b). The circuit design and PCB board design are provided in the Appendix B. AD7982 from Analog Device is selected as the ADC component. This ADC has 18 bit high resolution. It adopts SAR type architecture which can perform the conversion with high speed, i.e. 1 million samples per second (MSPS). The power consumption is low, i.e. 70 μ W at 10 kSPS, which is attractive for battery-powered system. With the ADC board developed, the BNC signal first passes through an attenuating amplifier AD 8475 with 0.4 gain to convert the input voltage to ± 4 Volts, bringing it within the input range (± 5 Volts) of the ADC AD 7982. After A/D conversion, the digital output is sent to the Due board through the SPI interface. The SPI interface also controls the timing of the ADC task using the clock on the master device (Arduino Due board in this case). Because the Due board only has one SPI interface which is required for both the ADXL 345 and the ADC board, the slave selection (SS) pin is utilized to control the communication with multiple slave devices as shown in Figure 3.3. Here the ADXL 345 and the ADC board are both slave devices.

The developed ADC board is first tested with constant voltage input from a voltage generator. The constant voltage is varied from 0V to 8V. The measured voltage is shown in Figure 3.4 (a-d) with sampling frequency 800 Hz. There is a measurement error due to

the circuit noise and quantization error. From the power spectral density (PSD) plot, the noise has a flat power intensity across the frequency range of interest. The RMS error is calculated with Equation (3.2) and listed in Table 3.2.

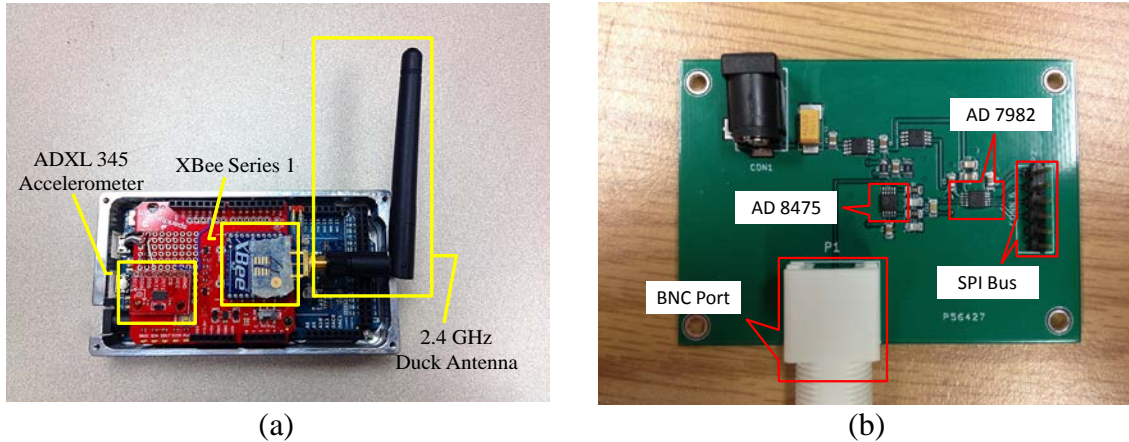


Figure 3.2. (a) Arduino based sensor board, (b) Developed ADC board.

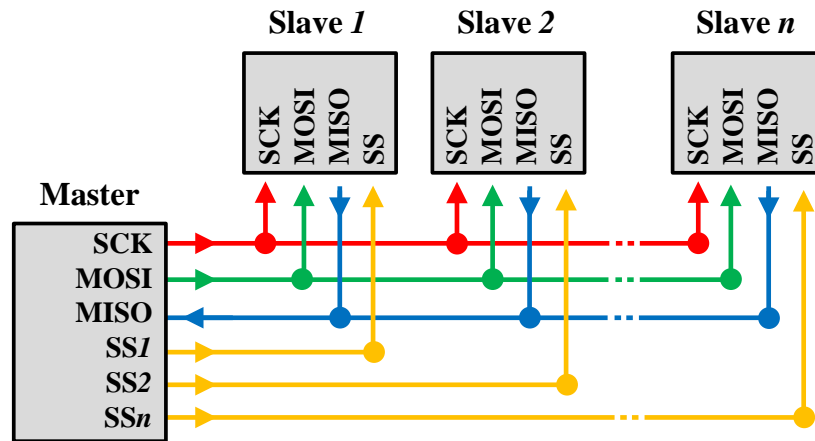


Figure 3.3. SPI interface for communication with multiple devices.

Additional sensing tests are conducted to verify the performance the ADXL 345 and the ADC board. The developed sensor board is attached to a single story shear structure as shown in Figure 3.5 (a). A wired accelerometer 333B40 from PCB Piezotronics, Inc. is

attached as the reference. Measurements from the ADXL 345 and the ADC with BNC input from the wired accelerometer are sampled at 100 Hz and 200 Hz, respectively. Measurements from the Vibpilot DAQ system are sampled at 400 Hz, since 100 Hz and 200 Hz are not options in the Vibpilot system. The results of these sensing tests are presented in Figure 3.5 (b-f). Measurement error is calculated using Equation (3.1). Measurement error $e_t = 0.132$ for the ADC board, and $e_t = 0.214$ for the ADXL 345 at 100 Hz; Measurement error $e_t = 0.135$ for the ADC board, and $e_t = 0.243$ for the ADXL 345 at 200 Hz. Based on the calculated results, the ADXL 345 has larger measurement error than the ADC board. This conclusion is also observed in Figure 3.5 (b-d). The ADXL 345 measurements are slightly larger than the ADC board and Vibpilot measurements. Also, as the sampling frequency increases, measurement noise of the ADXL 345 also increases. This is observed by comparing Figure 3.5 (c) and Figure 3.5 (f). Thus, 100 Hz sampling frequency is chosen for the ADXL 345 in the numerical simulation and experimental study.

$$e_t = \frac{\|x(t) - r(t)\|_2}{\|x(t)\|_2} \quad (3.1)$$

where $\|\cdot\|_2$ is the l_2 norm, e_t is the time domain error, $x(t)$ is the Vibpilot measurement, and $r(t)$ is the ADXL 345 measurement or the ADC board measurement. The Vibpilot measurements are down-sampled to the same frequency of ADXL 345 and ADC measurements to calculate the associated errors.

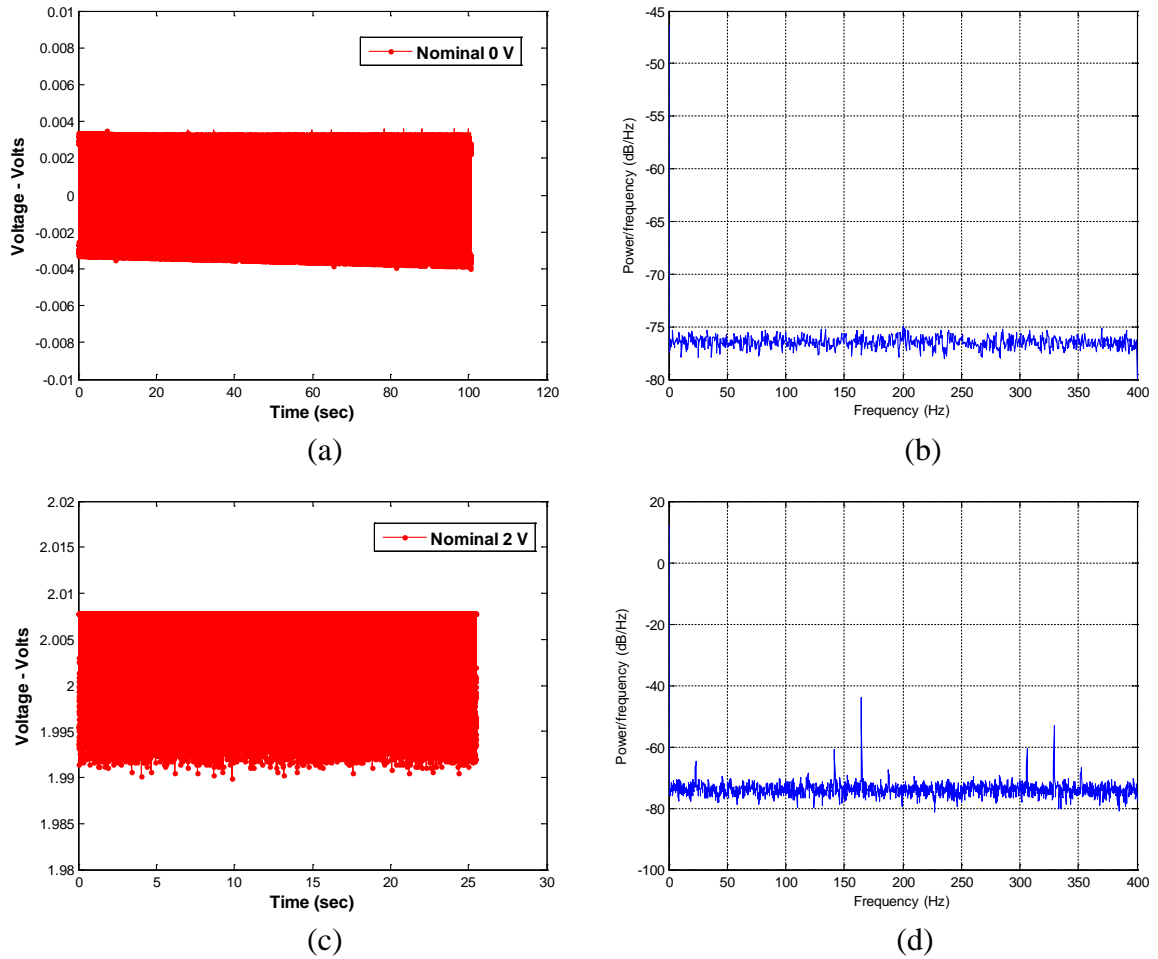


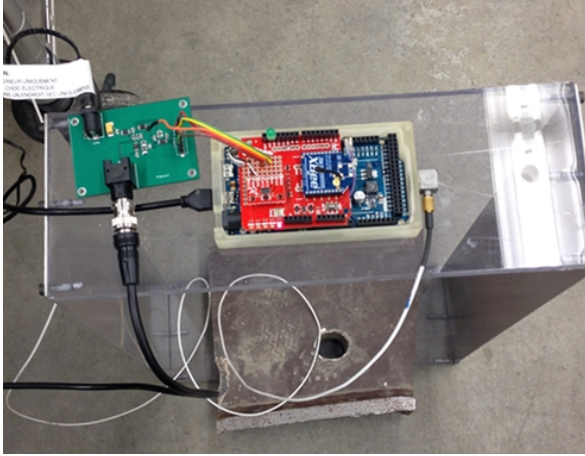
Figure 3.4. ADC board test results: (a) ADC measurements at 0V, (b) PSD of the measurements in (a); (c) ADC measurements at 2V, (d) PSD of the measurements in (c).

$$RMSE = \sqrt{\frac{\sum_{i=1}^n (y_i - y)^2}{n}} \quad (3.2)$$

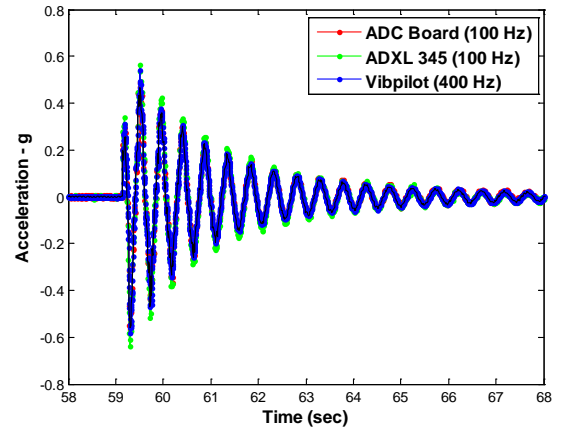
where n is the number of points, y_i is the measured value, y is the predicted value.

Table 3.2. Measurement error.

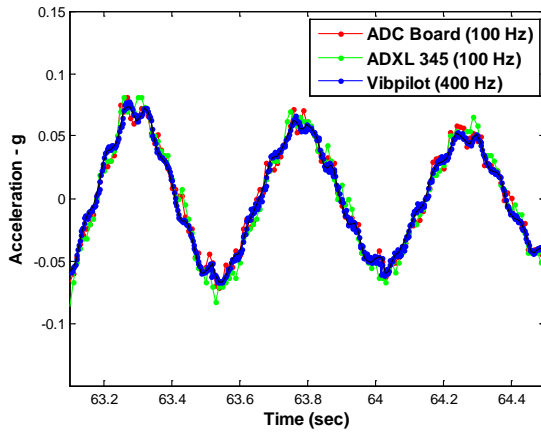
Voltage	0V	0.5V	1V	2V	3V	7V	8V
<i>RMSE</i>	3e-3	3.1e-3	3.3e-3	5.2e-3	2.6e-3	3.3e-3	4.7e-3



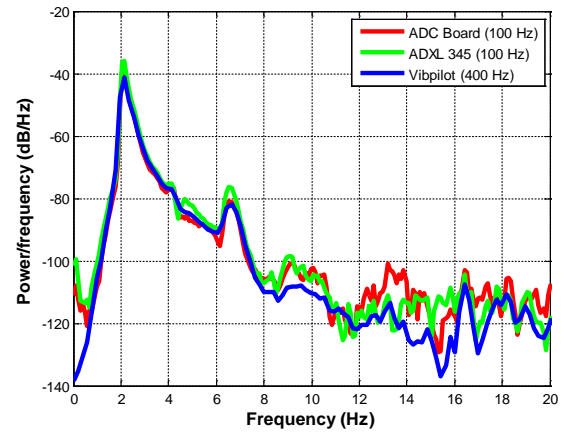
(a)



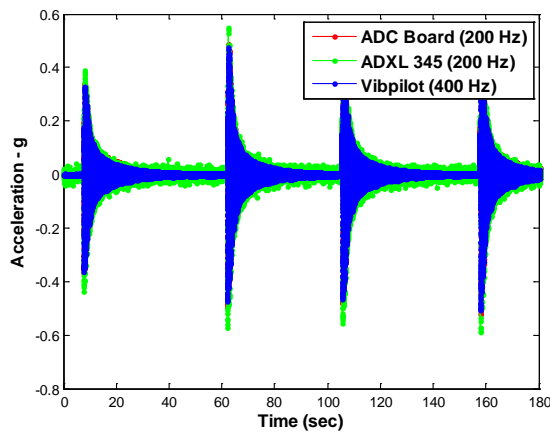
(b)



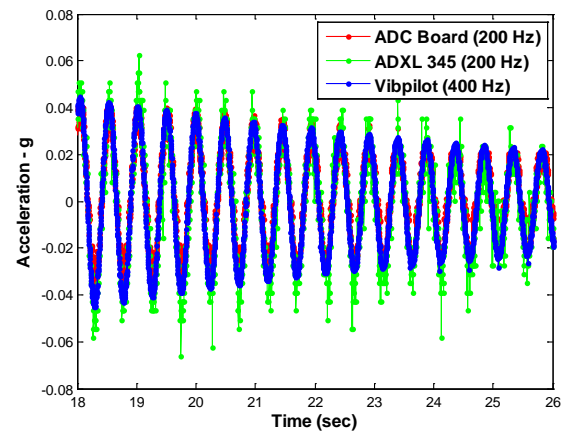
(c)



(d)



(e)



(f)

Figure 3.5. Sensor tests: (a) Test setup, (b) Test results at 100Hz, (c) Zoomed view of (b), (d) Frequency domain comparison, (e) Test results at 200Hz, (f) Zoomed view of (e).

3.3 Communication Module Development

An XBee Series 1(S1) with 802.15.4 stack from Digi International Inc. is adopted as the wireless transmission module. It has a dedicated microcontroller for wireless data transmission. Current consumption during transmission and reception is 50 mA at 3.3V. The power-down current is less than 10 μ A at 3.3V. The maximum transmission rate over-the-air is 250 kb/s. The maximum transmission range is 100 meters (XBee S1 Datasheet). Note that an enhanced version of XBee S1 is also available which has maximum transmission range 1500m. The tradeoff is higher current consumption (250 mA at 3.3V) during transmission. Communication of XBee S1 with Arduino Due is through the API mode. The maximum baud rate of 115200 is used for fastest communication speed between the Arduino and XBee (Sun, et al., 2015).

Transmission tests are conducted to measure the communication delay and data loss as shown in Figure 3.6. In this setup, there is one coordinator (gateway node) and two end devices (leaf nodes). The transmission delay is calculated with Equations (3.3-3.4)

$$\theta = (T'_1 - T_1 - T_2 + T'_2)/2 \quad (3.3)$$

$$\delta = (T'_1 - T_1 - \theta)/2 \quad (3.4)$$

where θ is the offset between the gateway node and leaf node, δ is the transmission delay in one direction, T_1 is the local time at the gateway node to send one package to the leaf node, T'_1 is the local time at leaf node after receiving the package from the gateway node, T'_2 is the local time at the leaf node to send one package to the gateway node, T_2 is the local time at the gateway node after receiving the package from the leaf node. Over five thousand transmission tests are conducted to calculate the transmission delay. The one

way transmission delay is shown in Figure 3.7 (a-b). The delay is below 5.7 msec, with a mean value 5.6 msec. The data loss is 4.5% in the tests.

It is worth mentioning that originally the XBee Series 2(S2) from Digi International Inc. was selected. It uses the ZigBee mesh network protocol with low power consumption (i.e. 45 mA at 3.3V during transmission and reception). However, the one-way transmission delay is over 15msec as provided in Figure 3.7 (c-d), which is not acceptable for this wireless control application. Therefore, the XBee Series 1 is utilized instead, which uses the basic IEEE 802.15.4 protocol and has much shorter transmission delay.

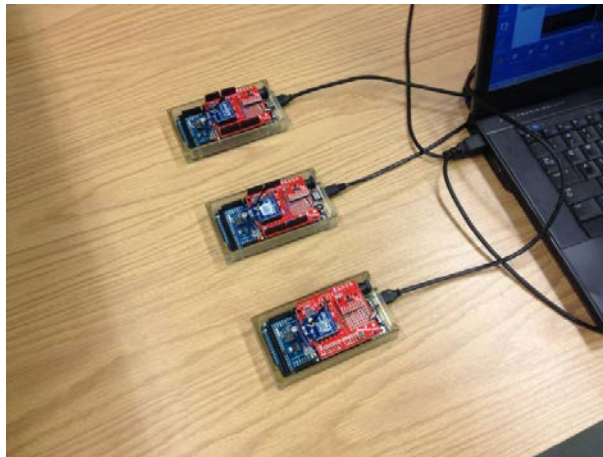


Figure 3.6. Transmission delay test.

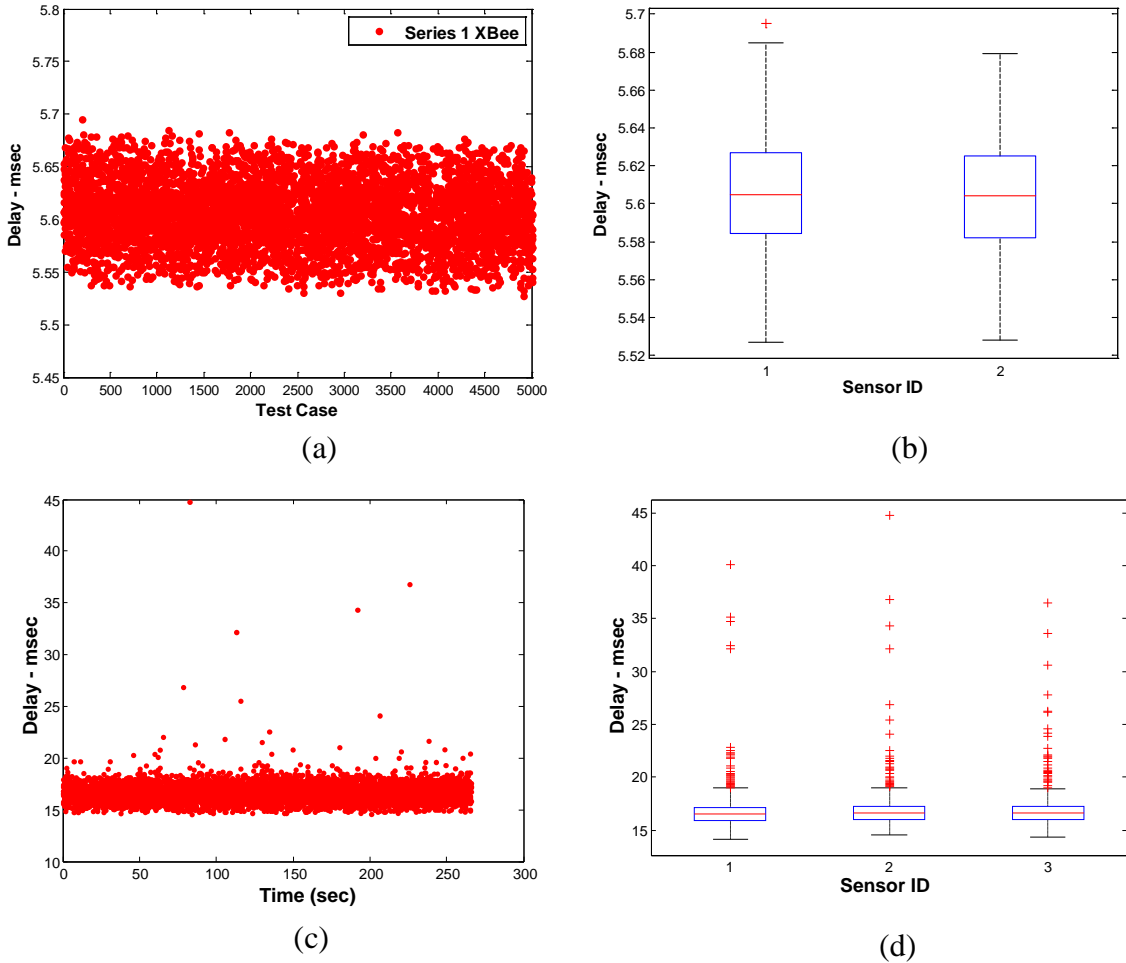


Figure 3.7. Transmission test results for XBee S1 (a) Sensor 1, (b) Sensor 1 and 2; Transmission test results for XBee S2 (c) Sensor 1, (d) Sensor 1, 2 and 3.

Time synchronization is achieved using the averaged offset calculated with Equation (3.3) to compensate for the time differences between the gateway node and leaf node. The XBee uses CSMA/CA multiple access method, however TDMA is emulated by disabling acknowledgement (ACK) and retransmission and assigning each sensor with a 10 msec time slot. With this setup, the wireless network can achieve 100 Hz sampling frequency with one leaf node, or 50 Hz with two leaf nodes.

Onboard computational time is calculated for the control implementation. A discrete controller is presented in Equations (3.5-3.6)

$$x(k+1) = A_d x(k) + B_d u(k) \quad (3.5)$$

$$y(k) = C_d x(k) + D_d u(k) \quad (3.6)$$

where $x(k) \in R^{n \times 1}$ is the states at $(k+1)^{\text{th}}$ step, $u(k) \in R^{1 \times 1}$ is the measurement input at k^{th} step, $y(k) \in R^{m \times 1}$ is the control force at k^{th} step. A_d, B_d, C_d, D_d are the discrete state space matrices of appropriate dimensions. Here, $\dim(y(k)) = 1$.

The controller is implemented on the Due board using various dimensions of the state space matrices as presented in Table 3.3. The “A” matrix is increased from 6x6 to 16x16 floating point numbers and the computational time is still less than 1 msec (as shown in Figure 3.8). The computational time is also calculated using the random number generation function to generate the “A” matrix with and without the ADXL 345 measurements as input (the black and blue line in Figure 3.8). When the measured input is obtained with the ADXL 345, additional sensing and ADC conversion time is required.

Table 3.3. Computational time.

Size of “A” matrix	6x6	8x8	10x10	11x11	12x12	14x14	16x16
Computation Time (μs)	100	181	265	275	315	483	577

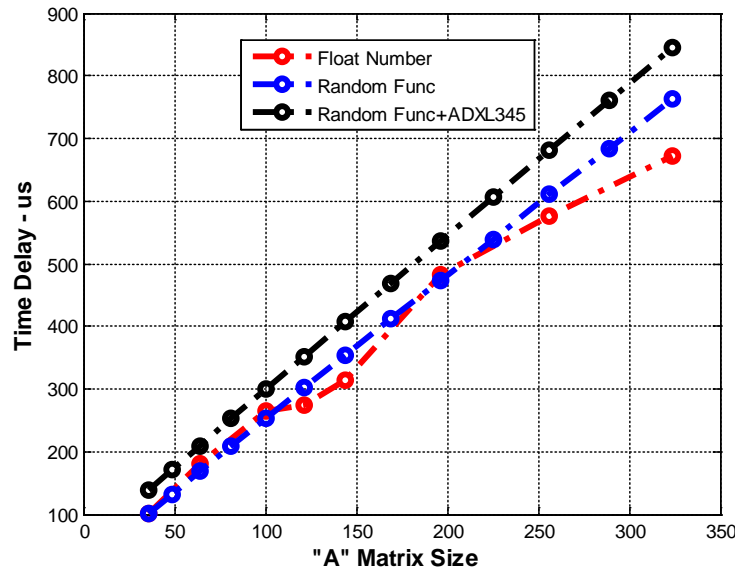


Figure 3.8. Computational time.

3.4 Actuation Module Tests

The actuation module is to provide a control command voltage to the damper in the wireless semi-active control tests. The onboard DAC is first tested. Voltage signal from the DAC pin is sent to the ADC pin and dSpace system. The nominal DAC command varies from 0V to 3.3V with 12 bit resolution, while the actual measurements by the ADC pin and dSpace system varies between 0.5V and 2.7V (see Figure 3.9 (a)). Apparently, there is a gain and DC offset in the circuit which narrows the voltage output range of the DAC. This DAC cannot be used in our application as the minimum voltage is not at 0V. Then, the onboard digital output pin is tested. The nominal digital output is either 0V (LOW) or 3.3V (HIGH), while the actual measurements by ADC pin and dSpace is either 0V (LOW) or 2.5V (HIGH) (see Figure 3.9 (b)). Since the actual digital

LOW is at 0V, the digital output pin is appropriate to control the damper force using the clipped optimal control strategy, which is explained in more detail in the next chapter.

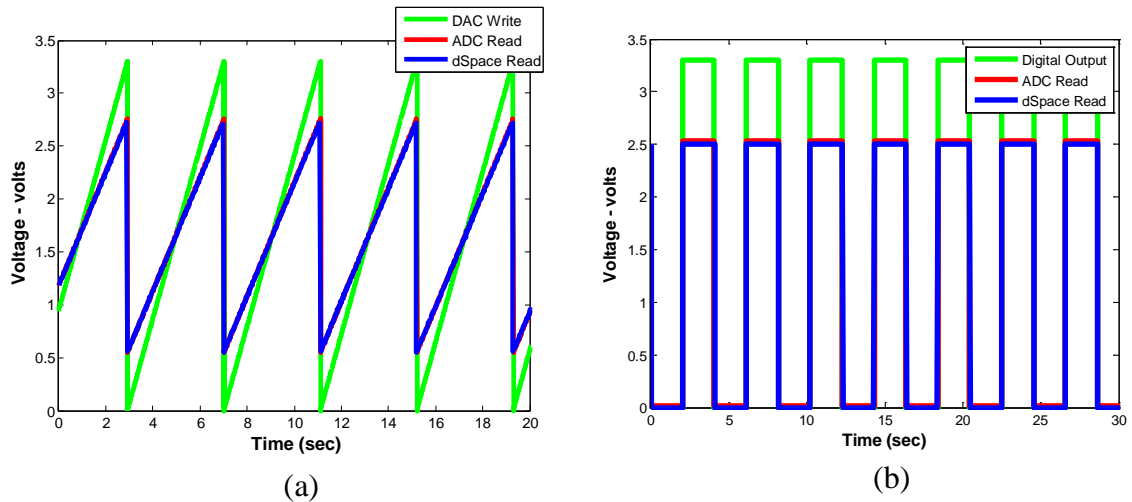


Figure 3.9. Actuation module test: (a) DAC test, (b) Digital output test.

3.5 Summary

In this chapter, a state-of-the-art wireless sensing and control system is developed based on the open source Arduino platform. Sensing and wireless communication modules are built onto the Arduino Due platform. An 18 bit high resolution ADC board is developed for converting an analog signal with $\pm 10V$ amplitude into a digital signal for the Due board. Verification tests are conducted to evaluate the performance of the sensing module, the high resolution ADC board, and the wireless transmission module as well as to assess the computational power of the onboard microcontroller. The actuation module is also tested for controlling the damper voltage. The verification test results are satisfactory for our application. The proposed wireless sensing and control platform will be shared with the community to promote wireless control studies.

CHAPTER 4. WIRELESS CONTROL OF A 3-STORY SHEAR BUILDING

The wireless sensing and control platform has been introduced in the previous chapter. In this chapter, performance of various wireless control approaches are first studied through numerical simulation. Wireless control of a 3-story shear structure is performed equipped with a semi-active control device (MR damper). A realistic damper model is obtained based on experimental tests. The performance of the various wireless control strategies (decentralized control, partially decentralized control, centralized control) is compared. Next, experimental studies are conducted using the wireless sensors to control the 3-story shear structure in the IISL lab. A six degree-of-freedom hydraulic shake table is used to generate seismic ground motions. The control performance is evaluated while considering the impact of modeling uncertainties, measurement noises as well as time delay and data loss induced by the wireless network.

4.1 Numerical Simulation

Numerical simulations are first conducted using the numerical model of a 3-story shear structure, equipped with a shear mode MR damper on the first floor (see Figure 4.1). The structure is modeled as a lumped mass system with 22.7 kg of mass on each floor. The stiffness of each floor is 297N/cm and a damping ratio of 0.5% is used for each mode.

The natural frequencies are 2.56 Hz, 7.18 Hz and 10.38 Hz. Assuming the system is linear time-invariant (LTI), the equation of motion can be written as

$$M\ddot{x} + C\dot{x} + Kx = -M\Gamma\ddot{x}_g + \Lambda f \quad (4.1)$$

where $x \in R^{3 \times 1}$ is the relative displacements with respect to the ground, $\Gamma \in R^{1 \times 1}$ is a column vector of ones, $\ddot{x}_g \in R$ is a one dimensional ground acceleration, $f \in R$ is the control force generated by the MR damper, and $\Lambda \in R^{3 \times 1}$ is the vector determined by the location of the MR damper. M , C , K are the mass matrix, damping matrix and stiffness matrix, respectively, defined as

$$M = \begin{bmatrix} 22.7 & 0 & 0 \\ 0 & 22.7 & 0 \\ 0 & 0 & 22.7 \end{bmatrix} kg$$

$$C = \begin{bmatrix} 11.1 & -3.3 & -0.7 \\ -3.3 & 10.4 & -4.0 \\ -0.7 & -4.0 & 10.4 \end{bmatrix} N/(m/s)$$

$$K = \begin{bmatrix} 5.94 & -2.97 & 0 \\ -2.97 & 5.94 & -2.97 \\ -0.7 & -2.97 & 2.97 \end{bmatrix} \times 10^4 N/m$$

The state space representation of the system is given by

$$\dot{x}_s = Ax_s + Bu + Ew \quad (4.2)$$

$$y = Cx_s + Du + Fw \quad (4.3)$$

where $x_s = \begin{bmatrix} x(t) \\ \dot{x}(t) \end{bmatrix}$ is the state of the system, u is the control force input, w is the ground excitation, y is the measurement vector, $A = \begin{bmatrix} 0 & I \\ -M^{-1}K & -M^{-1}C \end{bmatrix}$, $B = \begin{bmatrix} 0 \\ M^{-1}\Lambda \end{bmatrix}$, $E = [0 \ 0 \ 0 \ -1 \ -1 \ -1]'$, and C , D , F are matrices of appropriate dimensions depending on the measurement outputs.

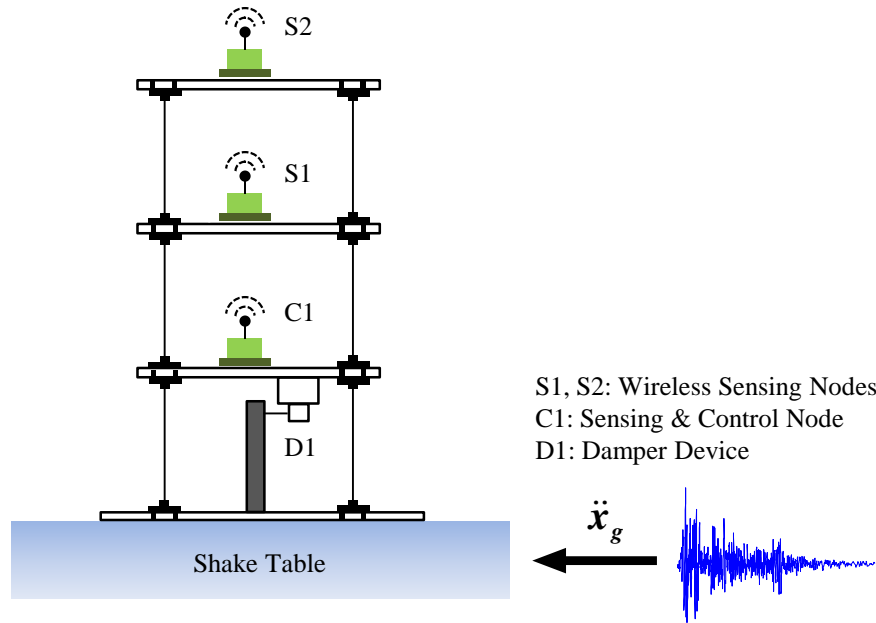


Figure 4.1. Three story shear building.

4.1.1 Damper Model Identification

MR dampers have the potential to mitigate structural vibrations in seismic events. An MR damper's operation is based on controllable MR fluids. MR fluids have the ability to change from a free-flowing, linear, viscous fluid condition to a semi-solid condition when exposed to a magnetic field. To realistically simulate wireless structural control, an effective damper model needs to be included in the numerical simulation. There are various models available to represent the nonlinear behavior of MR damper, such as the “Viscous + Dahl” model (Rodriguez, 2009), hyperbolic tangent model (Gavin, 2001), phenomenological Bouc-Wen model (Spencer, et al., 1997) and algebraic model (Song, 2005). In this study, the shear mode MR damper (Figure 4.2(a)) is modeled with Bouc-

Wen model found to be effective for this device as shown in Figure 4.2(b). The control force f is given by Yi, et al., (1999)

$$f = \alpha(u)z + c_0(u)\dot{x} + k_0x \quad (4.4)$$

The evolutionary variable z is governed as

$$\dot{z} = -\gamma|\dot{x}|z|z|^{n-1} - \beta(\dot{x})|z|^n + A(\dot{x}) \quad (4.5)$$

where $\alpha(u) = \alpha_a + \alpha_b u$, $c_0(u) = c_{0a} + c_{0b} u$, $\dot{u} = -\eta(u - v)$, v is the command voltage applied to the damper. The unknown parameters $[\alpha_a, \alpha_b, c_{0a}, c_{0b}, k_0, \gamma, \beta, A, \eta]$ need to be identified to simulate the behavior of this device.

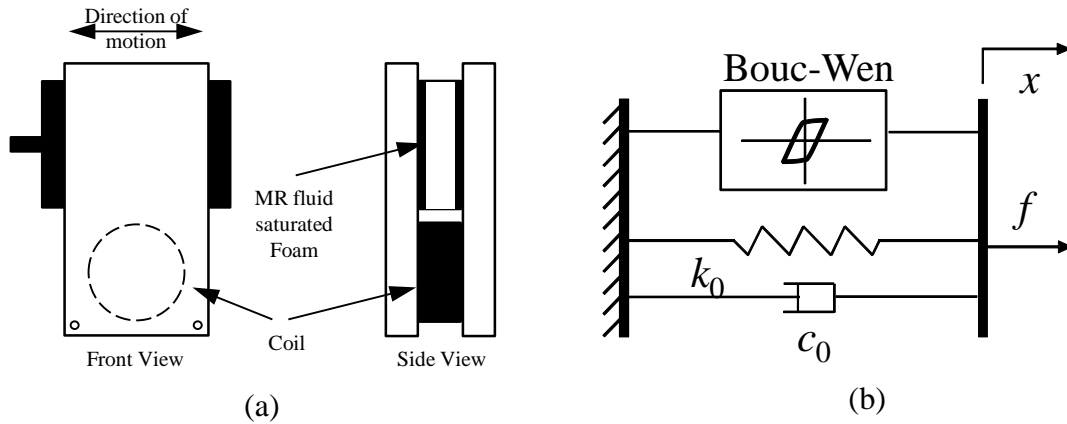


Figure 4.2. (a) Shear mode MR damper, (b) Bouc-Wen model.

The shear mode MR damper was provided by Lord Corporation as a prototype. The gap between the outer plates is 0.25 in. The thickness of the inner plate is 0.20 in. The gap between the outer plate and inner plate is 0.025 in. The maximum force of damper is around 30 N. The maximum displacement is ± 0.38 in. A series of tests are conducted to identify the unknown model parameters. The test setup is shown in Figure 4.3. Sine waves with an amplitude of 0.1 and frequencies of 2.5 Hz, 3 Hz and 4Hz, respectively,

are generated with an electro-dynamic shaker (VG-100 from Vibration Test Systems). Displacement is measured with an LVDT (DC-EC-1000; sensitivity 10.181 VDC/in; range ± 1 in) and the force produced by the MR damper is measured with a load cell (PCB 208B01; sensitivity 483.4 mV/lb; range 0-10 lb). The constant damper voltage control input for each sine wave test is 0V, 1V, 1.5V, 2V, 2.5V, 3V, respectively.

A nonlinear least squares function in Matlab (`lsqcurvefit.m`) is used to identify the damper parameters. The damper identification process is shown in Figure 4.4. This procedure is conducted for each case until the error is within a tolerance specified. The identified parameters in each case are averaged to obtain the updated damper parameters. The filtered responses with FIR low pass filter (fpass 20 Hz; fstop 40 Hz) is shown in Figure 4.5. The responses for identified parameters at 3 Hz sine 1.0V, 1.5V are provided in Figure 4.6 and Figure 4.7, respectively. These comparisons demonstrate a good reproduction of the physical damper behavior in the damper model. The identified parameters are listed in Table 4.1.

To control the damper force to structure, damper voltage is the only control variable. The clipped-optimal strategy proposed by Dyke, et al., (1996) is adopted for controlling the damper voltage. Damper voltage is determined by comparing the desired damper force and the measured damper force as shown in Equation (4.6)

$$v = V_{max}H\{(f_d - f_m)f_m\} \quad (4.6)$$

where V_{max} is the maximum voltage to the current driver which is 3V in the simulation, and $H\{*\}$ is the Heaviside step function.

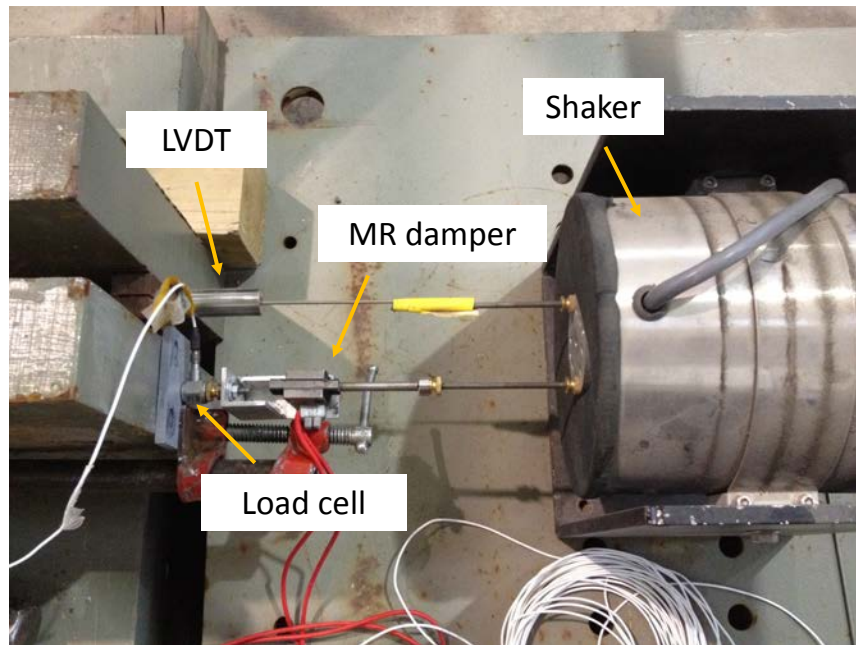


Figure 4.3. Damper identification test setup.

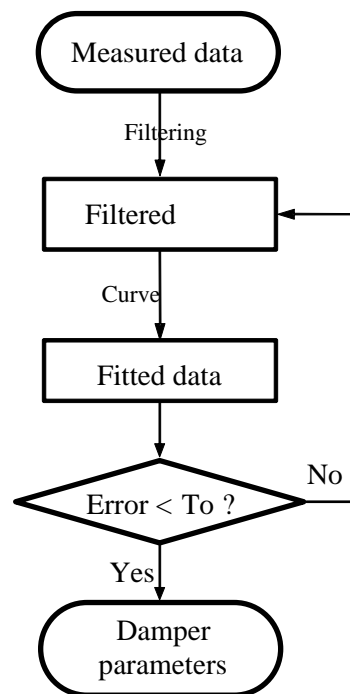


Figure 4.4. Damper ID procedure.

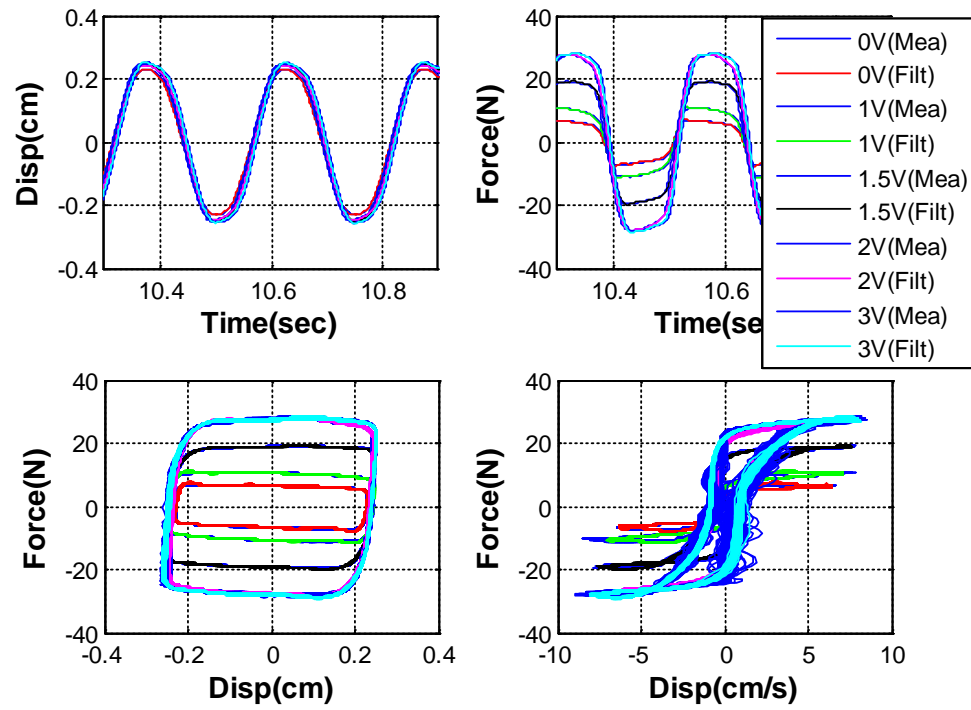


Figure 4.5. Measured data vs filtered data (4Hz sine wave).

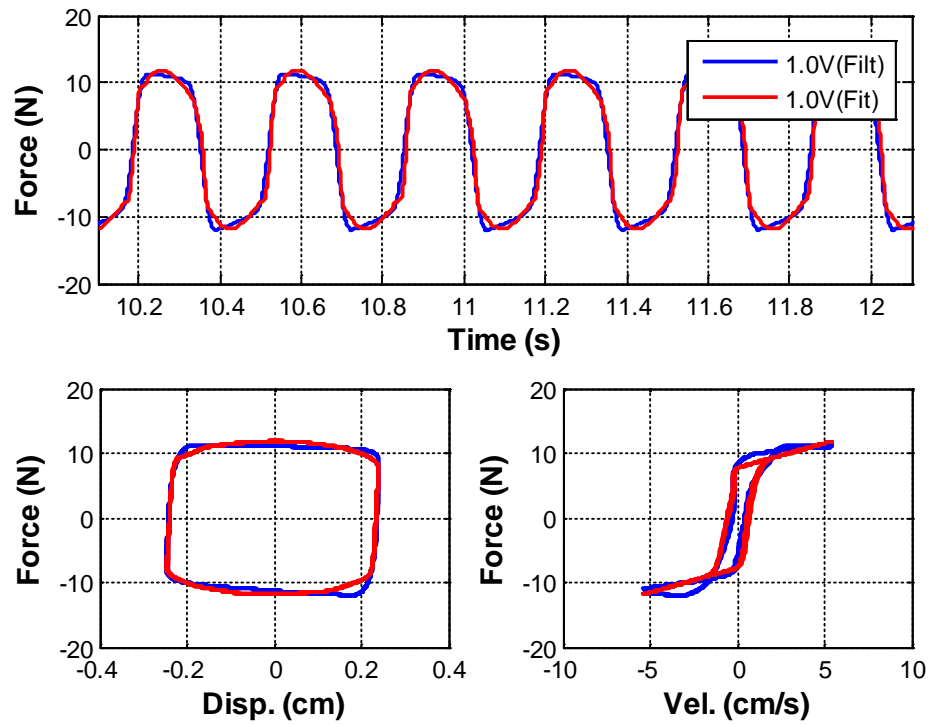


Figure 4.6. Filtered data vs identified model (3 Hz sine wave, 1.0V voltage).

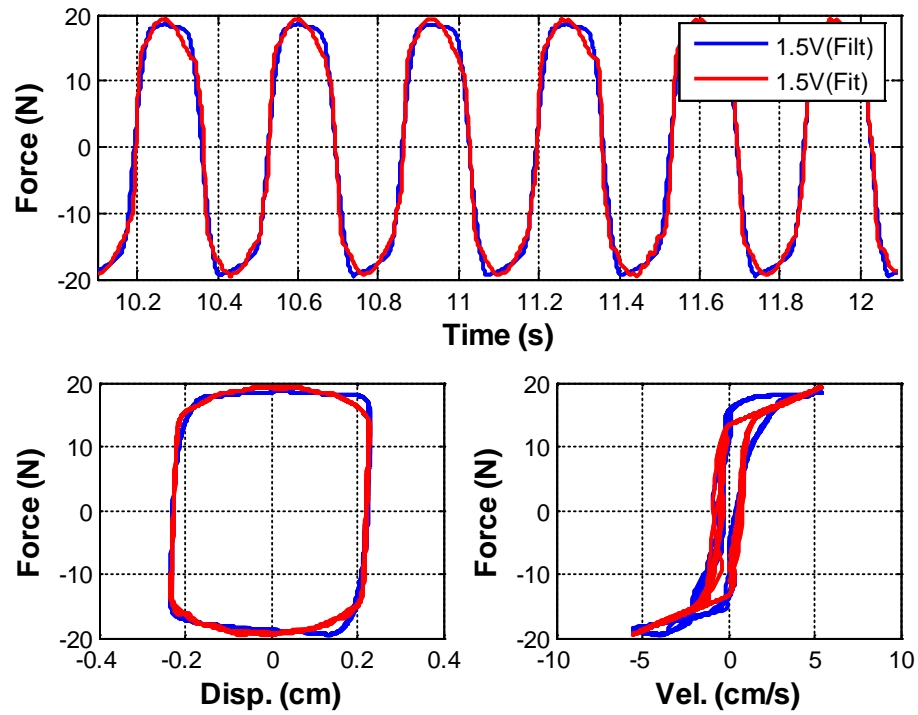


Figure 4.7. Filtered data vs identified model (3 Hz sine wave, 1.5V voltage).

Table 4.1. Identified damper parameters.

Parameter	Value	Unit
α_a	2.59	N/cm
α_b	9.91	N/(cmV)
c_{0a}	0.81	N·s/cm
c_{0b}	0.20	N·s/(cmV)
k_0	0.95	N/cm
γ	83.25	cm ⁻²
β	83.25	cm ⁻²
n	2	-
A	88	-
η	80	sec ⁻¹

4.1.2 Control Design

Several wireless control strategies are considered here as shown in Figure 4.8: 1) decentralized control, 2) partially decentralized control and 3) centralized control. Control design is performed for each control strategy, respectively.

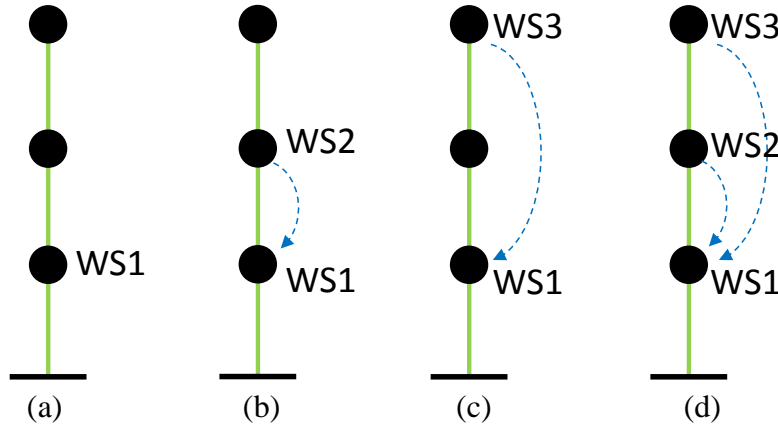


Figure 4.8. (a) Wireless case 1, (b) Wireless case 2, (c) Wireless case 3, and (d) Wireless case 4.

For decentralized control with one wireless node on the first floor as in Figure 4.8 (a), the wireless sensor conducts sensing, control, and actuation onboard. Since there is no wireless transmission involved, the control implementation can adopt a relatively high sampling frequency. Here $dt = 1/800$ sec is used for control design of wireless control case 1. The LQG control algorithm is adopted. The one step time delay is ignored in the control design. Based on the separation principle, the linear quadratic regular (LQR) and Kalman estimator are designed, separately. For LQR, the state feedback control law $u = -Kx$ minimizes the cost function

$$J = \int_0^{\infty} (x'Qx + u'Ru)dt \quad (4.7)$$

where K is given by

$$K = R^{-1}B'P \quad (4.8)$$

where P is obtained by solving the algebraic Riccati equation

$$A'P + PA - PBR^{-1}B'P + Q = 0 \quad (4.9)$$

For Kalman estimator, the system state space model is given in Equations (4.10-4.11).

The process noise w and measurement noise v are assumed unbiased with covariances $E\{ww'\}=S_w$, $E\{vv'\}=S_v$, respectively.

$$\dot{x} = Ax + Bu + Gw \quad (4.10)$$

$$y = Cx + Du + Hw + v \quad (4.11)$$

$$\dot{\hat{x}} = (A - LC)\hat{x} + Ly + (B - LD)u \quad (4.12)$$

$$u_d = -K\hat{x} \quad (4.13)$$

The steady state error covariance $E[\|x - \hat{x}\|^2]$ is minimized with the observer gain L in Equation (4.12). The absolute acceleration y and the measured control force u are the input to the estimator. The desired control force u_d is given in Equation (4.13), and the steady-state gain L is given by

$$L = PC'S_v^{-1} \quad (4.14)$$

where P is obtained by solving the algebraic Riccati equation

$$AP + PA' - PC'S_v^{-1}CP + GS_wG' = 0 \quad (4.15)$$

For partially decentralized control with one leaf node as shown in Figure 4.8 (b)-(c), the control node has its local measurement as well as the sensor data from the 2nd floor or the 3rd floor. TDMA is used for wireless transmission with a 10 msec time slot. Control and actuation time is included in the 10 msec slot. Wireless control dt is 10 msec in these two cases. The wireless transmission delay needs to be taken into account. The OTD control algorithm introduced in chapter 2 is adopted in these cases.

For centralized control with two leaf nodes as shown in Figure 4.8 (d), sensor measurements from all floors are send to the node 1 for centralized wireless control. The sensor node 2 and node 3 uses different time slot. The wireless control is implemented with $dt = 20$ msec. The OTD control algorithm is also adopted for this case. The weighting matrices in Equation (2.7) is optimized through numerical simulation.

4.1.3 Numerical Simulation

Wireless control case 1 is studied first. For wireless control case 1, the LQR weighting matrices $Q = q*[I^{6 \times 6}]$ and $R = [1]$, where q is chosen based on the numerical study. For the Kalman filter, the process noise and measurement noise variances are $S_w = [25]$, $S_v = [1]$. A band-limited white noise (BLWN) with a frequency range 0-15 Hz is used as the ground excitation. The Simulink diagram for wireless control with semi-active control device is shown in Figure 4.9. For a range of q values, the normalized maximum acceleration in Equation (4.16) versus the normalized maximum interstory drift in Equation (4.17) is shown in Figure 4.10. The normalized acceleration versus the maximum force is provided in Figure 4.11. The $q = 42.3$ is selected corresponding to the red square in the figures. The feedback gain is

$$K = [120.296 \quad -182.689 \quad 62.606 \quad 9.739 \quad 1.979 \quad 2.539]$$

The simulation results are shown in Figures 4.12-4.13 comparing the uncontrolled case, passive off (constant 0V command to the damper) case, passive on (constant 3V command to the damper) case, and wireless control case 1. Wireless control case 1 has effectively reduced structural responses compared to the other cases, especially on the 2nd and 3rd floor. The power spectrum of 3rd floor acceleration is shown in Figure 4.14. The

peaks at the first three natural frequencies are reduced to the greatest extent using wireless control case 1.

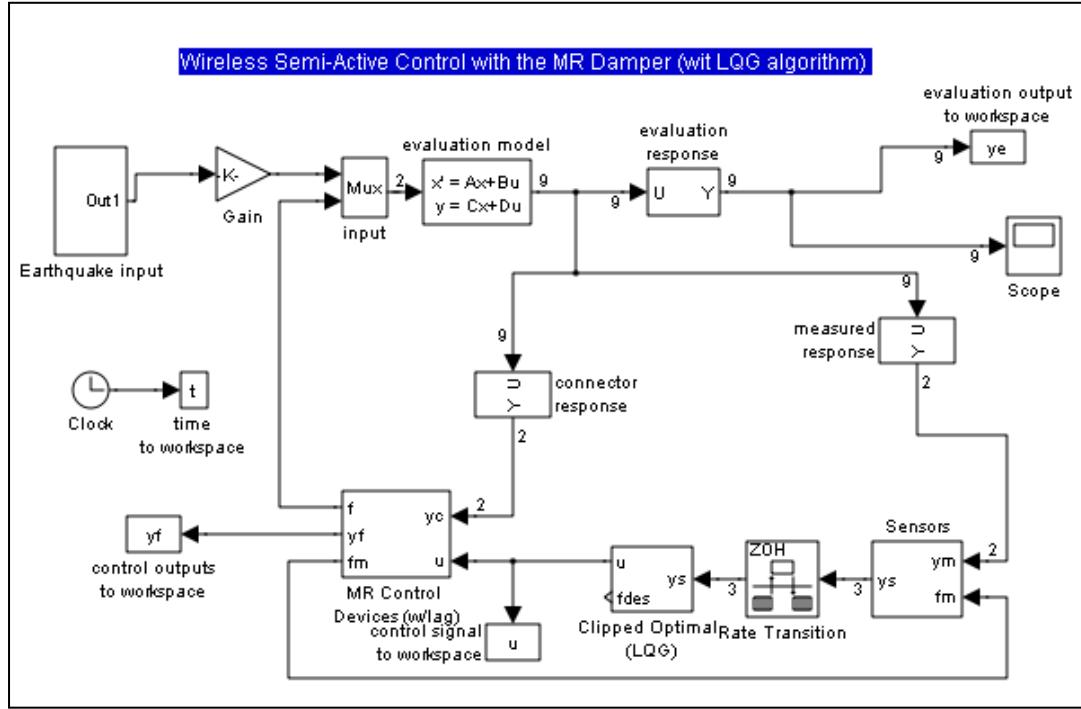


Figure 4.9. Simulink diagram for wireless control simulation.

$$J_1 = \frac{\max_i(\|\ddot{x}_i\|_2)}{\max_i(\|\ddot{x}_{i0}\|_2)} \quad (4.16)$$

$$J_2 = \frac{\max_i(\|d_i\|_2)}{\max_i(\|d_{i0}\|_2)} \quad (4.17)$$

where J_1 is the ratio of the maximum norm of acceleration to the maximum norm of acceleration of uncontrolled case, J_2 is the ratio of the maximum norm of interstory drift to the maximum norm of interstory drift of uncontrolled case, i is floor 1 to 3, interstory drift $[d_1, d_2, d_3] = [x_1, x_2 - x_1, x_3 - x_2]$.

$$J_3 = \left[1 - \frac{\sum_k J_{1k}}{N} \right] \times 100\% \quad (4.18)$$

$$J_4 = \left[1 - \frac{\sum_k E_{2k}}{N} \right] \times 100\% \quad (4.19)$$

where J_3 is the average acceleration reduction under different earthquakes, N is the number of earthquakes, k is earthquake 1 to N , J_4 is the average interstory drift reduction under different earthquakes.

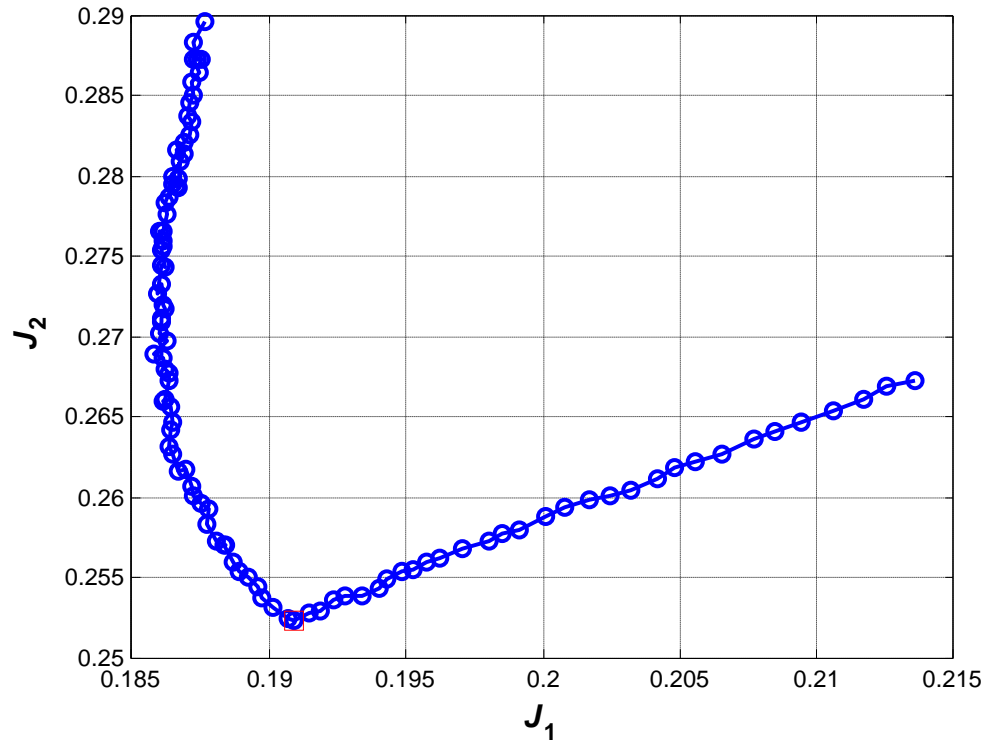


Figure 4.10. Normalized acceleration vs normalized drift.

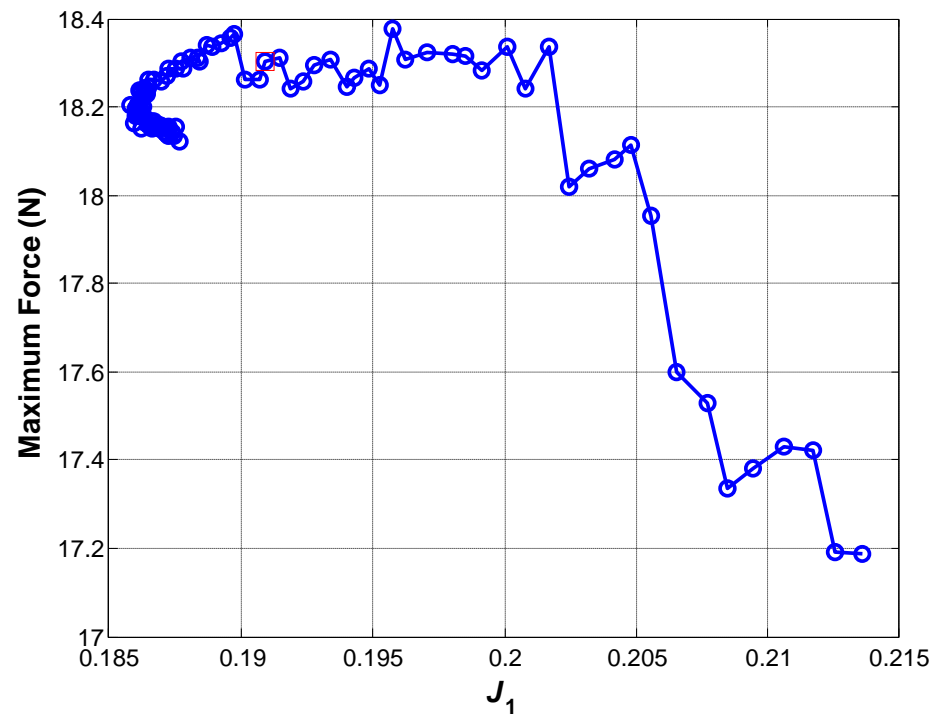


Figure 4.11. Normalized acceleration vs peak force.

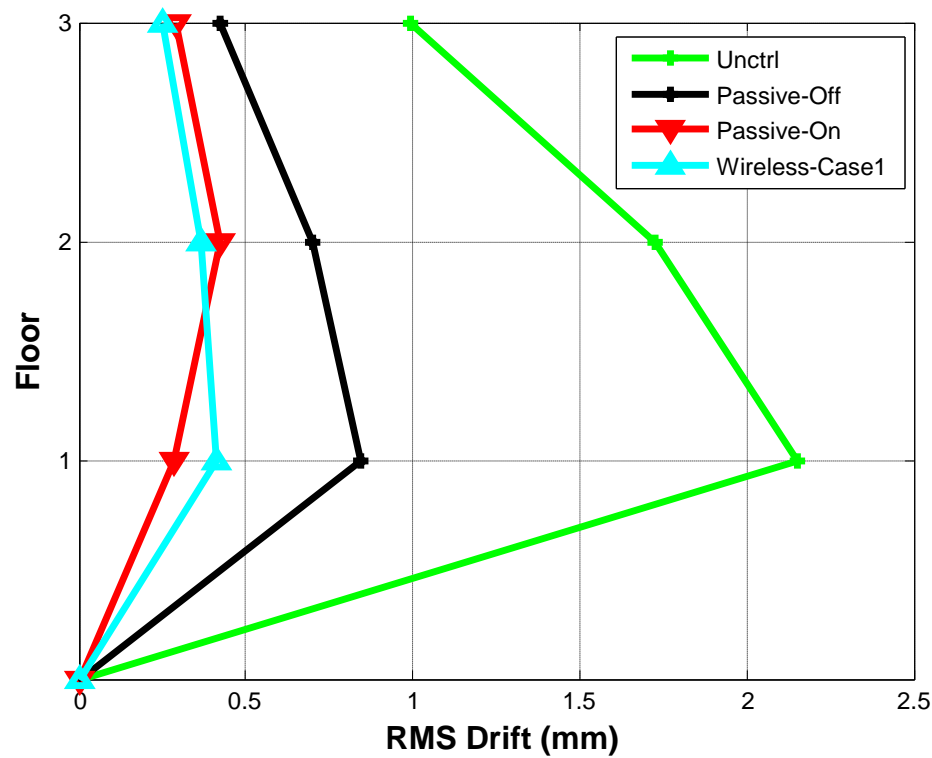


Figure 4.12. RMS interstory drift response under BLWN excitation.

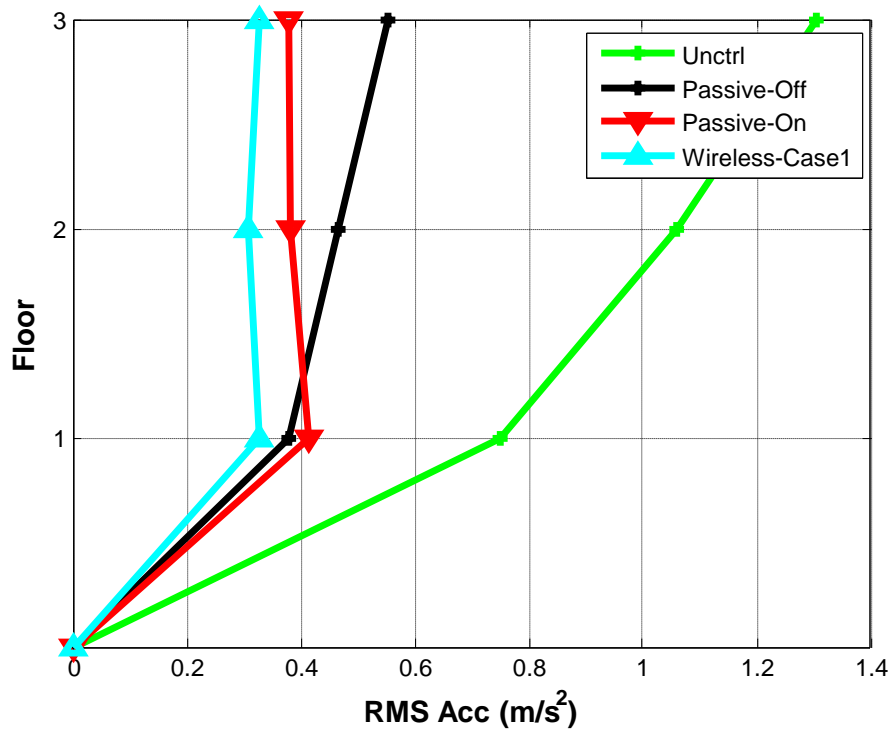


Figure 4.13. RMS acceleration response under BLWN excitation.

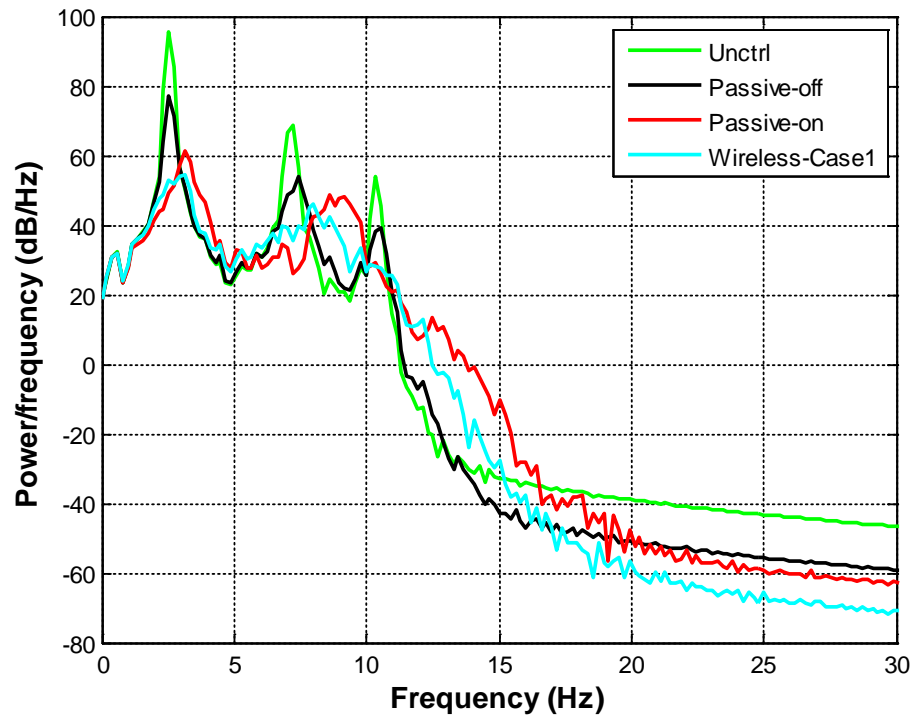


Figure 4.14. Power spectrum of 3rd floor acceleration.

Numerical simulations are then conducted for the four historical earthquakes, including the 1940 El Centro earthquake (Figure 4.15), the 1994 Northridge earthquake, the 1995 Kobe earthquake, and the 1968 Hachinohe earthquake. The RMS acceleration and RMS interstory drift under El Centro earthquake are shown in Figures 4.16-4.17. The maximum RMS acceleration and maximum RMS interstory drift under these four earthquakes are shown in Figures 4.18-4.19. For wireless control case 1, the average RMS acceleration reduction (Equation (4.18)) is 76%, while the average RMS drift reduction (Equation (4.19)) is 81%. The maximum force of the damper is about 4% the weight of the structure, but wireless control case 1 can achieve significant reduction in RMS interstory drift and RMS acceleration.

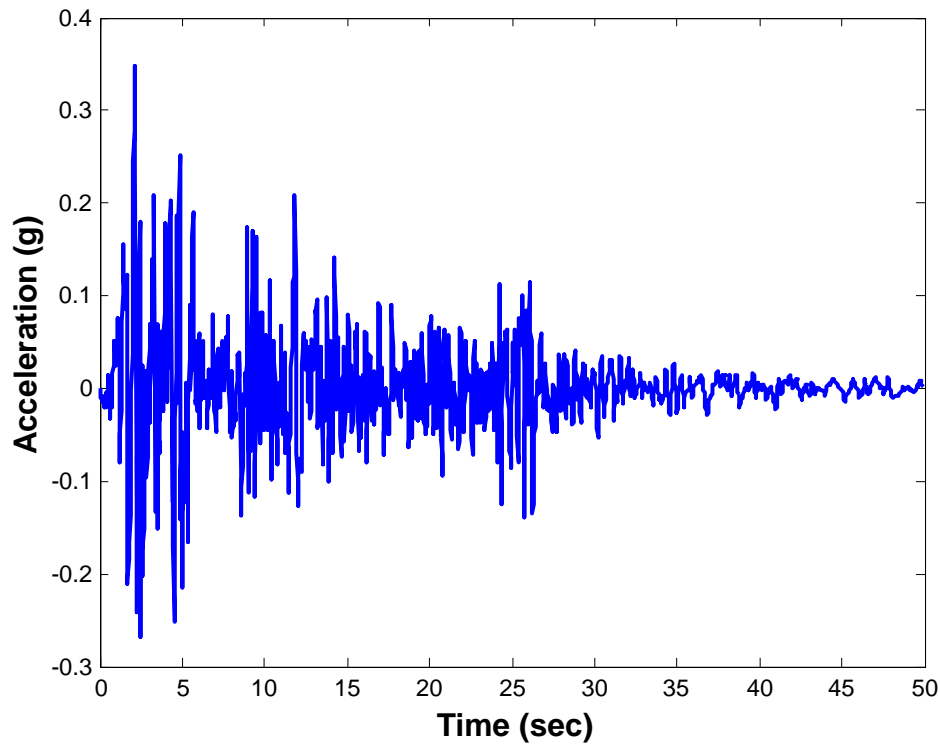


Figure 4.15. El Centro earthquake.

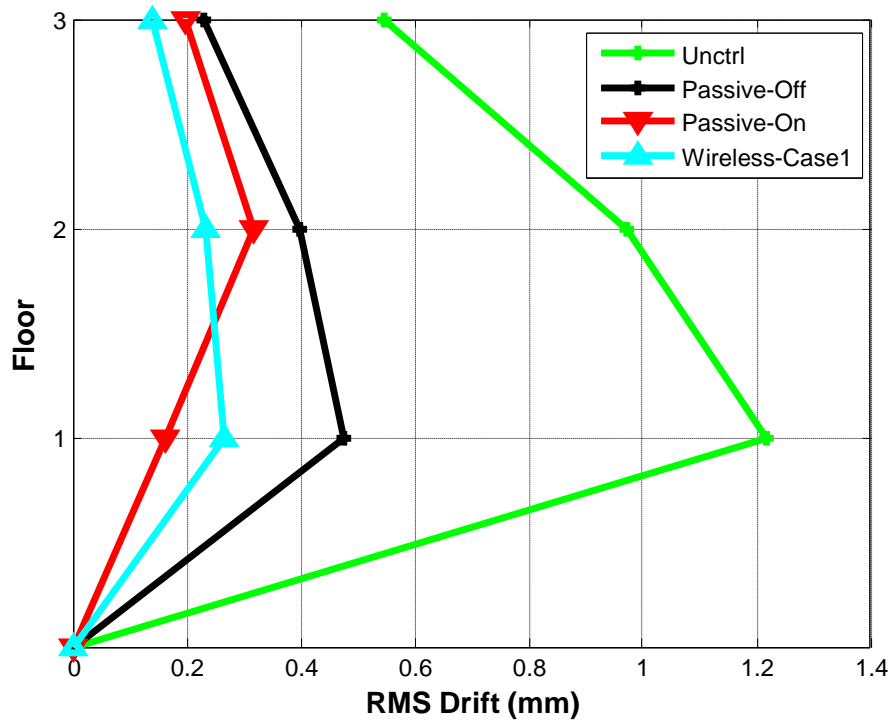


Figure 4.16. RMS interstory drift response under El Centro earthquake.

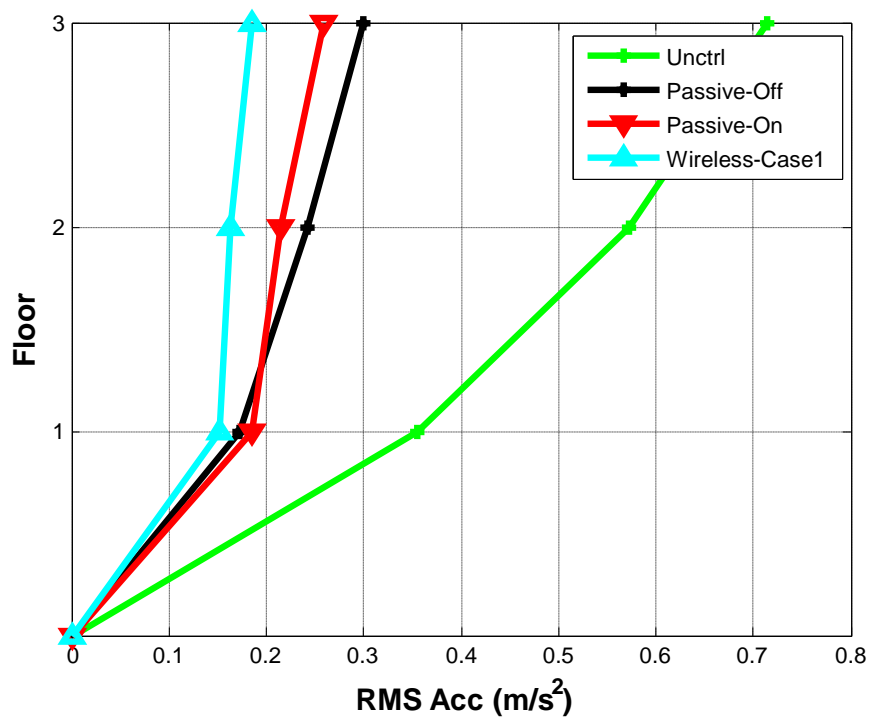


Figure 4.17. RMS acceleration response under El Centro earthquake.

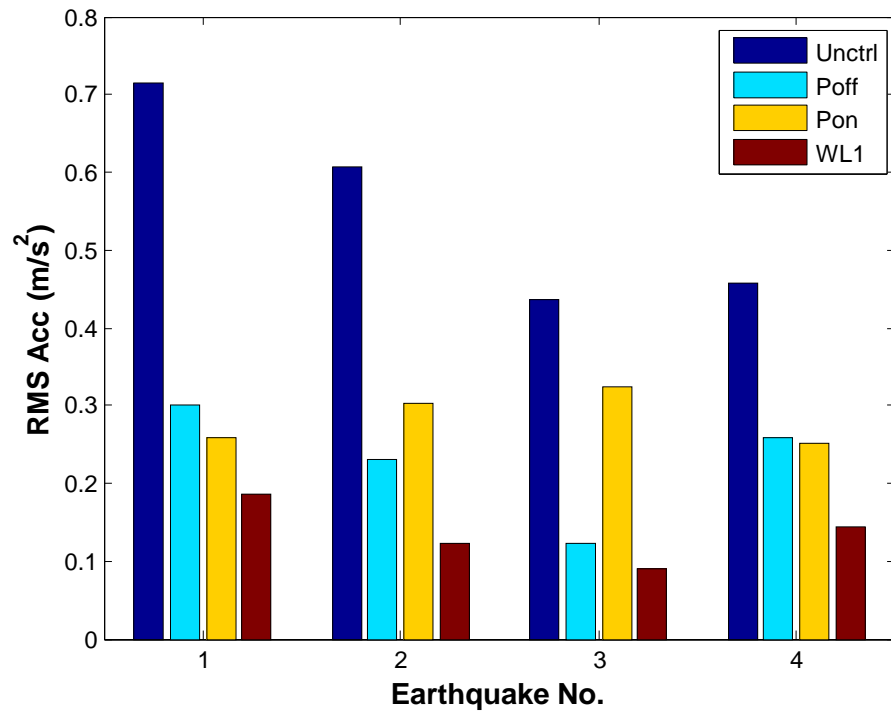


Figure 4.18. RMS acceleration response under E1: El Centro Earthquake, E2: Northridge Earthquake, E3: Kobe Earthquake, and E4: Hachinohe Earthquake.

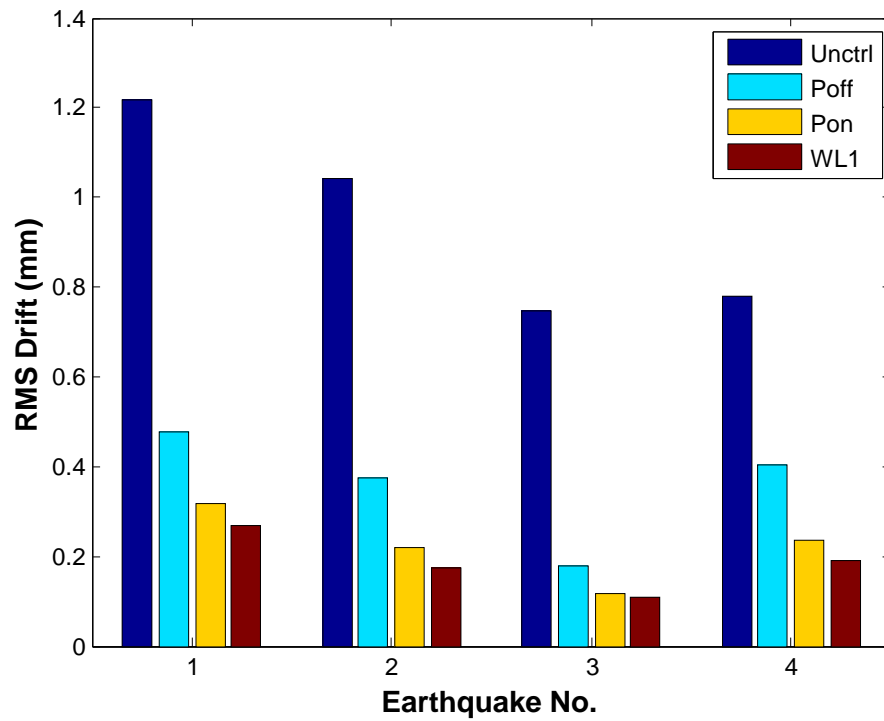


Figure 4.19. RMS drift response under E1-E4 earthquakes.

Next, wireless control cases 2-4 are studied in the simulation. Wireless control cases 2-4 adopt the OTD control algorithm to accommodate the time delay in the control design. Data loss is not considered here in the numerical simulation. The discrete system model used for control design is obtained with Tustin's method (Tustin's method, 2015). For wireless cases 2 and 3, the discrete time step is 10 msec. A one step delay is included in the simulation, so $l = 1$. The A_d and B_d matrices are

$$A_d = \begin{bmatrix} 0.0879 & 0.0058 & 0.0002 & 0.0009 & 0 & 0 \\ 0.0058 & 0.0881 & 0.0059 & 0 & 0.0009 & 0 \\ 0.0002 & 0.0059 & 0.0939 & 0 & 0 & 0.001 \\ -2.4176 & 1.1524 & 0.0371 & 0.0875 & 0.0059 & 0.0002 \\ 1.1524 & -2.3805 & 1.1895 & 0.0059 & 0.0877 & 0.0061 \\ 0.0371 & 1.1895 & -1.2281 & 0.0002 & 0.0061 & 0.0936 \end{bmatrix} \times 10$$

$$B_d = \begin{bmatrix} 0.0207 \\ 0.0006 \\ 0 \\ 4.1344 \\ 0.1298 \\ 0.0048 \end{bmatrix}$$

For the OTD control algorithm implementation, weighting matrices in Equation (2.7) in chapter 2 are chosen as $Q = q^*[I_{6 \times 6}]$, $R = [1]$, where q is obtained with numerical study. For wireless control cases 2 and 3, the obtained OTD control gain is

$$G = [37.2078 \quad 9.7033 \quad -5.8920 \quad -1.2925 \quad 0.0693 \quad -0.4172]$$

For wireless control case 4, the discrete time step is 0.02 sec and a one step time delay is included in the simulation. The A_d and B_d matrices are

$$A_d = \begin{bmatrix} 0.0604 & 0.0167 & 0.0019 & 0.0016 & 0.0002 & 0 \\ 0.0167 & 0.0623 & 0.0187 & 0.0002 & 0.0016 & 0.0002 \\ 0.0019 & 0.0187 & 0.0791 & 0 & 0.0002 & 0.0018 \\ -3.9615 & 1.6750 & 0.1950 & 0.0596 & 0.0169 & 0.002 \\ 1.6750 & -3.7665 & 1.8700 & 0.0169 & 0.0617 & 0.0189 \\ 0.1950 & 1.8700 & -2.0915 & 0.002 & 0.0189 & 0.0786 \end{bmatrix} \times 10$$

$$B_d = \begin{bmatrix} 0.0352 \\ 0.0037 \\ 0.0004 \\ 3.5206 \\ 0.3728 \\ -0.0446 \end{bmatrix}$$

Following the same approach as for wireless case 2 and 3, the OTD control gain obtained for wireless case 4 is

$$G = [67.1114 \quad -20.3794 \quad 6.1516 \quad -0.1521 \quad -0.1666 \quad -0.4518]$$

The simulation results for these four wireless control cases under the El Centro earthquake are shown in Figures 4.20-4.21. The responses under the Northridge earthquake are shown in Figures 4.22-4.23. The maximum RMS acceleration and maximum RMS interstory drift response profiles under these earthquakes are shown in Figures 4.24-4.25. Comparing the different wireless control cases, wireless control case 1 has the best performance in terms of RMS interstory drift reduction and RMS acceleration reduction.

With a larger control time step, the control performance degrades, despite the availability of more measurements with wireless control cases 2-4. From the results, wireless control cases 2 and 3 have similar control performance. Wireless control case 4 has the worst performance in terms of RMS acceleration reduction. For RMS drift reduction, however, wireless control case 4 has similar performance to wireless cases 2 and 3. These results illustrate the differences in control performances with different wireless control strategies. Experimental studies are conducted in the next section to implement the control algorithms onboard and evaluate wireless control performance.

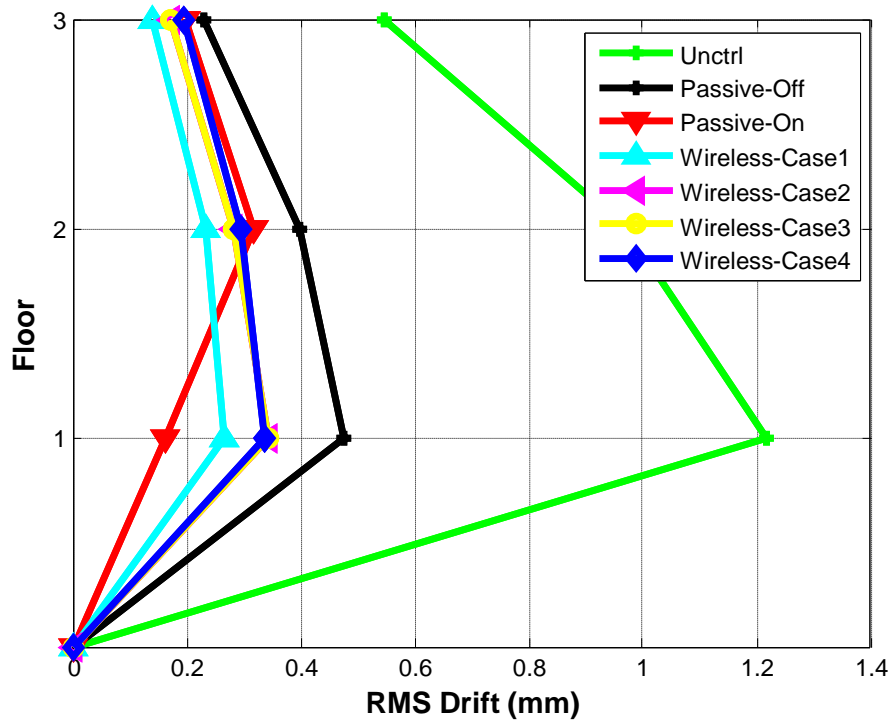


Figure 4.20. RMS interstory drift response under El Centro earthquake.

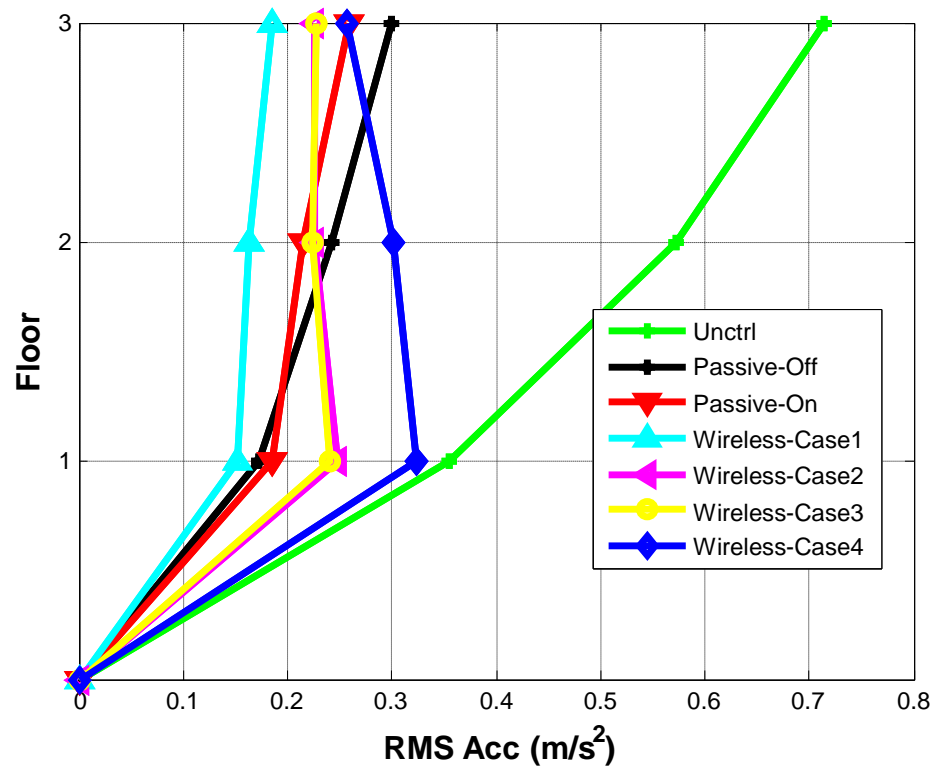


Figure 4.21. RMS acceleration response under El Centro earthquake.

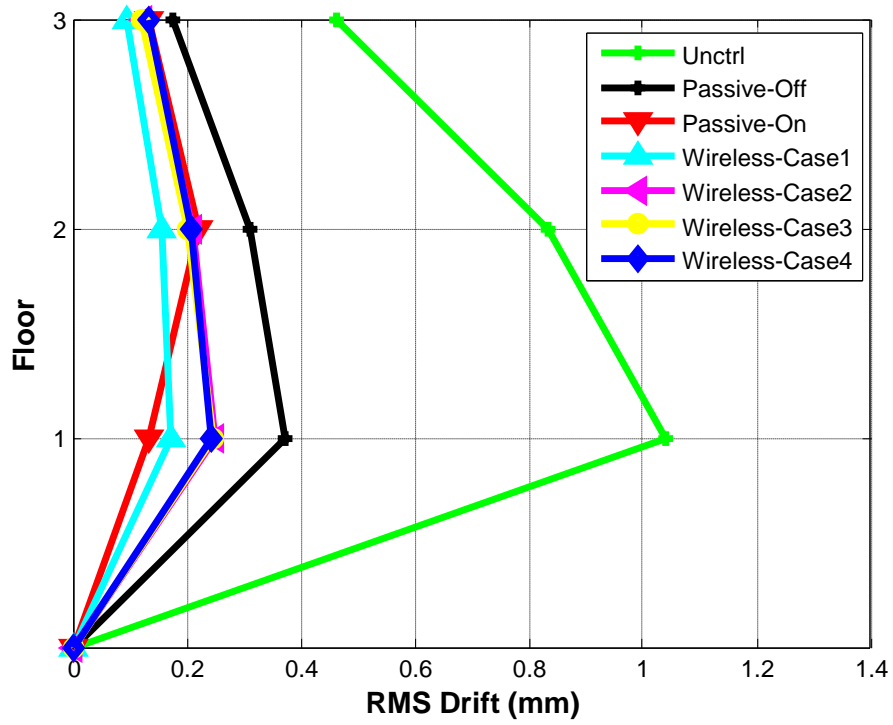


Figure 4.22. RMS interstory drift response under Northridge earthquake.

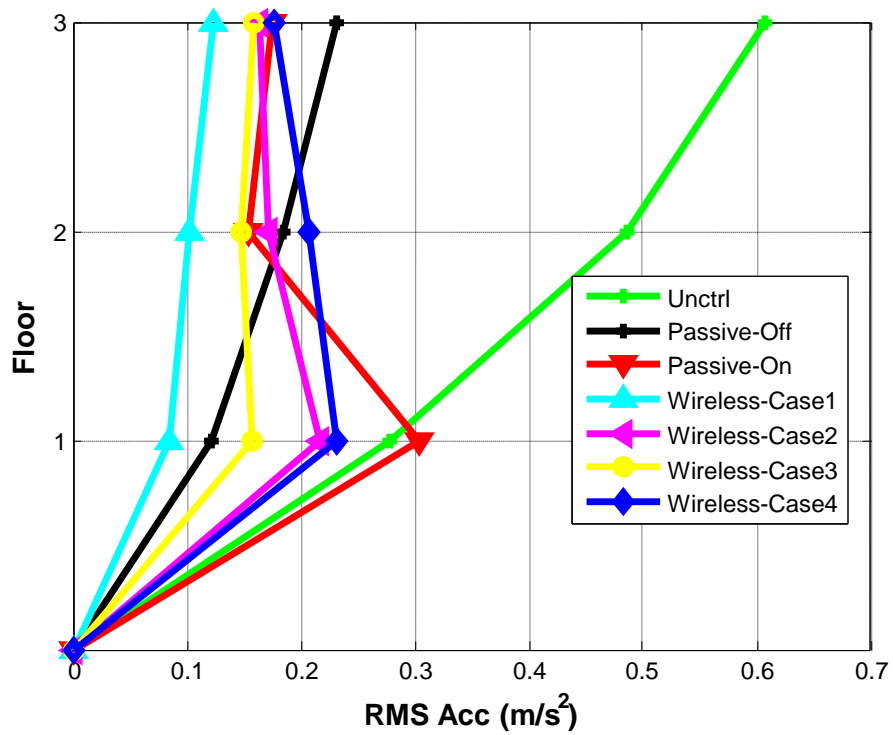


Figure 4.23. RMS acceleration response under Northridge earthquake.

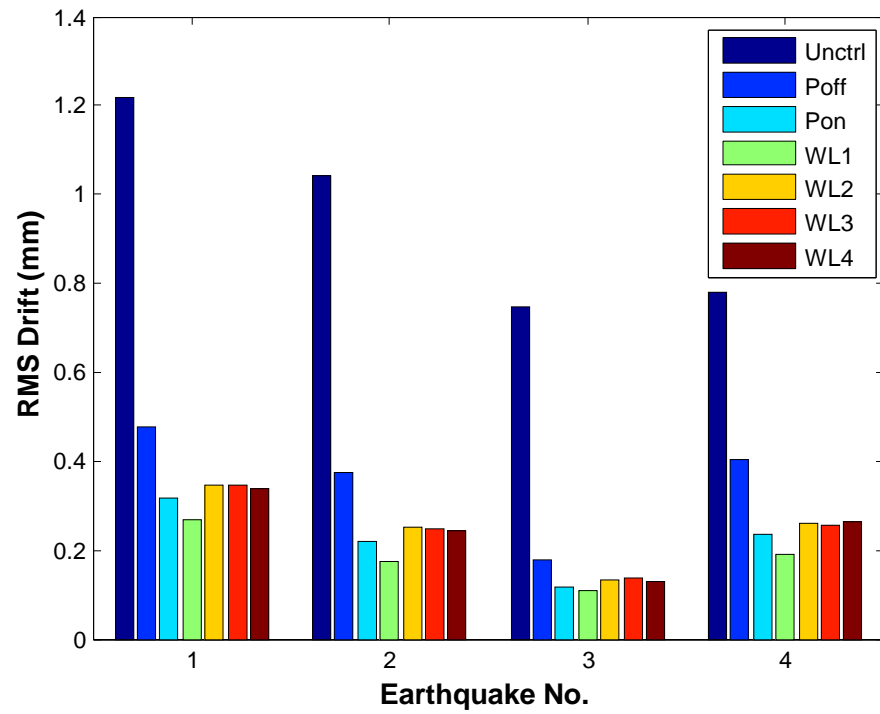


Figure 4.24. RMS drift response under E1-E4 earthquakes.

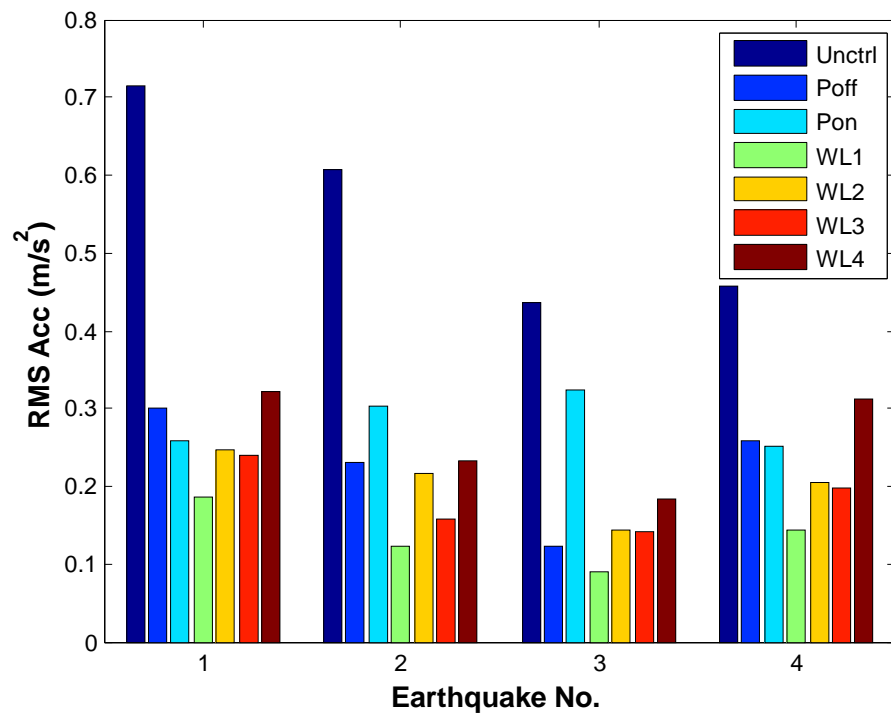


Figure 4.25. RMS acceleration response under E1-E4 earthquakes.

4.2 Experimental Study

Experimental studies are conducted on a small-scale 3-story shear structure in the IISL lab as shown in Figure 4.26. This structure is the basis for the structural model used in the numerical study. For the experimental studies, the structure is placed on the 6 DOFs hydraulic shake table. Ground excitations (i.e. BLWN input and earthquake motions) are generated with the shake table. Only 1D ground motion is considered, in the horizontal direction in which the structure is most flexible. Different wireless control strategies (decentralized, partially decentralized and centralized control) in the numerical simulation are considered and compared in the experimental study.

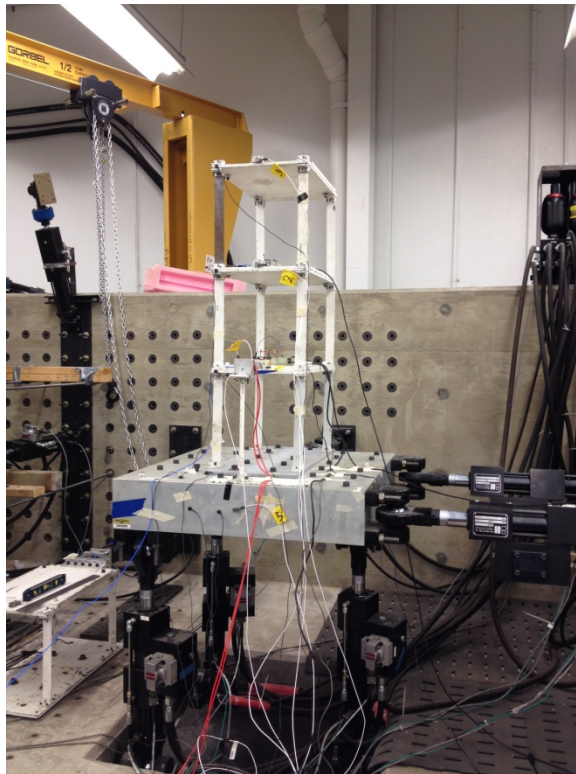


Figure 4.26. Experimental structure on the shake table.

For generation of ground motion, the desired displacement record of ground motion (y_d) is sent to shake table as shown in Figure 4.27. Displacement record is used since the shake table is controlled with displacement feedback control loop. The ground displacement is generated in Matlab Simulink and a real-time executable file is built and implemented with dSPACE processor board DS1006 as shown in Figure 4.28 (a). An I/O board DS 2201 is used to convert the displacement command to voltage signal (y_{dv}) and send it to the Shore Western system (CS-1151) (Figure 4.28 (b)). In the Shore Western system, a PID controller controls the motion of the shake table. The PID controller is tuned prior to the shake table tests. The shake table has a maximum displacement of ± 1.5 in, a maximum velocity of 26.5in/s and a maximum acceleration of 10.2g in the horizontal direction.

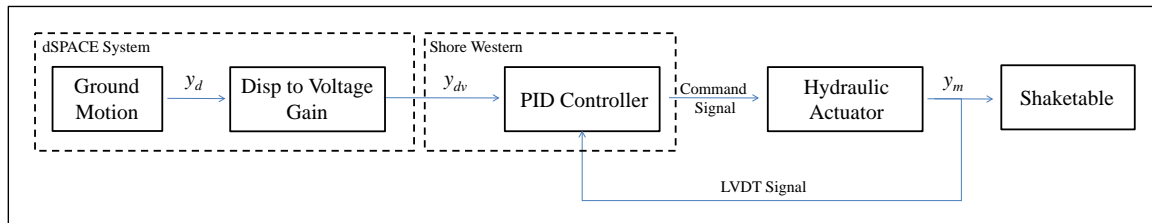


Figure 4.27. Ground input to shake table.



(a)



(b)

Figure 4.28. (a) dSPACE controller and I/O board, (b) Shore Western system.

4.2.1 System Identification

Before implementing wireless sensors on the structure, system identification is conducted to identify a numerical model to represent the experimental structure for control design. To perform system identification, shake table tests are performed with a BLWN excitation of 0-20 Hz as shown in Figure 4.29. Wired accelerometers (PCB 333B40; sensitivity 500 mV/g; range $\pm 10g$) are attached to each of the three floors of the structure and connected to the Vibpilot DAQ system (Figure 4.41 (a)), which has 8 channels of 24 bit ADC. A sampling frequency of 1024 Hz is used in the test. The experimental transfer functions (TFs) and identified TF models from ground acceleration to floor 1-3 accelerations are provided in Figures 4.30-4.32. Based on the comparisons, both the magnitude and phase are accurately represented in the model. The identified model is obtained by updating mass, damping and stiffness matrices using the method developed by Ozdagli, et al., (2012). The updated mass, damping and stiffness matrices are

$$M = \begin{bmatrix} 23.7801 & 0.0402 & -0.1283 \\ 0.0402 & 24.8034 & -0.3120 \\ -0.1283 & -0.3120 & 24.3216 \end{bmatrix} kg$$

$$C = \begin{bmatrix} 4.8727 & -0.7680 & 0.3857 \\ -0.7680 & 5.5828 & -0.5332 \\ 0.3857 & -0.5332 & 4.6811 \end{bmatrix} N/(m/s)$$

$$K = \begin{bmatrix} 5.9463 & -3.0243 & 0.0055 \\ -3.0243 & 6.4067 & -3.3774 \\ 0.0055 & -3.3774 & 3.3560 \end{bmatrix} \times 10^4 N/m$$

The comparisons of natural frequencies in the numerical model and updated model with experimental data are listed in Table 4.2. The comparison of mode shapes is shown in Figure 4.33. Hammer tests are also conducted by hitting the location where the MR damper will be located on the 1st floor (see Figure 4.34), so that the TFs from damper

force to structural acceleration responses are obtained. The power spectrum of hammer input is shown in Figure 4.35. As expected, the spectrum has a flat band in the frequency range 0-400 Hz. The TFs from hammer input to floor 1-3 accelerations are shown in Figures 4.36-4.38. The TFs from measured hammer force to the acceleration responses of identified model are compared with the experimental TFs. Based on the results, the identified model also has good representation of the TFs from hammer input to floor 1-3 accelerations up to 15 Hz. This model is used for control design in the experimental study.

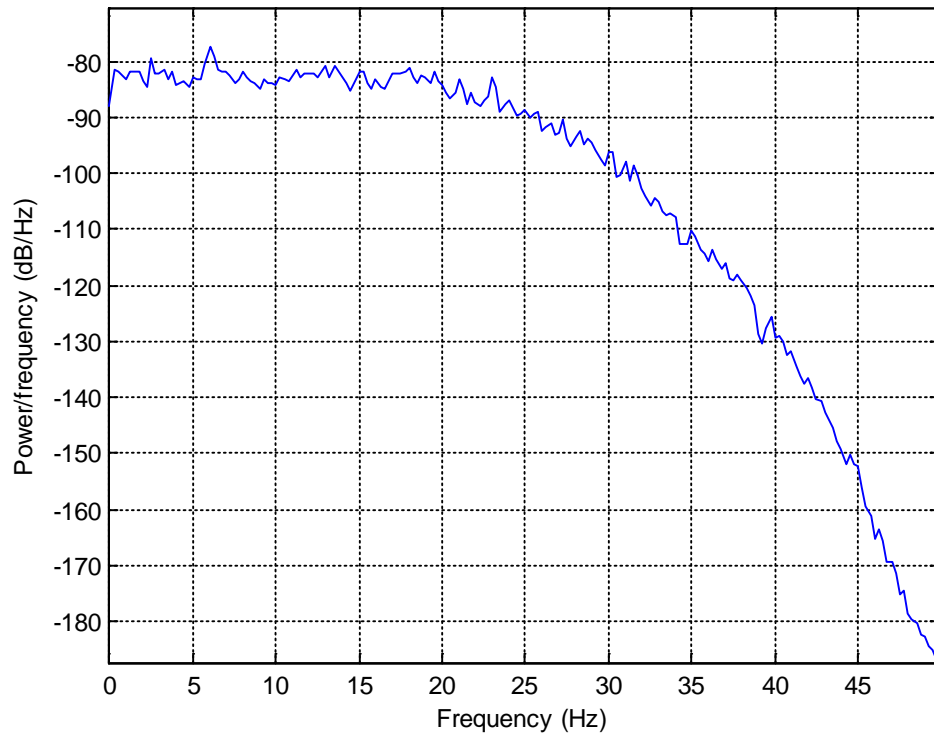


Figure 4.29. BLWN ground input spectrum.

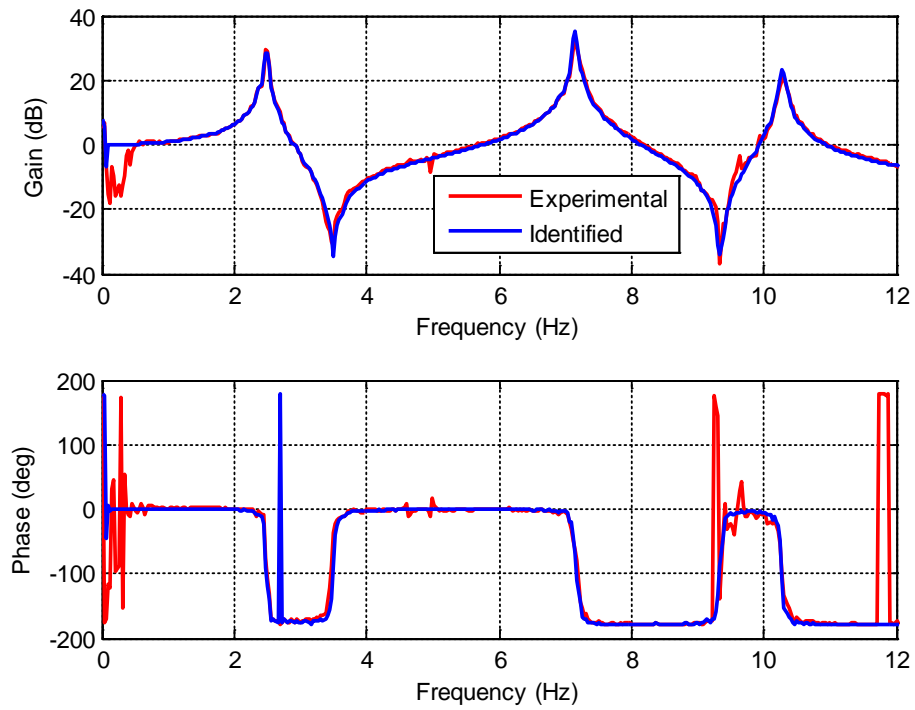


Figure 4.30. Transfer function from ground acceleration to 1st floor acceleration.

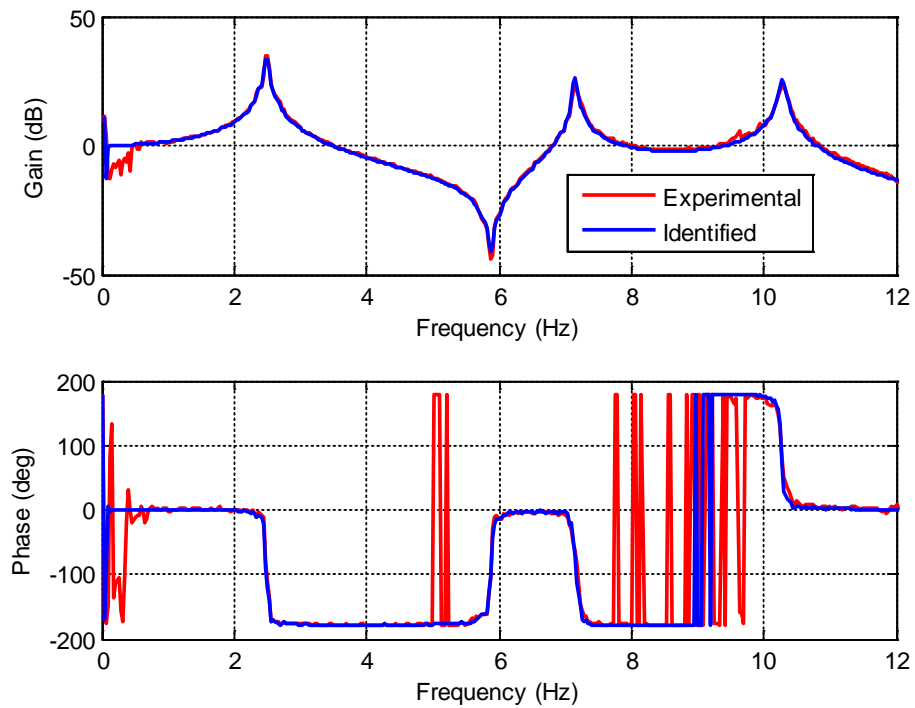


Figure 4.31. Transfer function from ground acceleration to 2nd floor acceleration.

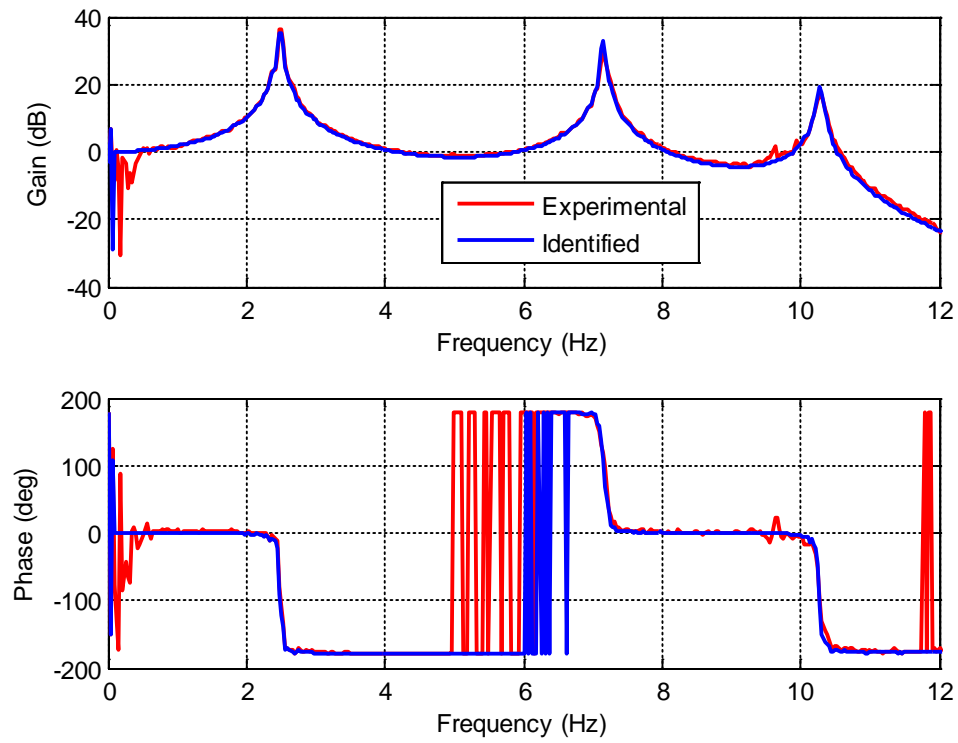


Figure 4.32. Transfer function from ground acceleration to 3rd floor acceleration.

Table 4.2. Comparison of natural frequencies.

Mode	Numerical Model	Identified Model
1	2.56 Hz	2.48 Hz
2	7.18 Hz	7.16 Hz
3	10.38 Hz	10.27 Hz

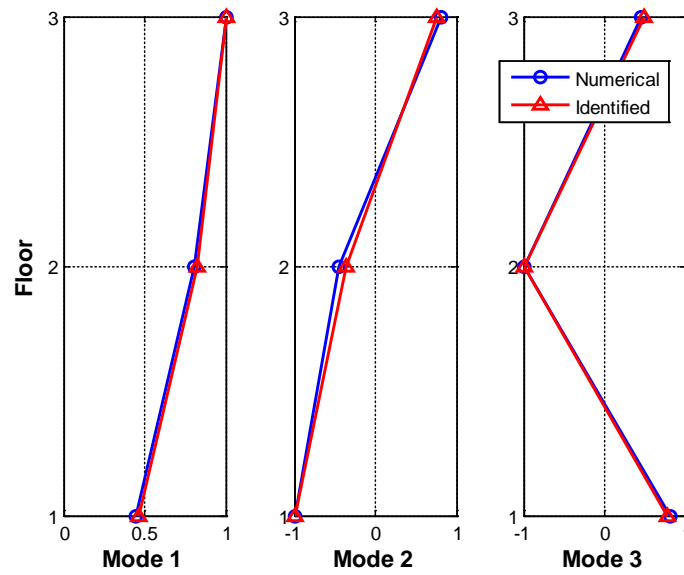


Figure 4.33. Comparison of mode shapes.

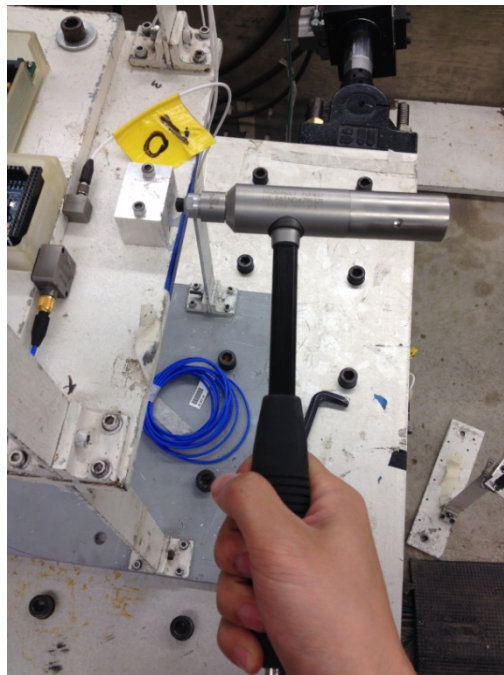


Figure 4.34. Hammer test.

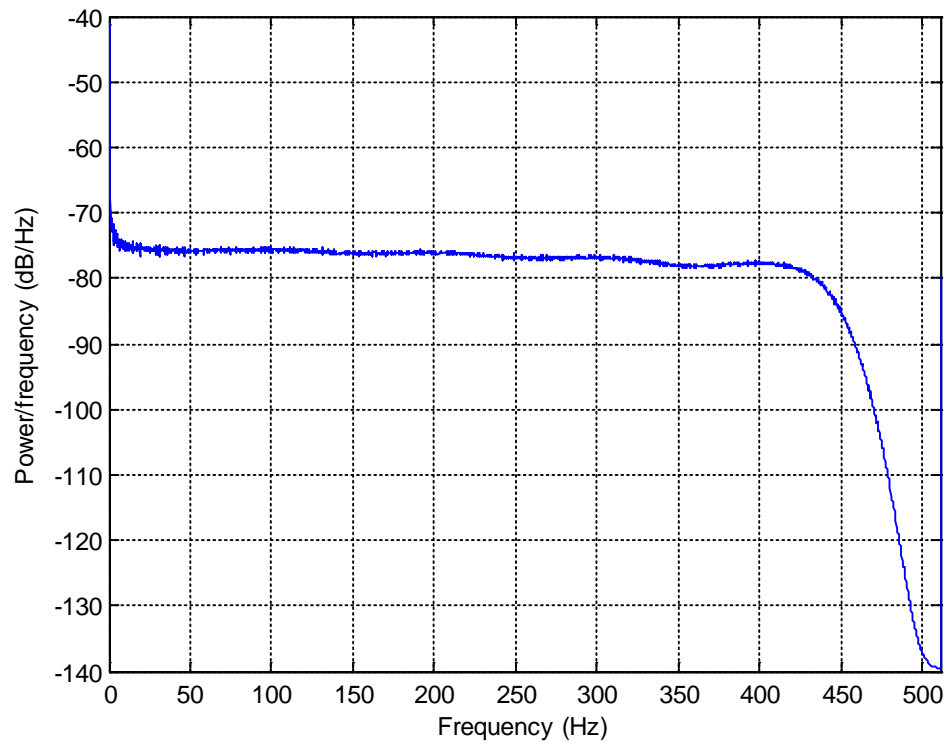


Figure 4.35. Hammer input power spectrum.

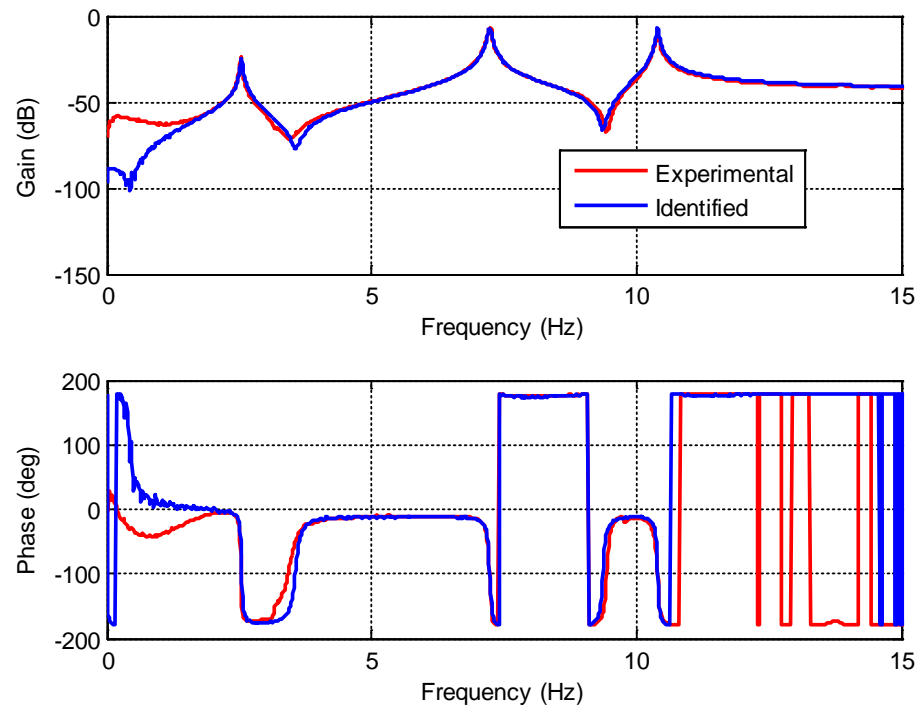


Figure 4.36. Transfer function from hammer force to 1st floor acceleration.

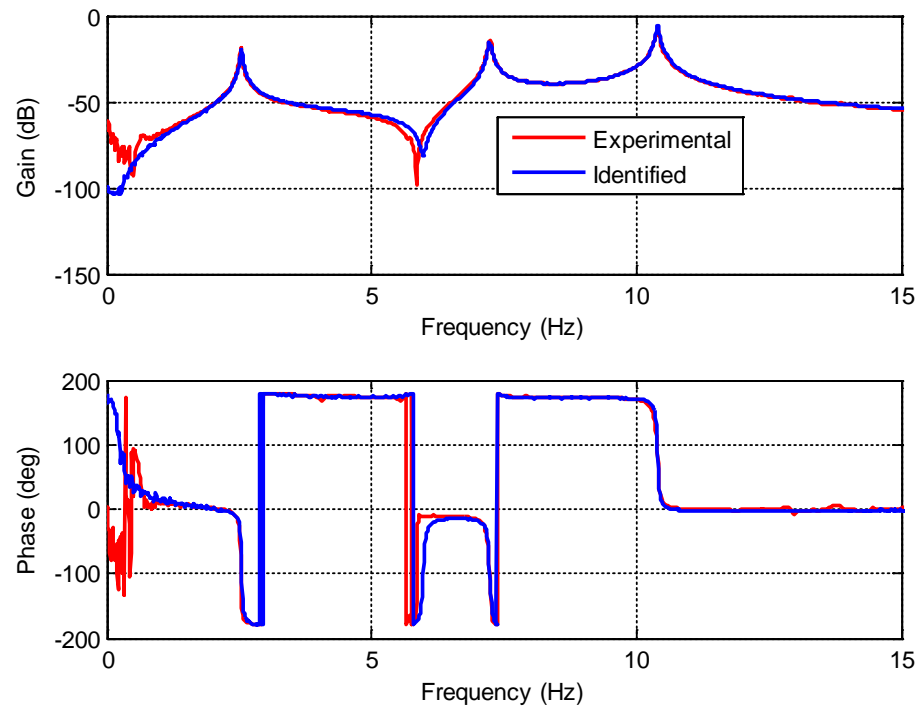


Figure 4.37. Transfer function from hammer force to 2nd floor acceleration.

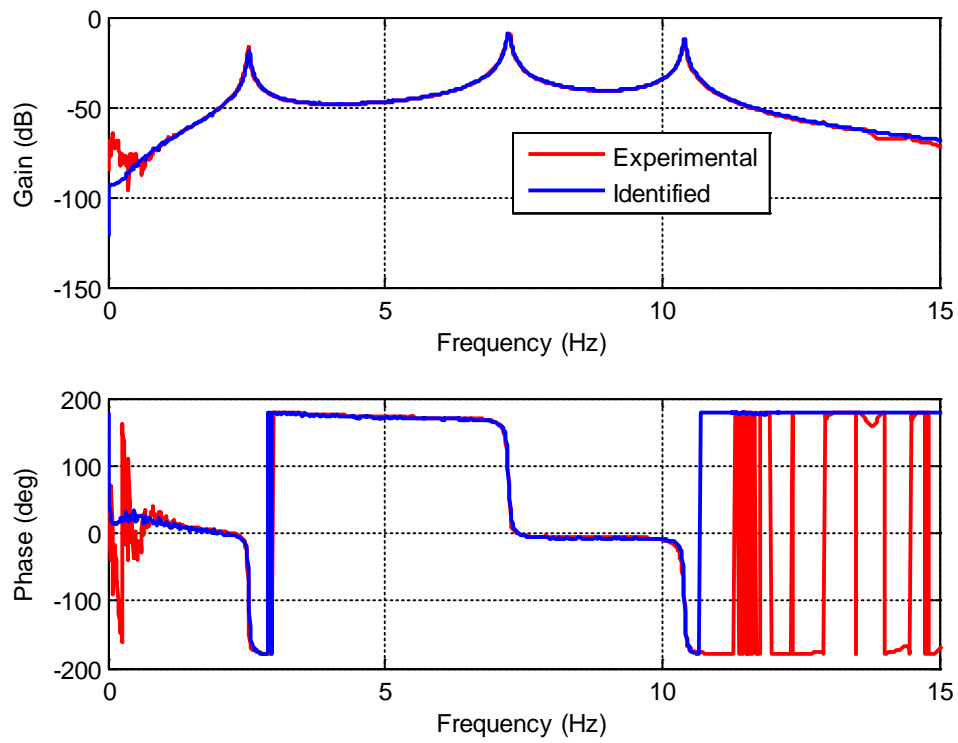


Figure 4.38. Transfer function from hammer force to 3rd floor acceleration.

4.2.2 Control System Setup

Four different control cases in the numerical simulation are considered in the experimental study, as listed in Table 4.3. Wireless sensors are attached to each of the three floors of the structure. Each sensor measures the acceleration at its respective floor. In addition to this, the wireless sensor on the first floor calculates the desired control force and generating voltage command to control MR damper force. Based on the number of wireless sensors in the network, different sensing and control frequencies are implemented. Case 1 is a fully decentralized case, as there is no wireless transmission in this case. Case 2 and Case 3 are partially decentralized cases, which includes wireless data transmission from one floor. Case 4 is a centralized case in the sense the acceleration data from all floors is sent to wireless node 1 for control calculation. The wireless control architecture is shown in Figure 4.39. The sampling and control time steps are controlled with time interrupt in the code.

The setup of wireless node and MR damper are shown in Figure 4.40 (a)-(b). To measure the structural responses, wired accelerometers and infrared LEDs are attached to each floor of the structure. Acceleration data is collected with the Vibplot DAQ system in Figure 4.41 (a), while displacement measurements are collected with the Krypton camera-based system (K600) in Figure 4.41 (b).

Table 4.3. Wireless control setup.

Wireless Control	Case 1	Case 2	Case 3	Case 4
Senor Number	1	2	2	3
Sensor Location (Floor)	1	1 & 2	1 & 3	1, 2, 3
Sampling Frequency (Hz)	100	100	100	50
Control Frequency (Hz)	800	100	100	50
Control Algorithm	LQG	OTD	OTD	OTD

Note: OTD is the optimal time-delay control in Section 2.2.

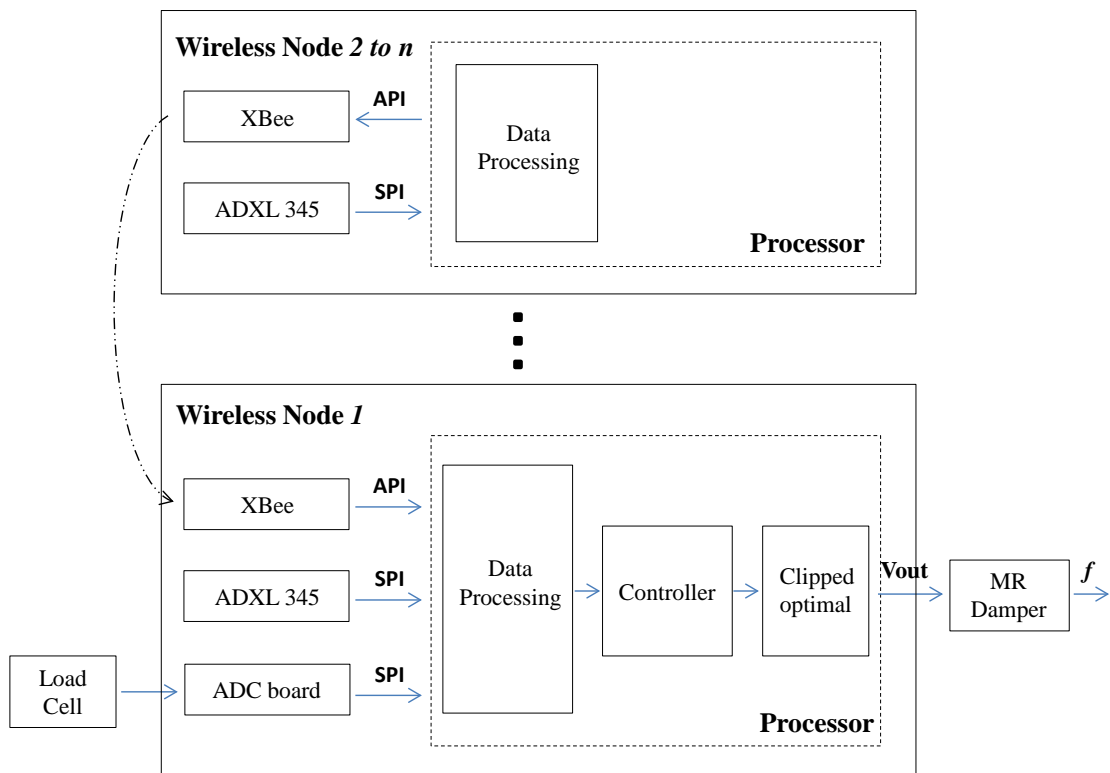


Figure 4.39. Wireless control architecture.

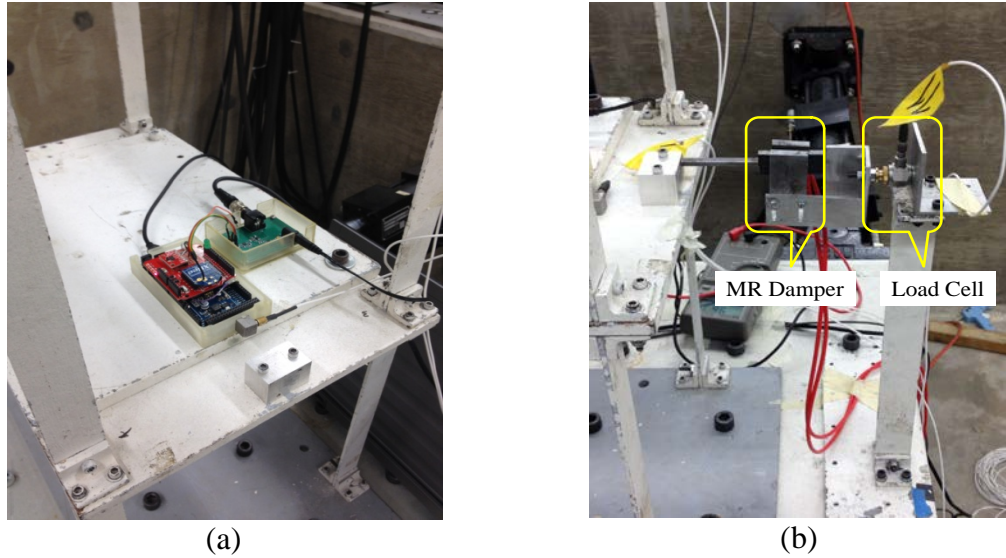


Figure 4.40. (a) Wireless sensor on the 1st floor, (b) MR damper setup.

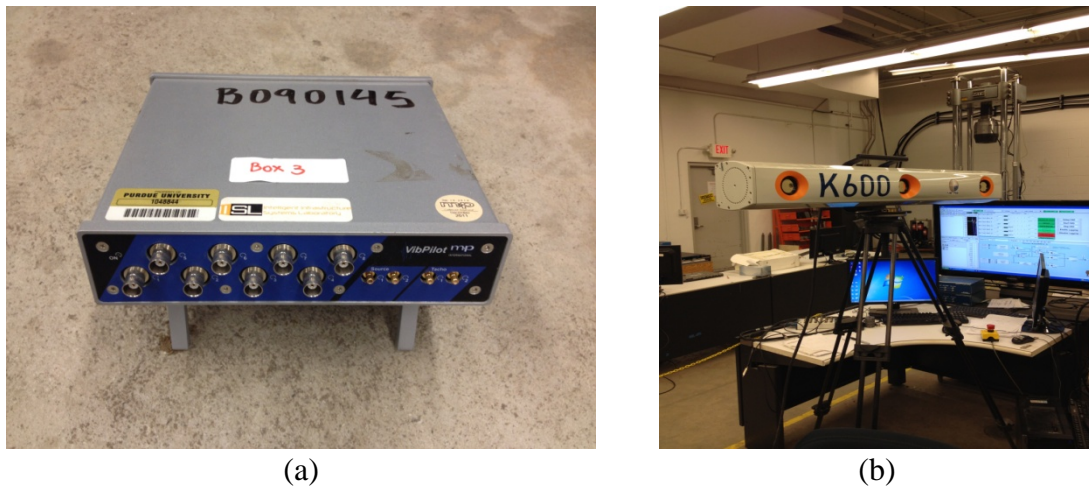


Figure 4.41. DAQ systems: (a) Vibpilot DAQ system, (b) Krypton system.

4.2.3 Verification Tests

Following the procedures discussed in Section 2.2, wireless control design is performed using the updated mass, damping and stiffness matrices. The feedback control gain for wireless control case 1 is

$$K = [286.034 \quad -502.208 \quad 216.707 \quad 148.907 \quad 14.246 \quad 40.162]$$

The optimal time delay control gain for wireless control cases 2-3 is

$$G = [219.368 \quad 61.615 \quad -46.338 \quad -9.040 \quad -0.058 \quad -3.388]$$

The optimal time delay control gain for wireless control case 4 is

$$G = [589.368 \quad -188.858 \quad 46.437 \quad -3.317 \quad -3.197 \quad -5.460]$$

The Kalman filters are designed separately for each case, based on the number of sensors available. Before the experimental study, verification tests are conducted to verify the onboard control implementation. Measured acceleration, measured force, desired control force and command voltage from onboard calculation are printed to a text file with USB serial port. The same control strategy is implemented in Matlab with the measured data from the text file. The desired force and command voltage are compared in Figures 4.42-4.43. The results match exactly, which verifies the onboard implementation. Wireless control cases 2-4 are similarly verified. The ADXL 345 acceleration measurement is also verified with wired measurement with measurement noise during the tests. The first floor acceleration is compared under BLWN excitation and under El Centro earthquake. The results are shown in Figures 4.44-4.45 and are found to be satisfactory, even with measurement noise. In the last verification test, the displacement measurement from the Krypton system is compared with the actuator LVDT measurement in Figures 4.46-4.47. The two systems exhibit good matching under El Centro earthquake ground displacement and Kobe earthquake ground displacement.

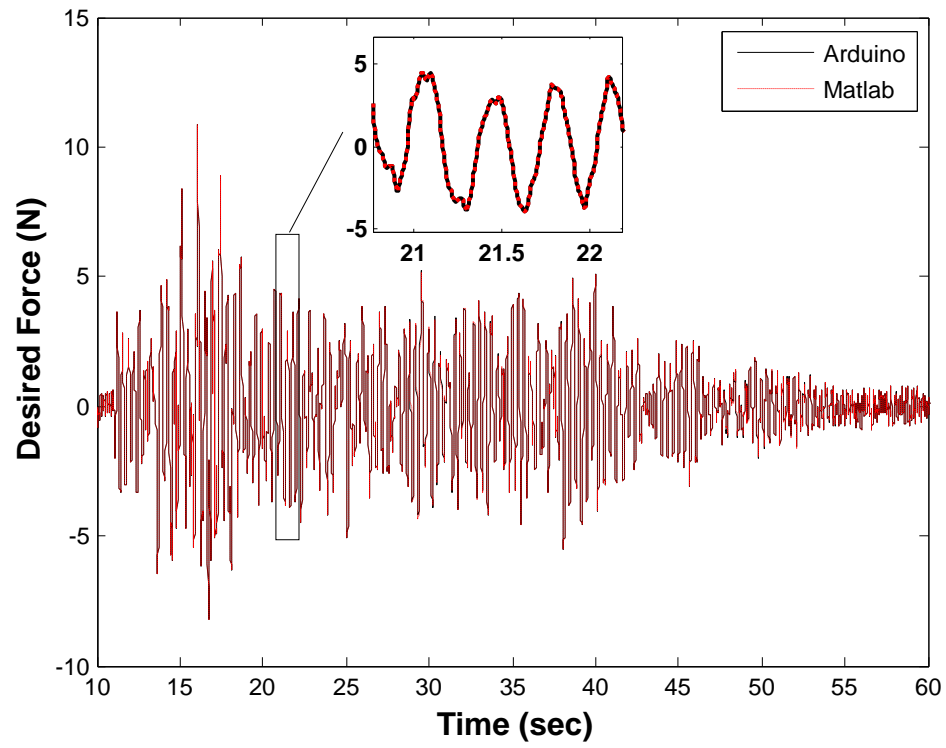


Figure 4.42. Force comparison.

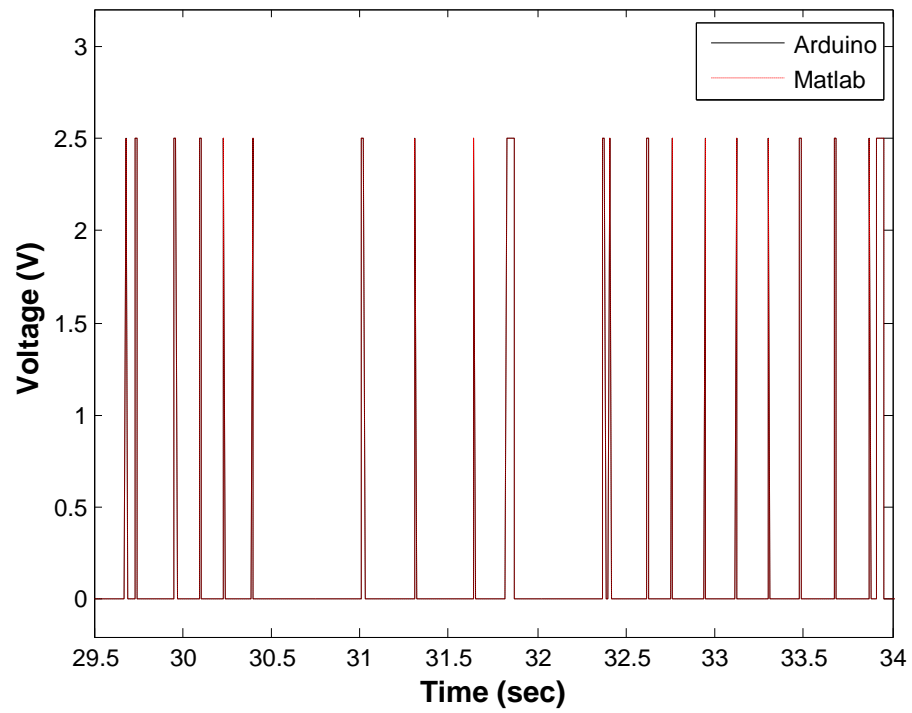


Figure 4.43. Voltage comparison.

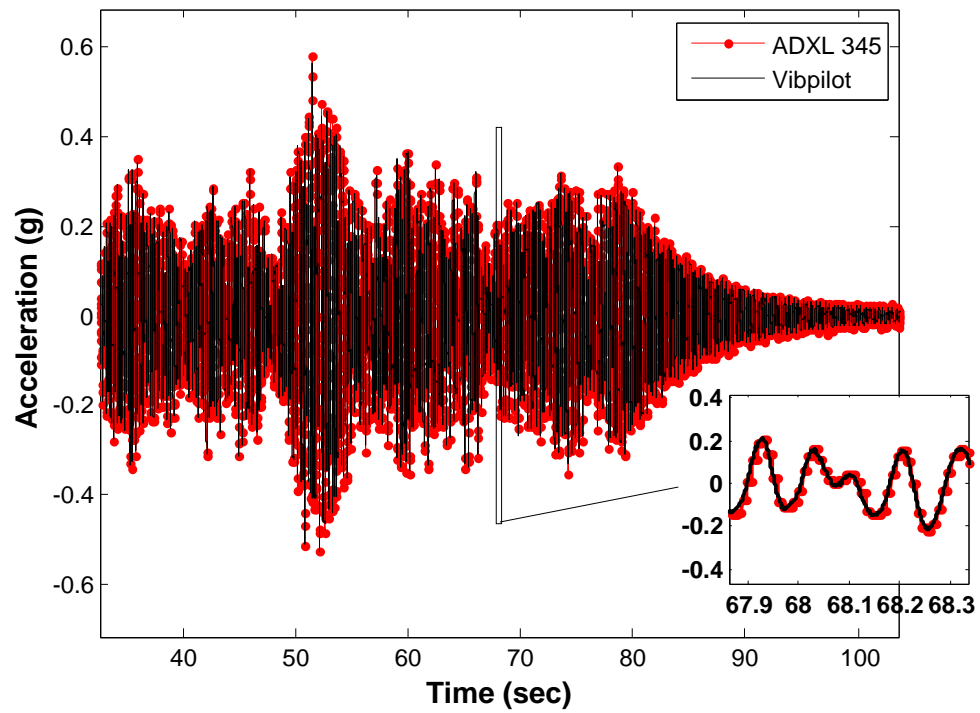


Figure 4.44. Acceleration comparison under BLWN excitation.

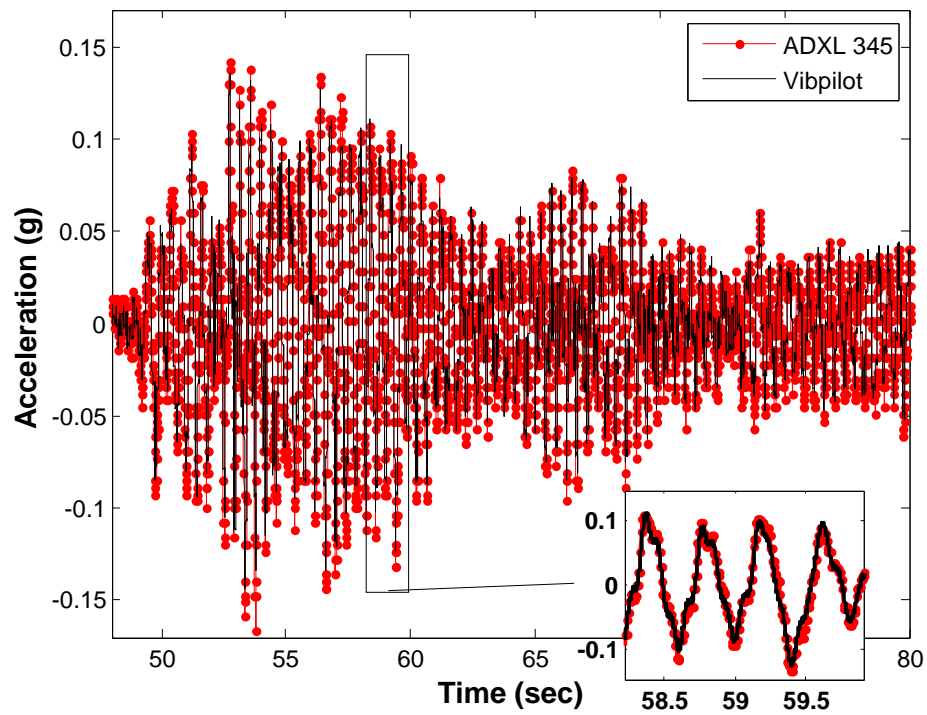


Figure 4.45. Acceleration comparison under El Centro excitation.

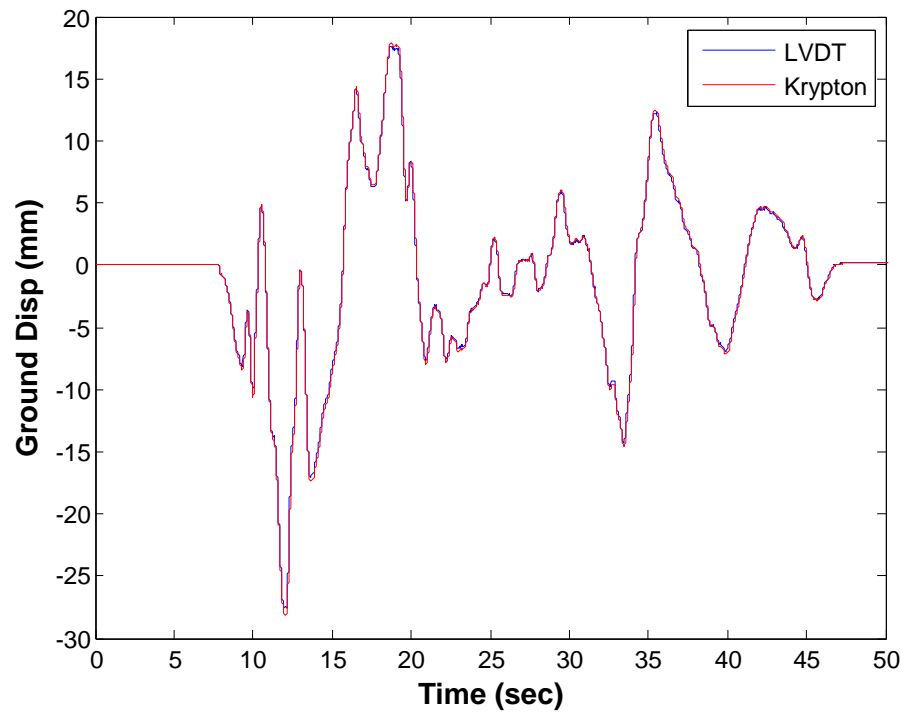


Figure 4.46. Ground displacement with El Centro earthquake.

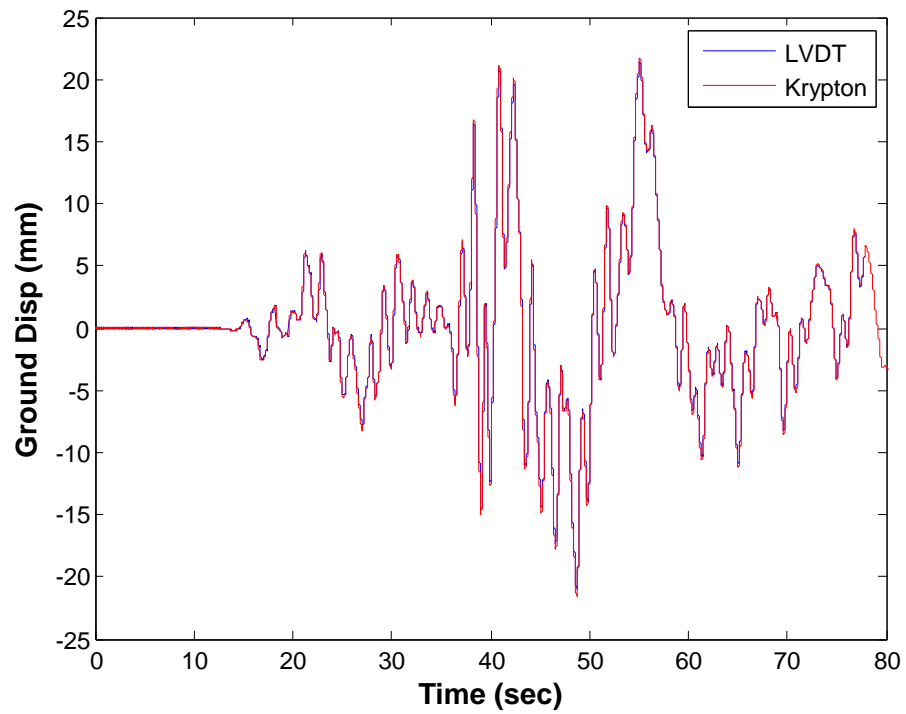


Figure 4.47. Ground displacement with Kobe earthquake.

4.2.4 Experimental Results

Experiments are conducted with the uncontrolled case, passive off (0V) case, passive on (2.5V) case, wired control case and wireless control cases. As the actual maximum digital pin output of Arduino Due is 2.5 V instead of 3.3 V, the passive on and wired control cases adopt a 2.5 V maximum voltage to make fair comparison. Wired control is implemented using the dSPACE system with the same control setup as in wireless case 1. The Simulink diagram for wired control is given in Figure 4.48. Four historical earthquakes: the 1999 Chichi earthquake, the 1940 El Centro earthquake, the 1994 Northridge earthquake and the 1995 Kobe earthquake are used in the experimental study. Due to the physical limitation imposed by the maximum displacement of the control device, the peak ground acceleration (PGA) is scaled to about 100 mg.

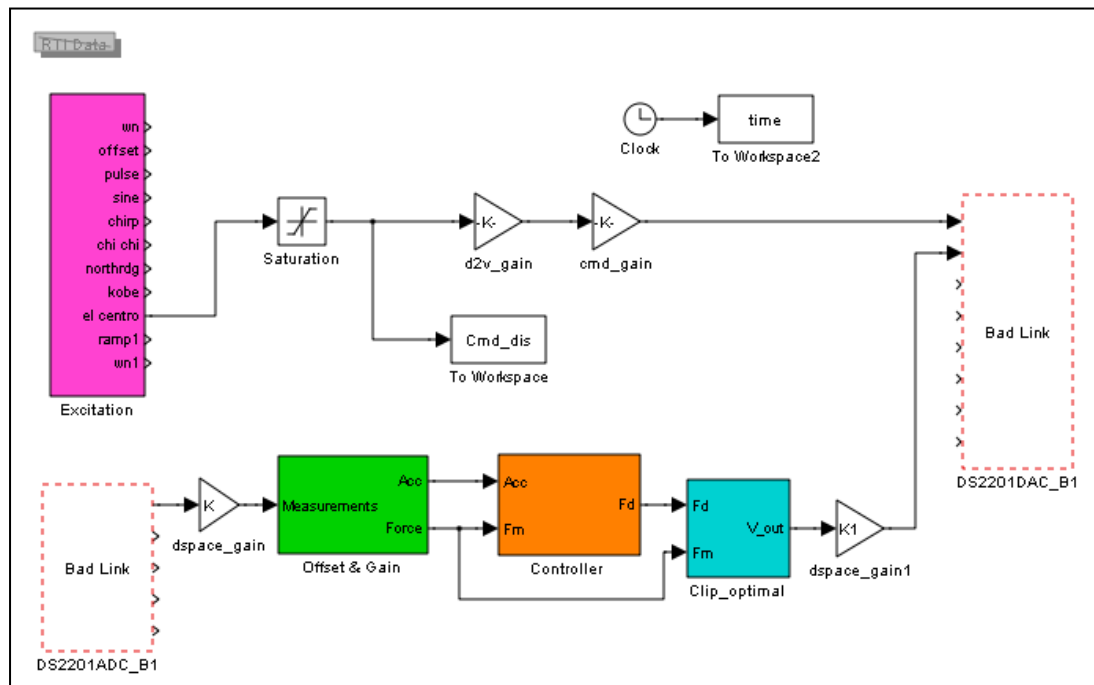


Figure 4.48. Wired control Simulink diagram for dSPACE.

The experimental results under the Chichi earthquake are shown in Figures 4.49-4.50. The results indicate an effective reduction in the RMS interstory drift and RMS acceleration of the structure in wireless control case 1. The peak drift and peak acceleration also show good reduction under this earthquake. The desired and measured control forces of MR damper are compared in Figure 4.51. The comparison between the desired and measured control voltages is shown in Figures 4.52-4.53. As shown in these figures, there is a “ripple” effect at the voltage transition points.

The experimental results under the El Centro earthquake, Northridge earthquake and Kobe earthquake are shown in Figures 4.54-4.59. Under these earthquakes, wireless control case 1 achieves similar performance to the wired control case. The RMS interstory drift and RMS acceleration are effectively reduced, especially for the 2nd and 3rd floor.

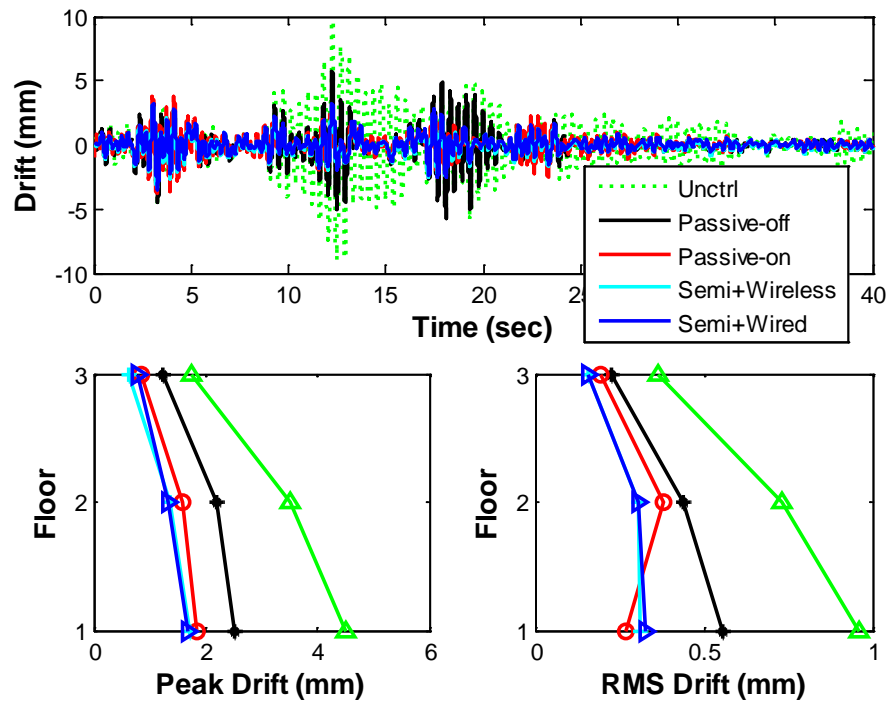


Figure 4.49. Interstory drift responses under Chichi earthquake.

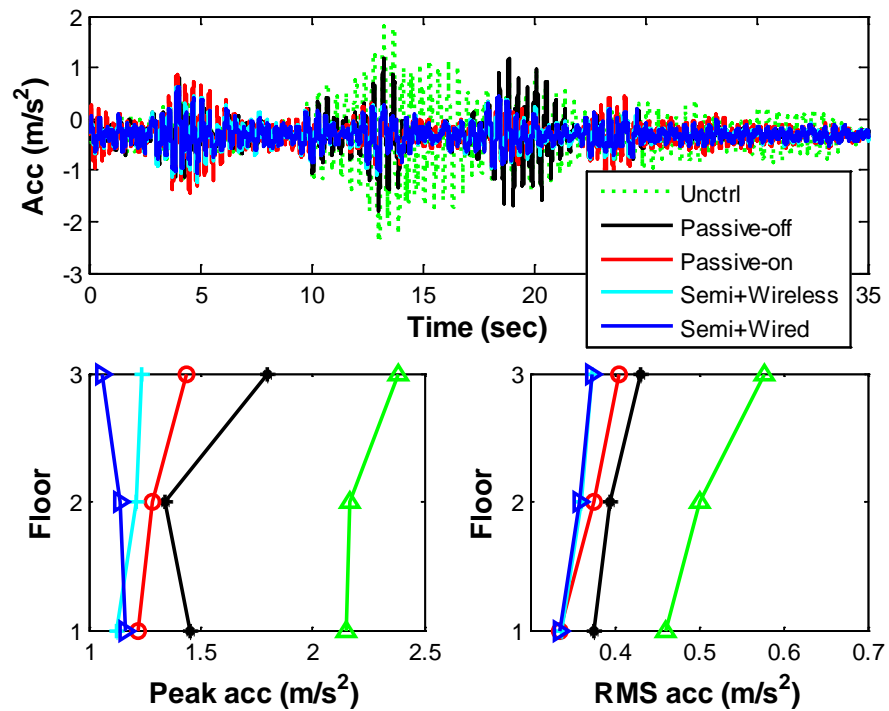


Figure 4.50. Acceleration responses under Chichi earthquake.

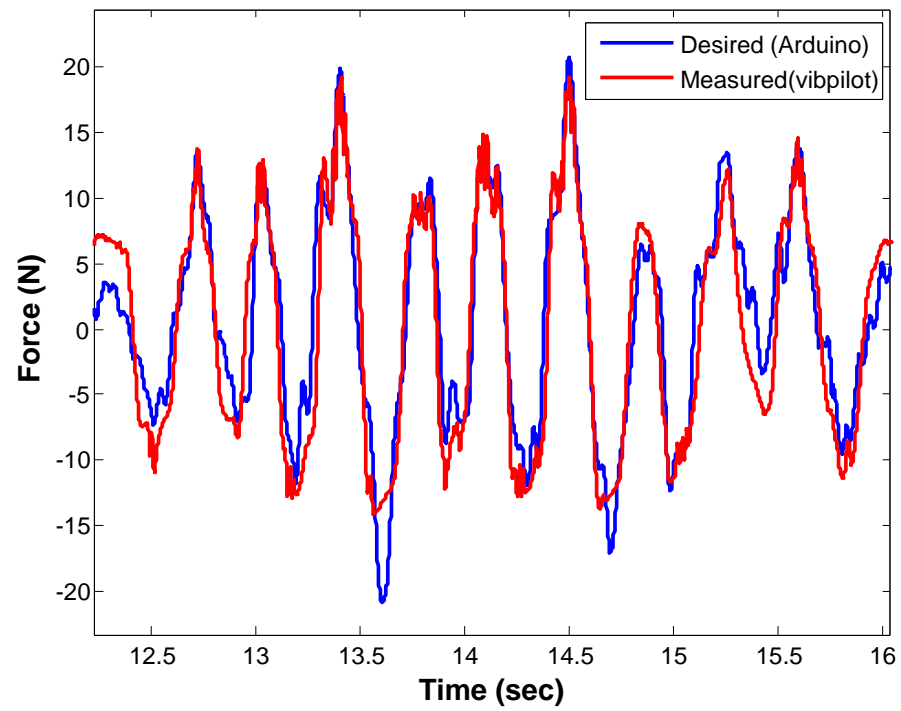


Figure 4.51. Force comparison.

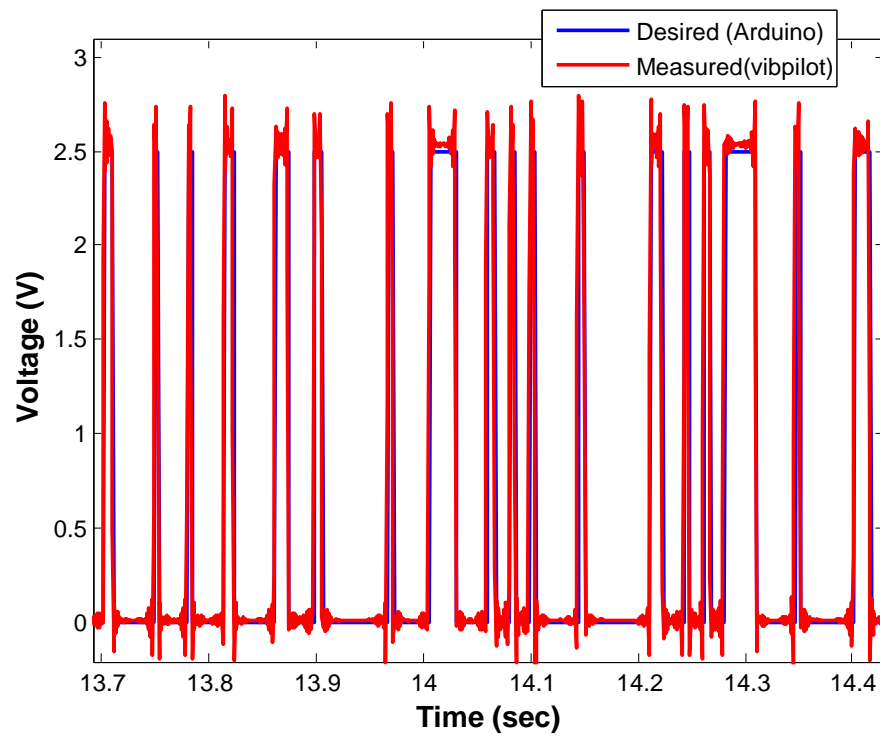


Figure 4.52. Voltage comparison.

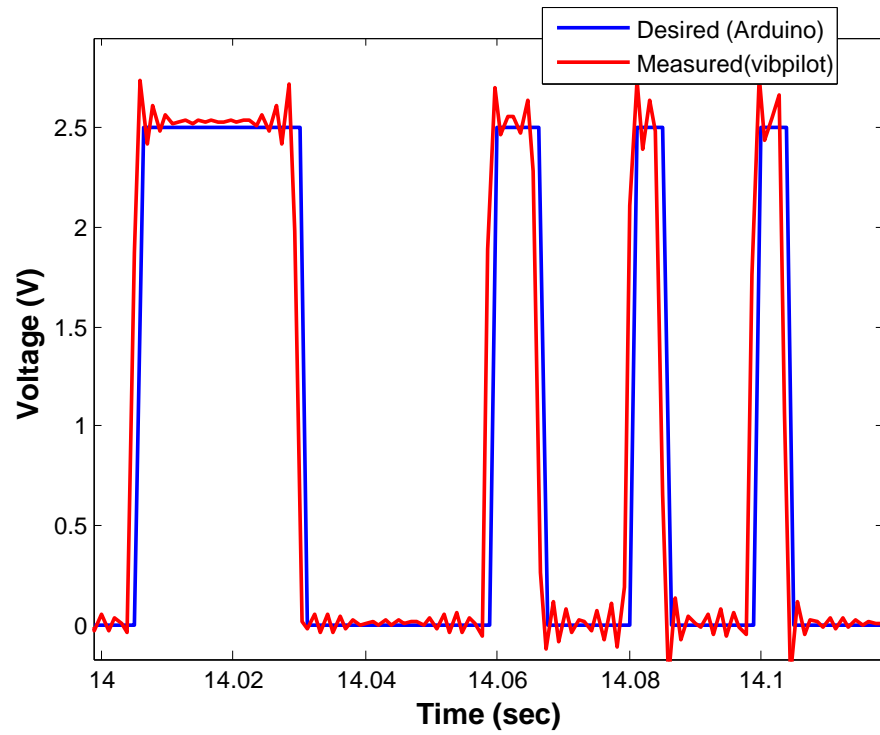


Figure 4.53. Voltage comparison (zoomed view).

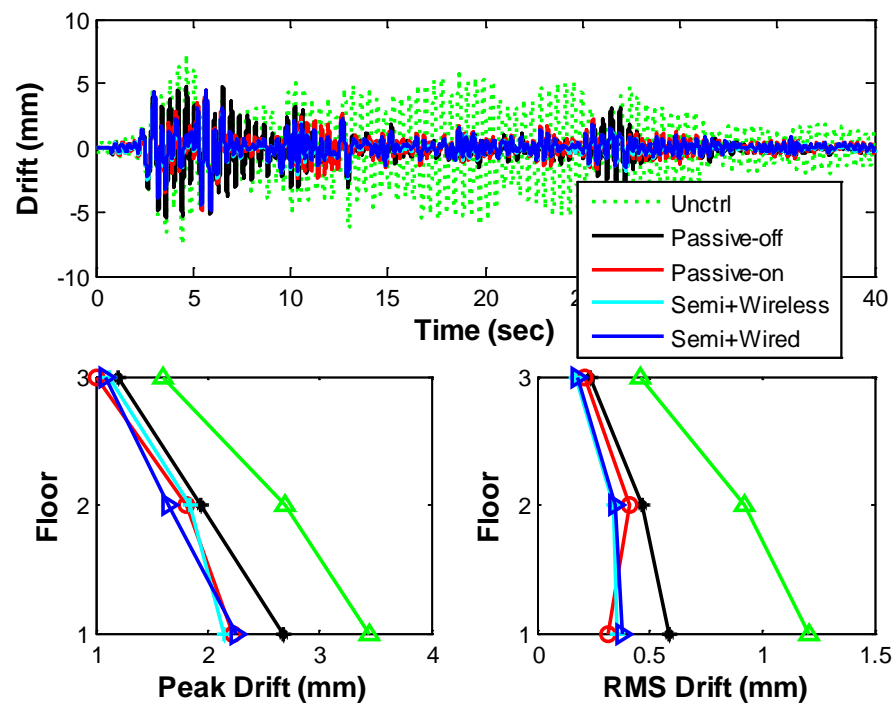


Figure 4.54. Interstory drift responses under El Centro earthquake.

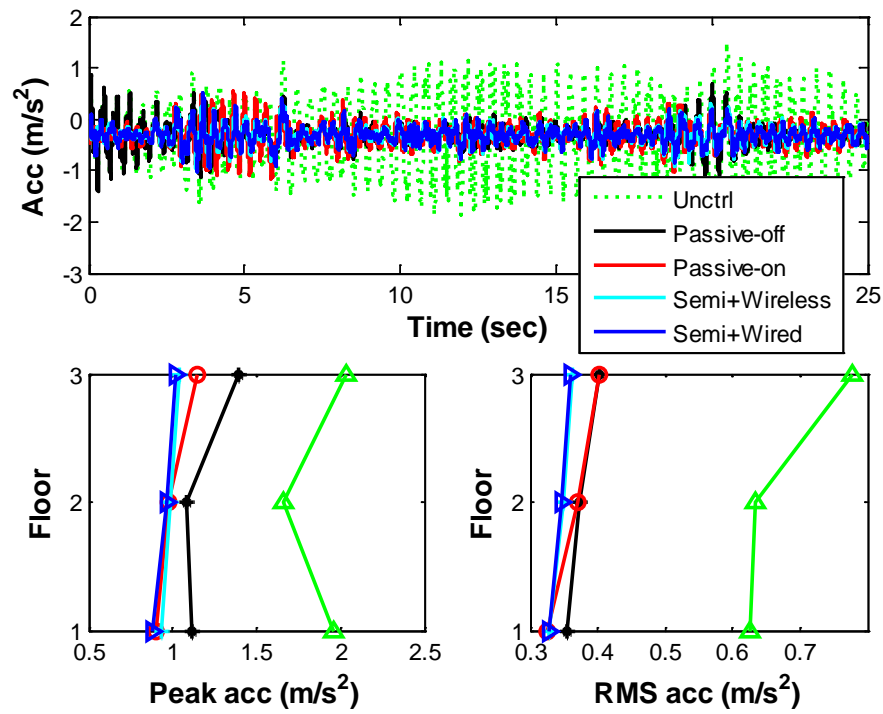


Figure 4.55. Acceleration responses under El Centro earthquake.

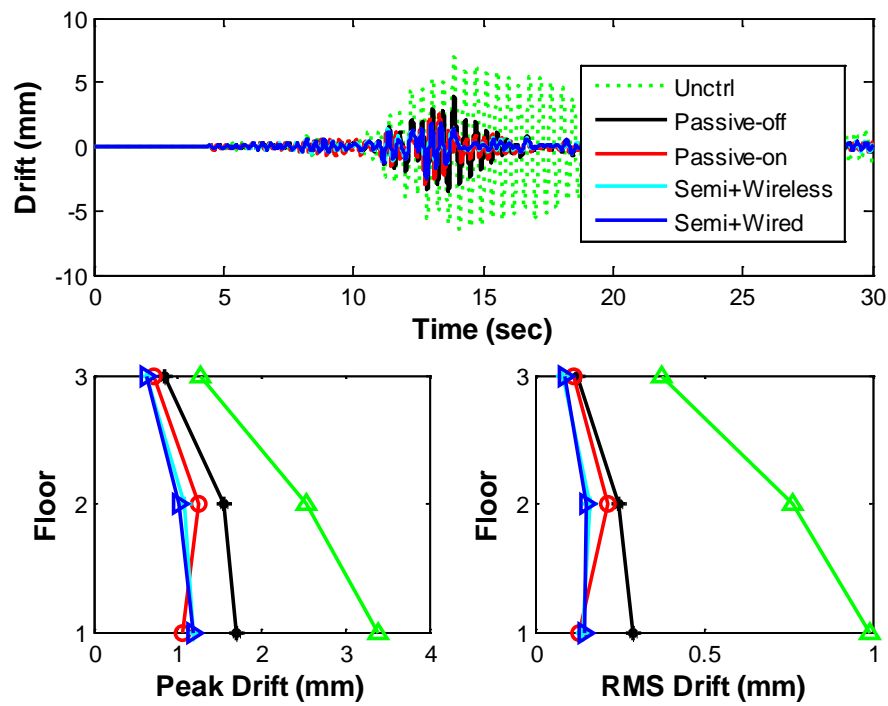


Figure 4.56. Interstory drift responses under Northridge earthquake.

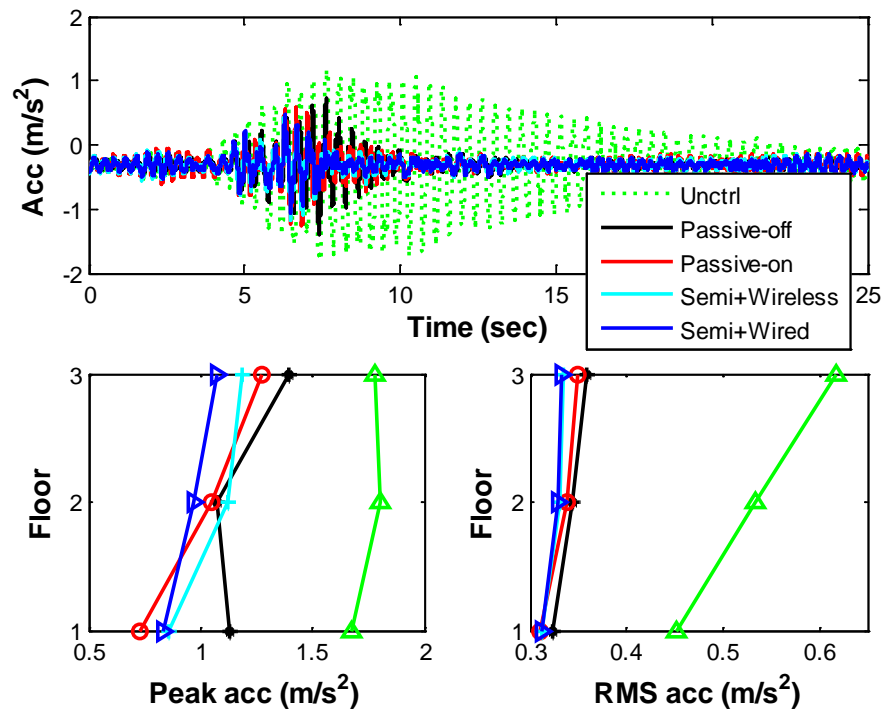


Figure 4.57. Acceleration responses under Northridge earthquake.

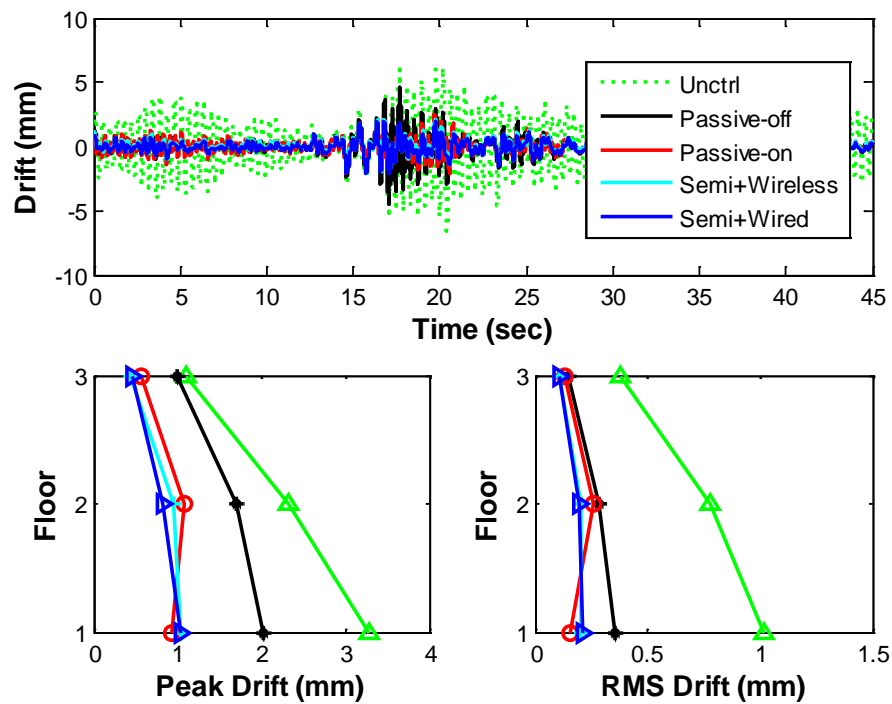


Figure 4.58. Interstory drift responses under Kobe earthquake.

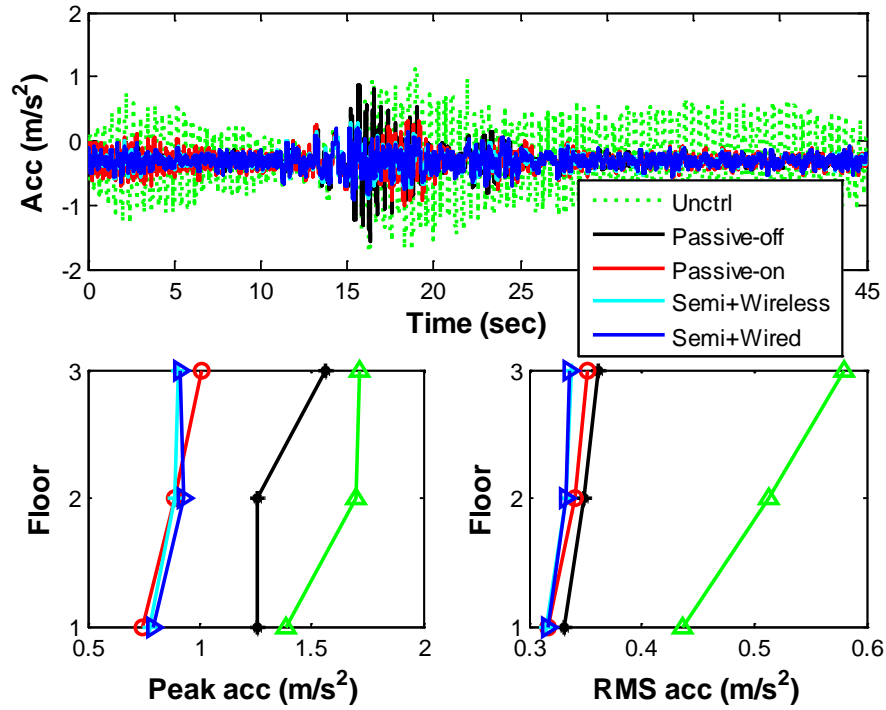


Figure 4.59. Acceleration responses under Kobe earthquake.

To quantitatively evaluate the control performance, four evaluation criteria in Spencer, et al. (1998) are adopted

$$J_1 = \max_t \left\{ \frac{|d_1(t)|}{d_{1_o}}, \frac{|d_2(t)|}{d_{1_o}}, \frac{|d_3(t)|}{d_{1_o}} \right\} \quad (4.20)$$

$$J_2 = \max_t \left\{ \frac{|\ddot{x}_1(t)|}{\ddot{x}_{3_o}}, \frac{|\ddot{x}_2(t)|}{\ddot{x}_{3_o}}, \frac{|\ddot{x}_3(t)|}{\ddot{x}_{3_o}} \right\} \quad (4.21)$$

$$J_3 = \max \left\{ \frac{\sigma_{d_1}}{\sigma_{d_{1_o}}}, \frac{\sigma_{d_2}}{\sigma_{d_{1_o}}}, \frac{\sigma_{d_3}}{\sigma_{d_{1_o}}} \right\} \quad (4.22)$$

$$J_4 = \max \left\{ \frac{\sigma_{\ddot{x}_{a1}}}{\sigma_{\ddot{x}_{a3_o}}}, \frac{\sigma_{\ddot{x}_{a2}}}{\sigma_{\ddot{x}_{a3_o}}}, \frac{\sigma_{\ddot{x}_{a3}}}{\sigma_{\ddot{x}_{a3_o}}} \right\} \quad (4.23)$$

where J_1 evaluates the maximum peak interstory drift normalized with uncontrolled 1st story drift (d_{1_o}); J_2 evaluates the maximum peak acceleration normalized with

uncontrolled 3rd story peak acceleration (\ddot{x}_{3_o}); J_3 evaluates the maximum RMS interstory drift normalized with uncontrolled 1st story RMS drift ($\sigma_{d_{1o}}$); J_4 evaluates the maximum RMS acceleration normalized with 3rd story RMS acceleration ($\sigma_{\ddot{x}_{a3o}}$).

The evaluation results for RMS interstory drift (J_3) and RMS acceleration (J_4) are provided in Figures 4.60-4.61. The RMS interstory drift with wireless control case 1 is reduced by 70% compared to uncontrolled case, while the RMS acceleration is reduced by 40%. The wireless control case 1 which is the decentralized case is more effective than the passive off case and passive on case in reducing RMS drifts and accelerations. The wireless control case 1 achieves the same level of performance as the wired control system. The complete evaluation results for different control strategies are provided in Table 4.4.

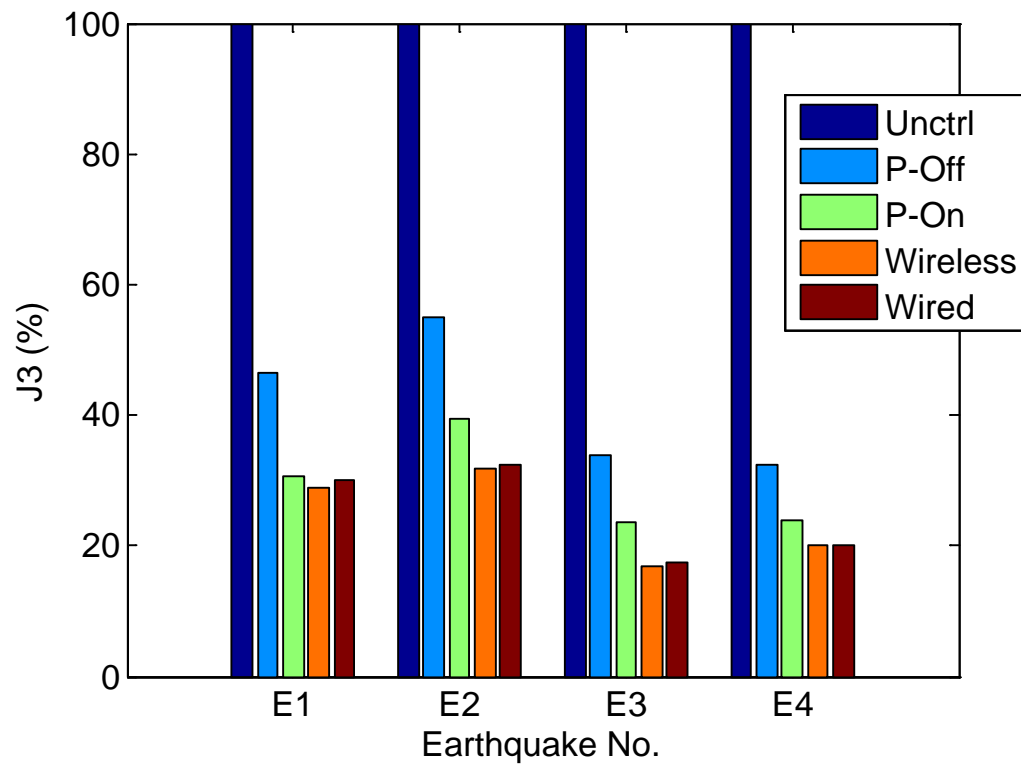


Figure 4.60. Normalized RMS drift (J_3) under E1: El Centro Earthquake, E2: Chichi Earthquake, E3: Northridge Earthquake, and E4: Kobe Earthquake.

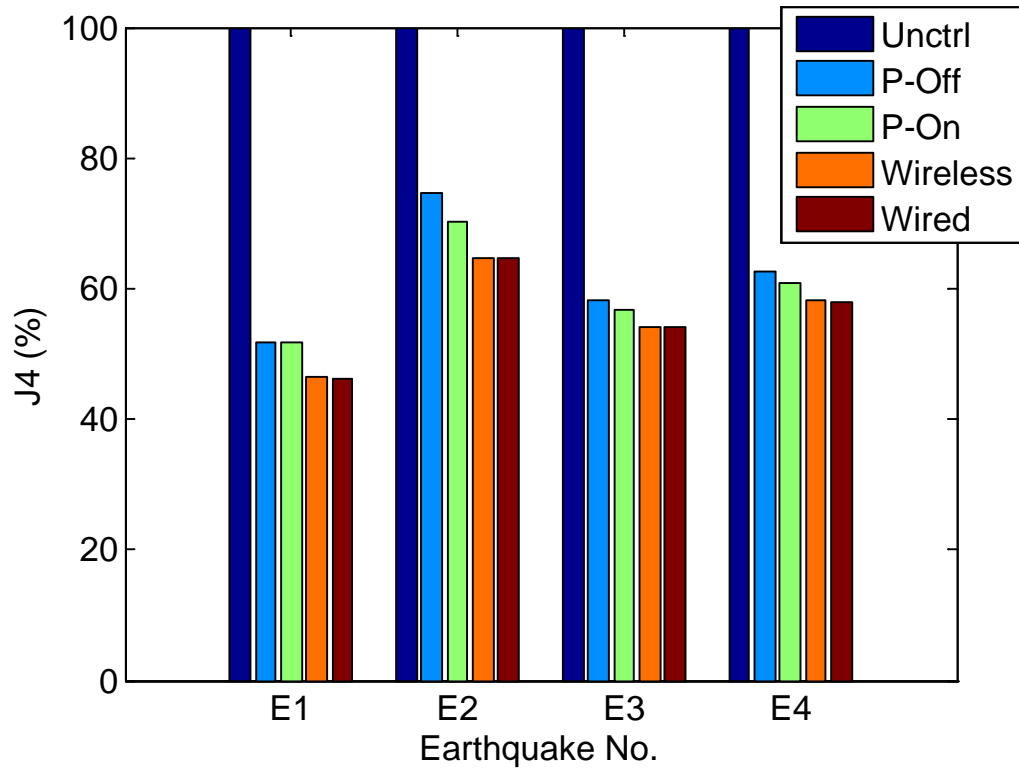
Figure 4.61. Normalized RMS acceleration (J_4) under E1-E4 earthquakes.

Table 4.4. Experimental results I.

Excitation	GPA	Control	J_1 (%)	J_2 (%)	J_3 (%)	J_4 (%)
El Centro	123mg	P-off	77.8	68.5	48.5	51.7
		P-on	64.8	56.2	33.9	51.7
		Wireless	62.5	50.7	29.5	46.5
		Wired	65.6	49.7	31.3	46.2
Chichi	114mg	P-off	56.0	75.5	57.9	74.5
		P-on	41.1	60.4	39.5	70.1
		Wireless	37.9	51.9	32.3	64.7
		Wired	37.5	48.8	34.3	64.7
Northridge	87mg	P-off	50.0	77.5	29.5	58.1
		P-on	37.1	70.6	21.5	56.7
		Wireless	34.9	65.8	16.2	54.2
		Wired	34.7	59.7	15.6	54.0
Kobe	108mg	P-off	61.1	91.3	34.7	62.5
		P-on	32.6	58.9	25.2	60.8
		Wireless	31.2	52.8	20.3	58.2
		Wired	31.2	54.4	20.7	58.0

After the evaluation of wireless control case 1, experiments with wireless control cases 2-4 are conducted to experimentally compare the performance of different wireless control strategies. With wireless transmission, the data loss of each sensor channel is less than 5% in the experiments. To perform a fair comparison, wireless case 1 and wired control case are repeated and conducted in the same day with the wireless control cases 2-4. The desired and measured force and voltage are compared for wireless control cases 2 and 4, in Figures 4.62-4.66. Note the desired force and voltage are obtained from the Arduino while the measured force and voltage are obtained from the Vibpilot system. The start time is manually triggered and is different for the two systems. Thus, voltage measurements are used to determine the correct time offset to compare the forces from the two systems.

Experimental results for the El Centro are shown in Figures 4.67-4.68. Evaluation results are provided in Figures 4.69-4.70 and the complete evaluation results are listed in Table 4.5. Based on the results of this case study, wireless control 1 performs slightly better than wireless cases 2 and 3. This is demonstrated from the evaluation results. Wireless control case 4 has the worst control performance compared to other wireless control cases in most scenarios. The increase in wireless transmission delay in the sensor measurements in wireless cases 2-4 degrades the performance of these cases as compared with wireless case 1. The tradeoff between the number of measurements available and the wireless network induced time delay is very interesting and worth further investigation in future studies. Based on the results of these experiments, the decentralized control strategy and partially decentralized control strategy are more attractive in this setup. Note

the maximum damper force (30 N) is only about 4.3% the total weight of the structure, but significant RMS drift reduction (70%) and RMS acceleration reduction (40 %) are achieved with decentralized wireless control.

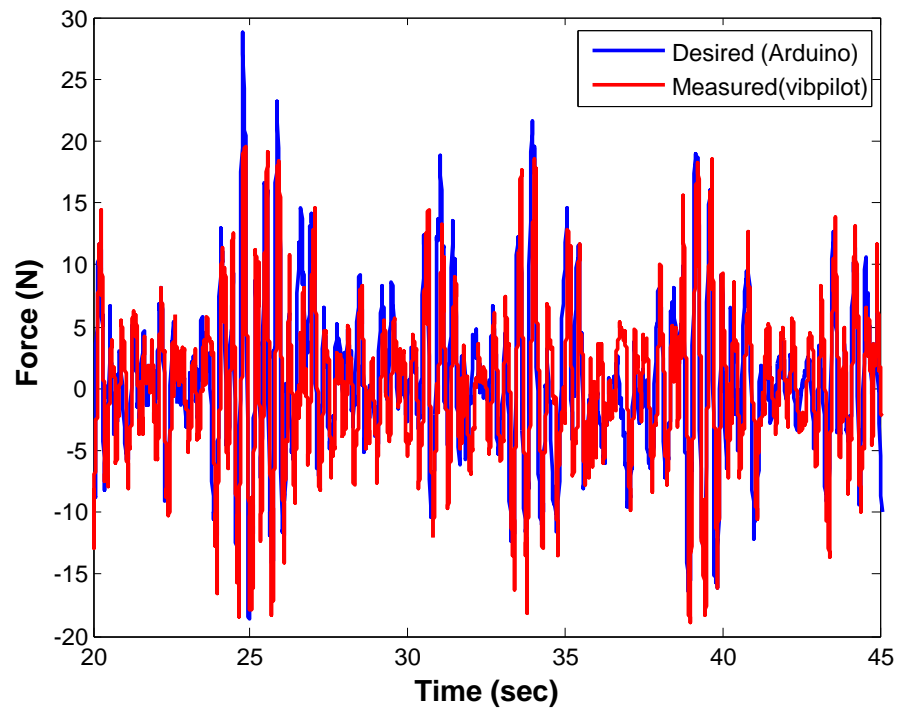


Figure 4.62. Force comparison of wireless case 2.

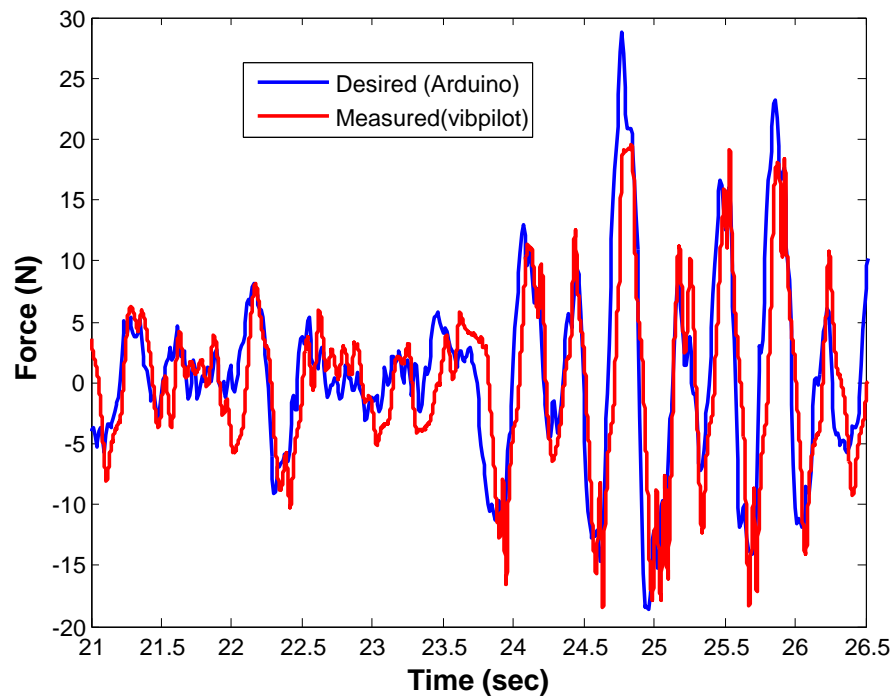


Figure 4.63. Force comparison of wireless case 2 (Zoomed view).

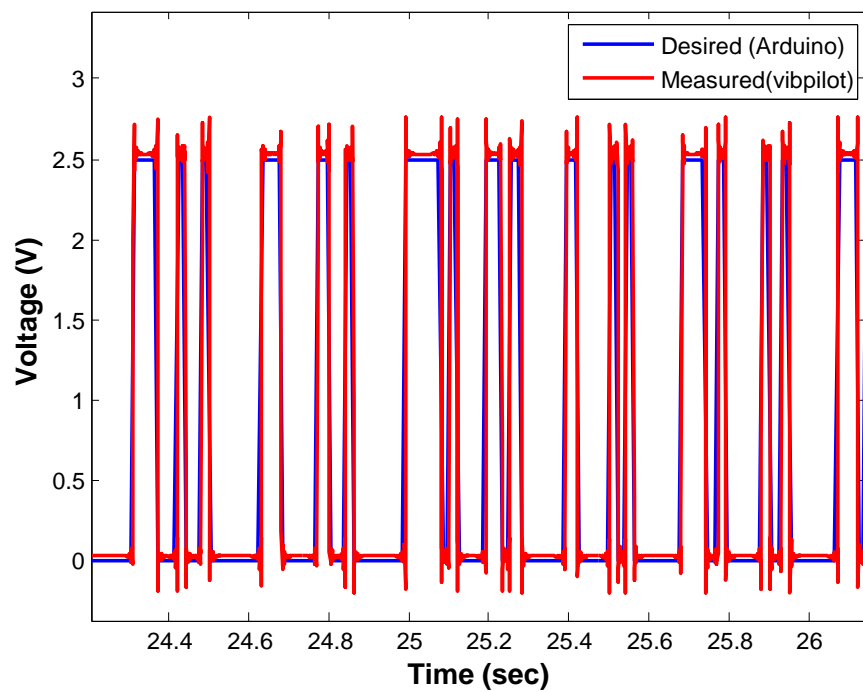


Figure 4.64. Voltage comparison of wireless case 2.

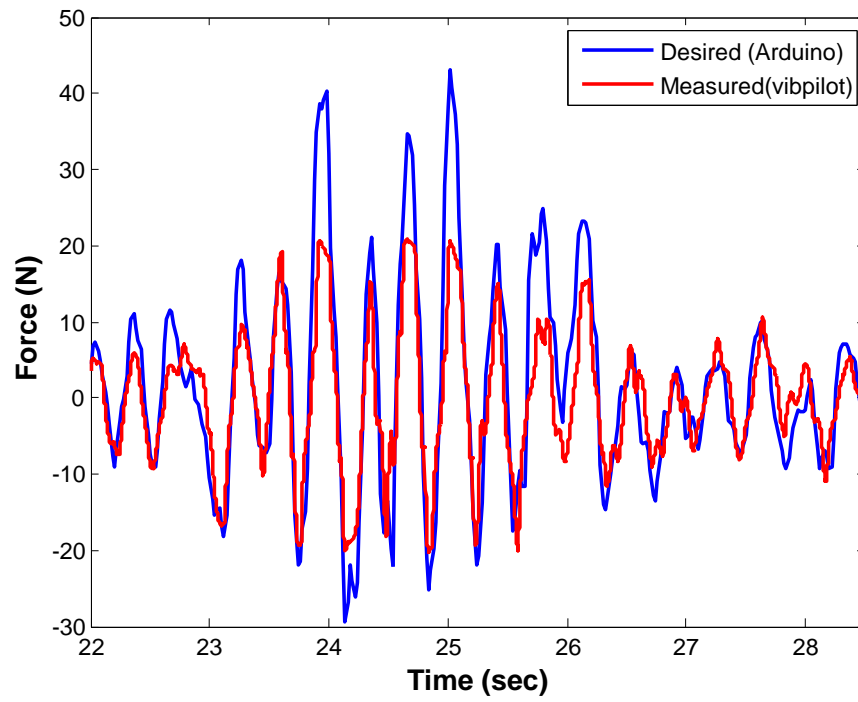


Figure 4.65. Force comparison of wireless case 4.

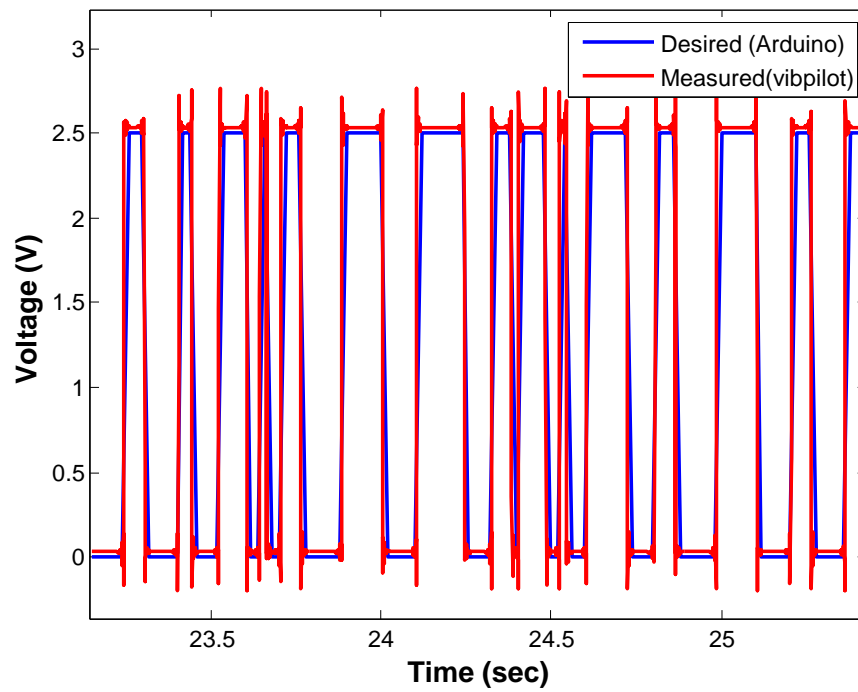


Figure 4.66. Voltage comparison of wireless case 4.

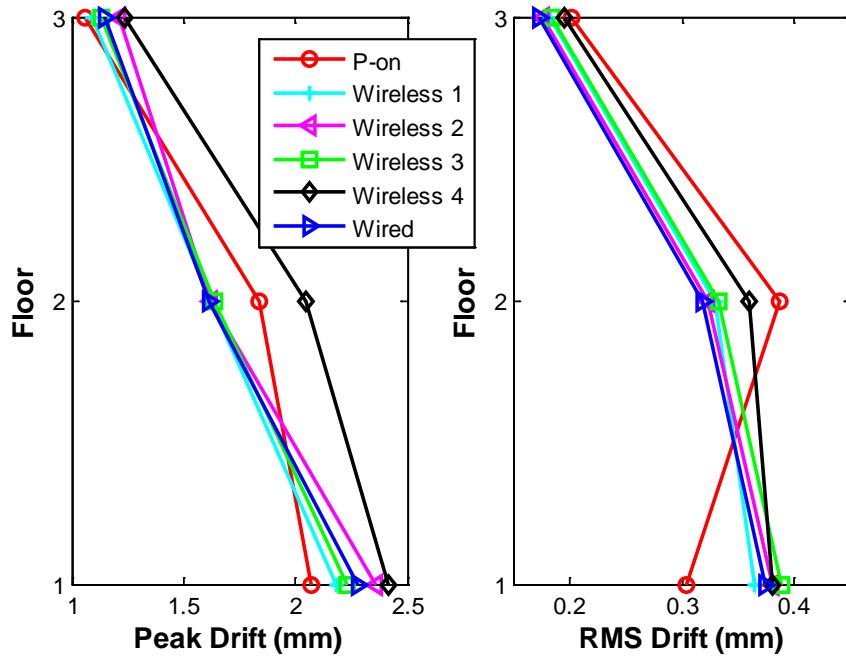


Figure 4.67. Interstory drift responses under El Centro earthquake.

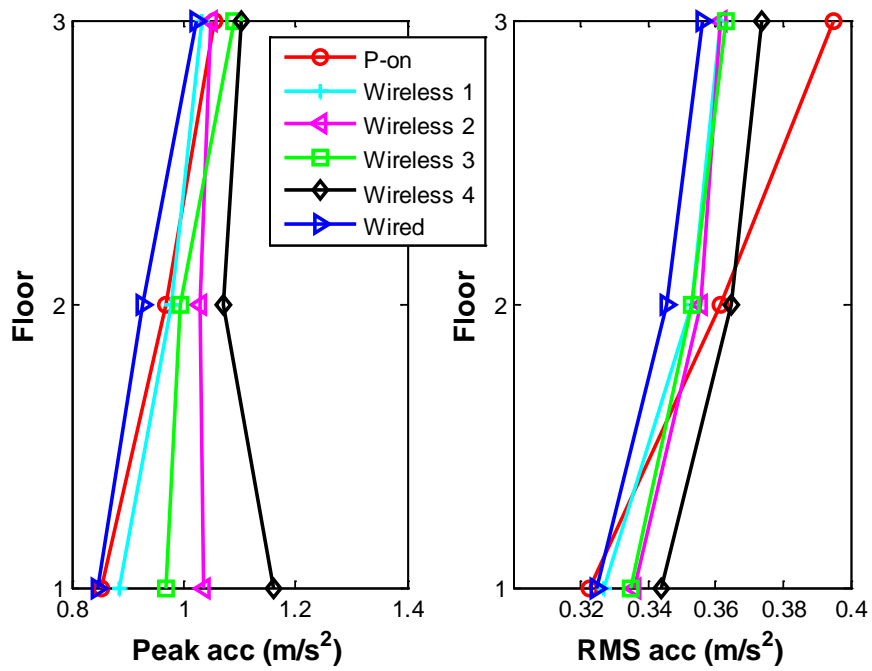


Figure 4.68. Acceleration responses under El Centro earthquake.

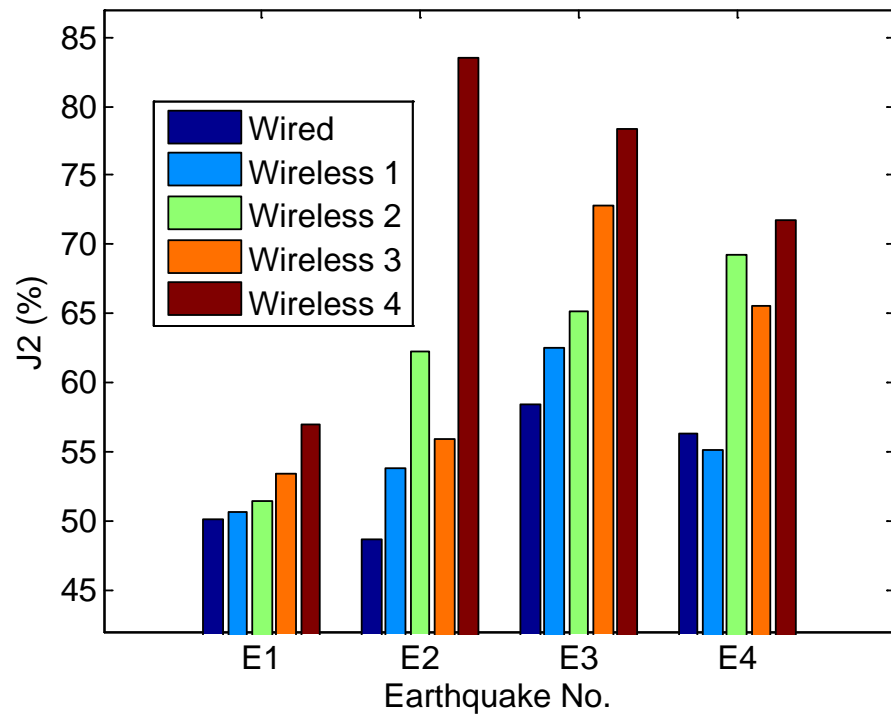


Figure 4.69. Normalized peak acceleration (J_2) under E1-E4 earthquakes.

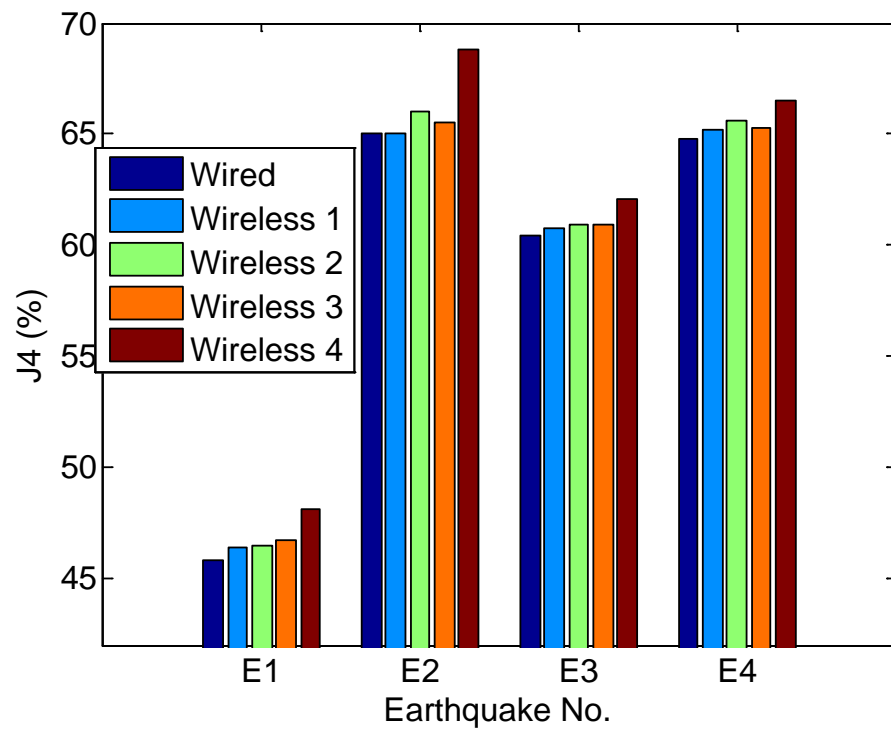


Figure 4.70. Normalized RMS acceleration (J_4) under E1-E4 earthquakes.

Table 4.5. Experimental results II.

Excitation	GPA	Control	J_1 (%)	J_2 (%)	J_3 (%)	J_4 (%)
El Centro	123mg	Wireless 1	60.4	50.6	28.9	46.4
		Wireless 2	65.3	51.5	30.2	46.5
		Wireless 3	62.6	53.4	30.8	46.7
		Wireless 4	66.8	57.0	31.2	48.1
		Wired	61.9	50.1	29.5	45.8
Chichi	114mg	Wireless 1	35.3	53.8	31.8	65.0
		Wireless 2	38.8	62.3	32.9	66.0
		Wireless 3	34.7	55.9	34.0	65.5
		Wireless 4	40.3	83.5	33.5	68.8
		Wired	35.0	48.7	32.3	65.0
Northridge	87mg	Wireless 1	33.7	62.5	17.0	60.8
		Wireless 2	34.2	65.2	17.6	60.9
		Wireless 3	34.0	72.8	17.2	60.9
		Wireless 4	35.2	78.4	18.1	62.1
		Wired	32.1	58.4	16.8	60.4
Kobe	108mg	Wireless 1	30.9	55.1	20.0	65.2
		Wireless 2	32.4	69.2	20.3	65.6
		Wireless 3	31.7	65.6	20.9	65.3
		Wireless 4	33.5	71.8	21.9	66.5
		Wired	30.2	56.3	20.1	64.8

4.3 Summary

In this chapter, numerical simulations are first performed, simulating wireless control of a 3-story structure equipped with an MR damper on the 1st floor. Various control strategies including decentralized control, partially decentralized control, centralized control are studied in the numerical simulation. Based on the simulation results, the decentralized wireless control (wireless case 1) has the best performance in terms of RMS interstory drift reduction and RMS acceleration reduction. Despite the availability of more measurements with wireless control cases 2-4, the control performance degrades due to the time delay and larger control time step. Next, experimental studies are conducted implementing the developed wireless control system on a 3-story lab structure.

Decentralized wireless control case is compared with the passive off case, passive on case, wired control case as well as partially decentralized wireless control case and centralized wireless control case. From the experimental results, decentralized wireless control outperforms passive control cases and it achieves similar performance as the wired counterpart with greatly reduced cost. The performance of partially decentralized wireless control are slightly degraded due to a longer time delay while the centralized wireless control has the worst performance. This observation is consistent with the results from numerical simulation which provides some guidance for the deployment of wireless control systems. The developed wireless control system is shown to be effective in controlling structural vibrations under several historical earthquake ground motions. Feasibility of the developed wireless control system is verified.

It is worth to mention, there is a tradeoff between the number of sensors and wireless transmission delay in the wireless control system. For the developed wireless control system in this work, the transmission delay has more impact than the number of sensor measurements. There are some research work on high speed wireless transmission (≤ 2 msec per transmission) in which the transmission delay is greatly reduced. For such wireless control systems, partially decentralized and centralized control may perform equivalently or even better performance than decentralized control.

CHAPTER 5. A CODESIGN APPROACH WITH PROPOSED SWITCHING ESTIMATOR

Wireless control systems offer several appealing features compared to their wired control counterparts. However, wireless transmission is prone to data loss in addition to sensor failure which also occurs in wired control system. Currently, the transmission strategy to deal with data loss is to send an acknowledgment message from the receiver to the transmitter after receiving data, and to do retransmit if the data is not received by the receiver. However, this strategy introduces an uncertain time delay which is undesirable for real-time control system. Having alternate method that takes into account the data loss or sensor failure in the wireless transmission would support the development of effective wireless control under realistic conditions. In this chapter, an estimator switching method (ESM) is proposed to work with OTD method to achieve codesign in wireless control. The robustness of this strategy is studied in terms of modeling error and measurement noise using the 3-story building in chapter 4.

5.1 Proposed Estimator Switching Method

Estimation methods are extensively studied in control engineering for networked control systems. Sinopoli, et al., (2004) develops a modified time varying Kalman estimator for a discrete-time linear dynamic system. The Kalman gain is updated at each time step with

the modified algebraic Riccati equation. An upper bound of data loss rate is obtained beyond which a transition to an unbounded state error covariance occurs. Smith & Seiler (2003) use the Markov chain to model the probabilistic data loss for a linear system. They propose a finite loss history estimator, which uses a precomputed gain selector based on the last r measurements. The precomputed gains depend on the probability of a package loss after a package reception and the probability of a package loss after a package loss. Fang & Wang (2008) transform the networked control system with package drop into a convex optimization problem. The closed loop system with control gain K and estimator gain L is exponentially mean-square stable if there exist positive definite matrices P and S that satisfy an LMI equation. Alavi & Saif (2013) propose an observer design method for nonlinear system with known probability of a package loss. A design procedure is proposed to compute the observer gain. It is worth mentioning that the observer gain which satisfies all the conditions in the paper may not exist. There are also methods which consider data loss as an additional measurement delay in the control system (Yu, et al., 2004; Gao, et al., 2008) which are beyond the scope of the discussion here.

In this section, a Kalman filter based estimator switching method is proposed for linear system with data loss. The dynamic system which has data loss is taken as a jump linear system

$$x(k+1) = A_d x(k) + B_d u(k) + E_d w(k) \quad (5.1)$$

$$y(k) = C_d(k)x(k) + F_d(k)v(k) \quad (5.2)$$

where $x(k) \in R^{n \times 1}$ are the states at $(k)^{\text{th}}$ step, $u(k) \in R^{q \times 1}$ are the control input at k^{th} step, $y(k) \in R^{m \times 1}$ are measurements at k^{th} step, $w(k)$ is the process noise, $v(k)$ is the

measurement noise, $A_d, B_d, E_d, C_d(k) \in \{C_{d1}, C_{d2}, \dots, C_{dr}\}, F_d(k) \in \{F_{d1}, F_{d2}, \dots, F_{dr}\}$ are matrices of appropriate dimension, and $r = 2^m$ since each measurement output has two states (loss or reception).

The process noise and measurement noise are zero-mean, uncorrelated with

$$E(w(k)) = 0, E(v(k)) = 0$$

$$E(w(k)w(k)^T) = Q, E(v(k)v(k)^T) = R, E(w(k)v(k)^T) = 0$$

The measurement output for original system without data loss is

$$y(k) = Cx(k) + v(k) \quad (5.3)$$

The estimator for the original system has the following state equation (Franklin, et al., 1990)

$$\hat{x}^-(k+1) = A_d \hat{x}(k) + B_d u(k) \quad (5.4)$$

$$\hat{x}(k+1) = \hat{x}^-(k+1) + L(y(k+1) - C\hat{x}^-(k+1)) \quad (5.5)$$

The steady-state Kalman gain is given by

$$L = PC^T(CPC^T + R)^{-1} \quad (5.6)$$

$$P = A_d[P - PC^T(CPC^T + R)^{-1}CP]A_d^T + E_dQE_d^T \quad (5.7)$$

The estimator switching method for linear system with data loss is provided as below.

Definition: The jump linear system in Equations (5.1-5.2) is said to be asymptotically stable if there exist L such that

$$\rho(A_d - L(k)C_d(k)A_d) < 1 \text{ for } k \in [1, \infty] \quad (5.8)$$

where $\rho(\cdot) < 1$ means that all the poles are located inside the unit circle in z-plane.

Proof:

The switching estimator can be written as

$$\hat{x}(k+1) = A_d \hat{x}(k) + B_d u(k) + L(k+1)[y(k+1) - C_d(k+1)\hat{x}^-(k+1)] \quad (5.9)$$

where $L(k) \in \{L_1, L_2, \dots, L_r\}$ is precomputed and selected at step k with the data loss knowledge of $y(k)$

By subtracting Equation (5.9) from Equation (5.1), we have

$$\begin{aligned} x(k+1) - \hat{x}(k+1) &= A_d(x(k) - \hat{x}(k)) + E_d w(k) \\ &\quad - L(k+1)(C_d(k+1)x(k+1) + F_d(k+1)v(k+1) \\ &\quad - C_d(k+1)\hat{x}^-(k+1)) \\ &= A_d(x(k) - \hat{x}(k)) + E_d w(k) \\ &\quad - L(k+1)(C_d(k+1)(A_d(x(k) - \hat{x}(k)) + E_d w(k)) \\ &\quad + F_d(k+1)v(k+1)) \end{aligned} \quad (5.10)$$

The estimation error at step k is given by

$$e(k) = x(k) - \hat{x}(k) \quad (5.11)$$

Then, Equation (5.10) can be rewritten as

$$\begin{aligned} e(k+1) &= (A_d - L(k+1)C_d(k+1)A_d)e(k) + (I - L(k+1)C_d(k+1))E_d w(k) \\ &\quad - L(k+1)F_d(k+1)v(k+1) \end{aligned} \quad (5.12)$$

The estimation error in Equation (5.12) converges with $\rho(A_d - L(k)C_d(k)A_d) < 1$ for $\forall k \in [1, \infty]$

Remark 1: A suboptimal Kalman filter based estimator switching method is proposed. The switching gains L_i are precomputed for each data loss case (the total number of cases is 2^m). Compared to existing methods, this method does not require online computation of the estimator gain which is computationally expensive. Also, knowledge of probability of data loss is not required to guarantee the stability of the estimator.

Remark 2: To apply this estimator switching method, the only required additional knowledge at each step is the data loss information from each sensor. This can easily be obtained based on the sensor ID in the wireless package (e.g. if sensor 2 has data loss, there is no data with sensor ID “2” at the base station at that step).

Remark 3: One way to find the gains L_i for each data loss case is to compute Equations (5.4-5.7) with constant C_{di} and F_{di} under the condition that (A_d, C_{di}) is detectable. When all data are lost for certain steps, $\rho(A_d) < 1$ is required to ensure stability. In this case, the estimator may have poor performance but the estimation error still converges.

Remark 4: The estimator switching method only takes into account sensor data loss or sensor transmission failure. A transmission delay would need to be considered separately by using a control algorithm for systems with delayed measurement (i.e. OTD control algorithm or Smith predictor).

5.2 Numerical Study to Evaluate the Estimator Switching Method

A numerical study is performed using the numerical model of the 3-story building in chapter 4. The 1st case study considers the numerical building control system with data loss but without transmission delay. An LQR controller is applied in conjunction with the estimator switching method. To examine the estimator switching method, we consider the cases in which there are 3 sensors in the network (one per floor). The total number of cases to evaluate is $2^3 = 8$ as shown in Table 5.1.

Table 5.1. Switching cases.

Case No.	Available Measurements	Switching Gain
1	1, 2&3	L_1
2	1&2	L_2
3	1&3	L_3
4	2&3	L_4
5	1	L_5
6	2	L_6
7	3	L_7
8	N.A.	L_8

With noise covariance $Q = 25$, $R = I^{3 \times 3}$, the L_i for each case is designed following the procedure in remark 3 of the previous section. The estimator gains obtained are shown below:

With sensor measurements from all floors

$$L_1 = \begin{bmatrix} -0.071 & -0.023 & -0.018 \\ -0.075 & -0.042 & -0.037 \\ -0.074 & -0.046 & -0.052 \\ -3.867 & -0.019 & -0.146 \\ -4.664 & -0.400 & -0.239 \\ -4.639 & -0.604 & -0.394 \end{bmatrix} \times 10^{-3}$$

With sensor measurements from floors 1 and 2

$$L_2 = \begin{bmatrix} -0.074 & -0.035 \\ -0.079 & -0.066 \\ -0.079 & -0.075 \\ -3.865 & -0.157 \\ -4.627 & -0.532 \\ -4.567 & -0.615 \end{bmatrix} \times 10^{-3}$$

With sensor measurements from floors 1 and 3

$$L_3 = \begin{bmatrix} -0.073 & -0.027 \\ -0.077 & -0.053 \\ -0.077 & -0.077 \\ -3.868 & -0.046 \\ -4.649 & -0.071 \\ -4.668 & -0.423 \end{bmatrix} \times 10^{-3}$$

With sensor measurements from floors 2 and 3

$$L_4 = \begin{bmatrix} -0.133 & -0.020 \\ -0.195 & -0.048 \\ -0.198 & -0.071 \\ -0.844 & -0.097 \\ -3.899 & -0.133 \\ -4.668 & -0.506 \end{bmatrix} \times 10^{-3}$$

With a sensor measurement from floor 1

$$L_5 = \begin{bmatrix} -0.098 \\ -0.125 \\ -0.136 \\ -3.858 \\ -4.361 \\ -4.415 \end{bmatrix} \times 10^{-3}$$

With a sensor measurement from floor 2

$$L_6 = \begin{bmatrix} -0.131 \\ -0.264 \\ -0.332 \\ 0.130 \\ -0.758 \\ -3.869 \end{bmatrix} \times 10^{-3}$$

With a sensor measurement from floor 3

$$L_7 = \begin{bmatrix} -0.149 \\ -0.217 \\ -0.223 \\ -1.198 \\ -3.889 \\ -4.002 \end{bmatrix} \times 10^{-3}$$

When no measurements are received, $L_8 = \mathbf{0}$.

The Simulink diagram for the 1st case study is shown in Figure 5.1. The estimator switching method is implemented with an embedded Matlab function block. The data loss is modelled as a Bernoulli process. Simulations are first performed assuming different probabilities of data loss in one sensor (the 3rd floor) under the El Centro earthquake. The normalized estimation error of system state and the averaged estimation error are calculated using Equation (5.13) and Equation (5.14), respectively.

$$Err = \frac{\|x(t) - x_e(t)\|_2}{\|x(t)\|_2} \quad (5.13)$$

$$Err_{avg} = \sum_{i=1}^n \frac{Err_i}{n} \quad (5.14)$$

where $x(t)$ is the true state of the system, and $x_e(t)$ is the estimated state, n is the number of states.

The estimation results for the original Kalman filter and switching estimator with one faulty sensor are shown in Figures 5.2-5.3. The switching estimator has much less error compared to the original Kalman filter in this case. The estimation results with different probabilities of data loss in sensor 3 (3rd floor) are provided in Figures 5.4-5.5. As the probability of data loss increases, the original Kalman estimator has worse performance while the switching estimator still performs well. The impact of the discrete time step to the estimator error is also analyzed. The time step is varied from 0.001 sec to 0.01 sec and the results are provided in Figures 5.6-5.7.

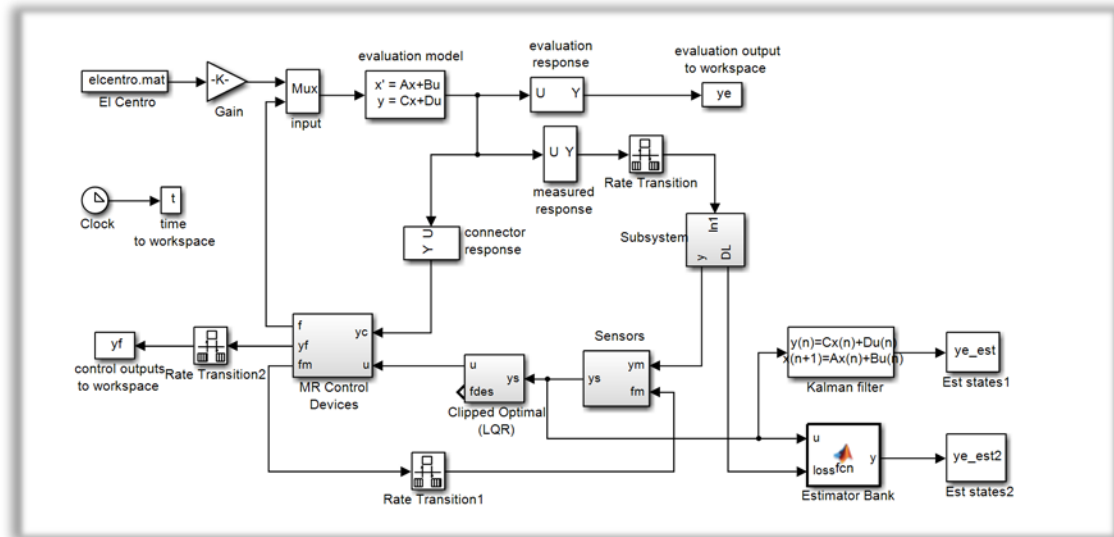


Figure 5.1. Simulink model including switching estimator.

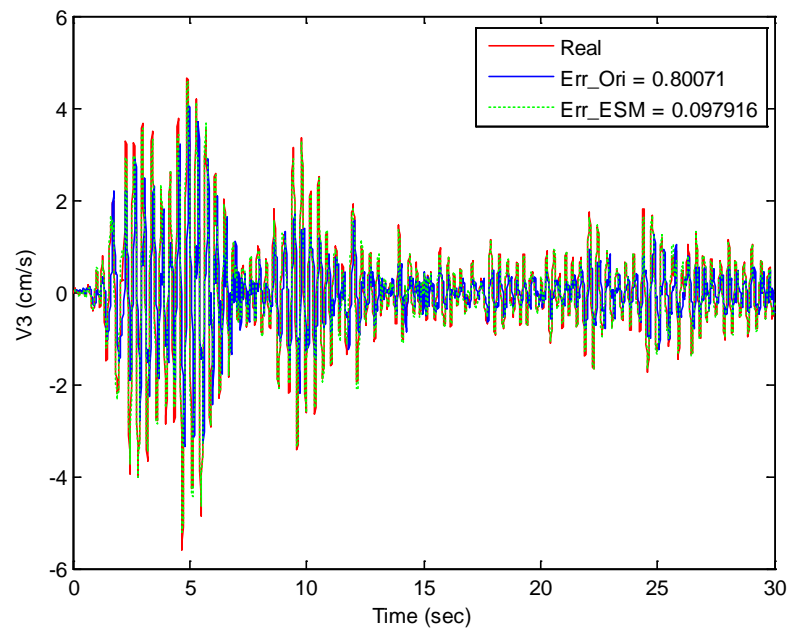


Figure 5.2. Estimation of 3rd story velocity with sensor failure.

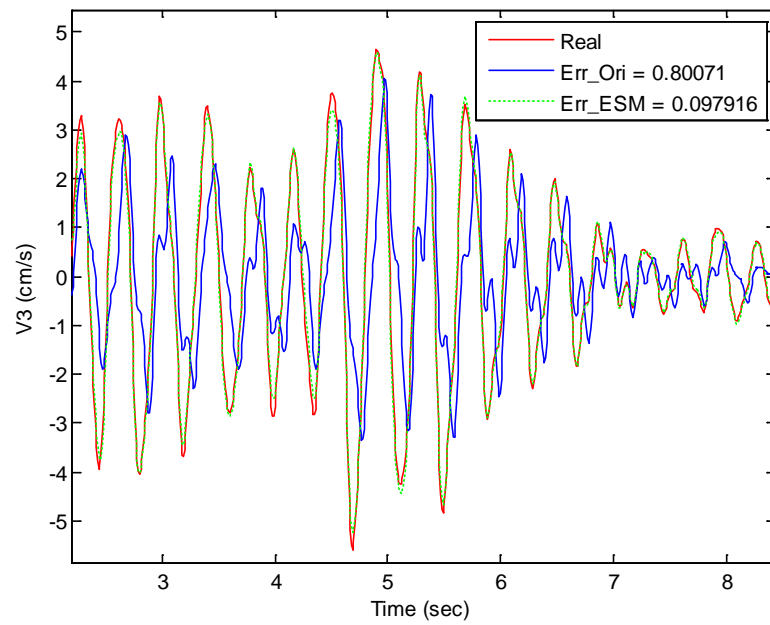


Figure 5.3. Zoomed view of figure 5.2.

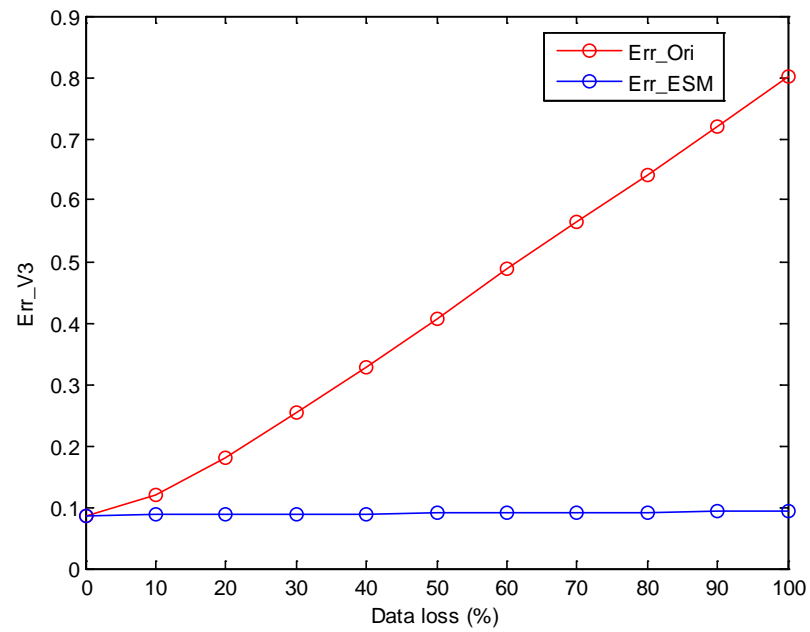


Figure 5.4. Estimation error with different probability of data loss.

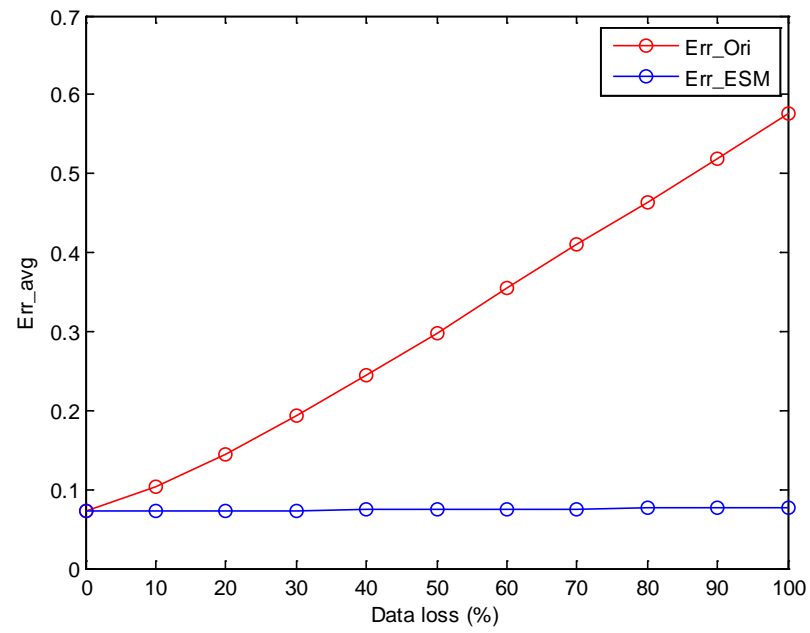


Figure 5.5. Average estimation error with different probability of data loss.

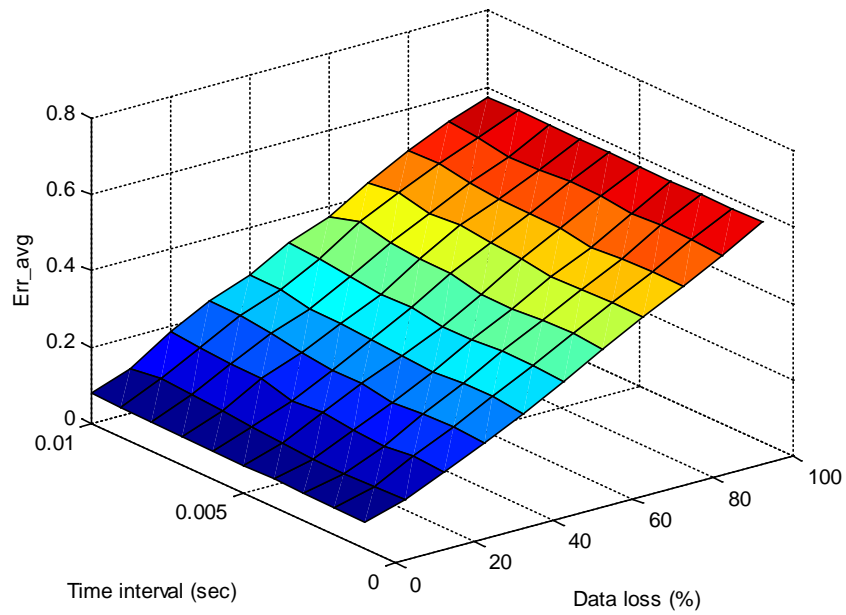


Figure 5.6. Estimation error of original Kalman filter with different time step and data loss.

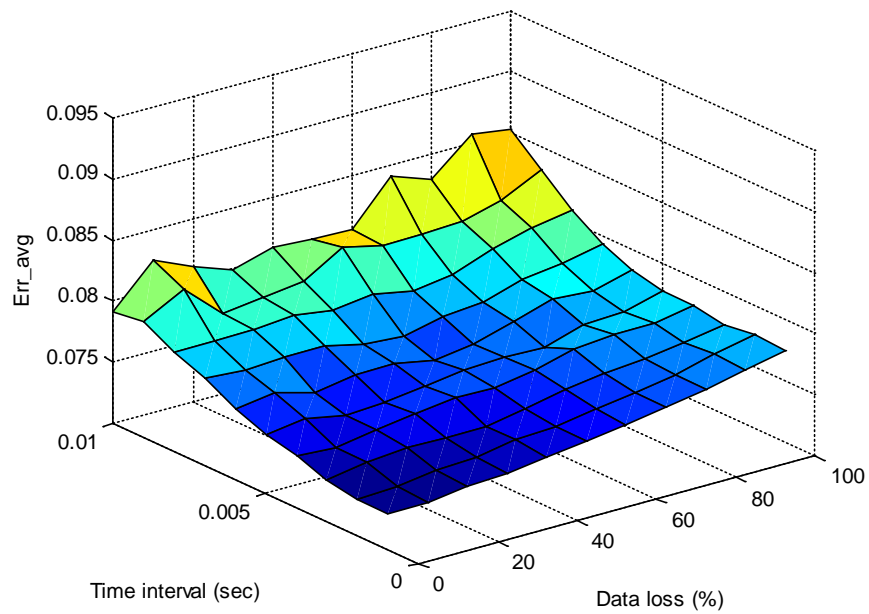


Figure 5.7. Estimation error of switching estimator with different time step and data loss.

With an understanding of the impact of data loss in one sensor on estimator performance, a number of simulations are conducted with data loss in all 3 sensors. The probability of data loss is increased from 0% to 50%. The results with a probability of 20% data loss in all sensors is illustrated in Figure 5.8. The estimation results for the original Kalman filter and the switching estimator with data loss in all sensors are shown in Figures 5.9-5.10. A 10% RMS noise is also added to all sensor channels to evaluate the robustness of the switching estimator to measurement noise. The results are shown in Figure 5.11. It can be seen that the error is slightly increased with 10 % RMS noise. A last test is conducted by adding the modeling error. A 50% error is added to the damping ratio, and a random error is added to the natural frequencies. The transfer functions of the system with modeling error (uncertainty) is shown in Figures 5.12-5.13. The red line in the figures is the transfer function of the nominal model. The result with a 50% error in damping ratio and a 2% error in the natural frequencies is given in Figure 5.14. With the same modeling error as before and 10% RMS measurement noise, the result is shown in Figure 5.15. Comparing this with Figure 5.14, the error is increased due to the measurement noise. The modeling error due to different uncertainty in frequencies is given in Figure 5.16. Apparently, the estimation error grows with increased modeling uncertainty.

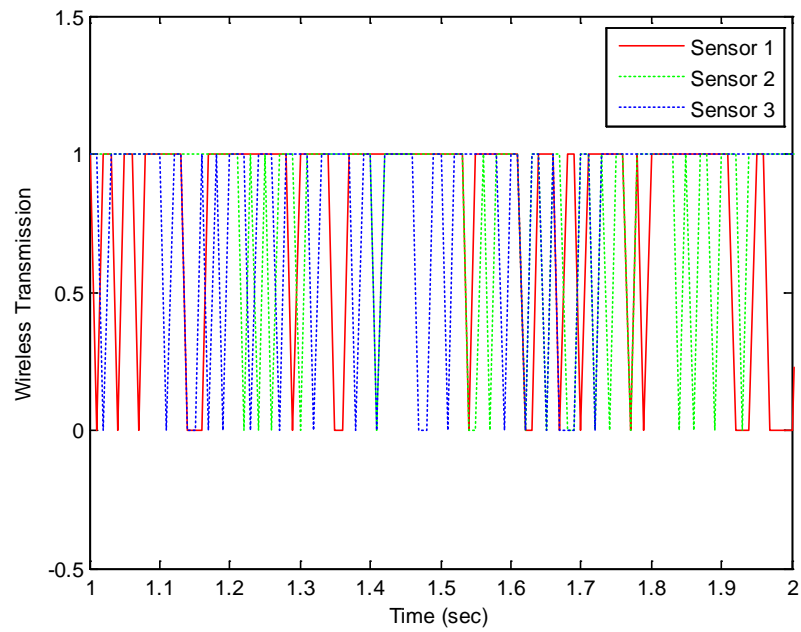


Figure 5.8. Typical realization of wireless transmission with 20% of data loss (1: data received, 0: data loss).

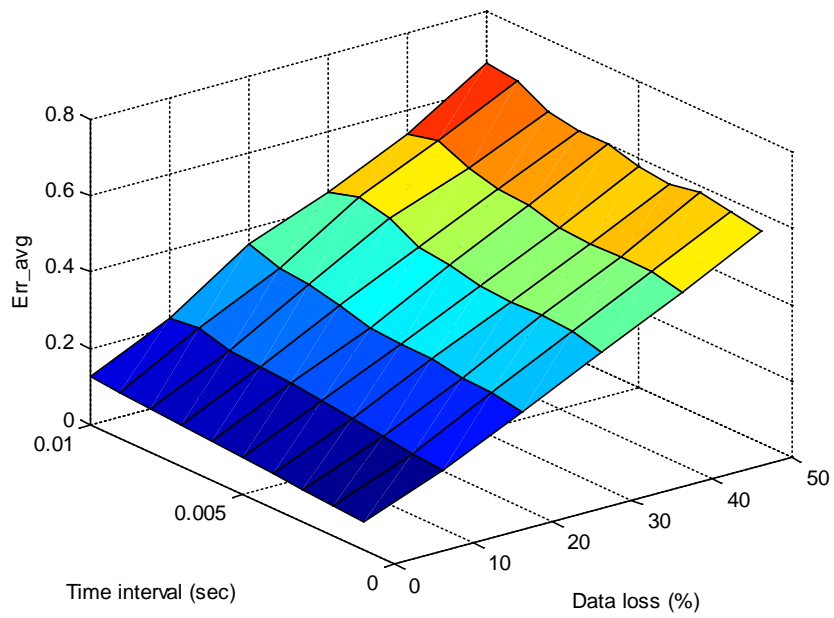


Figure 5.9. Estimation error of original Kalman filter with data loss in all sensors.

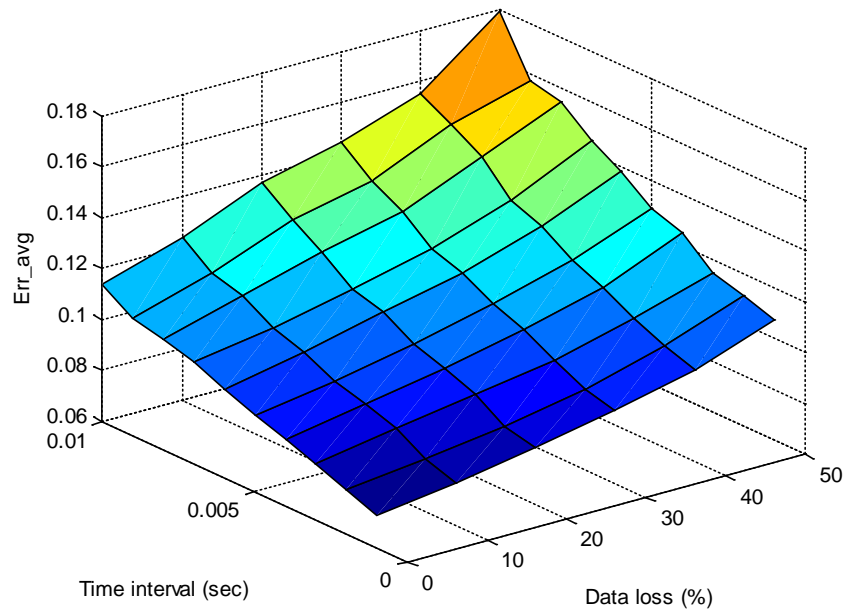


Figure 5.10. Estimation error of the switching estimator with data loss in all sensors.

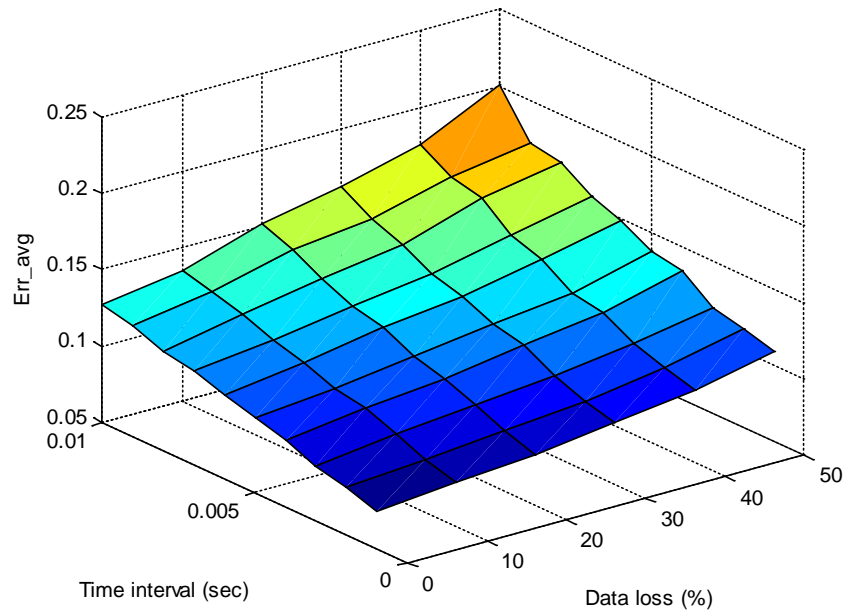


Figure 5.11. Estimation error of switching estimator with data loss in all sensors and 10% RMS measurement noises.

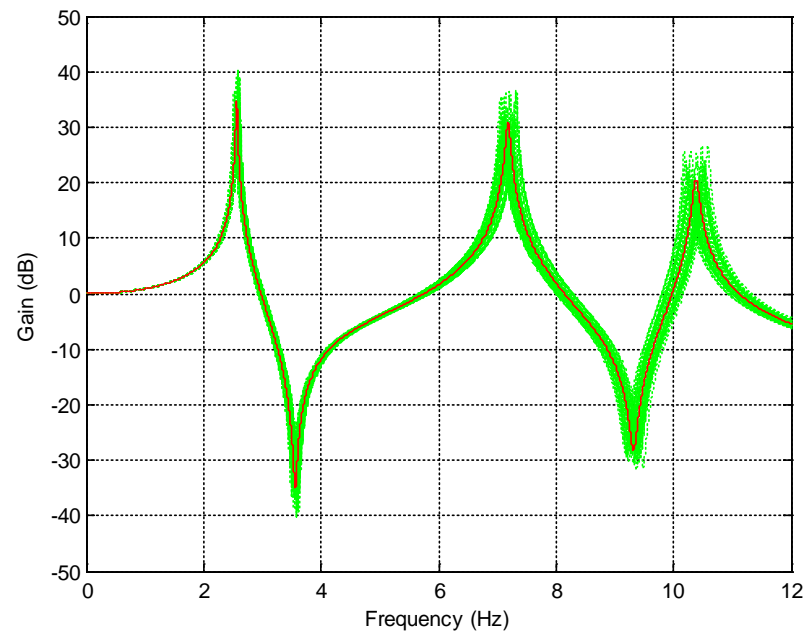


Figure 5.12. Transfer function of the system (magnitude) (red: nominal system, green: systems with modeling error).

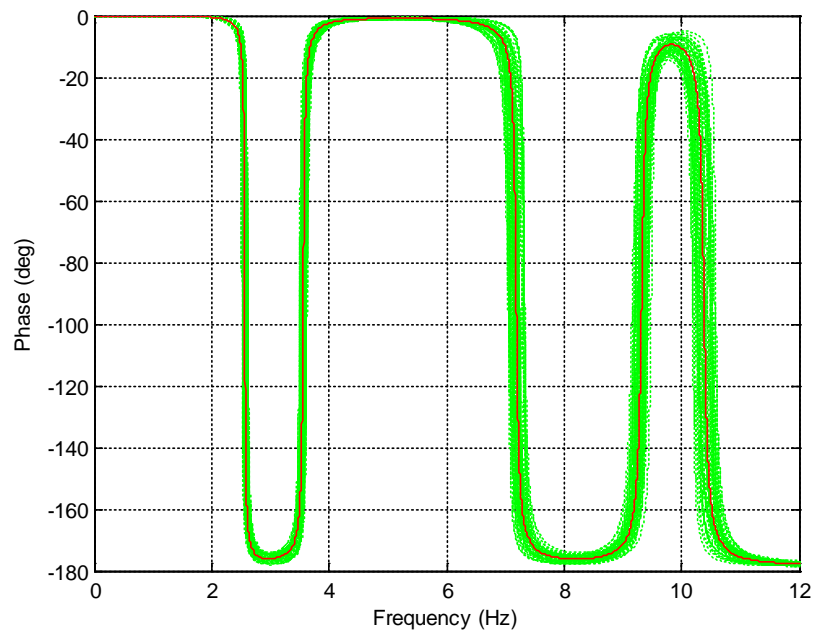


Figure 5.13. Transfer function of the system (phase) (red: nominal system, green: systems with modeling error).

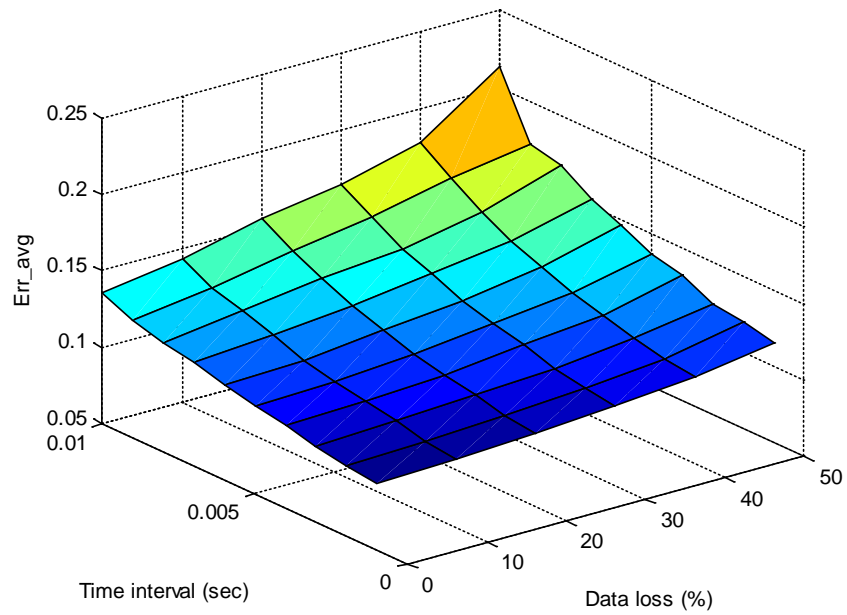


Figure 5.14. Estimation error of switching estimator with data loss in all sensors and 2% modeling error.

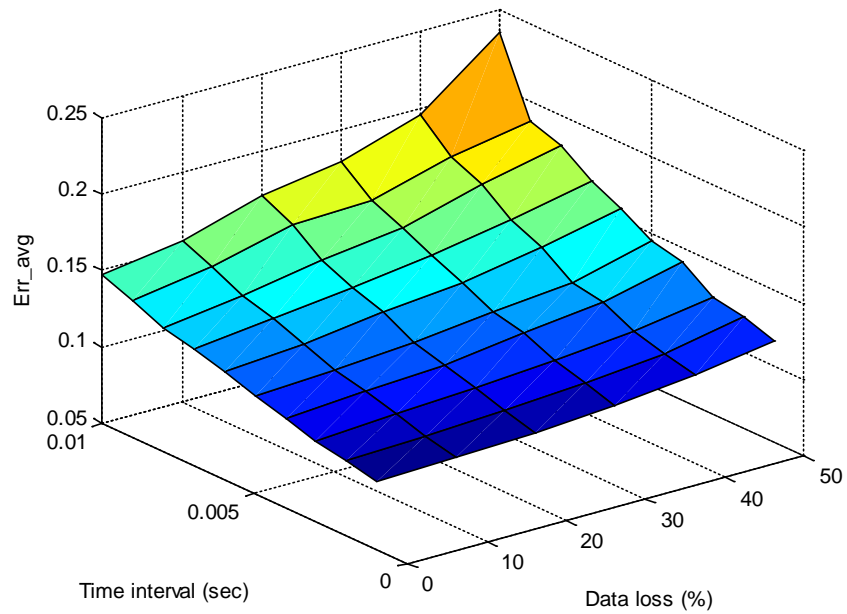


Figure 5.15. Estimation error of switching estimator with data loss in all sensors, 10% RMS measurement noises and 2% modeling error.

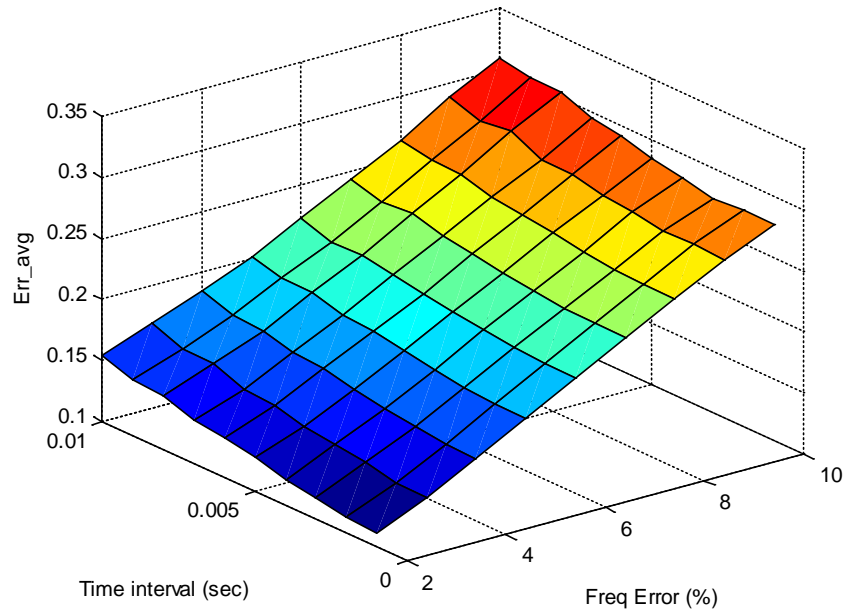


Figure 5.16. Estimation error of switching estimator with 20% data loss in all sensors and modeling error.

5.3 Numerical Investigation of the Estimator Switching Method with Transmission Delay

The 2nd case study of the estimator switching method considers the wireless control system with both transmission delay and data loss. In the 2nd case study, the OTD controller in chapter 4 is used to account for a one-step time delay. In the 1st case study, the states estimated with switching estimator are not used in the feedback control loop (see Figure 5.1). In this case study, the switching estimator is applied in the closed loop system as shown in Figure 5.17. The same switching gains as in the previous section are used. For the wireless network, a probability of 10% data loss for the sensor on the 2nd floor and a sensor failure on the 3rd floor are assumed. A BLWN input (0-15 Hz) as well as an El Centro earthquake, Hachinohe earthquake, and Gebze earthquake are adopted as the ground excitations.

The simulation results are shown in Figures 5.18-5.29 comparing the uncontrolled case, passive-off control case, passive-on control case, wired control case with LQG controller, and wireless control case without estimator switching and with estimator switching. It can be seen from these results that a wireless control system which employs estimator switching outperforms the case without estimator switching under the impact of the data loss and sensor failure. The wireless control with estimator switching achieves similar performance as the wired control case in terms of the RMS acceleration reduction and RMS drift reduction.

The impact of the measurement noise and modeling errors on the estimation and control performance is also investigated. Measurement noise is included by adding uncorrelated 10% RMS white noise to all the measurements. Modeling error is introduced by adding 5% or 10% error to the natural frequencies of the nominal 3-story building model and 50% error to the damping ratios of the model for the estimator design. To examine these factors under various random realizations, fifty runs are performed for the wireless control cases with and without estimator switching. The evaluation criteria in section 4.2 are adopted here to evaluate the control performance. The average evaluation results across the fifty realizations are provided in the Table 5.2. From the results, the control performance degrades due to the measurement noise and modeling error. However, the performance of the wireless control with estimator switching still surpasses the passive control cases and is shown to be effective in reducing the acceleration and inter story drift under various ground excitations.

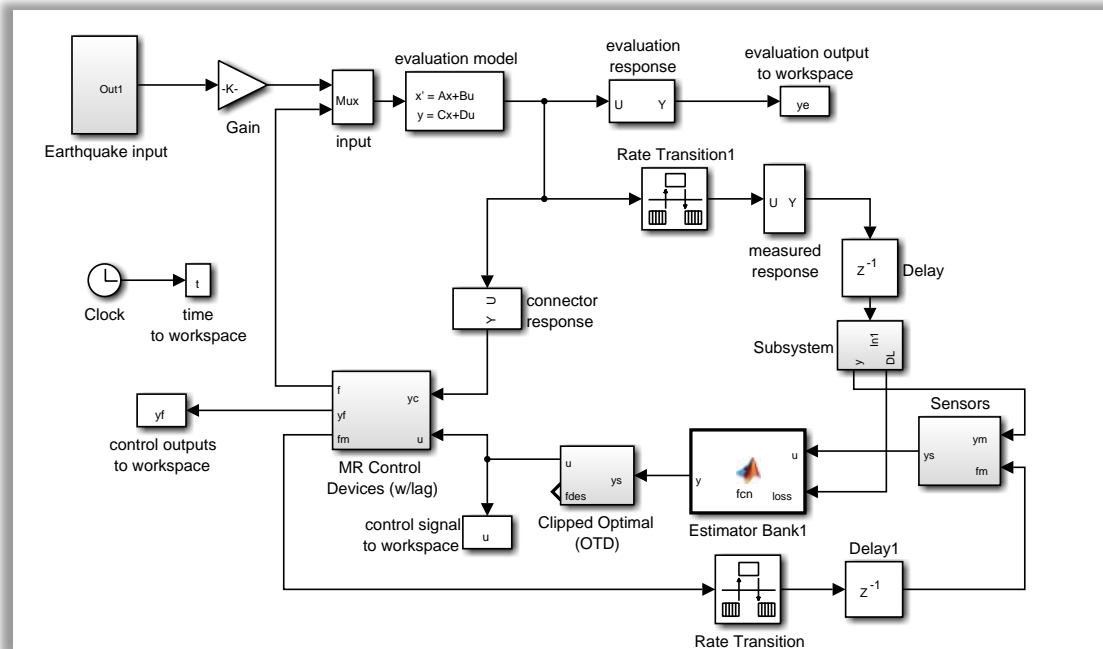


Figure 5.17. Simulink diagram for the 2nd case study.

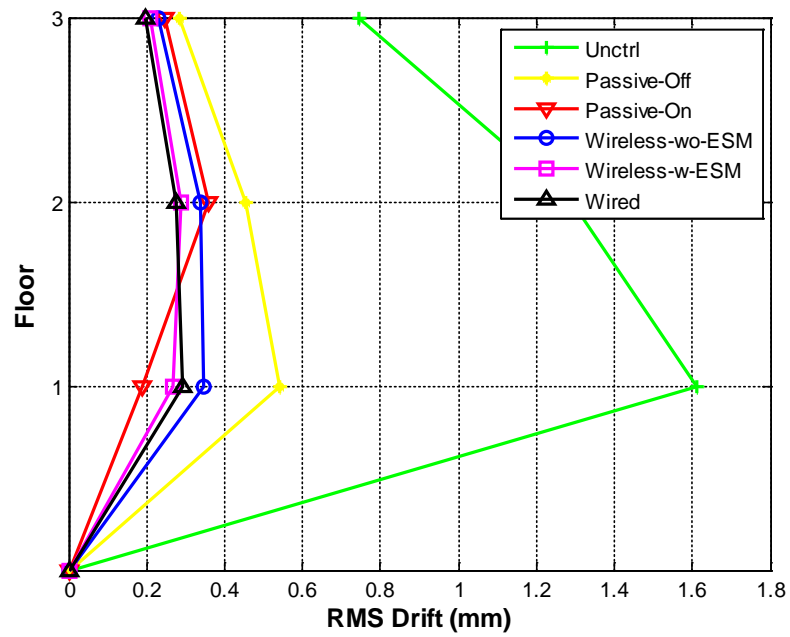


Figure 5.18. Comparison of RMS drift response under BLWN excitation.

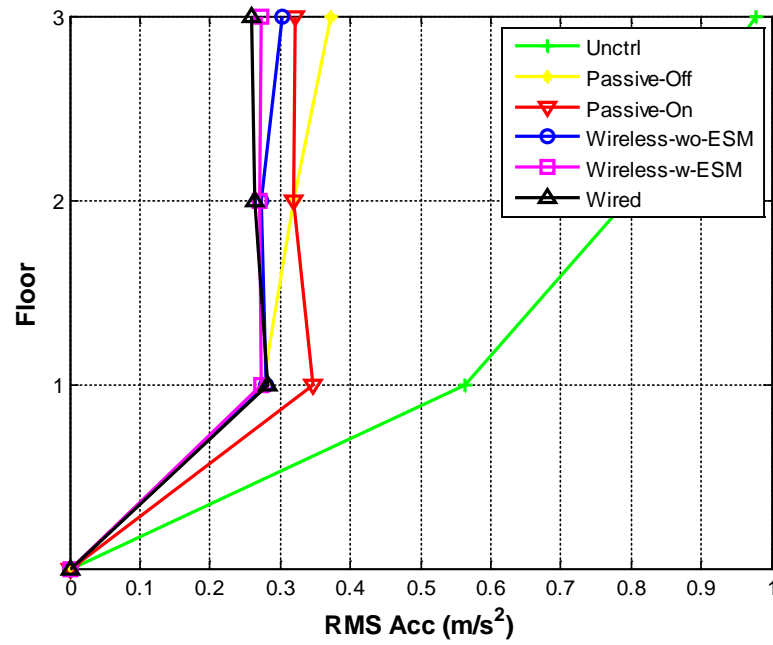


Figure 5.19. Comparison of RMS acceleration response under BLWN excitation.

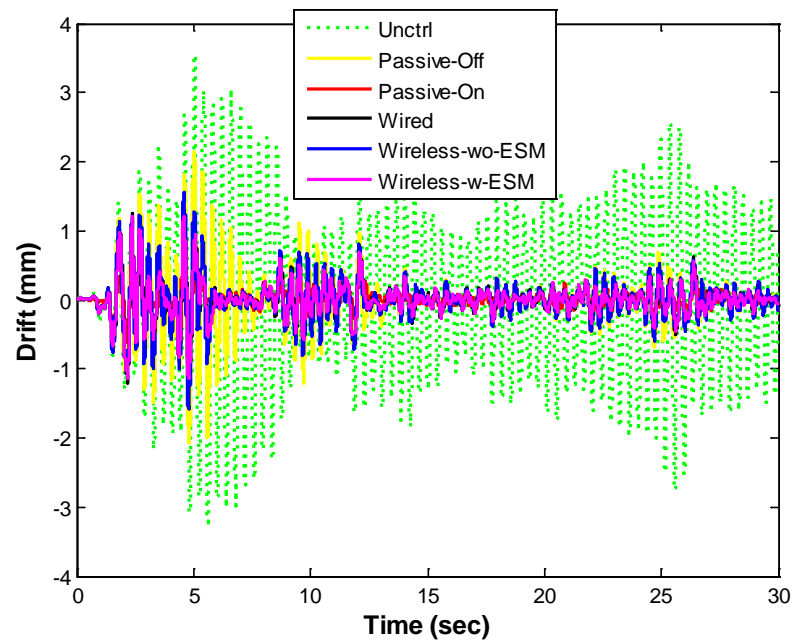


Figure 5.20. Comparison of 1st story drift response under El Centro earthquake.

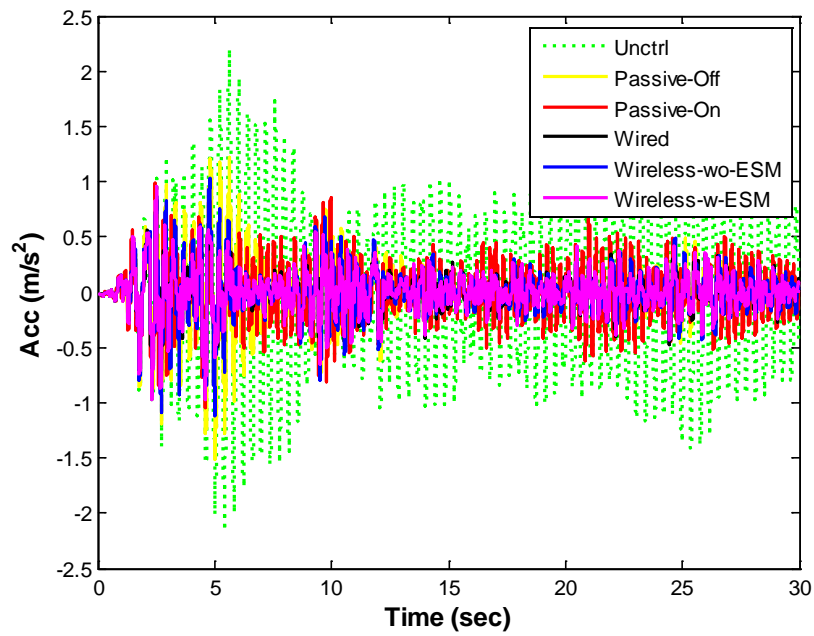


Figure 5.21. Comparison of 3rd story acceleration response under El Centro earthquake.

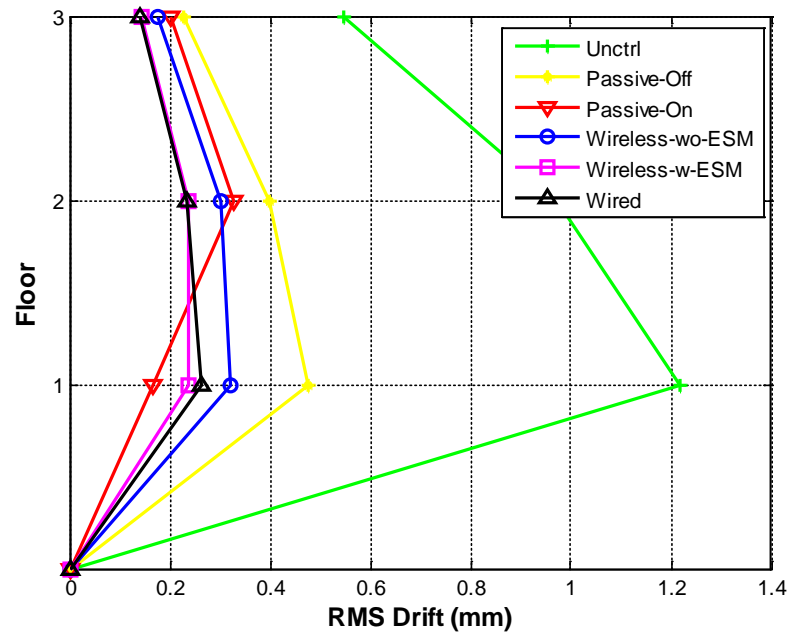


Figure 5.22. Comparison of RMS drift response under El Centro earthquake.

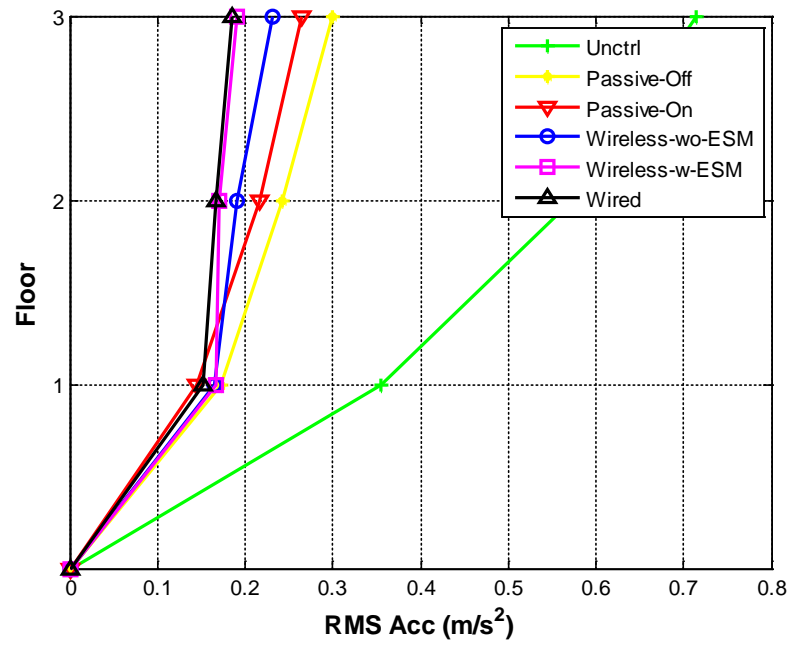


Figure 5.23. Comparison of RMS acceleration response under El Centro earthquake.

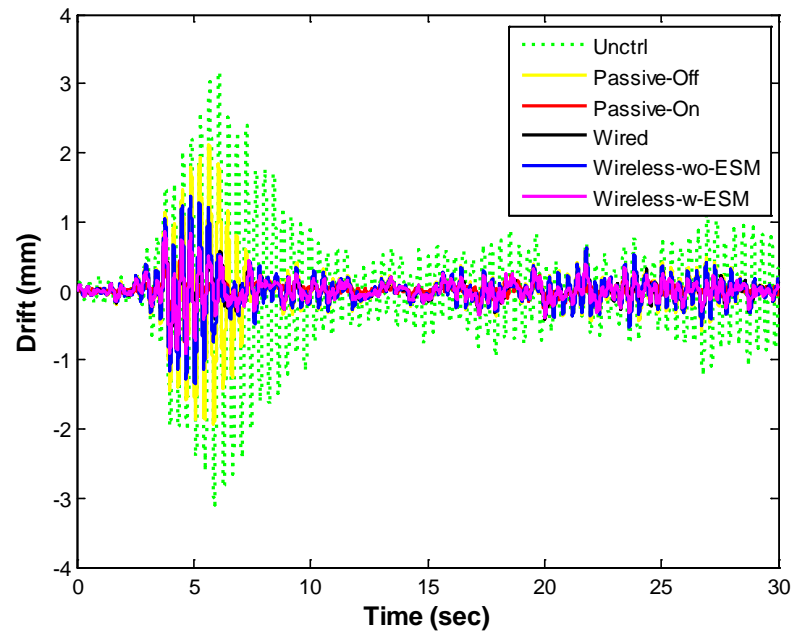


Figure 5.24. Comparison of 1st story drift response under Hachinohe earthquake.

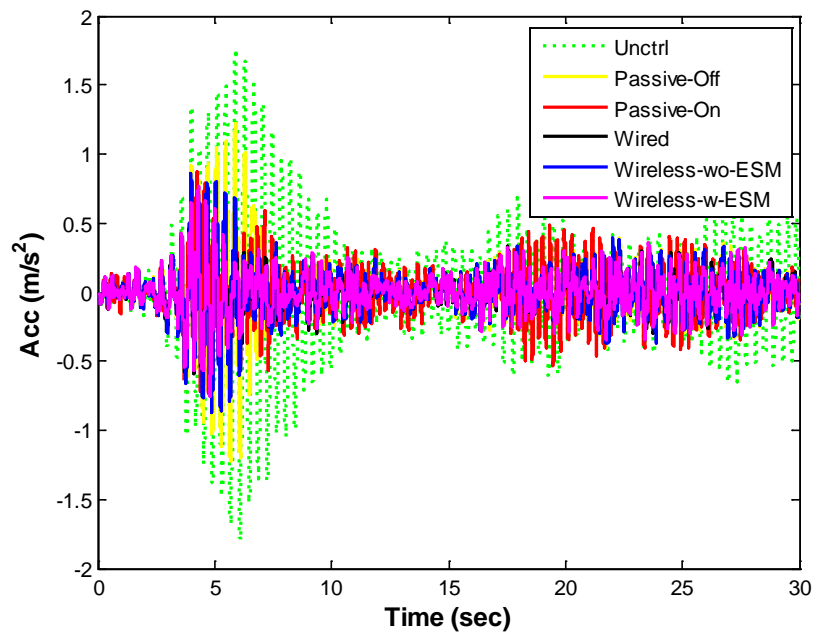


Figure 5.25. Comparison of 3rd story acceleration response under Hachinohe earthquake.

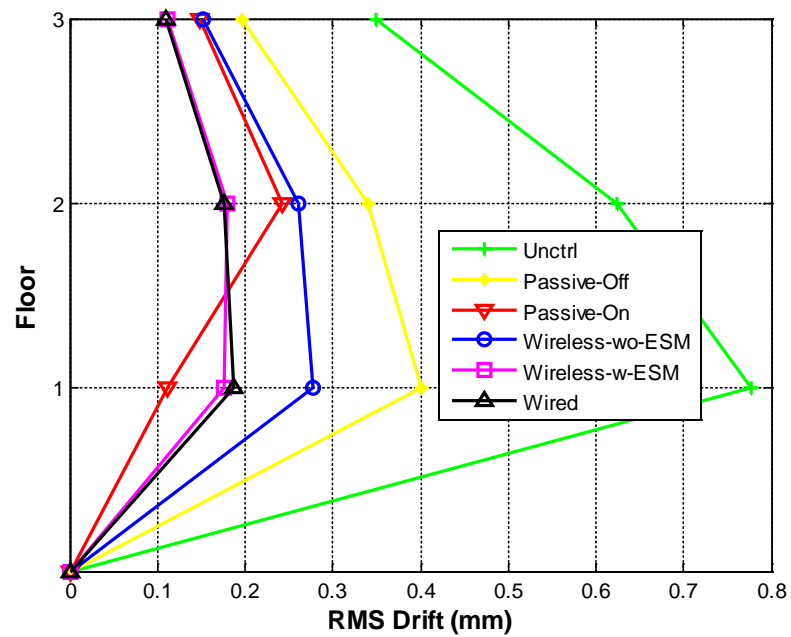


Figure 5.26. Comparison of RMS drift response under Hachinohe earthquake.

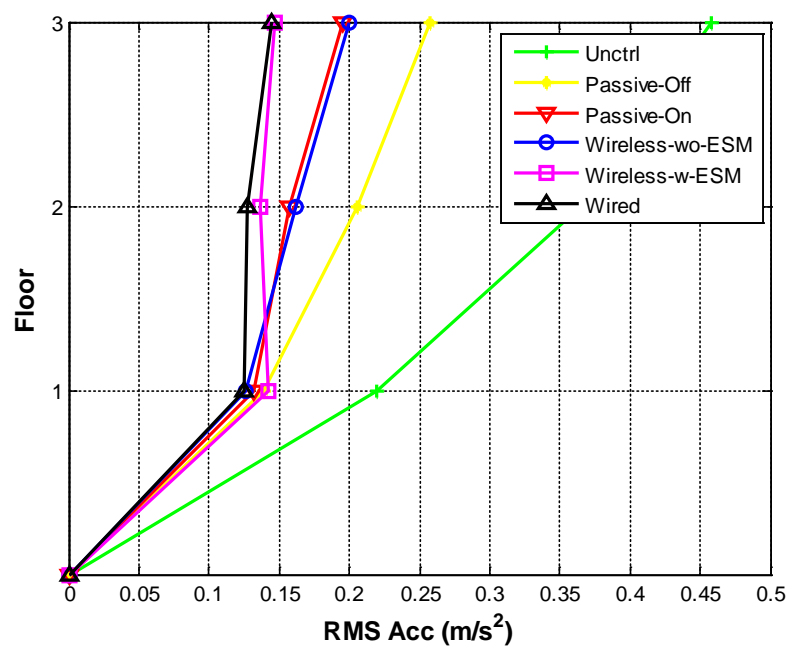


Figure 5.27. Comparison of RMS acceleration response under Hachinohe earthquake.

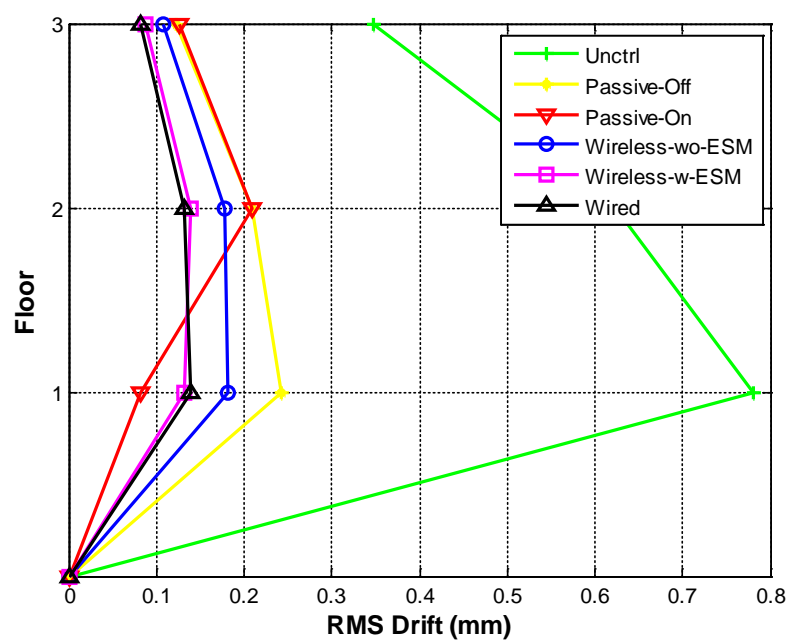


Figure 5.28. Comparison of RMS drift response under Gebze earthquake.

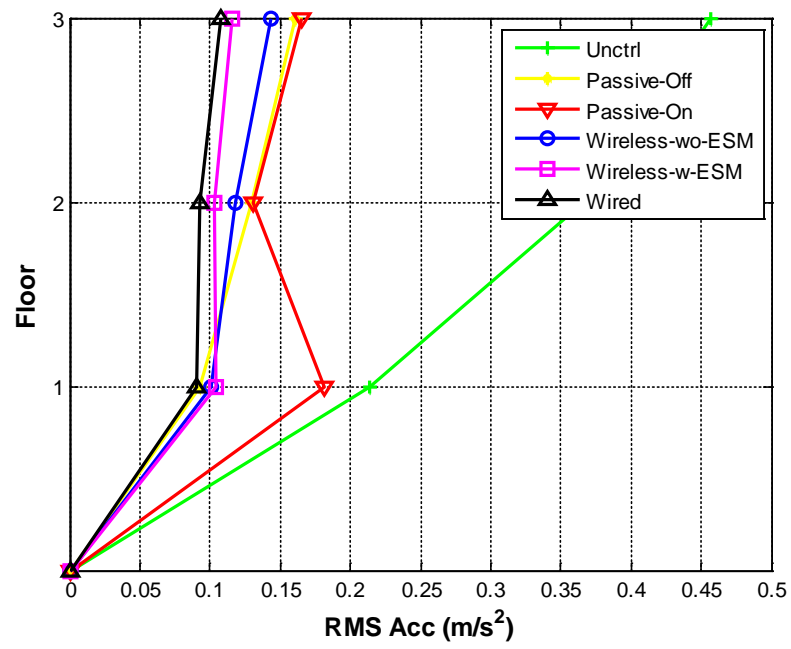


Figure 5.29. Comparison of RMS acceleration response under Gebze earthquake.

Table 5.2. Simulation results.

Excitation	Control	Noise/Error*	J_1 (%)	J_2 (%)	J_3 (%)	J_4 (%)
BLWN	P-off	-	-	-	33.5	38.0
	P-on		-	-	22.3	35.5
	Wired		-	-	17.4	26.3
	WL-wo-ES		-	-	21.8	34.7
	WL-w-ES		-	-	17.9	28.3
		10% Noise	-	-	18.0	28.8
		5% Error	-	-	18.0	29.4
		10% Error	-	-	18.6	32.1
El Centro	P-off	-	60.3	68.7	39.0	41.9
	P-on		29.7	50.9	26.8	37.1
	Wired		36.8	43.2	21.6	25.9
	WL-wo-ES		43.2	53.6	26.3	32.3
	WL-w-ES		34.1	43.7	19.5	26.4
		10% Noise	34.5	44.4	19.6	26.6
		5% Error	34.7	45.1	20.4	26.8
		10% Error	37.3	47.8	21.0	27.0
Hachinohe	P-off	-	66.3	68.3	51.6	56.2
	P-on		32.7	53.4	31.2	42.6
	Wired		30.6	37.6	24.0	31.5
	WL-wo-ES		43.7	47.9	35.8	44.4
	WL-w-ES		26.4	43.4	22.9	31.5
		10% Noise	26.7	45.3	23.3	32.8
		5% Error	29.4	46.9	23.7	33.0
		10% Error	32.5	49.6	24.2	39.2
Gebze	P-off	-	53.0	63.5	31.2	35.1
	P-on		39.1	44.8	26.8	39.7
	Wired		33.1	39.1	17.8	23.7
	WL-wo-ES		37.2	51.0	23.3	30.8
	WL-w-ES		34.4	42.0	17.7	25.1
		10% Noise	35.9	48.9	17.9	25.4
		5% Error	34.0	45.4	17.9	25.3
		10% Error	34.9	47.8	18.2	26.9

*Noise stands for RMS measurement noise; error denotes the modeling error.

5.4 Summary

In this chapter, a suboptimal Kalman filter based estimator switching method is proposed to deal with the realistic issue of data loss or sensor failure in the wireless control system. The switching gains are pre-calculated to enable real-time implementation and knowledge of probability of data loss is not required to derive the estimator gains. The only required knowledge is to check for data loss at each step to inform the switching of the estimator gains. One way to obtain estimator switching gains is discussed. The performance of this method is studied using a numerical model of a 3-story shear building model. In the 1st case, the switching estimator is compared with the original Kalman filter. In the presence of both data loss and sensor failure, the switching estimator surpasses the performance of the original Kalman filter. The switching estimator is also shown to be robust to certain levels of measurement noise and modeling error. In the 2nd case, the switching estimator is incorporated to work with the OTD controller in the codesigned wireless control system. With the specified data loss and sensor failure, the codesigned control system outperforms the original system without estimator switching. The codesigned control system is also shown to be effective in the presence of measurement noise and modeling errors. The feasibility of estimator switching method is verified through the two case studies.

CHAPTER 6. FAULT TOLERANCE IN WIRELESS CONTROL SYSTEM

In the previous researchers' work, wireless structural control systems are mostly studied with numerical simulation or shake table tests using small-scale lab structures. In this study, the wireless structural control is investigated using real-time hybrid simulation (RTHS). With RTHS, wireless structural control can be studied without the need for shake table tests and while offering a more realistic environment than numerical simulation. Here, fault tolerance is examined with real-time hybrid simulation (RTHS) to consider the impacts and potential solutions for sensor data loss and sensor failure cases in the wireless control system. In addition, the performance of the codesigned wireless control system that has an integrated switching estimator is evaluated with RTHS.

6.1 Fault Tolerance Study with RTHS

Fault tolerance generally falls into two categories: passive fault tolerance and active fault tolerance (Patton, 1997; Battaini & Dyke, 1998; Chihaiia, 2010; Patton, et al., 2007; Larbah & Patton, 2010; Yang & Chen, 2008). In passive fault tolerant system, the system is robust to a certain extent of fault, e.g. modeling uncertainty, measurement noise, sensor failure, etc. With that level of fault, the system is still able to operate while meeting all stability and performance requirements. In active fault tolerant system, the system is reconfigurable

which means it can have supervisory controllers to detect and isolate faulty devices, redundant sensors and actuators in the system, and adjustable control loops for faulty conditions. Here, passive fault tolerance of the wireless control system is studied with faulty conditions including sensor data loss and sensor failure.

6.1.1 RTHS Implementation

RTHS was introduced in dynamic test as an efficient alternative to traditional shake table test (Nakashima, et al., 1992; Mosqueda, et al., 2007; Christenson, et al., 2008). In RTHS, the entire system to be evaluated is divided into an experimental substructure and a numerical substructure. The relatively well-understood components are established in numerical substructure, while the parts which are not well understood are tested experimentally. Coupling between the two substructures is achieved by enforcing equilibrium and compatibility at the interface (Chen, et al., 2012). To avoid possible safety concerns related to sensor failure, control failure or physical limitations (i.e. size of the shake table and displacement limit), RTHS is used to perform this wireless structural control study.

The RTHS configuration is provided in Figure 6.1. A large-scale, 3-story steel frame with wireless sensors and controller are included in the numerical substructure, and a semi-active control device-MR damper is included in the experimental substructure. Interaction between the numerical and experimental substructures is enforced by imposing a displacement on the MR damper with a hydraulic actuator and measuring force feedback.

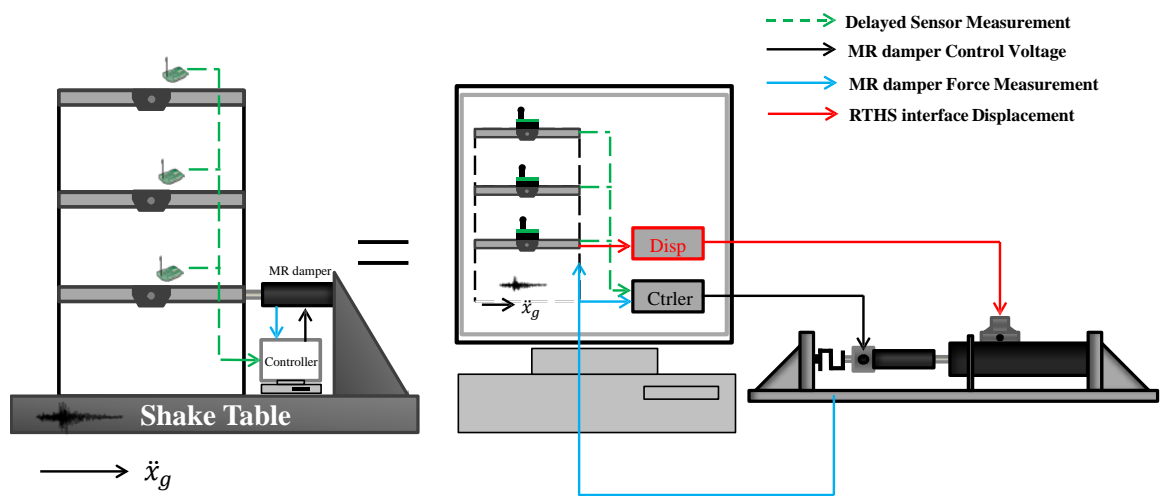


Figure 6.1. RTHS configuration for wireless control study.

The step by step procedure for the RTHS implementation is given as follows (where k indicates the k^{th} time step, % indicates the comments):

Table 6.1. RTHS implementation procedure.

<p>While ($k\Delta t \leq T_f$) % T_f is the simulation time length</p> <p> If ($k < l$) % wireless sensor data is not available</p> <p> 1.1 Generate displacement command x_k calculated from time step $k-1$ and send to the actuator; Measure damper force F_{k+1}^E;</p> <p> 1.2 Calculate numerical response (x_{k+1}, \dot{x}_{k+1}) using the integration scheme given earthquake input $\ddot{x}_{g,k+1}$ and control force F_{k+1}^E;</p> <p> 1.3 Let damper voltage $V_{k+1} = 0$, Send the voltage command to the MR damper;</p> <p> 1.4 Let $k = k+1$;</p> <p> Elseif ($k \geq l$) % delayed sensor data is available</p> <p> 2.1 Same as step 1.1;</p> <p> 2.2 Same as step 1.2;</p> <p> 2.3 Calculate desired control force u_{k+1} with delayed measurements \ddot{x}_{k-l}; Generate the damper voltage V_{k+1} based on F_{k+1}^E and u_{k+1};</p> <p> 2.4 Let $k = k+1$;</p> <p> End</p> <p>End</p>

The implementation is also presented in schematic drawing in Figure 6.2. The structural model, wireless network model and control design, actuator tracking control are explained in detail in the following sections.

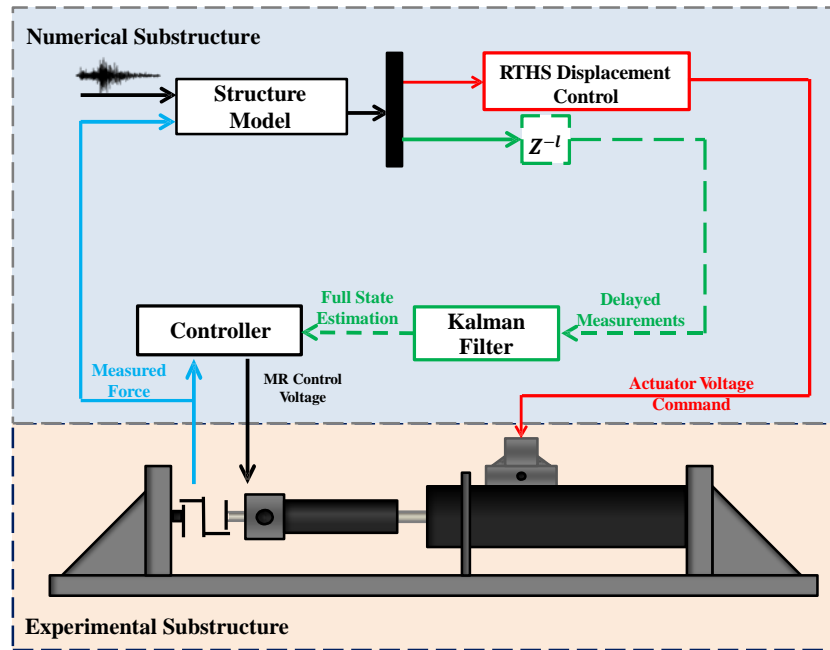


Figure 6.2. Schematic drawing of RTHS implementation.

6.1.2 Structural Model

The numerical model used in this study is based on a large-scale, three-story frame located at Harbin Institute of Technology, School of Civil Engineering (see Figure 6.3). The structure's floor plan is 1.84 m by 2.04 m with a story height of 1.2m. The columns, beams and girders are made of structural steel with an elastic modulus of 206 GPa and a shear modulus of 78 GPa. The structure is lightly damped and the identified modes of the structure are at 2.89 Hz, 8.07 and 12.29 Hz, respectively. The experimentally identified model of the structure has good representation of the structure up to 15 Hz as

shown in Figure 6.4. The mass, stiffness and damping matrices of the structure are obtained in Ozdagli, et al., (2012):

$$M = \begin{bmatrix} 419.5 & 4.4 & 2.2 \\ 4.4 & 364.5 & 10.0 \\ 2.2 & 10.0 & 319.4 \end{bmatrix} kg$$

$$C = \begin{bmatrix} 88.1 & -4.1 & -1.8 \\ -4.1 & 74.3 & -4.5 \\ -1.8 & -4.5 & 61.2 \end{bmatrix} N/(m/s)$$

$$K = \begin{bmatrix} 143.3 & -72.1 & 3.7 \\ -72.1 & 130.6 & -60.1 \\ 3.7 & -60.1 & 54.7 \end{bmatrix} \times 10^4 N/m$$



Figure 6.3. Three-story frame structure.

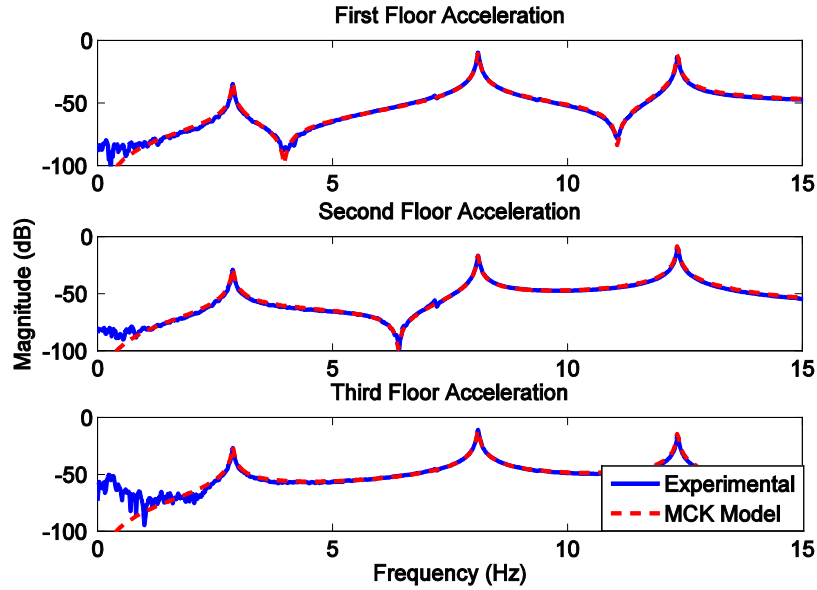


Figure 6.4. Comparison of experimental and identified transfer functions.

6.1.3 Wireless Sensor Network Model and Control Design

There are 3 wireless accelerometer nodes in the wireless sensor network. TDMA network is assumed for wireless transmission with a 10 msec TDMA time slot. The data aggregation strategy in section 2.2 is used to aggregate 3 samples (sampling step 10 msec) in each package. The TDMA network transmits data as follows, $t_i \rightarrow s_{[1, i-2 \dots i]}$ (which means sensor 1 at time step i transmits data from step $i-2$ to step i), $t_{i+1} \rightarrow s_{[2, i-2 \dots i]}$, $t_{i+2} \rightarrow s_{[3, i-2 \dots i]}$. The control calculation at t_{i+3} uses delayed measurements at t_{i-2} . In this way, the TDMA network induced delay is transformed to a constant 6-step delayed system. A Kalman filter is used to estimate the delayed states, with the discrete-time Kalman gain

$$L = \begin{bmatrix} -0.051 & -0.043 & -0.027 \\ -0.060 & -0.095 & -0.090 \\ -0.054 & -0.108 & -0.161 \\ 2.332 & 3.115 & 3.134 \\ 1.492 & 3.180 & 3.644 \\ 1.382 & 2.549 & 4.004 \end{bmatrix} \times 10^{-3}$$

The OTD controller with $l = 6$ is adopted in the control design. The control time step is 10 msec. The calculated control gain is

$$G = [-2.707 \quad 3.464 \quad -0.191 \quad 0.027 \quad -0.016 \quad -0.072] \times 10^3$$

To control the damper force applied to the structure, the clipped-optimal strategy given in Equation (4.6) is used to compute the damper voltage based on the desired control force and measured damper force.

6.1.4 Actuator Tracking Control

RTHS implementation requires both guaranteed execution of each test cycle in a small time step and appropriate compensation for actuator dynamics. A robust integrated actuator control (RIAC) algorithm proposed by Ou, et al., (2014) is adopted to compensate the actuator dynamics. The tracking performance is verified with BLWN input (0-15Hz) and 3Hz sine wave, respectively. The setup of the experimental substructure is shown in Figure 6.5. The comparisons between the desired displacement and the measured displacement are provided in Figures 6.6-6.7. The results show good alignment between the two signals. As listed in Table 6.2, the actuator tracking RMS error is below 6% for both cases. The tracking error is calculated as

$$Error = \frac{\sqrt{\frac{1}{N} \sum_{i=1}^N (y_i - r_i)^2}}{\max(r_i)} \times 100\% \quad (6.1)$$

where y_i is the measured displacement, and r_i is the desired displacement, N is the number of samples.

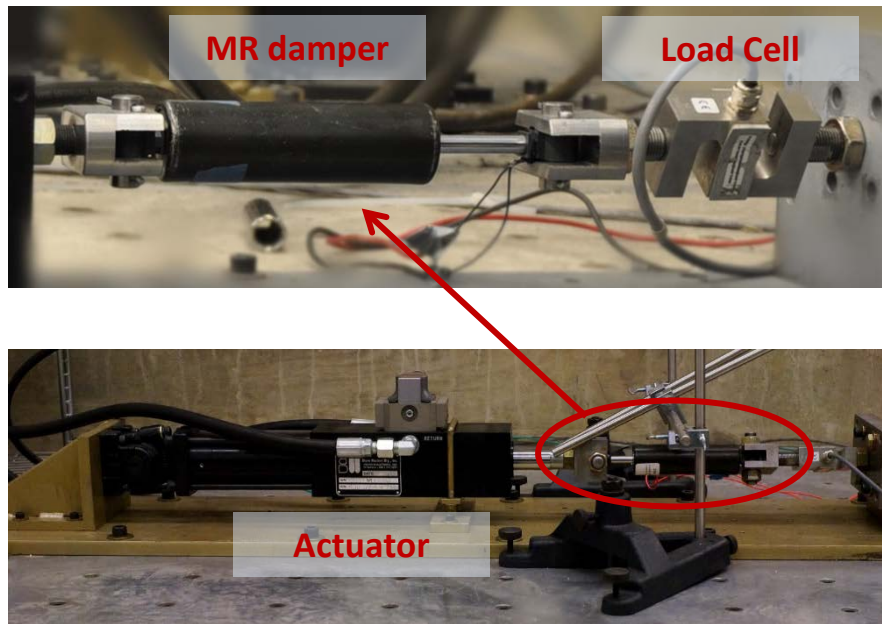


Figure 6.5. Experimental setup.

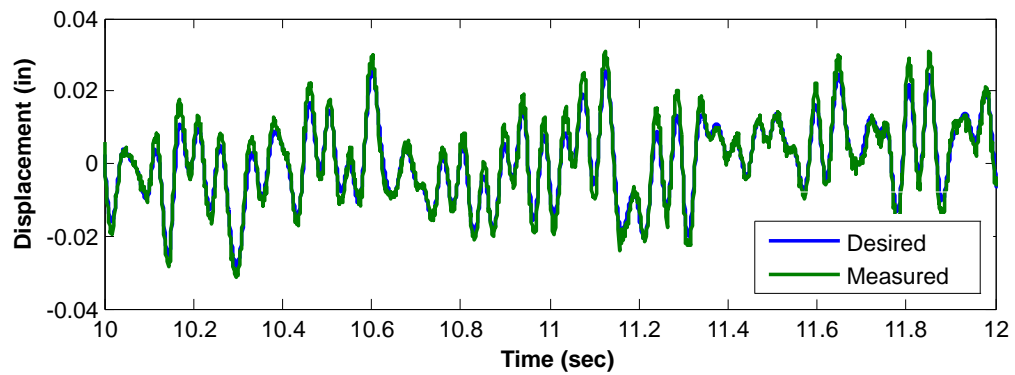


Figure 6.6. Comparison of desired displacement and measured displacement (BLWN) with RIAC controller.

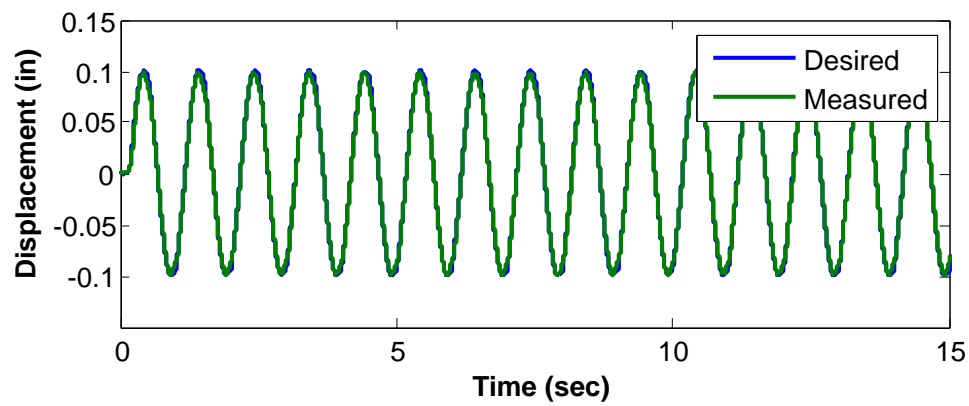


Figure 6.7. Comparison of desired displacement and measured displacement (Sine) With RIAC controller.

Table 6.2. Tracking performance.

	BLWN (0-15 Hz)	3 Hz Sinusoid
Tracking Error	5.92%	4.35%

6.1.5 Experimental Results of Fault Tolerance Study

To study the impact of data loss and sensor failure on the wireless control system performance, a probability of 10% data loss and 100% data loss (representing sensor failure) are considered in different cases. The cases considered are listed in Table 6.3. Based on a previous study (Sun, et al., 2015), it is reasonable to assume a 7%~10% data loss from each floor. Three historical earthquake records and a BLWN input are used as ground excitations for this study. They are E1: 1940 El Centro NS-peak ground acceleration (PGA): 0.35 g; E2: 1985 Mexico City-PGA: 0.14 g; E3: 1999 Turkey Gebze NS-PGA: 0.27 g; and E4: BLWN: 0-15Hz. Two excitation magnitudes of the three earthquake records are chosen, half-scale and full-scale.

Table 6.3. Data loss cases studied.

Data loss cases	Floor 1	Floor 2	Floor 3
<i>Case A</i>	10%	10%	10%
<i>Case B</i>	10%	10%	100%*
<i>Case C</i>	10%	100%	10%
<i>Case D</i>	100%	10%	10%
<i>Case E</i>	100%	10%	100%
<i>Case F</i>	100%	100%	10%
<i>Case G</i>	10%	100%	100%

*100% data loss represents sensor failure

RTHS results for the full-scale Mexico City and Gebze earthquakes are given in Figures 6.8-6.9. The evaluation results (using the evaluation criteria in section 4.2) for the eight cases with data loss and no data loss case are provided in Figures 6.10-6.14. For wireless control with semi-active control devices, the worst case with all sensors failure is equivalent to the passive-off case, and thus is not tested specifically. From the experimental results, with 10% data loss in all sensors, the control performance is not degraded much compared to the no data loss case. Comparing all nine cases, cases B, E, and G have worse performance than the other cases which indicate sensor measurements from the 3rd floor have the greatest impact on the control performance among all sensors. Case G has the worst performance among the two sensor failure scenario (cases B, E, and G), which indicates the first floor measurement has less impact. This finding is also supported by comparing case C and D (single sensor failure scenario). The complete list of evaluation results of all the cases are shown in Table 6.4. The relative importance of each sensor is evaluated which indicates that sensors located at higher floors have larger impact on the control performance for this control setup. This outcome may be taken account in sensor design for real applications, i.e. redundant devices may be provided for the sensors that are more critical.

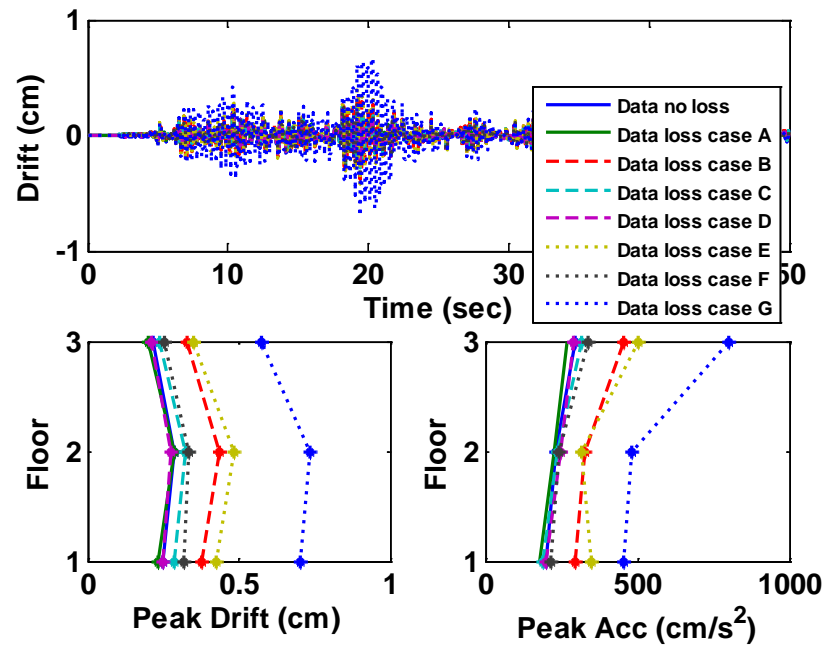


Figure 6.8. Structural response under Mexico City earthquake.

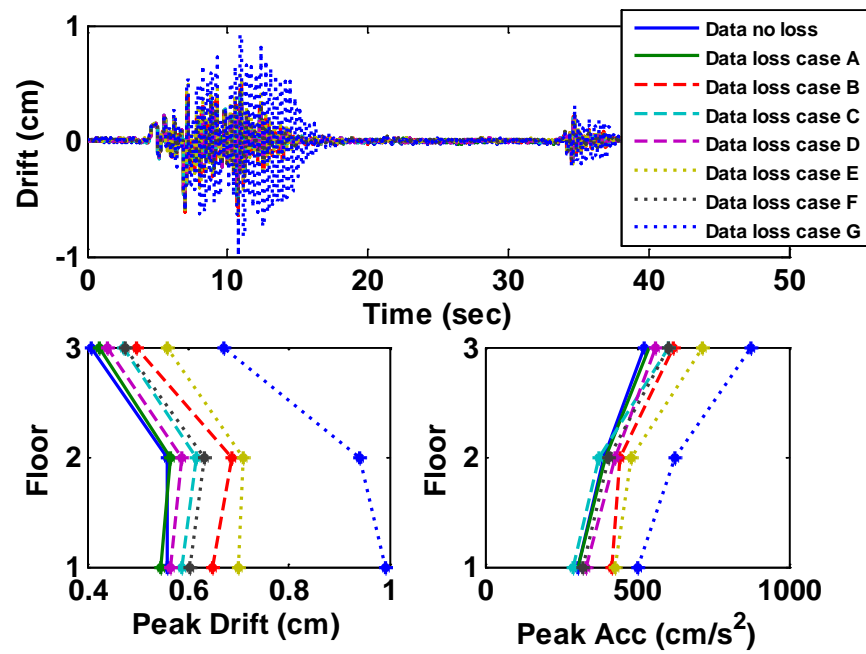
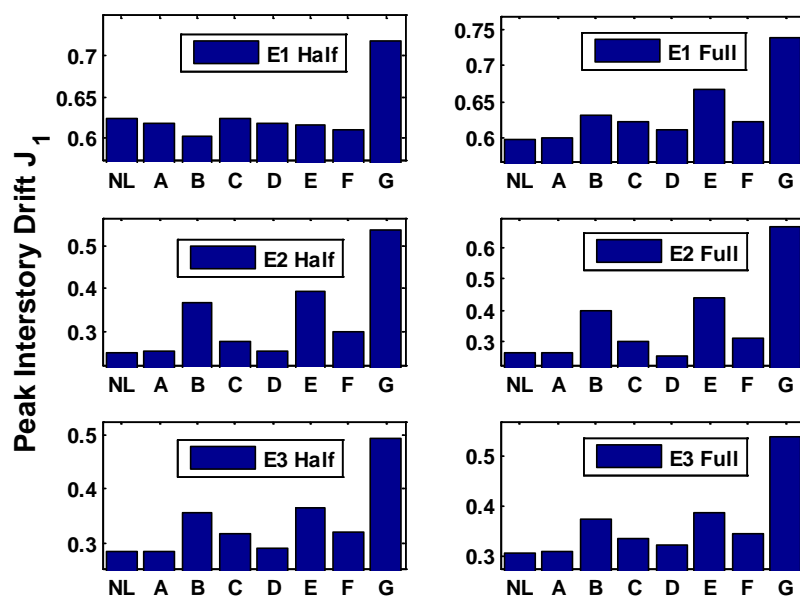
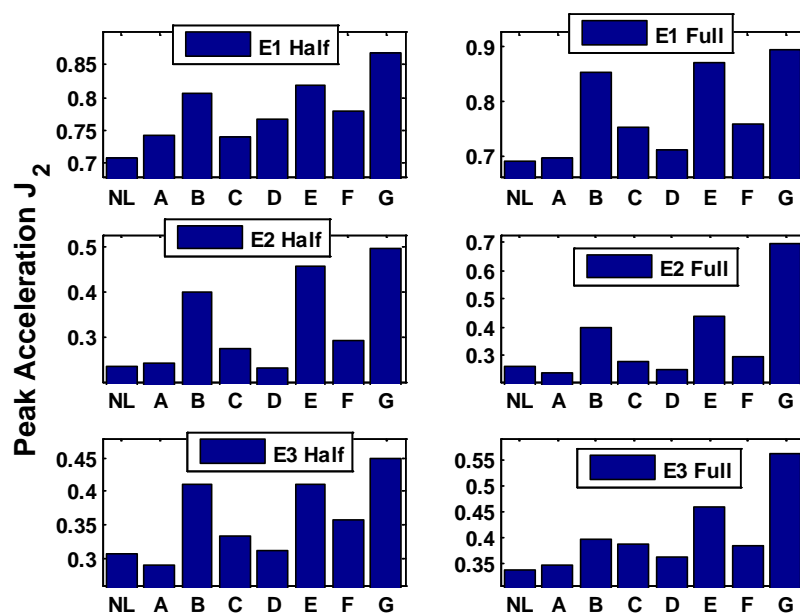


Figure 6.9. Structural response under Gebze earthquake.

Figure 6.10. Evaluation results for criterion J_1 .Figure 6.11. Evaluation results for criterion J_2 .

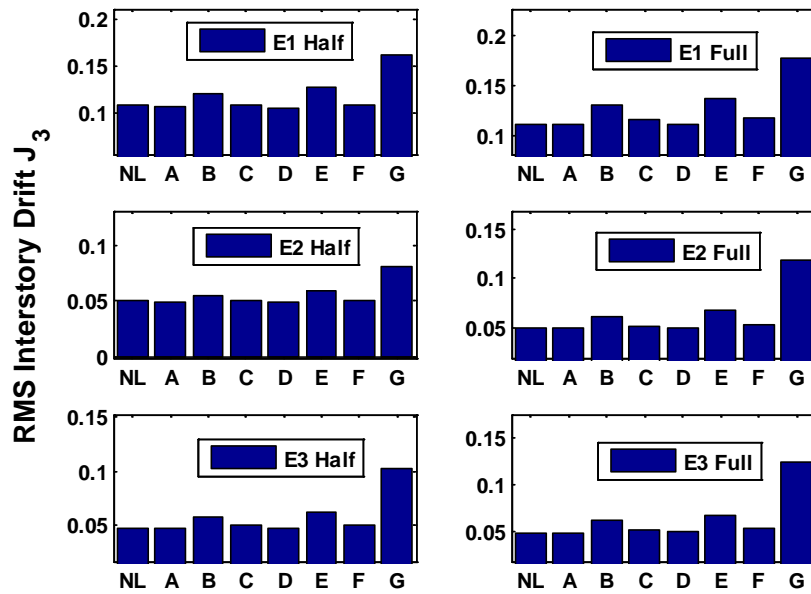


Figure 6.12. Evaluation results for criterion J3.

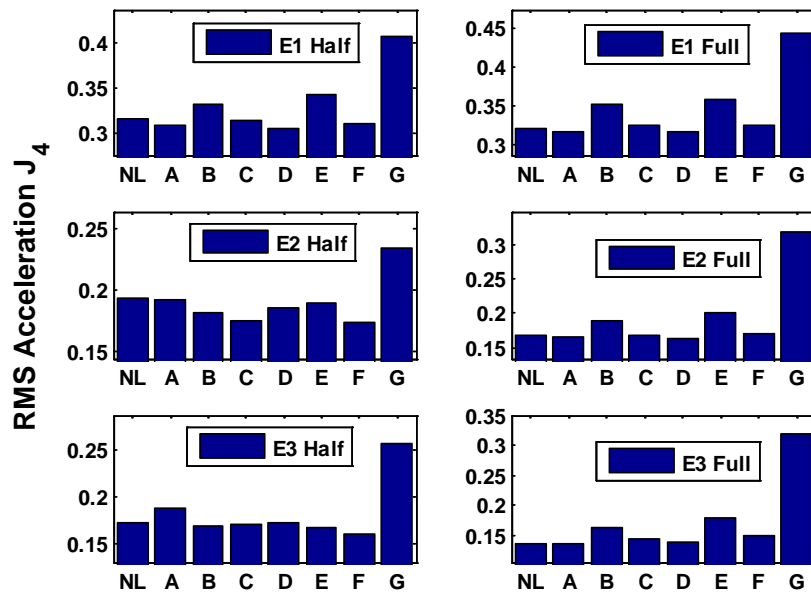


Figure 6.13. Evaluation results for criterion J4.

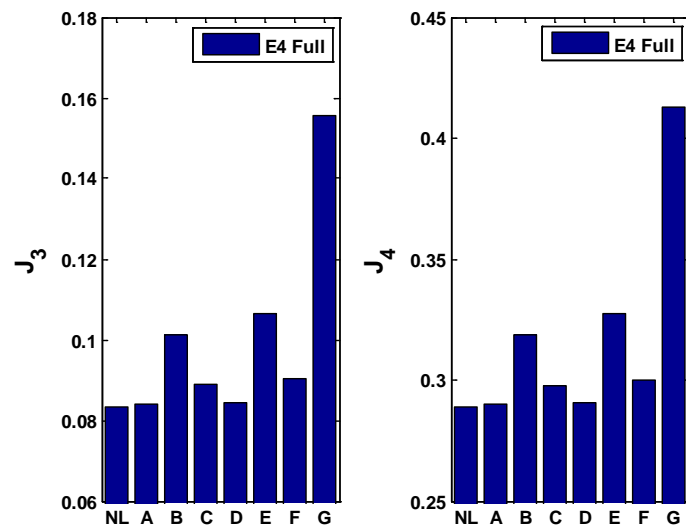


Figure 6.14. Evaluation results for BLWN excitation.

Table 6.4. Control performance of different cases.

E1-Half	$J_1(\%)$	$J_2(\%)$	$J_3(\%)$	$J_4(\%)$	E1-Full	$J_1(\%)$	$J_2(\%)$	$J_3(\%)$	$J_4(\%)$
No loss	62.4	70.7	10.8	31.5		59.7	69.1	11.3	32.0
Case A	61.9	74.4	10.7	30.9		60.0	69.9	11.2	31.6
Case B	60.3	80.7	12.1	33.3		63.1	85.4	13.2	35.1
Case C	62.5	74.1	11.0	31.4		62.1	75.5	11.7	32.5
Case D	61.9	76.7	10.7	30.5		61.1	71.3	11.2	31.6
Case E	61.6	81.9	12.8	34.3		66.6	87.2	13.7	35.8
Case F	61.0	77.9	11.0	31.0		62.1	76.0	11.9	32.6
Case G	71.7	86.9	16.1	40.7		73.9	89.6	17.8	44.3
E2-Half					E2-Full				
No loss	25.2	23.8	5.0	19.3		25.9	25.8	5.0	16.9
Case A	25.4	24.2	4.9	19.2		25.9	23.6	4.9	16.4
Case B	36.9	40.0	5.5	18.1		39.6	39.5	6.1	18.9
Case C	27.8	27.6	5.0	17.4		29.6	27.6	5.2	16.9
Case D	25.4	23.2	4.9	18.5		25.2	25.0	4.9	16.4
Case E	39.6	45.5	5.9	18.9		44.0	43.7	6.7	20.1
Case F	29.9	29.4	5.1	17.4		30.6	29.3	5.3	17.1
Case G	53.6	49.6	8.1	23.3		66.9	69.6	11.9	31.8
E3-Half					E3-Full				
No loss	28.5	30.8	4.7	17.3		30.5	33.8	4.9	13.6
Case A	28.3	29.0	4.7	18.8		30.8	34.7	4.8	13.4
Case B	35.7	41.0	5.7	16.8		37.5	39.7	6.2	16.4
Case C	31.7	33.4	5.0	17.0		33.7	38.7	5.2	14.5
Case D	29.2	31.2	4.7	17.3		32.1	36.2	4.9	13.7
Case E	36.6	41.1	6.2	16.8		38.7	45.9	6.7	17.9
Case F	32.0	35.8	5.1	16.0		34.5	38.6	5.4	14.8
Case G	49.5	44.9	10.1	25.7		54.0	56.3	12.4	32.1
E4									
No loss			8.3	28.9					
Case A			8.4	29.0					
Case B			10.1	31.9					
Case C	NA	NA	8.9	29.8					
Case D			8.4	29.1					
Case E			10.7	32.8					
Case F			9.0	30.0					
Case G			15.5	41.3					

Analytical study is conducted to further understand the contributions of each sensor measurement to the control force. The control system with sensor measurements input

and control force output is shown in Figure 6.15 (the constant delay term is omitted here). The estimator and controller is converted to the continuous-time for this analysis. The transfer function matrices G in Equation (6.2) has 3 elements representing 3 separate transfer functions from each measurement input to the force output. The transfer functions obtained are shown in Figure 6.16. It can be seen that transfer function from sensor 3 has the largest amplitude, which means it has the most contribution to the control force, while sensor 1 has the least contribution. This analytical results matches the observations in the experimental study.

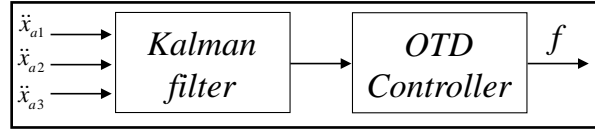


Figure 6.15. Control system representation with 3 sensor measurements.

$$G = [G_{f\ddot{x}_{a1}} \quad G_{f\ddot{x}_{a2}} \quad G_{f\ddot{x}_{a3}}] \quad (6.2)$$

where G is the transfer function matrices, $G_{f\ddot{x}_{ai}}$ is the transfer function from sensor input i to control force f .

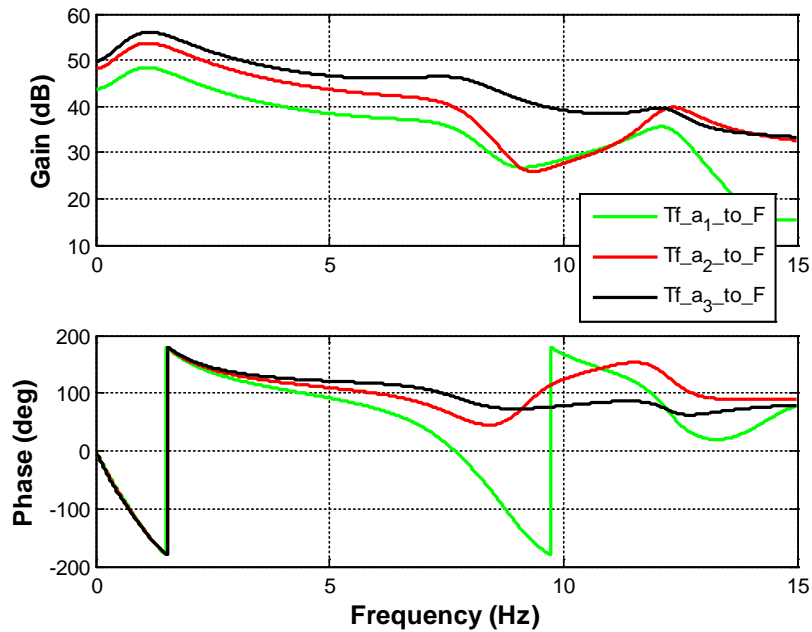


Figure 6.16. Evaluation results for BLWN excitation.

6.1.6 Sensitivity of RTHS Tests

The RTHS tests discussed in the previous section examine the impact of sensor data loss and sensor failure on the control performance. However, the timing of data loss may also affect the RTHS results, i.e. the data loss occurs close to peak ground acceleration may have larger impact. To better understand the RTHS results due to the random occurrence of the data loss, a sensitivity study is performed. Ten RTHS tests are conducted for each of the eight cases under three historical earthquakes (the total number of tests are $10 \times 8 \times 3 = 240$). The experimental results are shown in Figures 6.15-6.17. On each boxplot, the central mark is the median value, the edges of the box are the 25th and 75th percentiles, the whiskers extend to the most extreme data points not considered outliers and outliers are plotted individually. From the results, the peak responses have a larger variation than the RMS responses. The same observation is obtained from these sensitivity tests as in

the original tests. The sensor on the higher floor has more impact on the control performance in this setup.

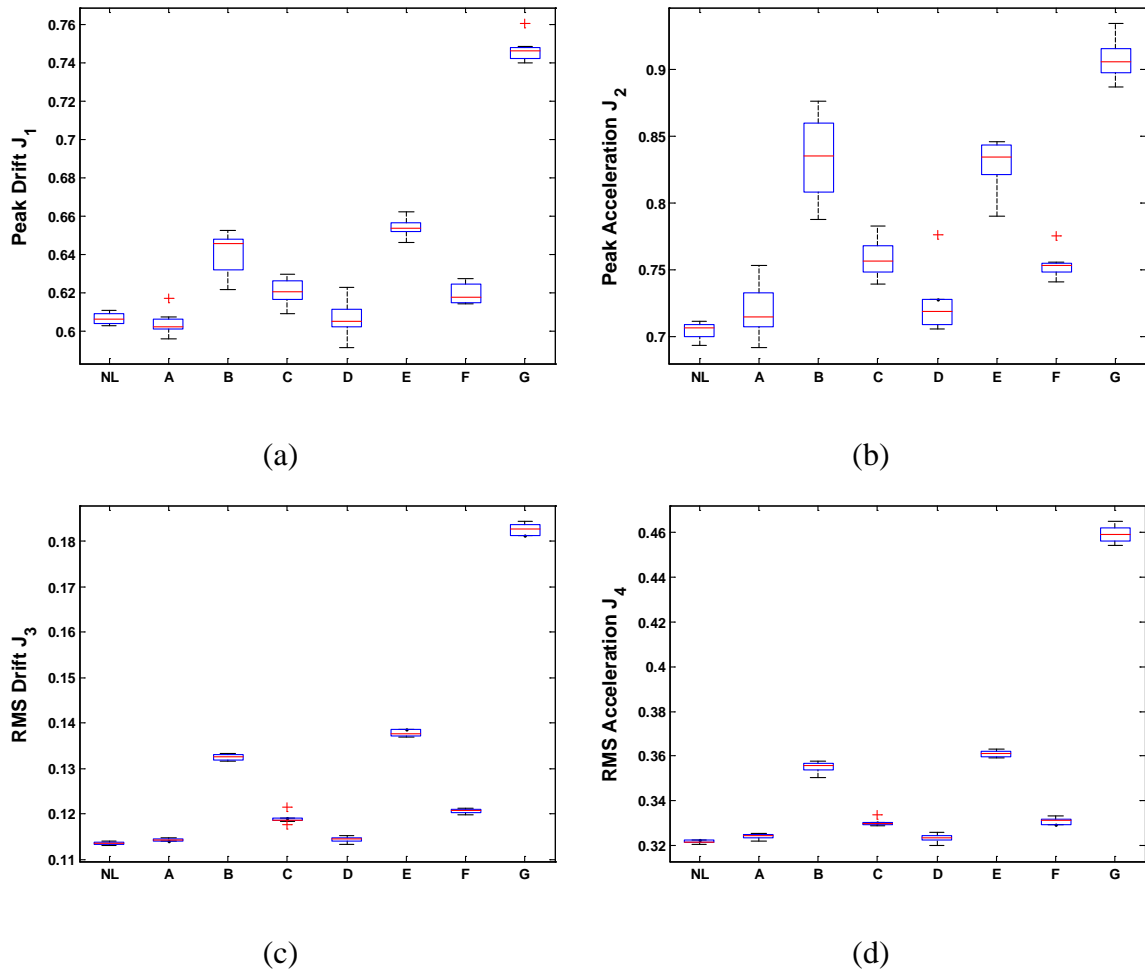


Figure 6.17. Boxplot of evaluation criterion (a) J_1 , (b) J_2 , (c) J_3 , and (d) J_4 under El Centro earthquake.

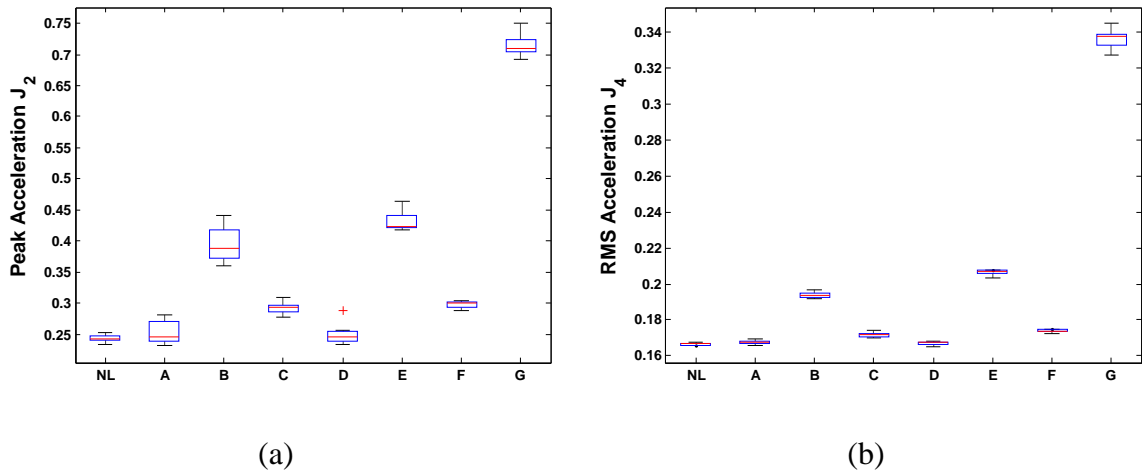


Figure 6.18. Boxplot of criterion (a) J_2 and (b) J_4 under Mexico City earthquake.

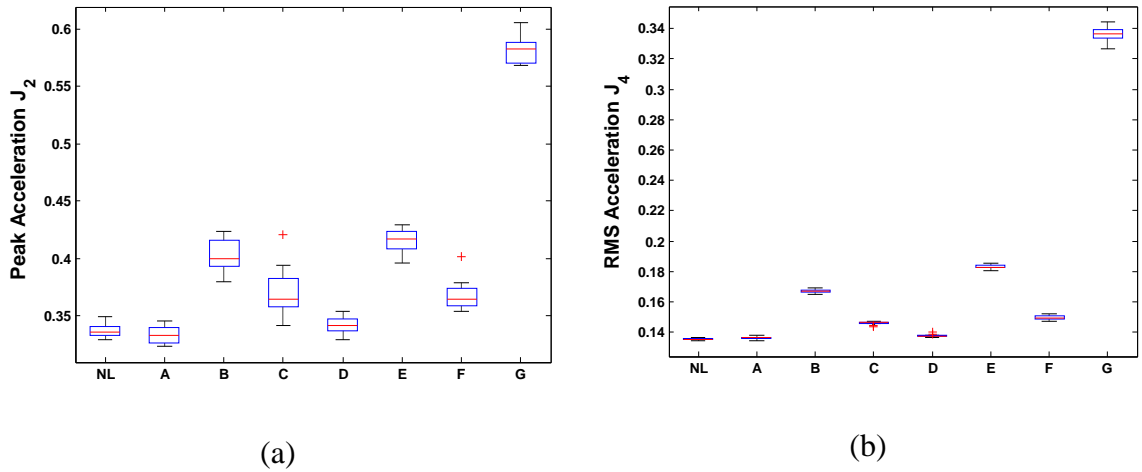


Figure 6.19. Boxplot of criterion (a) J_2 and (b) J_4 under Gebze earthquake.

6.2 Evaluation of Estimator Switching Method with RTHS

In this section, the proposed estimator switching method in the previous chapter is evaluated experimentally with RTHS tests (using the setup in the previous section). The same data loss and sensor failure cases are considered as in Table 6.3. The Kalman filter in the numerical substructure is replaced with the switching estimator in the RTHS setup. The switching gains L_i are calculated following the remark 3 in section 5.1. There all 8

switching cases with 3 wireless nodes. The pre-calculated gains for this large-scale structure are listed below

With sensor measurements from all floors

$$L_1 = \begin{bmatrix} -0.051 & -0.043 & -0.027 \\ -0.060 & -0.095 & -0.090 \\ -0.054 & -0.108 & -0.161 \\ 2.332 & 3.115 & 3.134 \\ 1.492 & 3.180 & 3.644 \\ 1.382 & 2.549 & 4.004 \end{bmatrix} \times 10^{-3}$$

With sensor measurements from floor 1 and floor 2

$$L_2 = \begin{bmatrix} -0.076 & -0.074 \\ -0.087 & -0.204 \\ -0.081 & -0.295 \\ 3.570 & 4.599 \\ 2.507 & 5.150 \\ 1.979 & 5.123 \end{bmatrix} \times 10^{-3}$$

With sensor measurements from floor 1 and floor 3

$$L_3 = \begin{bmatrix} -0.082 & -0.053 \\ -0.116 & -0.148 \\ -0.100 & -0.252 \\ 3.472 & 4.861 \\ 2.227 & 5.663 \\ 1.833 & 5.688 \end{bmatrix} \times 10^{-3}$$

With sensor measurements from floor 2 and floor 3

$$L_4 = \begin{bmatrix} -0.077 & -0.043 \\ -0.140 & -0.106 \\ -0.137 & -0.190 \\ 4.588 & 3.769 \\ 3.981 & 4.162 \\ 2.967 & 4.762 \end{bmatrix} \times 10^{-3}$$

With sensor measurements from floor 1

$$L_5 = \begin{bmatrix} -0.201 \\ -0.348 \\ -0.433 \\ 7.170 \\ 6.256 \\ 5.663 \end{bmatrix} \times 10^{-3}$$

With sensor measurements from floor 2

$$L_6 = \begin{bmatrix} -0.106 \\ -0.227 \\ -0.346 \\ 7.601 \\ 7.447 \\ 7.243 \end{bmatrix} \times 10^{-3}$$

With sensor measurements from floor 3

$$L_7 = \begin{bmatrix} -0.155 \\ -0.296 \\ -0.367 \\ 7.618 \\ 7.197 \\ 6.557 \end{bmatrix} \times 10^{-3}$$

When no measurement is received, $L_8 = \mathbf{0}$. The three historical earthquakes at full-scale are used as ground excitations. The RTHS results comparing cases B, E, G with and without switching estimator as well as no data loss case and case A with switching estimator are shown in Figures 6.18-6.20. The evaluation results for all cases with switching estimator are provided in Figures 6.21-6.22 and also listed in Table 6.5. The results show that the performance of different cases are very close to each other, which indicate the switching estimator is working effectively to compensate for the impact of data loss and sensor failure. The feasibility of incorporating the switching estimator in codesigned wireless control system is verified in the RTHS tests.

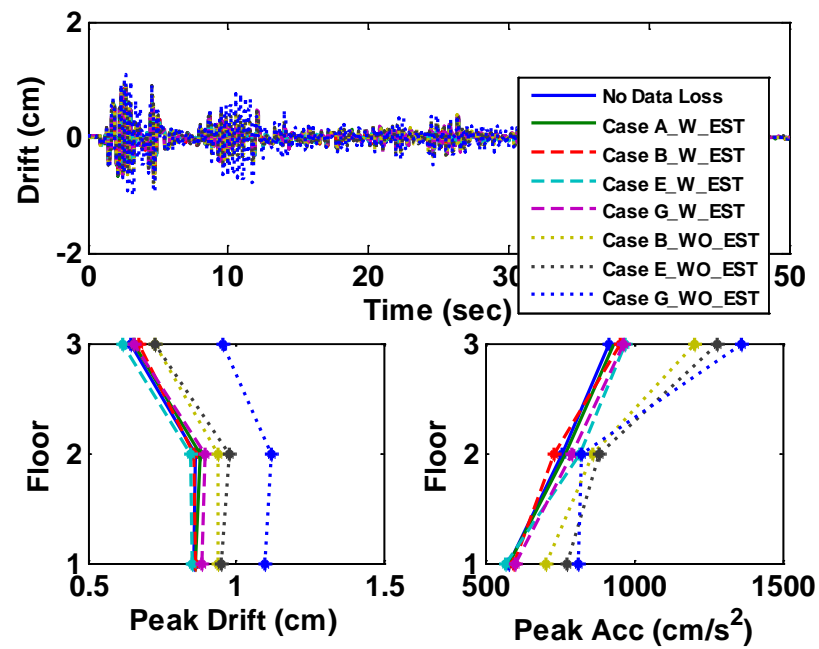


Figure 6.20. Structural response under El Centro earthquake.

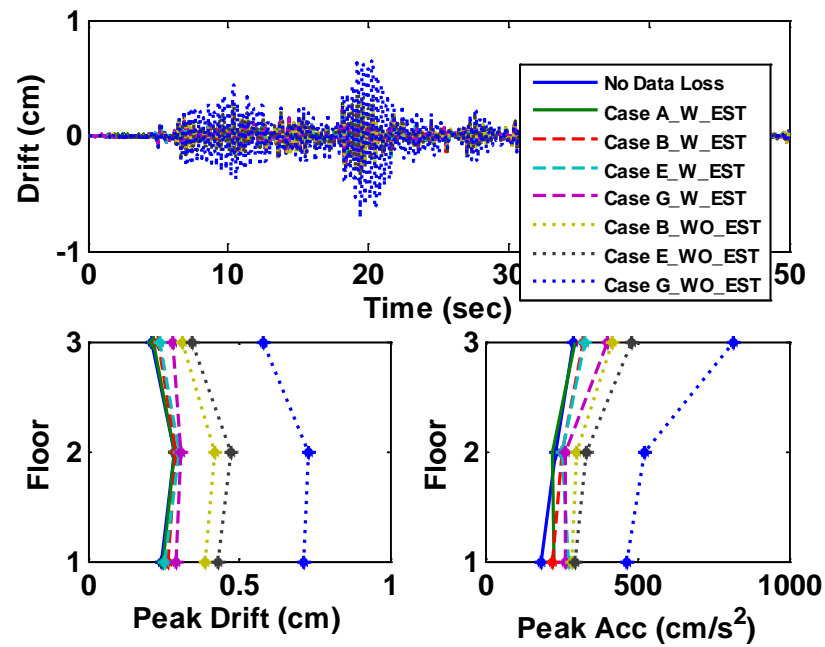


Figure 6.21. Structural response under Mexico City earthquake.

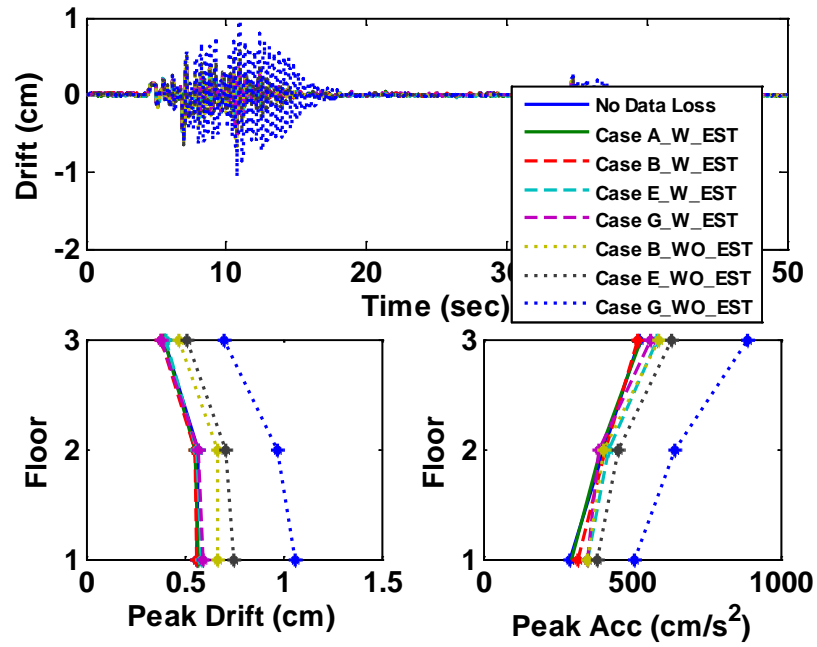


Figure 6.22. Structural response under Gebze earthquake.

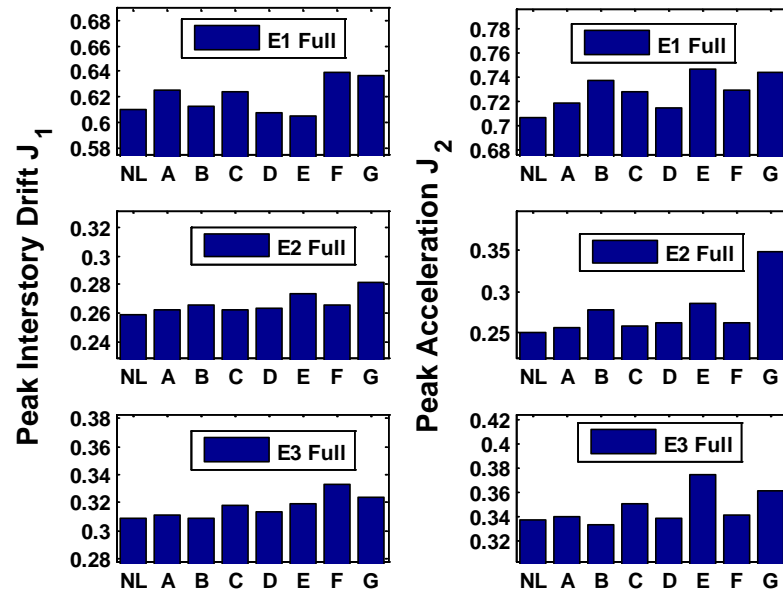


Figure 6.23. Evaluation results of J_1 and J_2 .

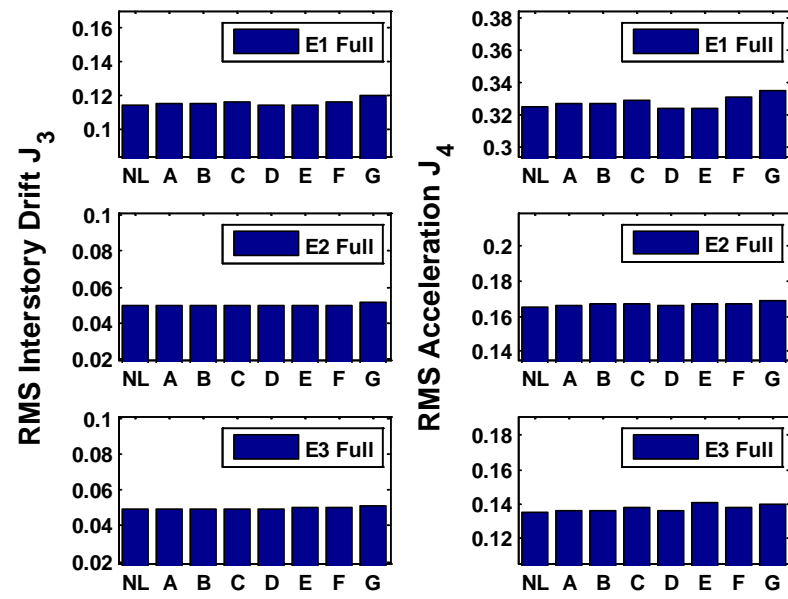


Figure 6.24. Evaluation results of J3 and J4.

Table 6.5. Control performance of different cases with switching estimator.

E1-Full	$J_1(\%)$	$J_2(\%)$	$J_3(\%)$	$J_4(\%)$
No loss	61.0	70.7	11.5	32.5
Case A	62.5	71.8	11.6	32.7
Case B	61.3	73.7	11.5	32.7
Case C	62.4	72.8	11.6	32.9
Case D	60.8	71.5	11.5	32.4
Case E	60.6	74.6	11.5	32.4
Case F	63.9	73.0	11.7	33.0
Case G	63.6	74.3	12.0	33.5
E2-Full				
No loss	25.9	25.0	5.0	16.5
Case A	26.2	25.6	5.0	16.6
Case B	26.6	27.9	5.0	16.7
Case C	26.2	25.9	5.0	16.7
Case D	26.4	26.3	4.0	16.6
Case E	27.3	28.5	5.0	16.7
Case F	26.6	27.3	5.0	16.7
Case G	28.2	34.9	5.1	16.9
E3-Full				
No loss	30.9	33.8	4.9	13.6
Case A	31.1	34.0	4.9	13.7
Case B	30.9	33.4	5.9	13.6
Case C	31.8	35.1	5.0	13.8
Case D	31.3	33.8	4.9	13.6
Case E	31.9	37.5	5.1	14.1
Case F	33.3	34.2	5.0	13.8
Case G	32.4	36.2	5.1	14.0

6.3 Summary

In this chapter, fault tolerance of wireless structural control is examined using RTHS. The fault tolerance study is examined by conducting tests in which data loss and sensor failure are simulated under several historical earthquakes. The relative importance of sensor location is evaluated through varying the location of the sensors with losses. The results indicate that, in this simulation, the sensor located at higher floor has larger impact on control performance. This analysis may be performed to determine sensor placement for the design in real application, i.e. backup devices may be provided for sensors that are

more critical to the performance of the controller. The codesigned control system with switching estimator is verified with RTHS tests. The experimental results indicate that the switching estimator works effectively in these cases. This switching estimator provides an alternative method to compensate for the impact of data loss and sensor failure on the system performance.

CHAPTER 7. CONCLUSIONS AND FUTURE WORK

The adoption of CPS codesign approach to wireless control systems in civil infrastructure enables us to consider the wireless sensor network (cyber) perspective and structural control (physical) perspective in a holistic manner to achieve better control performance than considering those two parts in an isolated way. In this dissertation, the focus is on establishing a framework facilitating cyber-physical codesign of wireless structural control system. This framework provides codesign tools (the WCPS and wireless sensor platform) to evaluate and validate wireless control design as well as the codesign strategies to implement on real-world structures for wireless structural control. The research findings and potential future work are summarized in this chapter.

7.1 Summary of Conclusions

Although wireless structural control systems have many appealing features, there are challenges associated with wireless control system design including wireless network induced time delay, potential data loss and sensor failure. The challenges need to be considered jointly from both the control and network perspectives. In this work, the WCPS is developed first to realistically simulate wireless structural control. The WCPS

integrates structural models developed in Matlab (Simulink) and wireless sensor network simulated in TOSSIM, a state of the art sensor network simulator. TDMA network is adopted since the network delays are deterministic under a TDMA protocol (which is desirable for the control design). TOSSIM simulates the wireless transmission based on a probabilistic signal to noise ratio model. Two cases studies are developed within the WCPS framework, each combining a structural model with wireless signal and noise traces collected from real-world environments. The building case study combines a representative benchmark building model and wireless traces collected from a multi-story building on the Washington University in St. Louis campus. The bridge study combines the structural model of the Cape Girardeau bridge over the Mississippi River and wireless traces collected from a similar bridge (the Jindo bridge) in South Korea. The case studies shed light on the challenges of wireless control system and the limitations of a traditional structural control approach under realistic wireless conditions. A cyber-physical codesign approach to wireless control system is proposed which integrates a data aggregation strategy (for communication and control) and an optimal time delay controller that improves structural control performance in both cases. WCPS also offers a tool for wireless control studies in a broad range of disciplines.

Following the development of WCPS, a wireless sensing and control platform is developed to experimentally implement and evaluate codesigned wireless control system. The sensor platform is based on the open source Arduino board. The developed wireless sensor platform is intended to be open source in both software and hardware, so that researchers in the community can access and contribute to it. Low cost, low power

wireless sensing and communication modules are built on the Arduino platform. An 18-bit high resolution ADC board is developed. Structural control algorithms are embedded within the wireless sensor board for feedback control. The wireless sensor board is validated through a series of verification tests. Furthermore, experimental studies are carried out by implementing it on the 3-story shear structure in the Intelligent Infrastructure Systems Lab (IISL) with various wireless control strategies (decentralized control, partially decentralized control, centralized control). The tradeoff between the number of measurements available and the wireless network induced time delay is studied. In this setup with TDMA network (10 msec time slot) and one semi-active control device installed on the 1st floor, decentralized control strategy outperforms the partially decentralized and centralized control strategy. With the maximum damper force (30 N) about 4.3% the total weight of the structure, significant RMS drift reduction (70%) and RMS acceleration reduction (40 %) are achieved with decentralized wireless control.

In addition to the development of numerical simulator and experimental platform, a suboptimal Kalman filter based estimator switching method is proposed for state estimation with data loss or sensor failure. The switching gains are pre-calculated which is computational inexpensive for real-time implementation and the knowledge of probability of data loss is not required to derive the estimator gains. The only required knowledge is the data loss at each step to switch the estimator gains. One way to find estimator switching gains is given. The performance of this method is evaluated using the numerical model of a 3-story shear building model. With the impact of data loss and sensor failure, the switching estimator surpasses the performance of the original Kalman

filter. The switching estimator is also shown to be robust to some extent of measurement noise and modeling error.

In this last part of the dissertation, a fault tolerance study is conducted using real-time hybrid simulation (RTHS) to consider sensor data loss and sensor failure cases in a wireless control system. Performing wireless structural control tests with the RTHS technique facilitates study of sensor failure or control failure without safety concerns. Meanwhile, it offers more realistic results than numerical simulations when the experimental facilities are not available. The relative importance of sensor location is evaluated which indicates that the sensor located at higher floor has a larger impact on control performance for this setup. This could be taken account into sensor placement design in real application, i.e. backup devices can be provided for the sensors that are more critical. The codesigned control system with switching estimator is evaluated with RTHS tests. The experimental results indicate that the switching estimator works effectively in these cases. This switching estimator provides an alternative method to compensate for the impact of data loss and sensor failure.

In summary, the key contributions of this work include:

- Development of a numerical tool (the WCPS) to model the complex behavior of wireless structural control system. The WCPS is available to the community at <http://wcps.cse.wustl.edu>. The building case study is established as a wireless building control benchmark problem available at https://nees.org/groups/wireless_control_benchmark.

- Proposed a codesign approach for the wireless control case studies which consider the wireless sensor network (cyber) perspective and structural control (physical) perspective in a holistic manner.
- Development of an experimental wireless sensing and control platform to implement and evaluate codesigned wireless control system. Validated the wireless sensing and control platform on a lab structure and achieved significant structural responses reduction under earthquake ground motions in shake table tests.
- Proposed an estimator switching method to compensate for data loss and sensor failure in a wireless control system. Evaluated the switching estimator in the codesigned control system through numerical simulation and RTHS tests.
- Investigated fault tolerance of the wireless control system with real-time hybrid simulation technique. Obtained the knowledge of sensor data loss and sensor failure to the wireless control performance as well as the relative importance of sensor locations for this control setup.

7.2 Future Work

This research addresses several critical aspects of wireless structural control system with cyber-physical codesign approach. Meanwhile, a number of future research directions are identified based upon some of the remaining challenges and the limitations of current approaches. The future research directions are detailed below:

- The case studies of the wireless cyber-physical simulator consider two linear systems. Extension to nonlinear wireless control systems would have more impact.

The estimation and control algorithms for nonlinear system need to be investigated. The existing estimation algorithms for nonlinear system including extended Kalman filter and unscented Kalman filter are demonstrated to be successfully in various applications. Incorporating these algorithms into a nonlinear wireless control system need to be explored.

- Based on the size of the network and dynamics of the system, guideline should be developed to evaluate the tradeoffs to choose centralized control, partially decentralized control or decentralized control, i.e. for centralized wireless control with TDMA wireless network, the network induced delay grows proportional to the size of the network which makes it not advisable to work with large size of network.
- In the WCPS, a TDMA network is adopted intentionally, since the network transmission delay is deterministic in TDMA network. However, providing other network protocols such as CSMA/CA network and FDMA network would increase the flexibility of the simulator and provide more options to the users.
- Sample codesign approaches are provided for the two WCPS case studies. Other advanced control algorithms i.e. model predictive control and agent-based control should be considered in the codesigned wireless control system in the future study.
- A commercial off-the-shelf XBee radio is used as transmission module of developed sensor board. Open-source transmission modules should be considered in the future which provides more freedom in modifying the protocol to reduce the transmission overhead (delay). Also high resolution time synchronization

algorithms (i.e. the flooding time synchronization protocol) can be implemented on the open source module.

- Each wireless sensor node has certain computational power and this computational capability will continue to grow with the rapid development of sensor hardware. Utilizing the computational capability more efficiently and effectively requires continuous research effort.
- A powerful dual core Arduino board will be released soon. Utilizing a dual core processor allows dedicating one core to the sensing operations and the other core for embedded computation and real-time control law execution. Multi-rate control implementation can be achieved with the dual core sensor board.
- Applying the wireless sensing and control platform to other applications should be explored, i.e. wind turbine monitoring and vibration control system. The low cost and low power wireless control platform with flexible interfaces is appealing to such applications.

LIST OF REFERENCES

LIST OF REFERENCES

- AD7982 Datasheet*. (2013). Retrieved from <http://www.analog.com/media/en/technical-documentation/data-sheets/AD7982.pdf>
- ADXL 345 Datasheet*. (2013). Retrieved from <http://www.analog.com/en/mems-sensors/mems-inertial-sensors/adxl345/products/product.html>
- Ahlawat, A. S., & Ramaswamy, A. (2001). Multiobjective optimal structural vibration control using fuzzy logic control system. *Journal of Structural Engineering*, 127(11), 1330-1337.
- Alavi, S. M., & Saif, M. (2013). Fast state estimation subject to random data loss in discrete-time nonlinear stochastic systems. *International Journal of Control*, 2302-2314.
- Anson, M., Ko, J. M., & Lam, E. S. (2002). *Advances in Building Technology*. Elsevier Science Ltd.
- Arduino*. (2014). Retrieved from <http://en.wikipedia.org/wiki/Arduino>
- Arduino Forum*. (2013). Retrieved from <http://forum.arduino.cc/>
- Asl, F. M., & Ulsoy, A. G. (2003). Analysis of a System of Linear Delay Differential Equations. *J. Dyn. Sys., Meas., Control*, 215-223.
- Bahill, A. (1983). A simple adaptive smith-predictor for controlling time-delay systems. *IEEE Control Systems Magazine*, 16-22.

- Bani-Hani, K., & Ghaboussi, J. (1998). Neural networks for structural control of a benchmark problem, active tendon system. *Earthquake Engineering & Structural Dynamics*, 1225-1245.
- Battaini, M., & Dyke, S. J. (1998). Fault tolerant structural control systems for civil engineering applications. *Journal of Structural Control*, 5-26.
- Battaini, M., Casciati, F., & Faravelli, L. (1998). Fuzzy control of structural vibration. An active mass system driven by a fuzzy controller. *Earthquake Engineering and Structural Dynamics*, 27(11), 1267-1276.
- Bridge Diagnostics, Inc.* (2015). Retrieved from <http://bridgetest.com/products/>
- Casciati, S., & Chen, Z. (2012). An active mass damper system for structural control using real-time wireless sensors. *Structural Control and Health Monitoring*.
- Casciati, S., & Chen, Z. C. (2013). Digital Wireless Solutions for Structural Control. *Advances in Science and Technology*, 157-166.
- Chang, C. M., Wang, Z. H., & Spencer, B. F. (2009). Application of Active Base Isolation Control. *Proc. of SPIE*.
- Chen, C., Ricles, J. M., Karavasilis, T. L., Chae, Y., & Sause, R. (2012). Evaluation of a Real-time Hybrid Simulation System for Performance Evaluation of Structures with Rate Dependent Devices Subjected to Seismic Loading. *Engineering Structures*, 71-82.
- Chihaia, C. (2010). *PhD Dissertation: Active Fault-Tolerance in Wireless Networked Control Systems*. Universitt Duisburg-Essen.
- Chile earthquake.* (2010). Retrieved from http://en.wikipedia.org/wiki/2010_Chile_earthquake

- Chintalapudi, K., Fu, T., Paek, J., Kothari, N., Rangwala, S., Caffrey, J., . . . Masri, S. (2006). Monitoring civil structures with a wireless sensor network. *Internet Computing, IEEE*, 10(2), 26-34.
- Cho, S. J., Jo, H., Jang, S., Park, J. W., Jung, H. J., Yun, C. B., & Seo, J. W. (2010). Structural health monitoring of a cable-stayed bridge using wireless smart sensor technology: data analyses. *Smart Structures and Systems*, 461-480.
- Christenson, R., Lin, Y. Z., Emmons, A., & Bass, B. (2008). Large-Scale Experimental Verification of Semiactive Control through Real-Time Hybrid Simulation. *Journal of Structural Engineering*, 522-534.
- Chung, L. L., Lin, C. C., & Lu, K. H. (1995). Time-delay control of structures. *Earthquake Engineering & Structural Dynamics*, 24(5), 687-701.
- Cyber-physical system*. (2014). Retrieved from http://en.wikipedia.org/wiki/Cyber-physical_system
- Dang, X., Guan, Z. H., Li, T., & Zhang, D. X. (2012). Joint Smith predictor and neural network estimation scheme for compensating randomly varying time-delay in networked control system. *Control and Decision Conference (CCDC)*.
- Dyke, S. J., Spencer, B., Sain, M. K., & Carlson, J. D. (1996). Modeling and Control of Magnetorheological Dampers for Seismic Response Reduction. *Smart Materials and Structures*, 565-575.
- Dyke, S., Caicedo, J., Turan, G., Bergman, L., & Hague, S. (2003). Phase I Benchmark Control Problem for Seismic Response of Cable-stayed Bridges. *Journal of Structural Engineering*, 857-872.
- Fallah, A. Y., & Taghikhany, T. (2013). Time-delayed decentralized H2/LQG controller for cable-stayed bridge under seismic loading. *Structural Control and Health Monitoring*, 354-372.
- Faludi, R. (2010). *Building Wireless Sensor Networks*. O'Reilly Media.

- Fang, X., & Wang, J. (2008). Stochastic observer-based guaranteed cost control for networked control systems with packet dropouts. *Control Theory & Applications*, 980-989.
- Farrar, C. R., Park, G., Allen, D. W., & Todd, M. D. (2006). Sensor network paradigms for structural health monitoring. *Structural control and health monitoring*, 13(1), 210-225.
- Fisco, N. R., & Adeli, H. (2011). Smart structures: Part II - Hybrid control systems and control strategies. *Scientia Iranica*, 285-295.
- Fornazier, H., Martin, A., & Messner, S. (2012). *Wireless Communication : Wi-Fi, Bluetooth, IEEE 802.15.4, DASH7*.
- Franklin, G. F., Powell, J. D., & Workman, M. L. (1990). *Digital Control of Dynamic Systems*. Addison-Wesley.
- Friedman, A. (2012). *PhD dissertation: Development and experimental validation of a new control strategy considering device dynamics for large-scale MR dampers using real-time hybrid simulation*. West Lafayette: Purdue University.
- Gao, H., Chen, T., & Lam, J. (2008). A new delay system approach to network-based control. *Automatica*, 39-52.
- Gutierrez, J. A., Winkel, L., Callaway, E. H., & Barrett, R. L. (2011). *Low-Rate Wireless Personal Area Networks: Enabling Wireless Sensors With IEEE 802.15.4*. Standards Information Network.
- Hackmann, G., Guo, W., Yan, G., Sun, Z., Lu, C., & Dyke, S. (2014). Cyber-Physical Codesign of Distributed Structural Health Monitoring with Wireless Sensor Networks. *Parallel and Distributed Systems, IEEE Transactions on*, 63-72.
- Haiti earthquake*. (2010). Retrieved from http://en.wikipedia.org/wiki/2010_Haiti_earthquake

- Housner, G. W., Bergman, L., Caughey, T. K., Chassiakos, A. G., Claus, R. O., Masri, S. F., . . . Yao, J. T. (1997). Structural control: past, present, and future. *Journal of Engineering Mechanics*, 123(9), 897-971.
- Hu, H. (2012). *Master dissertation: Response control of seismically excited buildings: Application of viscous damping and negative stiffness control algorithm*. Purdue University.
- Imote2 Datasheet*. (2010). Retrieved from http://web.univ-pau.fr/~cpham/ENSEIGNEMENT/PAU-UPPA/RESA-M2/DOC/Imote2_Datasheet.pdf
- Ivanovienė, I., & Rimas, J. (2015). Complement to method of analysis of time delay systems via the Lambert W function. *Automatica*, 25-28.
- Jang, S., Jo, H., Cho, S., Mechitov, K., Rice, J. A., Sim, S. H., & Agha, G. (2010). Structural health monitoring of a cable-stayed bridge using smart sensor technology: deployment and evaluation. *Smart Structures and Systems*, 439-459.
- Kane, M. B. (2014). *PhD dissertation: Wirelessly Enabled Control of Cyber-Physical Infrastructure with Applications to Hydronic Systems*. University of Michigan.
- Kim, S., Pakzad, S., Culler, D., & etc. (2007). Health Monitoring of Civil Infrastructures Using Wireless Sensor Networks. *In IPSN*. ACM.
- Kottapalli, V. A., Kiremidjian, A. S., Lynch, J. P., Carryer, E., Kenny, T. W., Law, K. H., & Lei, Y. (2003). Two-tiered wireless sensor network architecture for structural health monitoring. *Proc. SPIE 5057, Smart Structures and Materials 2003: Smart Systems and Nondestructive Evaluation for Civil Infrastructures*.
- Kwok, K. C., & Samali, B. (1995). Performance of tuned mass dampers under wind loads. *Engineering Structures*, 17(9), 655-667.
- Larbah, E., & Patton, R. J. (2010). Fault tolerant control in high building structures. *Conference on Control and Fault-Tolerant Systems*.

- Lee, H., Cerpa, A., & Levis, P. (2007). Improving Wireless Simulation Through Noise Modeling. *Information Processing in Sensor Networks*, (pp. 25-27).
- Lee, J. S., Su, Y. W., & Shen, C. C. (2007). A Comparative Study of Wireless Protocols: Bluetooth, UWB, ZigBee, and Wi-Fi. *Industrial Electronics Society, 2007. IECON 2007. 33rd Annual Conference of the IEEE*, (pp. 46-51).
- Levis, P., Lee, N., Welsh, M., & Culler, D. (2003). TOSSIM: Accurate and Scalable Simulation of Entire TinyOS Applications. *In Proceedings of the First ACM Conference on Embedded Networked Sensor Systems*.
- Li, B., Sun, Z., Mechitov, K., Hackmann, G., Lu, C., Dyke, S., . . . Spencer, B. (2013). Realistic Case Studies of Wireless Structural Control. *International Conference on Cyber-Physical Systems (ICCPS)*.
- Li, H. Y., Liu, H. H., Gao, H. J., & Shi, P. (2012). Reliable Fuzzy Control for Active Suspension Systems With Actuator Delay and Fault. *Fuzzy Systems, IEEE Transactions on*, 342-357.
- Linderman, L. (2014). *PhD dissertation: Smart wireless control of civil structures*.
- Linderman, L. E., Mechitov, K. A., & Spencer, B. F. (2013). TinyOS-based real-time wireless data acquisition framework for structural health monitoring and control. *Structural Control and Health Monitoring*, 1007-1020.
- Liu, L., Dyke, S., & Veto, R. (2007, 7 26-31). Wireless Sensing and Control of Structural Vibration from Earthquake., (pp. 194-198).
- Loh, C., Lynch, J., Lu, K., Wang, Y., Chang, C., Lin, P., & Yeh, T. (2007). Experimental verification of a wireless sensing and control system for structural control using MR dampers. *Earthquake Engineering & Structural Dynamics*, 1303-1328.
- Lord Microstrain Inc. (2015). Retrieved from <http://www.microstrain.com/wireless/g-link>

- Lynch, J. P., & Law, K. H. (2002a). Decentralized Control Techniques for Large-Scale Civil Structural Systems. *Proceedings of the 20th International Modal Analysis Conference*. Los Angeles.
- Lynch, J. P., & Law, K. H. (2002b). Market-Based Control of Linear Structural Systems. *Earthquake Engineering and Structural Dynamics*, 1855-1877.
- Lynch, J. P., & Law, K. H. (2004). Decentralized Energy Market-Based Structural Control. *Structural Engineering and Mechanics*, 557-572.
- Lynch, J. P., & Loh, K. J. (2006). A summary review of wireless sensors and sensor networks for structural health monitoring. *Shock and Vibration Digest*, 38(2), 91-130.
- Lynch, J. P., & Tilbury, D. M. (2005). Implementation of a Decentralized Control Algorithm Embedded within a Wireless Active Sensor. *Proc. of the 2nd Annual ANCRiSST Workshop*, (pp. 21-24).
- Lynch, J. P., Wang, Y., Swartz, R. A., Lu, K. C., & Loh, C. H. (2008). Implementation of a closed-loop structural control system using wireless sensor networks. *Structural Control and Health Monitoring*, 518-539.
- Memsic Inc.* (2015). Retrieved from <http://www.memsic.com/>
- Mosqueda, G., Stojadinovic, B., & Mahin, S. (2007). Real-Time Error Monitoring for Hybrid Simulation. Part I: Methodology and Experimental Verification. *Journal of Structural Engineering*, 1100-1108.
- Nagayama, T., & Spencer, B. F. (2008). *Structural Health Monitoring Using Smart Sensors*. Newmark Structural Engineering Laboratory. University of Illinois at Urbana-Champaign.
- Nagayama, T., Spencer, B. F., & Rice, J. A. (2009). Autonomous decentralized structural health monitoring using smart sensors. *Structural Control and Health Monitoring*, 842-859.

- Nakashima, M., Kato, H., & Takaoka, E. (1992). Development of real-time pseudo dynamic testing. *Earthquake Engineering & Structural Dynamics*, 79-92.
- National Instruments, Inc. (2015). Retrieved from <http://www.ni.com/wsn/>
- Ou, G., Ozdagli, A., Dyke, S. J., & Wu, B. (2014). Robust Integrated Actuator Control: Experimental Verification and Real Time Hybrid Simulation Implementation. *Earthquake Engineering and Structural Dynamics*.
- Paek, J., Chintalapudi, K., Caffrey, J., Govindan, R., & Masri, S. (2005). A wireless sensor network for structural health monitoring: Performance and experience. *Center for Embedded Network Sensing*.
- Pall, A. S., & Pall, R. (1996). Friction-dampers for seismic control of buildings "a canadian experience". *11th world conference on earthquake engineering*. Elsevier Science Ltd.
- Park, P. (1999). A delay-dependent stability criterion for systems with uncertain time-invariant delays. *IEEE Transactions on Automatic Control*, 876-877.
- Patton, R. J. (1997). Fault tolerant control: the 1997 situation. *IFAC Symposium on Fault Detection Supervision and Safety for Technical Processes*, (pp. 1033-1054).
- Patton, R. J., Kambhampati, C., Casavola, A., Zhang, P., Ding, S., & Saute, D. (2007). A Generic Strategy for Fault-Tolerance in Control Systems Distributed Over a Network. *European Journal of Control*, 280-296.
- Peckens, C. A. (2014). *PhD dissertation: Bio-Inspired Compressive Sensing based on Auditory Neural Circuits for Real-time Monitoring and Control of Civil Structures using Resource Constrained Sensor Networks*.
- Polastre, J., Szewczyk, R., & Culler, D. (2005). Telos: Enabling Ultra-Low Power Wireless Research. In *Proc. Fourth International Conference on Information Processing in Sensor Networks: Special track on Platform Tools and Design Methods for Network Embedded Sensors (IPSN/SPOTS)*.

- Rice, J., & Spencer, B. F. (2008). Structural health monitoring sensor development for the Imote2 platform. *The 15th International Symposium on: Smart Structures and Materials & Nondestructive Evaluation and Health Monitoring*. International Society for Optics and Photonics.
- Rice, J., & Spencer, B. F. (2009). *Flexible Smart Sensor Framework for Autonomous Full-scale Structural Health Monitoring*. Newmark Structural Engineering Laboratory. University of Illinois at Urbana-Champaign.
- Saaed, T., Nikolakopoulos, G., Jonasson, J., & Hedlund, H. (2013). A state-of-the-art review of structural control systems. *Journal of Vibration and Control*.
- Sánchez-Peña, R., Bolea, Y., & Puig, V. (2009). MIMO Smith predictor: Global and structured robust performance analysis. *Journal of Process Control*, 163-177.
- Sazonov, E., Janoyan, K., & Jha, R. (2004). Wireless intelligent sensor network for autonomous structural health monitoring. *Smart Structures and Materials*, 305-314.
- Seth, S., Lynch, J. P., & Tilbury, D. M. (2005). Wirelessly networked distributed controllers for real-time control of civil structures. *American Control Conference*, (pp. 2946-2952).
- SHM Toolsuite*. (2015). Retrieved from <http://shm.cs.illinois.edu/software.html>
- Sichuan earthquake*. (2008). Retrieved from http://en.wikipedia.org/wiki/2008_Sichuan_earthquake
- Sidhu, B., Singh, H., & Chhabra, A. (2007). Emerging wireless standards WiFi, ZigBee and WiMAX. *Proc. World Academy of Science, Engineering and Technology*, (pp. 308-313).
- Sim, S., & Spencer, B. (2009). *Decentralized Strategies for Monitoring Structures using Wireless Smart Sensor Networks*. Newmark Structural Engineering Laboratory. University of Illinois at Urbana-Champaign.

- Sinopoli, B., Schenato, L., Franceschetti, M., Poolla, K., Jordan, M. I., & Sastry, S. S. (2004). Kalman filtering with intermittent observations. *Automatic Control, IEEE Transactions on*, 1453-1464.
- Smith, O. J. (1957). Posicast Control of Damped Oscillatory Systems. *Proceedings of the IRE*, (pp. 1249-1255).
- Smith, S. C., & Seiler, P. (2003). Estimation with lossy measurements: jump estimators for jump systems. *Automatic Control, IEEE Transactions on*, 2163-2171.
- Sohn, H., Farrar, C. R., Hemez, F., & Czarnecki, J. (2003). *A Review of Structural Health Monitoring Literature: 1996–2001*. Los Alamos National Laboratory Report LA-13976-MS.
- Soong, T. T., Lin, R. C., Riley, M. A., Wang, Y. P., Aizawa, S., & Higashino, M. (1992). *Active bracing system: a full scale implementation of active control*. National Center for Earthquake Engineering Research.
- Spencer, B. F., & Nagarajaiah, S. (2003, July). State of the Art of Structural Control. *Journal of Structural Engineering*, 845-856.
- Spencer, B. F., Dyke, S., & Deoskar, H. (1998, November). Benchmark problems in structural control: part I-Active Mass Driver system. *Earthquake Engineering & Structural Dynamics*, 27(11), 1127-1139.
- SPI*. (2014). Retrieved from http://en.wikipedia.org/wiki/Serial_Peripheral_Interface_Bus
- Straser, E. G., & Kiremidjian, A. S. (1998). *A Modular, Wireless Damage Monitoring System for Structures*. Stanford: John A. Blume Earthquake Engineering Center.
- Sun, J., Liu, G. P., Chen, J., & Rees, D. (2010). Improved delay-range-dependent stability criteria for linear systems with time-varying delays. *Automatica*, 466-470.
- Sun, Y. (2009). *PhD dissertation: Time-Delay Systems: Analysis and Control using the Lambert W Function*. University of Michigan.

- Sun, Z., Li, B., Dyke, S. J., & Lu, C. (2012). Evaluation of performances of structural control benchmark problem with time delays from wireless sensor network. *Joint Conference of the Engineering Mechanics Institute and ASCE Joint Specialty Conference on Probabilistic Mechanics and Structural Reliability (EMI/PMC'12)*.
- Sun, Z., Li, B., Dyke, S. J., & Lu, C. (2013). A novel data utilization and control strategy for wireless structural control systems with TDMA network. *2013 ASCE International Workshop on Computing in Civil Engineering (ASCE IWCCE 2013)*.
- Sun, Z., Li, B., Dyke, S., Lu, C., & Linderman, L. (2015). Benchmark problem in active structural control with wireless sensor network. *Structural Control and Health Monitoring*. doi:10.1002/stc.1761.
- Swartz, R. A., Jung, D., Lynch, J. P., Wang, Y., Shi, D., & Flynn, M. P. (2005). Design of a wireless sensor for scalable distributed in-network computation in a structural health monitoring system. *In 5th international workshop on structural health monitoring*, (pp. 1570-1577).
- Swartz, R., & Lynch, J. (2009). Strategic Network Utilization in a Wireless Structural Control System for Seismically Excited Structures. *Journal of Structural Engineering*, pp. 597-608.
- Symans, M. D., & Constantinou, M. C. (1999). Semi-active control systems for seismic protection of structures: a state-of-the-art review. *Engineering structures*, 469-487.
- Sztipanovits, J., & Ying, S. (2013). *Strategic R&D Opportunities for 21st Century Cyber-Physical Systems*. National Institute of Standards and Technology.
- Tanaka, T., Yamamoto, M., Katayama, T., Nakahira, K., Yamane, K., Shimano, Y., & Hirayama, K. (2003). Recent applications of structural control systems to high-rise buildings. *Earthquake Engineering and Engineering Seismology*, 4(1), 75-93.
- Taylor, S. G. (2013). *A Multi-scale Approach to Statistical and Model-based Structural Health Monitoring with Application to Embedded Sensing for Wind Energy*. Los Alamos National Lab.

- TelosB Datasheet*. (2014). Retrieved from http://www.memsic.com/userfiles/files/Datasheets/WSN/telosb_datasheet.pdf
- Tustin's method*. (2015). Retrieved from http://en.wikipedia.org/wiki/Bilinear_transform
- Uma, S., & Rao, S. (2014). Enhanced modified Smith predictor for second-order non-minimum phase unstable processes. *International Journal of Systems Science*.
- Wang, M. L., Lynch, J. P., & Sohn, H. (2014). *Sensor Technologies for Civil Infrastructures, 1st Edition*. Elsevier BV.
- Wang, X., & Gordaninejad, F. (1999). Flow analysis of field-controllable, electro- and magneto-rheological fluids using Herschel-Bulkley model. *Journal of Intelligent Materials, Systems and Structures*, 10(8), 601-608.
- Wang, Y., Lynch, J. P., & Law, K. H. (2007b). Decentralized H_∞ Controller Design for Large-scale Wireless Structural Sensing and Control Systems. *Proceedings of the 6th International Workshop on Structural Health Monitoring*. Stanford.
- Wang, Y., Swartz, R. A., Lynch, J. P., Law, K. H., Lu, K.-C., & Loh, C.-H. (2007a). Decentralized civil structural control using real-time wireless sensing and embedded computing. *Smart Structures and Systems*, 3(3), 321-340.
- Wilde, K., Gardoni, P., & Fujino, Y. (2000). Base isolation system with shape memory alloy device for elevated highway bridges. *Engineering Structures*, 222-229.
- XBee S1 Datasheet*. (2013). Retrieved from <https://www.sparkfun.com/datasheets/Wireless/Zigbee/XBee-Datasheet.pdf>
- Yang, S. S., & Chen, J. (2008). Design and Assessment of a Multiple Sensor Fault Tolerant Robust Control System. *Journal of Control Science and Engineering*.
- Yi, F., Dyke, S., Caicedo, J. M., & Carlson, J. D. (1999). Seismic response control using smart dampers. *1999 American Control Conference*.

- Yi, X., Cho, C., Cooper, J., Wang, Y., Tentzeris, M. M., & Leon, R. T. (2013). Passive wireless antenna sensor for strain and crack sensing - electromagnetic modeling, simulation, and testing. *Smart Materials and Structures*.
- Yick, J., Mukherjee, B., & Ghosal, D. (2008). Wireless sensor network survey. *Computer networks*, 52(12), 2292-2330.
- Ying, S., & Sztipanovits, J. (2013). *Foundations for Innovation in Cyber-Physical Systems*. National Institute of Standards and Technology. Retrieved from <http://www.nist.gov/el/upload/CPS-WorkshopReport-1-30-13-Final.pdf>
- Yook, J. K., Tilbury, D. M., & Soparkar, N. R. (2002). Trading computation for bandwidth: reducing communication in distributed control systems using state estimators. *Control Systems Technology, IEEE Transactions on*, 503-518.
- Yu, M., Wang, L., Chu, T., & Hao, F. (2004). An LMI approach to networked control systems with data packet dropout and transmission delays. *CDC. 43rd IEEE Conference on*.
- Yuen, K. V., & Beck, J. L. (2003). Reliability-based robust control for uncertain dynamical systems using feedback of incomplete noisy response measurements. *Earthquake engineering & structural dynamics*, 32(5), 751-770.
- Zhang, Y., Kurata, M., & Lynch, J. P. (2012). Retrieved from Permanent Wireless Monitoring System on the New Carquinez Suspension Bridge: http://wims2.org/report/project_pdf.html?id=161
- Zhou, X., & Peng, L. (2009). A new type of damper with friction-variable characteristics. *Earthquake Engineering and Engineering Vibration*, 8(4), 507-520.
- Zimmerman, A. T., Swartz, R. A., & Lynch, J. P. (2008). Automated identification of modal properties in a steel bridge instrumented with a dense wireless sensor network. *Bridge Maintenance, Safety, Management, Health Monitoring and Informatics*, 1608-1615.

APPENDICES

APPENDIX A. WIRELESS NODE WIRING DIAGRAM

As discussed in chapter 3, the developed wireless sensor has sensing, communication and actuation module. The wiring diagram is shown in Figure A.1. Note that the leaf nodes are equipped with the accelerometer ADXL345 and wireless transmission module XBee S1, the control node is connected with an additional ADC board to measure force input.

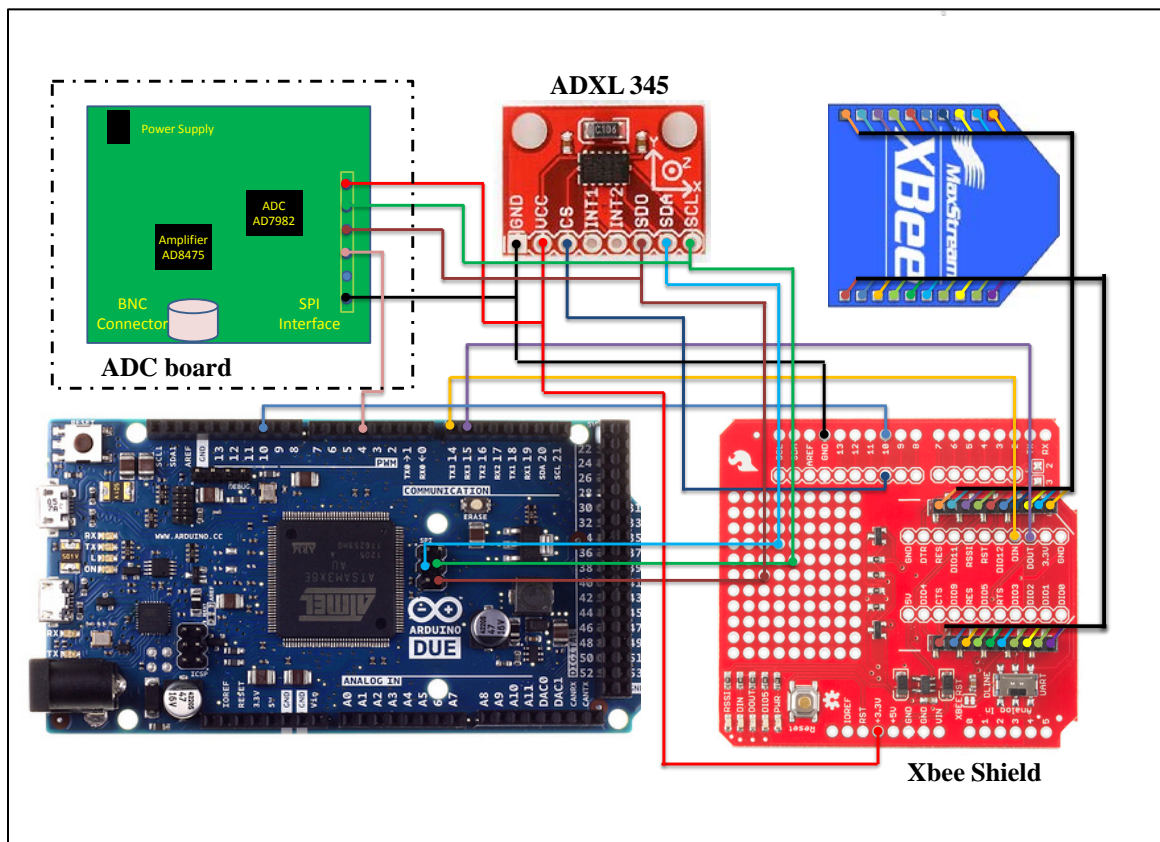


Figure A.1. Wiring diagram of wireless node (the dashed component is only available on the control node).

Arduino Sample Codes

The sample codes are provided to 1) communicate with ADXL 345, 2) to communicate with the ADC board, 3) to send data to a receiver with XBee, 4) to receive data from a transmitter, and 5) to setup the time interrupt. These scripts are developed with reference to ADXL 345 Datasheet, (2013), AD7982 Datasheet, (2013), SPI, (2014), XBee S1 Datasheet, (2013), Arduino Forum, (2013).

Arduino script to communication with ADXL 345:

```
#include <SPI.h>

Serial.begin(115200); // setup USB serial baud rate


int statusLed = 13;

int errorLed = 13;

int CS = 10; //chip selection pin


// ADXL 345 parameter setup
char POWER_CTL = 0x2D; //Power Control Register
char DATA_FORMAT = 0x31;
//char FIFO_MODE = 0x38;
char BW_RATE = 0x2C;


char DATA0 = 0x32;      //X-Axis Data 0
```

```
char DATAX1 = 0x33;    //X-Axis Data 1
char DATAY0 = 0x34;    //Y-Axis Data 0
char DATAY1 = 0x35;    //Y-Axis Data 1
char DATAZ0 = 0x36;    //Z-Axis Data 0
char DATAZ1 = 0x37;    //Z-Axis Data 1

char values[10];
uint32_t x;

void setup() {

    //debug led
    pinMode(errorLed, OUTPUT);
    digitalWrite(13, LOW);
    pinMode(CS, OUTPUT);

    SPI.begin();
    SPI.setDataMode(SPI_MODE3);

    //Before communication starts, the Chip Select pin needs to be set high.
    digitalWrite(CS, HIGH);
```

```
//Put the ADXL345 into +/- 2G range by writing the value 0x00 to the
DATA_FORMAT register.
```

```
writeRegister(DATA_FORMAT, 0x00);
```

```
//Put the ADXL345 into +/- 4G range by writing the value 0x01 to the
DATA_FORMAT register.
```

```
//writeRegister(DATA_FORMAT, 0x01);
```

```
writeRegister(POWER_CTL, 0x08); // set power mode
```

```
writeRegister(FIFO_MODE, 0x80); // set FIFO mode
```

```
writeRegister(BW_RATE, 0x0A); // set sampling freq
```

```
}
```

```
void loop() {
```

```
readRegister(DATA_X0, 6, values); //read data
```

```
x = ((int)values[1]<<8)|(int)values[0]; //convert data to the right format
```

```
}
```

```
void writeRegister(char registerAddress, char value){
```

```
//Set Chip Select pin low to signal the beginning of an SPI packet.
```

```
digitalWrite(CS_ACC, LOW);
```

```

//Transfer the register address over SPI.

SPI.transfer(registerAddress);

//Transfer the desired register value over SPI.

SPI.transfer(value);

//Set the Chip Select pin high to signal the end of an SPI packet.

digitalWrite(CS_ACC, HIGH);

}

void readRegister(char registerAddress, int numBytes, char * values) {

    //Since we're performing a read operation, the most significant bit of the register
    address should be set.

    char address = 0x80 | registerAddress;

    //If we're doing a multi-byte read, bit 6 need to be set as well.

    if (numBytes > 1)address = address | 0x40;

    //Set the Chip select pin low to start an SPI packet.

    digitalWrite(CS, LOW);

    //Transfer the starting register address that needs to be read.

    SPI.transfer(address);

    //Continue to read registers until we've read the number specified, storing the
    results to the input buffer.

    for (int i = 0; i < numBytes; i++) {

```

```

    values[i] = SPI.transfer(0x00);

}

//Set the Chips Select pin high to end the SPI packet.

digitalWrite(CS, HIGH);

}

```

Arduino script to communicate with ADC board:

```

#include <SPI.h>

int CS_BNC = 4; //chip selection pin

void setup() {
  pinMode(CS_BNC, OUTPUT);
  digitalWrite(CS_BNC, HIGH);
}

void loop() {

  // read BNC

  SPI.setDataMode(CS_BNC,SPI_MODE2);

  SPI.setBitOrder(CS_BNC,MSBFIRST);

  //SPI.setBitOrder(MSBFIRST);

```

```

    digitalWrite(CS_BNC, LOW); // Start of data retrieval

    //delay(10);

    result = SPI.transfer(0x00);

    result = result << 8 | SPI.transfer(0x00);

    result = result << 2 | SPI.transfer(0x00);

    digitalWrite(CS_BNC, HIGH);

}

```

Arduino script to transmit data to a receiver with XBee:

```

#include <XBee.h>

#include <stdlib.h>

#define NUM_OF_SAMPLES 1 // data samples

#define SENSOR_NUM 1 // sensor ID, change with sensors

struct dataStruct {

    //int32_t time[NUM_OF_SAMPLES];

    int16_t x_accl[NUM_OF_SAMPLES];

```

```

int8_t sensorNum;

}__attribute__((packed));

XBee xbee = XBee();

struct dataStruct payl;
struct dataStruct *data = &payl;
uint8_t *payload = (uint8_t *)data;

XBeeResponse response = XBeeResponse();
Rx16Response rx16 = Rx16Response();
//Tx16Request tx = Tx16Request(0x0002, payload, sizeof(payload));

TxStatusResponse txStatus = TxStatusResponse();

void setup() {
  Serial3.begin(111702);
  xbee.setSerial(Serial3);
}

void loop() {

  data->x_accl[0] = x; //acceleration data

```

```

data->sensorNum = SENSOR_NUM;

Tx16Request tx2 = Tx16Request(0x0002, payload, sizeof(struct dataStruct));
// receiver ID 0x0002

tx.setFrameId(0);

xbee.send(tx);

//startTimer(TC1, 0, TC3_IRQn, 100); //last one is the frequency

}

```

Arduino script to receive data from a transmitter with XBee:

```

#include <XBee.h>

#include <stdlib.h>

#define NUM_OF_SAMPLES 1 // data samples

struct dataStruct {

    //int32_t time[NUM_OF_SAMPLES];

    int16_t x_accl[NUM_OF_SAMPLES];
}

```

```
int8_t sensorNum;

}__attribute__((packed));

uint8_t payload[sizeof(struct dataStruct)];

struct dataStruct *data = (struct dataStruct*)payload;

XBee xbee = XBee();

XBeeResponse response = XBeeResponse();

Rx16Response rx16 = Rx16Response();

void setup()
{
    Serial3.begin(111702);
    xbee.begin(Serial3);
}

void loop()
{
    do {
        xbee.readPacket();
    }

    while(!xbee.getResponse().isAvailable());
```

```
if (xbee.getResponse().getApiId() == RX_16_RESPONSE)
{
    xbee.getResponse().getRx16Response(rx16);

    unpackData(rx16, payload, 4);

    x2 = data->x_accl[0];

    ID = data->sensorNum;
}
}

void unpackData(Rx16Response rx16, uint8_t *array, int len)
{
    for (int i = 0; i < len; i++)
    {
        array[i] = rx16.getData(i);
    }
}
```

Time interrupt script (Arduino Forum, 2013):

```
startTimer(TC1, 0, TC3_IRQn, 800); // TC1 channel 0, setup time interrupt at 800Hz

void TC3_Handler() { //
    TC_GetStatus(TC1, 0);
}

void startTimer(Tc *tc, uint32_t channel, IRQn_Type irq, uint32_t frequency) {
    pmc_set_writeprotect(false);
    pmc_enable_periph_clk((uint32_t)irq);
    TC_Configure(tc, channel, TC_CMR_WAVE | TC_CMR_WAVSEL_UP_RC |
    TC_CMR_TCCLKS_TIMER_CLOCK1);
    uint32_t rc = VARIANT_MCK/2/frequency;
    TC_SetRA(tc, channel, rc/2); //50% high, 50% low
    TC_SetRC(tc, channel, rc);
    TC_Start(tc, channel);
    tc->TC_CHANNEL[channel].TC_IER=TC_IER_CPCS;
    tc->TC_CHANNEL[channel].TC_IDR=~TC_IER_CPCS;
    NVIC_EnableIRQ(irq);
}
```

APPENDIX B. A/D CONVERTER BOARD DESIGN

The 18-bit high resolution A/D Converter board is explained in section 3.2. The electronic circuit and PCB board is designed with KiCad software. The circuit diagram is provided in Figure B 1, while the PCB design is shown in Figures B 2 and B 3.

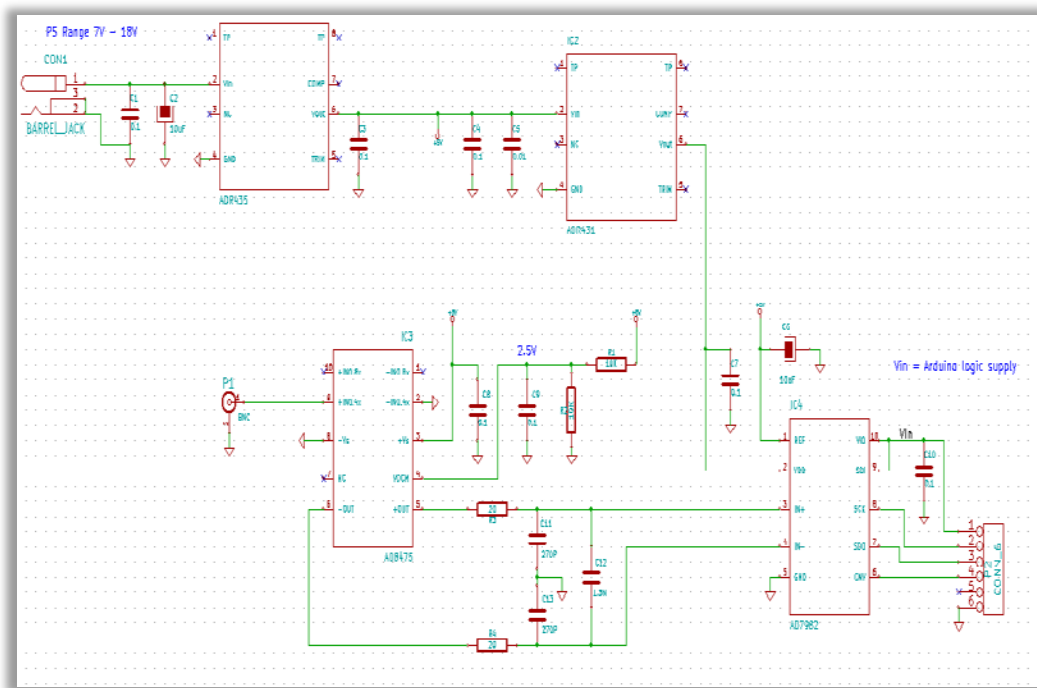


Figure B.1. Electronic circuit of the ADC board.

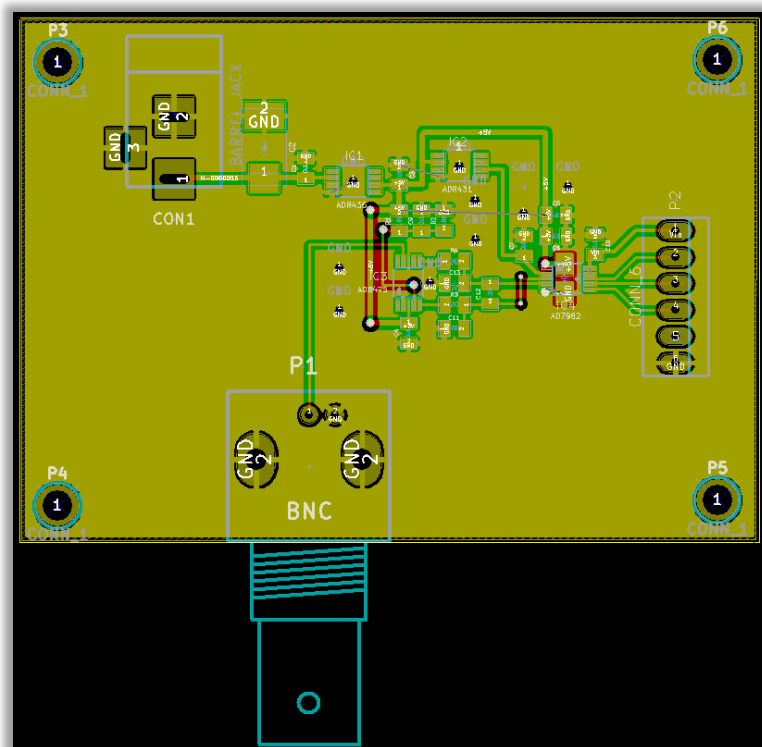


Figure B.2. PCB layout design of the ADC board.

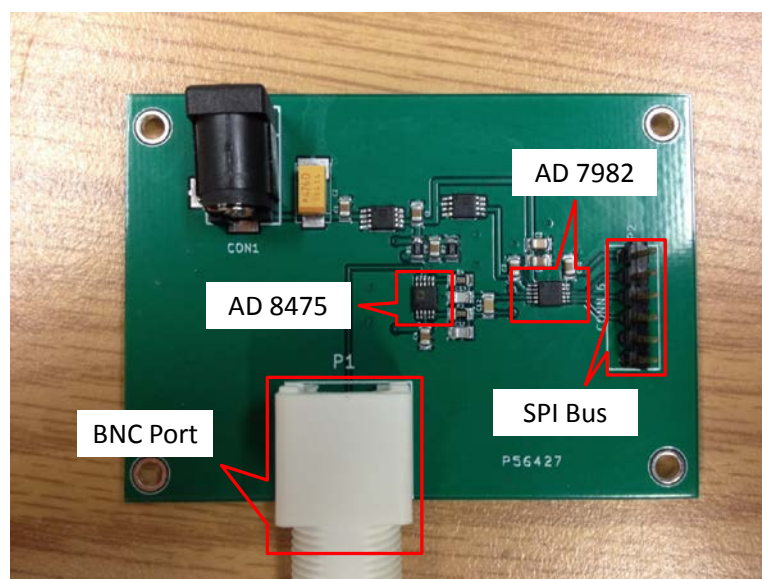


Figure B.3. Fabricated ADC board.

APPENDIX C. CONTROLLER AND ESTIMATOR GAIN OF THE BRIDGE CASE STUDY

The reduced order *design* model of the bridge has 30 states and there are 8 force input to the structure. Thus, the dimension of the OTD controller is 30×8 . The obtained discrete-time control gain is given as

$G = 1.0\text{e-}3 *$

[0.7159	0.7159	0.1822	0.1822	4.1263	4.1263	4.4615	4.4615;
0.4467	0.4467	0.1799	0.1799	0.8499	0.8499	1.1021	1.1021;
-1.4005	-1.4005	-0.9493	-0.9493	4.7297	4.7297	4.1503	4.1503;
-2.1689	-2.1689	-1.4949	-1.4949	3.4798	3.4798	2.3070	2.3070;
-1.6605	-1.6605	0.8711	0.8711	-2.8269	-2.8269	0.5843	0.5843;
0.6887	0.6887	0.8882	0.8882	-3.5079	-3.5079	0.0686	0.0686;
-1.8465	-1.8465	0.1641	0.1641	-0.8747	-0.8747	-0.2987	-0.2987;
-0.2692	-0.2692	-1.7704	-1.7704	0.7001	0.7001	-1.5315	-1.5315;
0.0566	0.0566	0.1435	0.1435	-0.8830	-0.8830	-0.7509	-0.7509;
1.2557	1.2557	-1.1285	-1.1285	-1.0524	-1.0524	3.8710	3.8710;
-2.0064	-2.0064	-0.4643	-0.4643	0.7510	0.7510	1.6104	1.6104;
0.0414	0.0414	0.4678	0.4678	-1.3894	-1.3894	1.9480	1.9480;
-0.4241	-0.4241	2.0789	2.0789	2.5278	2.5278	-3.0356	-3.0356;
-3.7357	3.7357	-0.0748	0.0748	0.3385	-0.3385	0.0237	-0.0237;
-0.1637	-0.1637	-1.1959	-1.1959	2.3027	2.3027	-0.9730	-0.9730;
-0.3821	0.3821	-0.0751	0.0751	0.1027	-0.1027	0.1144	-0.1144;
0.0222	-0.0222	-1.9916	1.9916	-0.1266	0.1266	0.5612	-0.5612;
1.7145	1.7145	0.6328	0.6328	-4.3651	-4.3651	-4.6690	-4.6690;
0.0179	-0.0179	1.7205	-1.7205	-0.0273	0.0273	-0.4585	0.4585;
-0.2687	0.2687	3.4267	-3.4267	0.0248	-0.0248	-0.0550	0.0550;
0.8838	0.8838	0.4941	0.4941	-2.4521	-2.4521	-3.3373	-3.3373;
0.1044	-0.1044	0.8619	-0.8619	0.0113	-0.0113	0.3715	-0.3715;
-1.0806	-1.0806	0.1387	0.1387	4.5090	4.5090	-2.2216	-2.2216;
-0.5490	-0.5490	0.2147	0.2147	1.4538	1.4538	-1.7380	-1.7380;
-2.0839	-2.0839	1.4930	1.4930	1.0966	1.0966	0.4129	0.4129;
-0.6277	0.6277	-0.0384	0.0384	0.0648	-0.0648	-0.0344	0.0344;
-1.6799	-1.6799	1.3166	1.3166	0.7477	0.7477	0.1556	0.1556;
3.5801	-3.5801	0.0637	-0.0637	0.0763	-0.0763	0.0324	-0.0324;

0.1666 -0.1666 0.2167 -0.2167 -0.0256 0.0256 0.0576 -0.0576;
 0.2492 -0.2492 0.0768 -0.0768 -0.0611 0.0611 -0.0079 0.0079]^T

The number of measurements is 9, while the number of states of the system is 30. Thus, the Kalman gain has a dimension of 9×30 . The discrete-time estimator gain is given as

$L = 1.0\text{e}+05 *$

[0.2789 -1.0273 -1.0273 -0.0572 -0.0572 -2.1639 -2.1639 -1.2714 -1.2714;
 0.2585 -0.8494 -0.8494 0.0289 0.0289 -1.6706 -1.6706 -0.9195 -0.9195;
 0.1625 -0.5996 -0.5996 -0.0450 -0.0450 -1.2887 -1.2887 -0.7649 -0.7649;
 0.1432 -0.4534 -0.4534 0.0392 0.0392 -0.8215 -0.8215 -0.4243 -0.4243;
 0.0942 -0.0739 -0.0739 0.1272 0.1272 -0.0270 -0.0270 0.0505 0.0505;
 0.1685 -0.4770 -0.4770 -0.1137 -0.1137 -0.5857 -0.5857 -0.2215 -0.2215;
 -0.0434 0.3111 0.3111 0.1679 0.1679 0.4757 0.4757 0.2373 0.2373;
 0.1577 0.0537 0.0537 0.3255 0.3255 0.2903 0.2903 0.2837 0.2837;
 0.0771 0.3662 0.3662 0.4939 0.4939 0.0903 0.0903 0.1208 0.1208;
 -0.1362 0.0272 0.0272 -0.2754 -0.2754 0.2852 0.2852 0.0792 0.0792;
 -0.0184 -0.0571 -0.0571 -0.1880 -0.1880 -0.1045 -0.1045 -0.1223 -0.1223;
 0.0071 0.3667 0.3667 0.3373 0.3373 0.1548 0.1548 0.0852 0.0852;
 -0.0650 -0.0439 -0.0439 -0.0824 -0.0824 -0.0883 -0.0883 -0.0783 -0.0783;
 0.0000 0.0000 0.0000 0.0000 0.0000 0.0000 0.0000 0.0000 0.0000;
 0.0096 -0.1760 -0.1760 -0.1390 -0.1390 -0.3428 -0.3428 -0.2399 -0.2399;
 0.0000 0.0000 0.0000 0.0000 0.0000 0.0000 0.0000 0.0000 0.0000;
 0.0000 0.0000 0.0000 0.0000 0.0000 0.0000 0.0000 0.0000 0.0000;
 0.2172 -0.2513 -0.2513 0.2471 0.2471 -0.3342 -0.3342 -0.0848 -0.0848;
 0.0000 0.0000 0.0000 0.0000 0.0000 0.0000 0.0000 0.0000 0.0000;
 0.0000 0.0000 0.0000 0.0000 0.0000 0.0000 0.0000 0.0000 0.0000;
 -0.0015 -0.5417 -0.5417 -0.6524 -0.6524 -0.5557 -0.5557 -0.4070 -0.4070;
 0.0000 0.0000 0.0000 0.0000 0.0000 0.0000 0.0000 0.0000 0.0000;
 -0.0358 0.0428 0.0428 -0.0491 -0.0491 0.0725 0.0725 0.0223 0.0223;
 0.0044 0.1102 0.1102 0.1409 0.1409 0.0956 0.0956 0.0767 0.0767;
 0.0028 -0.0206 -0.0206 0.0099 -0.0099 -0.0357 -0.0357 -0.0208 -0.0208;
 0.0000 0.0000 0.0000 0.0000 0.0000 0.0000 0.0000 0.0000 0.0000;
 0.0042 -0.0122 -0.0122 0.0037 0.0037 -0.0271 -0.0271 -0.0136 -0.0136;
 0.0000 0.0000 0.0000 0.0000 0.0000 0.0000 0.0000 0.0000 0.0000;
 0.0000 0.0000 0.0000 0.0000 0.0000 0.0000 0.0000 0.0000 0.0000;
 0.0000 0.0000 0.0000 0.0000 0.0000 0.0000 0.0000 0.0000 0.0000;]

VITA

VITA

Zhuoxiong Sun was born in Tangshan, China in 1987. He received his B.S. in Mechanical Engineering from Zhejiang University in 2010 and his M.S. in Mechanical Engineering from Purdue University in 2012.